

**Development of Deposition-Controlled Printhead for  
Printing Multifunctional Devices**

Development of Deposition-Controlled Printhead for Printing  
Multifunctional Devices

By

Islam Hassan, B.Sc., M.Sc.

A Thesis

Submitted to the School of Graduate Studies in Partial Fulfillment of the Requirements  
for the Degree Doctor of Philosophy

McMaster University

© Copyright by Islam Hassan, April 2022



## **Lay Abstract**

3D printing techniques, such as extrusion-based multimaterial printing, have recently been utilized to process silicones due to their versatility in different smart applications, including multigradient material and soft actuators. Although it represents significant progress, there are still several challenges, including the proper mixing during printing with a laminar flow regime, the fast switching between different inks, and the printing over complex topographies. Therefore, various printhead designs have been developed in this thesis to tackle these challenges. In particular, a mixer printhead has been designed to allow mixing during printing for building multigradient objects. Also, a scalable printhead has been developed to allow fast switching for creating pixelated structures. Finally, a simple mechanical system has achieved multimaterial printing over various nonplanar surfaces. To the best of the author's knowledge, the developed printheads can be used in many fields, such as soft robotics and smart devices.

## **Abstract**

3D printing technology, which has its origins in rapid prototyping, is increasingly used to build functional devices. Although 3D printing technology has been well developed for thermoplastic polymers and metals, it is still in the research phase for soft polymeric materials such as silicones. Silicones are an industrially vital polymer characterized by a broad spectrum of chemical and physical properties for several smart applications, including on skin printing, smart sensors, multigradient material, and soft actuators. Extrusion-based multimaterial printing is one of the 3D printing techniques that have been adapted due to its compatibility to process silicone-based materials for constructing various functional devices. However, there are several challenges such as achieving on the fly mixing at low Reynolds numbers regime, achieving fast switching while using Newtonian/non-Newtonian inks, and achieving multimaterial printing on nonplanar surfaces. The development of suitable and robust printheads that are able to tackle those challenges can expand the application of this technology to a wide range of fields. In this thesis, several deposition-controlled printhead designs have been created for 3D printing multifunctional devices using an understanding of microfluidics. The established printhead can be controlled to formulate different multigradient structures through on the fly mixing during the material printing. Moreover, the developed printhead can be adapted to print multi viscous inks with high switching rates up to 50 Hz. Through the developed system, the printhead was able to track topologies in real-time, allowing objects to be printed over complex substrates. These new capabilities were applied to fabricate functional structures in order to demonstrate the potential of the developed printhead approaches that can be

used in various applications, including smart sensors, soft robotics and multigradient objects.

## **Acknowledgment**

I am very grateful to my supervisor, Prof. P. Ravi Selvaganapathy, for his continuous support, encouragement, and advice. I would like to thank him for being always available to provide answers, research guidance, and discussions throughout this critical time. Thanks for being so understanding as I worked through critical time requirements. I have learnt extensively from him valuable lessons, both professional and personal. Your excessive support, teaching, and encouragement are appreciated more than you know.

I would like to express my sincere gratitude to Prof. Michael Brook and my collaborator, Sijia Zheng for their precious support and sharing their knowledge. Without this guidance it would not be possible to conduct this research. I also would like to thank BIOINTERFACES INSTITUITE specially Dr. Mehdi Keramane and to the technicians of the machine shop of the mechanical department, Mark Mackenzie, John Colenbrander for all the provided facilities and assistance.

Next, I would like to thank all partners and members of CAMEF group, for all your support, advice, friendship, and remarkable memories.

Lastly, I would like to express my indebtedness to my parents for their prayers, unconditional love, support, and blessed wishes throughout my life. Thanks to all my family, my brothers for their love and support. Words cannot express my gratitude to my wife Hagar Mustafa and my son Yahia for all the patience, love, and endless support.

# Table of Contents

<b>Acknowledgment</b> .....	<b>vi</b>
<b>Table of Contents</b> .....	<b>vii</b>
<b>List of Figures</b> .....	<b>xi</b>
<b>List of Tables</b> .....	<b>xxii</b>
<b>1 Chapter 1</b> .....	<b>1</b>
1.1 Introduction .....	1
1.1.1 In-situ DIW mixing systems .....	4
1.1.2 Rapid switching multimaterial DIW systems .....	5
1.1.3 Nonplanar DIW printing systems .....	5
1.2 Literature review .....	7
1.2.1 Soft polymer materials .....	7
1.2.1.1 Silicones .....	9
1.2.2 Additive manufacturing techniques .....	13
1.2.2.1 Powder bed fusion .....	16
1.2.2.2 VAT photopolymerization .....	18
1.2.2.3 Material jetting .....	22
1.2.2.4 Extrusion printing.....	25
1.2.3 Silicone 3d printing techniques.....	29
1.2.3.1 Vat polymerization technique for silicones.....	29
1.2.3.2 Inkjet technique for silicones .....	33
1.2.3.3 Extrusion-based techniques for silicones .....	39
1.2.4 Multimaterial 3D printing approaches for silicones .....	46
1.2.4.1 DIW multimaterial techniques for silicones.....	48
1.2.5 Printing silicones patterns over non-planar morphology .....	63
1.2.6 Multimaterial 3D printing applications for silicones .....	66
1.3 Thesis Motivation.....	69
1.4 Research Objectives .....	70
1.5 Thesis Outline .....	70
<b>2 Chapter 2</b> .....	<b>90</b>
2.1 Abstract .....	91

2.2	Introduction .....	91
2.3	Materials and Methods .....	94
2.4	Results and Discussion.....	96
2.4.1	TENG Fabrication Process .....	96
2.4.2	Evaluation of Snow-TENG Electrical Performance .....	98
2.4.3	Snow-TENG Working Mechanisms .....	100
2.4.4	Snow-TENG as a Self-Powered Arctic Weather Station.....	104
2.4.5	Snow-TENG as a Self-Powered Biomechanical Monitor .....	106
2.5	Conclusions .....	108
	References.....	109
<b>3</b>	<b>Chapter 3.....</b>	<b>112</b>
3.1	Abstract .....	113
3.2	Introduction .....	113
3.3	Experimental details and methods.....	116
3.3.1	Materials .....	116
3.3.2	Fabrication of MM-PHM Devices .....	117
3.3.3	Experimental Setup.....	119
3.3.4	Rheological Measurements.....	120
3.3.5	Numerical model Governing Equations.....	120
3.4	Results and Discussion.....	122
3.4.1	Printer Design .....	122
3.4.2	Active Mixing MM-PHM for Multimaterial 3D Printing.....	124
3.4.3	Simulation of The Mixing Process .....	128
3.4.4	Optimization of Mixing in the Printhead .....	131
3.4.5	Optimization of Mixing in the Printhead .....	135
3.4.6	Pneumatic Control of Mixing .....	137
3.4.7	Printing Compositionally Graded 2D and 3D Objects using MM-PHM..	141
3.5	Conclusions .....	143
<b>4</b>	<b>Chapter 4.....</b>	<b>148</b>
4.1	Abstract .....	149
4.2	Introduction .....	149
4.3	Materials and Methods.....	151

4.3.1	Materials .....	151
4.3.2	Fabrication of MSN3D Printhead .....	152
4.3.3	Experimental Setup.....	153
4.3.4	Rheological Measurements.....	155
4.3.5	Stress-Strain Curve Measurements.....	156
4.3.6	Numerical model Governing Equations.....	156
4.4	Results and Discussion.....	157
4.4.1	Printer Design .....	157
4.4.2	Simulation and Optimization of Multimaterial Switching of Viscous Inks 159	
4.4.3	2D Printing with Switching .....	163
4.4.4	3D Printing of Actuators.....	168
4.5	Conclusion.....	171
<b>5</b>	<b>Chapter 5.....</b>	<b>175</b>
5.1	Abstract .....	176
5.2	Introduction .....	177
5.3	Materials and Methods.....	179
5.3.1	Materials .....	179
5.3.2	Fabrication of Single Material Tracker.....	180
5.3.3	Numerical model Governing Equations.....	180
5.4	Results and Discussion.....	184
5.4.1	Printer Design .....	184
5.4.2	FEA Modeling .....	186
5.4.2.1	Mode-Frequency Analysis (Modal Analysis Modeling).....	186
5.4.2.2	Transient Structural Analysis.....	188
5.4.3	Optimization of tracker design using FEA .....	189
5.4.4	Printing on Wavy Surface.....	194
5.4.5	Printing on Dome Surface.....	197
5.4.6	Printing 2D and 3D patterns over complex surfaces .....	199
5.4.7	Multimaterial Printing 2D pattern over complex surfaces.....	203
5.5	Conclusion.....	207
<b>6</b>	<b>Chapter 6.....</b>	<b>211</b>
6.1	Conclusion.....	211

6.2	Recommendations for future work.....	215
<b>7</b>	<b>Appendix 1.....</b>	<b>219</b>
7.1	Flowrate measurements.....	220
<b>8</b>	<b>Appendix 2.....</b>	<b>227</b>
<b>9</b>	<b>Appendix 3.....</b>	<b>231</b>

## List of Figures

<b>Figure 1-1:</b> PDMS molecular structure in which n is several repeating monomers [SiO (CH <sub>3</sub> ) <sub>2</sub> ] unit. ....	10
<b>Figure 1-2.</b> Schematic diagram of the Powder bed fusion technique.[84].....	18
<b>Figure 1-3.</b> Schematic diagram of the vat photopolymerization technique.[97] .....	22
<b>Figure 1-4.</b> Schematic diagram of the inkjet printing technique.[119].....	25
<b>Figure 1-5</b> Schematic view of extrusion 3D printing techniques: (a) FDM and (b) DIW.[138].....	29
<b>Figure 1-6</b> Deposition strategies of ink; first is layer strategy, and the second is line strategy. Ink A is yellow, and Ink B is blue. After the mixing and curing processes, the printed lines turn to green.[153].....	36
<b>Figure 1-7 a)</b> Illustrations of the printhead configuration with a magnified view of the outlet region.[193] <b>b)</b> Multicore–shell nozzles and ink rheology. Optical image of the coaxial printhead connected to the core, interface, and shell ink reservoirs, and a schematic cross-sectional view of the C–S printhead.[199] <b>c)</b> Multicore-shell 3D printing illustration with a cross-sectional view of nozzle-based printhead and core-shell dielectric elastomer fiber (DEF).[200].....	50
<b>Figure 1-8</b> Optical image of the impeller-based active mixer, and schematic illustration of the mixing nozzle in operation for 3D printing of two inks with particles of a different colour.[201].....	52
<b>Figure 1-9 a)</b> Multi-material microfluidic printhead. Illustration of the nozzle outlet with dimensions. [182] <b>b)</b> Illustration of the 3D printing system with all connections joined to the junction and needle.[180] <b>c)</b> Schematic of switching printheads that control the extrusion pressures $p_1$ – $p_4$ for materials 1–4, with a Voxelated matter created using a $4 \times 4$ -nozzle, four-material, 2D printhead.[47].....	54
<b>Figure 1-10</b> Fluid types with the influence of shear rate on (a) viscosity and (b) shear stress. [217, 218].....	57

**Figure 1-11** Typical operation ranges of micromixers, a) Passive mixer, b) Active mixers..... 61

**Figure 2-1** 3D printing process, architecture along with optical and mechanical properties of the snow TENG. (a) Schematic illustration of the printing process of the snow TENG, (a-i) printing of a conductive polymer electrode; inset shows the chemical composition of the PEDOT:PSS ink, (a-ii) Printing of the triboelectrification layer based on UV curable silicone ink; inset reveals the chemical composition of the silicone ink. (b) Schematic illustration of the structure of the device, featuring micropatterned surface of the UV curable silicone. SEM images on the left showing the micropattern at different magnifications. Scale bars are 100 $\mu$ m and 50 $\mu$ m, respectively. (c) The working principle of the device based on snow triboelectrification. (d) A photograph showing the high transparency of the silicone layer; the logo of McMaster University shown in the background can be clearly recognized through the silicone layer. (e) Exposure of the snow TENG to different stretching conditions. .... 98

**Figure 2-2** Evaluation of the electrical performance of snow TENG for harvesting energy from falling snow. (a)  $V_{oc}$  and  $J_{sc}$  define the triboelectrification performance of snow TENG using different positive and negative triboelectric materials. (b, c) Influence of the UV light intensity and curing time of the triboelectrification layer (silicone) on the electrical output of the device. The plots compare open circuit voltage, short-circuit current, and short circuit charge under different conditions. .... 100

**Figure 2-3** The working mechanisms and FEM simulations of snow TENG. (a, b, c) Schematic illustration showing the working mechanism of snow TENG utilizing three different operating modes including tapping, sliding, and snowfall. (d, e, f) FEM simulation results for the corresponding operation modes. .... 101

**Figure 2-4** Characterization of the electrical properties of snow TENG in tapping and sliding scenarios. (a) The testing setup showing a vertical linear motor, snow layer, and the fabricated snow TENG. (b) Open circuit voltage,  $V_{oc}$ , (c) Short circuit current  $J_{sc}$ , and (d) External load dependent peak power in tapping scenario. (e) The charging profile of 1  $\mu$ F capacitor. (f)  $V_{oc}$  during 8000 cycles of repeated loading and unloading, reflecting the stability of the snow TENG device. (g) A visionary scene for a snowy

location where the snow TENG can be using for harvesting energy of moving bicycles or cars. (h) A photograph of an energy-harvesting unit attached to a bicycle. Inset: Actual snow TENG device on the wheel. (i) Measured Voc, (j) measured Jsc, and (k) external load dependent peak power in the sliding scenario. .... 104

**Figure 2-5** Snow TENG as a Self-powered arctic weather station. Snow TENG can be used as a multifunctional weather station for measuring several functions including (a) Snowfall angles or the direction of falling snow. (b) Snowfall rate. (c) The speed of the wind. (d) The snow accumulation depth..... 106

**Figure 2-6** Investigation of snow TENG as a wearable energy harvester and self-powered biomechanical monitor. (a) Harnessing and sensing biomechanical movements by attaching snow TENG to different locations of the human body. (b) Measurement of the electrical output from a snow TENG device that uses a snowfall mode when attached on the (i) shoulder, (ii) wrist, and (iii) knee. (c-i) A photograph of the snow TENG device assembled and attached to the bottom of a snow boot as a self-powered biomechanical sensor. (c-ii) Electrical outputs from the snow TENG as the wearer performs different movements – running, jumping, walking, and marching..... 107

**Figure 3-1** Direct ink writing 3d printing platform. A schematic diagram of the customized printhead mixer is attached to the ink barrels connected to pressure regulators. **i)** Schematic description of the UV-aided mixing printhead. The UV-curable silicone is deposited through a micronozzle and exposed to UV radiation using a set of optical fibers synchronized with the extrusion printhead mixer. The rapid curing lets the production of a 3D-shaped structure along the path of the UV-direct writing mixing tool. **ii)** A CAD model of the microfluidics printhead mixer consisting of the four independently actuated pneumatic flow circuits controlled the inlet pressure of each material through a metal needle 25 gauge and heat threaded inserts/ check valves on the top. Red and blue arrows are UV curable silicone liquids fed into the microfluidic printhead mixer from the pneumatic barrel syringes and exited from the output..... 124

**Figure 3-2** MM-PHM configurations. **a)** Two modes have been used for mixing **i-** active mixing mode using pressure segmentation with three different configurations, **ii-** hybrid mixing routine using static mixer along with pressure segmentation pulses. **b)** Schematic

illustration of the section views of the MM-PHM nozzle, **i-** The exploded 3D model of the MM-PHM, **ii-** Schematic illustration of the Fluid volume in operation for 3D printing of four inks with different particles color. Each ink enters the mixing chamber of diameter  $d_i$  through a separate inlet and is homogenized in a mixing chamber of width  $d_m$  by a static mixer of diameter  $d_s$  with outlet diameter of  $d_o$ . **c)** Optical image of the MM-PHM, **i-** outlet needle diameter, **ii-** an actual image of the static mixer, **iii-** end of inlet chamber body, **iv-** the top of mixing chamber body..... 128

**Figure 3-3** Operating scheme of the multi-material mixer printhead in case of simulation and experimental process. **a)** An illustration depicting the process parameters of the inlet pressure pulses, including cycle period, pulse amplitude, phase shift, and duty cycle. **b)** Principle of MM-PHM operation. Inks A and B enter the MM-PHM and are combined within the mixer (volume  $\approx 10-45 \mu\text{L}$ ). The pneumatic pressure signal applied to the ink input inlets (input A, B) determines the volume of plugs injected ( $P_v$ ) and its sequence. The length of this pulsing volume region was determined by the pulsing frequency of the inlet pressure signal. Expanding the diameter of the mixer volume chamber further enhanced the mixing. **c)** The simulation setup and boundary conditions applied for simulating flow through the printhead geometry to optimize the mixing process. **i)** The computational model of the multi-material mixer printhead consists of two central regions; the first is the channel structure with pressure inlet regime, and the second is the printing trace block along with the boundary conditions for both regions. **ii)** A schematic illustration for the experimental scheme for mixing using the pulsing technique..... 130

**Figure 3-4** Simulation and experimental validation of mixing in the printhead. **a)** Numerical and experimental evaluations of mixing index at different Strouhal number "St" at low Reynolds number 0.017 with different proposed configurations. **b)** CFD inks concentration distribution contours generated from simulation analysis under modulating driving pressure "6 bar" at the inlet 1 and 2 with different frequencies (2, 5, 9, and 20 Hz) at steady state (after 12 sec). The images also show the cross-section of the extruded ink at the nozzle (section A-A) and its comparison with the actual printed trace of the filaments extruded under the same conditions..... 134

**Figure 3-5** a) Comparison between the proposed configurations showing the degree of mixing obtained and switching time for each case. b) Transient simulation of inks concentration contours at 9 Hz and the mixing chamber diameter 2 mm for the mixing junction and printed trace with sections at different locations, i) mode 1: without a static mixer, and ii) mode 2: with a static mixer. .... 137

**Figure 3-6** a) Numerically calculated mixing index for different Reynolds number "Re" ranging from 0.00025 to 0.0025 illustration the effect of pulse amplitude on the mixing index by examining the mixing index at each Re for different St ranging from 0.005 to 0.12, inset is showing the optimized St at each Re with the corresponding maximum mixing index obtained. b) Numerically calculated mixing index for phase shift angles ranging from 0 to 360°. The middle blue region shows the best mixing range. c) The plot of duty cycle (pulse duration /total cycle time) at mixing ratio (Ink 1: Ink 2) at satisfied Re 0.0017 and St 0.045. The green zone is the range of duty cycles over which composition can be controlled linearly. d) Image of a 2D carpet structure showing the effect of mixing ratio on the printed color area, the color changing from yellow at the right to the blue at the left of the 2D carpet—the color gradient rectangle on the top showing the color gradient fill. .... 140

**Figure 3-7** a) Gradient-colored model printed along with the actual image of the printhead mixer with four different inlets. b) 2D printed color map. i) A schematic illustration of the 2D color map, including the four inlets inks with different colors magenta, yellow, cyan, and green. Insets are "on-left" the bottom of the actual printhead mixer image, and "on-right" 3d printing process under UV light for instant curing. ii- The actual 2D color map, printing nine different colors using four inlet colors by mixing between different colors. c) 3D printed Rubix cube. i) A schematic illustration of the 3D Rubix cube. ii) The actual image of the 3D Rubix cube, showing the capabilities of 3d printing structure. .... 142

**Figure 4-1** Direct ink writing 3d printing platform for multimaterial highly switchable nozzle 3D printhead (MSN3D). a) Schematic of the MSN3D design. Both the MSN3D movements and UV optical fibers are synchronized to cure the deposited ink of the micro-single nozzle by exposure to UV radiation. i) A schematic of the MSN3D half-

section shows red, green, and blue indicators for different inks supplied into the MSN3D pneumatically, with channel diameter of 500  $\mu\text{m}$  and length of 6 mm, printhead outlet diameter of 230  $\mu\text{m}$ . **b)** Images of the fabricated printhead **i-** the top (top) and side (**ii-** middle and **iii-** bottom side) views of a single nozzle, four-material MSN3D printhead, Scale bars, 5 mm. .... 158

**Figure 4-2 Operating scheme of viscous ink flow through the MSN3D printhead. a)**

Schematic of the MSN3D printhead operation, where  $P_H$ – $P_L$  represents the extrusion pressures for materials 1–2. The low-pressure  $P_L$  has to be defined to eliminate any backflow in the low-pressure channel. Below is an illustration representing the process parameters of the inlet pressure pulsations, including cycle period, pulse amplitude, and phase shift. **b)** CFD simulation to optimize the switching process for backflow elimination. The MSN3D printhead computational model includes two core regions: the channel structure with pressure inlet regime, the printing trace block, and boundary conditions for both areas. **c)** The corresponding pressure difference between the intersection pressure and lower pressure  $P_L$  with different lower pressure percentages presented on the left y-axis, while the on the right axis, the corresponding backflow shift (zero means no backflow, a positive value means coaxial filament, negative value mean backflow) with lower pressure percentage. **d)** CFD distribution contours. **i)** CFD inks concentration, to find the  $P_L$  value at which backflow vanishes,  $P_H$  kept at “6 bar” at the inlets, and  $P_L$  changed from 3-5.2 bar with frequency 9Hz at steady state (after 1 sec). **ii)** CFD pressure contours, to show the pressure difference on the printhead channels at different  $P_L$  values (3-5.2 bar). **e)** The corresponding pressure difference and backflow shift with different frequencies at different lower pressure values. **f)** To show the effect of the frequency on the backflow at the critical  $P_L$ ,  $P_H$  kept at “6 bar” at the inlets and  $P_L$  kept at “4 bar” with different frequencies (3, 9, and 20 Hz) at a steady-state (after 1 sec). **j)** CFD inks concentration distribution contours at 20 Hz,  $P_L$  4 bar,  $P_H$  6 bar with different feeding rates, showing the effect of feed rates on the printed segment length. .... 163

**Figure 4-3 Printing segmented objects with equal distances. a)** One continuous filament output with increased switching frequencies from a two-material nozzle. **b)** A multi-material MSN3D printhead with a circular print path using silicone inks (V35H). **i-**

two inks, **ii**- four inks. Scale bars in b, 10 mm. **c**) A multi-material MSN3D printhead with a segmented printed board using silicone inks (V35H) with the target printed board. **i**- The printed segmented board with different segments width, scale bar 16mm. Two magnified photos of for the segmented board, the upper one with a scale bar, 4 mm, lower one with a scale bar, 2 mm. **ii**- The relative intensity of the red and blue colors from the transition zones in both X and Y directions, the shaded area is the standard deviation from n=4 measurements..... 165

**Figure 4-4 Printing segmented objects with random distances.** **a**) Printing a two-material pattern using a single nozzle printhead by switching between two materials (V35H black, V35H white) for creating CAMEF logo word. **i**- The target pattern created by the G-code, **ii**- The actual printed pattern, Scale bar, 10 mm. **b**) Printing a 2D pattern McMaster word. **i**- The actual printed pattern, Scale bar, 10 mm, **ii**- The target pattern created by the G-code. **c**) Raster scan printing of a random triangular pattern in silicone V35H (black) and silicone V35H (white) using an MSN3D printhead. **i**- The actual printed pattern, Scale bar, 10 mm, **ii**- The target pattern created by the G-code. .... 168

**Figure 4-5 MSN3D printing of soft-actuator gripper.** **a**) MSN3D printing of a soft actuator using two-material MSN3D printhead. Print time, 40 min, **i**- the printed actuator after curing, scale bar, 10 mm. **b**) Illustration of the design elements of the actuator, **i**- actuation pattern for the single actuator used to produce bending motion. **c**) Actuation pattern for three soft actuators network used to work like a gripper. **d**) Illustration of the bending angle of a single actuator as a function of input pressure. Front view of the soft actuator under, **i**- P=0 KPa, **ii**- P=70 KPa. **e**) Stress-strain curves from n = 4 tensile tests for stiff heat-curable silicone “HSC” (2.4 MPa; red) and Flexible HSC (0.75 MPa; blue). **f**) Photographs of the soft gripper under two states, **i**- pressure off, **ii**- pressure on grasping and lifting test empty conical tube. **g**) The soft gripper was attached to the 3d printer frame for the grasping test. **i**- 30 g weight inside a conical tube, **ii**- 180 g weight inside a conical tube, **iii**- 250 g weight. **h**) Illustration of the bending angle of a single actuator as a function of actuation frequency at input pressure 100 KPa. .... 170

**Figure 5-1 Direct ink writing 3d printing platform with a passive mechanical system tracker.** **a**) A schematic diagram of the customized printhead attached to the ink barrel

connected to pressure regulators. **i)** On the left is the actual mechanical model for tracking  $z$  motion. **ii)** The internal structure of the ball bearing chamber showing the free rotating ball and ink opening. **b)** At the contact between the needle and the complex surface, different ball support configurations have been used to allow smooth movement, **i)** one ball support configuration, **ii)** two balls support configuration, and **iii)** three balls support configuration. .... 186

**Figure 5-2** Finite element analysis for investigating the operating frequencies and optimizing the process parameters. **a)** Modal analysis FEA with showing the used boundary conditions and constraints. **b)** The first three mode shapes show each mode's natural frequencies while the maximum working frequency will not exceed 20 Hz. **c)** Transient structure analysis FEA model, showing the simplified model used in the transient analysis and boundary conditions, on the right are the parameters investigated using the transient model. **d)** The support configurations showing the studied probes in each configuration; **i)** one ball support, **ii)** two balls support, and **iii)** three balls support. .... 189

**Figure 5-3** FEA results **a)** FEA validation by conducting a Comparison between FEA deflection and experiment results using on ball confirmation, on the left the moving bath used in the FEA and experimental. Then, we tested different parameters, illustrated the moving path on the left, and investigated the process parameters to get minimum deflection. **b)** needle length using one ball configuration with two different values at feed rate eight mm/s, coefficient of friction of 0.2, a load of 10 N. **c)** The effect of feed rate on the structure deflection, while using a coefficient of friction of 0.5, a load of 10 N and needle length of 4 mm. **d)** The effect of friction between ball and substrate on the model deflection, while using feed rate of 1 mm/s, a load of 10 N and needle length of 4 mm. **e)** The effect of the structure weight on the model deflection, while using feed rate of 8 mm/s, coefficient of friction of 0.2 and needle length of 4 mm. **f)** Comparing between the three-ball support configurations on the model deflection, while using feed rate of 8 mm/s, a load of 10 N, coefficient of friction of 0.2 and needle length of 4 mm. .... 193

**Figure 5-4** Printing feasibility study of each configuration with complex wavy surface. **a)** Feasibility contours by varying the wavy relative height and wavelength using

longitudinal path pattern. The actual printed patterns with different wavy textures are on the right using the three ball support configurations: **b)** one peak wavy surface, **c)** two peaks wavy surface, **d)** three peaks wavy surface, and **e)** multiple peaks wavy texture. All scale bars are 10 mm. .... 196

**Figure 5-5 a)** Printing feasibility over dome surface by creating interfered structure like mesh pattern using the three-ball support configurations two different dome heights. **b)** Investigating the printed line thickness range with different inlet air pressure. We got a minimum thickness of 0.8 mm; however, the bath was not continuous. **c)** Spiral pattern printing over a doom planer using one ball configuration. All scale bars are 10 mm. ... 199

**Figure 5-6 a)** Mesh printing over a Bézier surface using the one ball configuration, with mesh element size 5mm\*5mm. **b)** Mesh printing over an inclined surface using the one ball configuration, with mesh element size 5mm\*5mm. **c)** Spiral pattern printing over an actual hand planer using one ball configuration, with a pitch of 4 mm. **d)** 3D Wall printing over dome surface using a hybrid system in two steps, **i, ii)** printing low aspect ratio over a nonplanar surface using the three-ball support configuration, then **iii, iv)** print higher aspect ration structure "yellow color" using conventional extrusion printing. All scale bars are 10 mm **v)** The print thickness as different number of layers are printed using the tracker first, then continue with a conventional extrusion printing..... 203

**Figure 5-7** Multimaterial printing over complex surfaces. **a)** Multimaterial passive control mechanical system for printing over nonplanar surfaces by integrating microfluidics printhead with the tracking mechanism, the actual figure on the left before loading the inks, and the right one after loafing four barrels inks. **b)** Printing a multimaterial spiral pattern over an actual hand planer using one ball configuration with three different inks. Printing four colors regions over complex surfaces using one ball configuration; **c)** dome surface, and **d)** Bézier surface. All scale bars are 10 mm ..... 206

**Figure 7-1 a)** Flowrate as a function of Pressure by varying it from 1 to 7 bar. **b, c)** Reynolds number and entrance length as a function of flow rate from 50 to 500  $\mu\text{l}/\text{min}$ . ..... 221

**Figure 7-2** Shows the periodic and continuous deposition regions for the **a)**  $Q=70\mu L/min$ , **b)**  $Q=127\mu L/min$ , **c)**  $Q=195\mu L/min$ , **d)**  $Q=263\mu L/min$ , **e)**  $Q=331\mu L/min$ , **f)**  $Q=403\mu L/min$ , **g)**  $Q=455\mu L/min$  condition. **h)** The resulting traces under four lights with 4 cm distance between the light and needle tip at an intensity of 20% - at 7 bar, with **(i-iii)** real example of three printing deposition continuous, slopped, and periodic. .... 222

**Figure 7-3** Trace height, trace width, and aspect ratio as functions of pressure at **(a-c)** 4 lights configuration. **(d-f)** 2 lights configuration. **(g)** comparison between maximum aspect ratio between different settings. **(n)** Schematic and real photo of the 4-light setup. .... 224

**Figure 7-4** RGB analysis for quantifying the printed object homogeneity, for three different regions **a)** blue zone, **b)** green zone, and **c)** yellow zone. For each zone **i- R**, **ii- G**, **iii-B**, and **iv-** average RGB intensities were presented. .... 225

**Figure 7-5** Homogeneity index measurements for three different printed zones. .... 225

**Figure 8-1** Rheological properties of different silicone inks. Log–log plots of the apparent viscosity (i) and the shear stress (ii) as a function of shear rate for UV curable silicone elastomer inks (a-Newtonian inks, b- Viscoelastic inks), fitted by the Herschel–Bulkley model. .... 228

**Figure 8-2a)** Material transitions schemes for the raster and vector scan methods of printing. **b)** Offset length and print-path design. **i-** Due to the finite output of the channel,  $L_o$ , and inertance in the system, a delay occurs when switching between materials. This delay can be corrected by introducing an offset length and during parallel printing of horizontal lines in silicones (red, and blue). **ii-** Offset corrected printing of resolution grids using silicone viscous inks, showing gradually smaller features. Scale bars: bottom, 8 mm; top, 4 mm. **c)** Printing a CAMEF logo word (V35H black, V35H white) for without using offset, which created a distorted pattern. **d)** Segmental pattern using MSN3D printhead with two different inks, UV curable silicone V35; black, UV curable adhesive NOA68, white. .... 229

**Figure 8-3** MSN3D printing of soft-robotic actuator. **a)** MM3D printing of a soft robotic MSN3D printhead under UV curing. **b)** Illustration of the design elements of the two

chambers actuator. i- schematics of the two states on/off actuator corresponding to the step pulse. ii- Cad model of the actuator. c, d) Photographs of the printed actuator and the assembled actuators. e) Stress–strain curves from tensile tests for V35H stiff (0.6 MPa) and V35H flexible (0.8 MPa) silicones. f) Printed 3d patterns like finger with two materials with different periodical arrangements. .... 229

**Figure 8-4** Assembling steps used to create a soft-gripper. a) Dip coating process using UV curable silicone, to create thin film covering the printed soft actuator (around 1 mm). b) Assembling operation with the gripper arm, which made from PLA using conventional 3d printer. The arm was attached to the soft actuator using super glue and left for 24 hrs for curing..... 230

**Figure 9-1 FEA results** a) Deformation contours in case of one ball configuration with different needle length showing the deflection with different positions. Then, we tested different parameters investigated the process parameters to get the effect on the generate stress; **b)** needle length using one ball configuration with two different values at feed rate 8 mm/s, coefficient of friction of 0.2, load of 10 N. **c) i-** The effect of the structure weight on the model equivalent stress, while using feed rate of 8 mm/s, coefficient of friction of 0.2 and needle length of 4 mm. **ii-** The effect of feed rate on the structure deflection, while using a coefficient of friction of 0.5, a load of 10 N and needle length of 4 mm. **d)** The effect of feed rate on the structure equivalent stress, while using coefficient of friction of 0.5, load of 10 N and needle length of 4 mm. **e)** The effect of friction between ball and substrate on the model equivalent stress, while using feed rate of 1 mm/s, load of 10 N and needle length of 4 mm. **f)** Comparing between the three ball support configurations with the model equivalent stress, while using feed rate of 8 mm/s, load of 10 N, coefficient of friction of 0.2 and needle length of 4 mm. .... 232

**Figure 9-2 Printing feasibility study of each configuration with complex wavy surface.** a) Feasibility contours by varying the wavy relative height and wavelength using transverse path pattern. On the right is the actual printed patterns with different wavy surfaces using the three ball support configurations, **b)** one peak wavy surface, **c)** two peaks wavy surface, **d)** three peaks wavy surface, and **e)** multiple peaks wavy surface. .... 233

**Figure 9-3** a) Mesh wavy interfered pattern printing over an inclined surface using the one ball configuration, with mesh element size 2mm\*2mm. b) Zig-zag pattern printing over a dome surface using the one ball configuration, with pitch size of 4 mm. c) Wavy zig-zag pattern printing over an inclined surface using one ball configuration, with pitch of 7 mm. All scale bars are 10 mm. .... 233

**Figure 9-4** a) 2D plot for thickness uniformity for the printed color maps over the dome surface. b) 3D surface contour for the printed color maps over the dome surface. c) the gap scheme in case of i) the top of the dome surface and ii) at the near bottom level, showing how the gap is decreased in which affects the printed thickness. .... 234

## List of Tables

<b>Table 1-1</b> AM approaches for polymers besides the advantages and disadvantages. ....	15
<b>Table 1-3</b> Comparison of the silicone 3d printing features for available AM techniques. .....	46
<b>Table 1-4</b> Comparison of multi-ink printing approaches for silicones. ....	54
<b>Table 1-5</b> Passive and active mixing techniques comparison in the microfluidic field. ...	61
<b>Table 3-1</b> UV curable silicone inks formulations used in this work given in weight percentage .....	123
<b>Table 7-1.</b> Comparison between the published mixing printing systems with the current work. ....	225
<b>Table 8-1</b> UV curable silicone inks formulations used in this work given in weight percentage .....	228
<b>Table 8-2</b> Heat curable silicone inks formulations used in this work given in weight percentage. ....	228
<b>Table 9-1.</b> Comparison between the published tracking printing systems with the current work. ....	234

# 1 Chapter 1

## Introduction and Background

### 1.1 Introduction

In recent years, additive manufacturing (AM), also sometimes referred to as 3D printing, has become a useful method to create complex functional devices from several materials such as metals, ceramics, and polymers.[1-6] Using 3D printers, the required 3D structures are created layer by layer over moving stages controlled by a computer numerical controlled system. Unlike other traditional manufacturing techniques, 3D printing can reproduce complex 3D geometries from digital computer-aided designs and create them without material waste. Additionally, 3D printing has gained popularity in academic research and industrial production due to its ability to produce on-demand products. As a result, many researchers have started to utilize additive manufacturing technology to build soft operational structures with high complexity that are difficult or impossible to accomplish using traditional manufacturing approaches. Today, there are many 3D printing techniques based on different working principles to satisfy different material, speed, and resolution requirements. These printing techniques can be divided into seven categories: powder bed fusion, vat photopolymerization, material jetting, material extrusion, binder jetting, sheet lamination, and energy deposition.[1-4, 6] One of the most frequently used materials for AM is soft polymers due to their wide range of mechanical and chemical properties.

Due to its unique structure and material characteristics, many applications in medicine and manufacturing use soft polymeric materials. In molecular terms, polymers consist mainly of a large number of similar units connected together. Polymers include a variety of synthetic and natural materials, including thermoplastics, thermosetting, and elastomers.[1-4] Due to their repeating subunits, which can easily be deformed, polymers have many distinctive physical features, such as softness, compliance and elasticity.[1-4] Polymers are of interest for use in devices that interact with living beings, such as soft robotics,[7-10] biomedical equipment and devices,[11-13], and wearable electronic devices.[14-16] Examples of polymers used to mimic the properties of biological materials are hydrogels, silicone elastomers, and biodegradable polymers such as polycaprolactone (PCL).[1-4] These polymers are commonly fabricated by plastic extrusion, injection moulding, and/or soft lithography.[1-4] However, these processes require a high-cost equipment setup, especially when incorporating more than one polymer, preventing complex multimaterial structures from being designed.[1-4] Thus, 3D printing techniques have been developed to pattern different soft polymeric materials on demand.

The direct ink writing “DIW” method is one of the widely used 3D printing methods for printing soft polymers. DIW requires a flow actuation mechanism for extruding the print material, such as air pressure or a piston.[17-19] This actuation results in the deposition of a fiber of the material (ink) on the print substrate. After the ink is deposited in the required shape, there are two main factors to maintain its extruded shape. The first factor is the ink rheological properties. For instance, print material with viscoelastic behaviour like shear thinning can facilitate easy extrusion from a narrow nozzle while still retaining the printed shape, as the ink viscosity increases after it leaves

the nozzle tip.[17-19] The curing process is the second factor that can be used to solidify the printed shape. Curing can be light-based or heat-based depending on the ink's chemical compositions.[17-19] Depending on the ink viscosity, the curing process can be introduced during the ink deposition or after ink deposition. Such compatibility of DIW with different curing mechanisms makes it suitable for printing a large variety of materials. Therefore, many soft materials have been printed using DIW, such as polyurethane (PU),[20] silicone elastomers,[21, 22], and hydrogels.[23-25]

In general, multimaterial 3D printing can be considerably useful in order to embed functional properties into the product or part. DIW printing is better suited for multimaterial printing over other techniques like vat photopolymerization.[1-4] In the case of DIW printing, a printhead is used to deposit the ink at the target locations. This feature makes the switching of the printed material more manageable, especially with the adaptable 3D printer assembly design. In addition, the extrusion process and curing process can be achieved in a single or separate operation.[1-4] Despite the capabilities of the DIW method for multimaterial printing, several challenges need to be overcome to fabricate complex devices with soft materials. One of these challenges is achieving the mixing of constituent materials deposited at low Reynolds numbers.[26, 27] Another interesting challenge is achieving fast multi-ink printing of a single object with heterogeneous material compositions with different soft materials. [26, 27] Another challenge is creating complex features using DIW by printing over nonplanar surfaces, requiring more investigation to adjust printing conditions.[28, 29]

### 1.1.1 In-situ DIW mixing systems

An essential challenge of DIW printing is attaining in-situ mixing of soft materials delivered at low Reynolds number flow regimes.[30] There are different methods for achieving mixing within the DIW printing, which can be categorized into two main types. The first type is passive mixing, which is significantly dependent on the volume flow rate and design of the mixing element. Microfluidic channels have been utilized to passively mix small volumes of fluids [31] using chaotic advection or secondary flows.[32, 33] By and large, passive mixers are better suited to low-viscosity fluids, with diffusion being the primary mode for mixing and do not work well at higher viscosities. They also need significant priming volume for complete mixing. Alternatively, the active mixer can be used for achieving high degree mixing within a small volume and rapidly, especially for those fluids that have higher viscosity or those with viscoelastic behaviour.[34] For example, a rotational impeller has been integrated inside the printhead to initiate the mixing process while printing the mixed material.[35-38] Although useful for mixing, the rotational element needs an external power supply, making active mixers more complicated and bulkier.[39] On the other hand, simpler static mixers are used to mix up to three different inks [40-42], but their mixing performance is closely related to their flow rate and priming volume, limiting the printing complexity. The ability to mix several fluid streams in small volumes with a high degree of uniformity and speed would enable advances in DIW 3D printing. Yet, the previously mentioned DIW mixing systems are not scalable and still suffer from a slow switching process between compositions ( $> 6$  sec).[27, 40] Ideal DIW mixing systems should be scalable and have the ability to achieve a complete on the fly mixing between a large number of inks with switching rapidly between compositions.

### **1.1.2 Rapid switching multimaterial DIW systems**

DIW 3D printing has not only focused on single material deposition, but researchers have also used the DIW technique with a variety of materials to create functional devices with excellent uniformity towards end-use.[41, 42] Yet, there are still several challenges associated with multimaterial printing by the DIW technique, including fast switching printing to create pixelated patterns. Systems have been developed to achieve multimaterial printing through multinozzle printheads, each containing a different ink that discontinuously deposits multiple materials based on the design.[43-46] However, the printing speed in these systems reduce as the number of nozzles/syringes is increased along with using a syringe pump-driven system. That can lead to printing imprecisions during start-stop operations, especially during 3D pixelated printing. Alternatively, a continuous multiple ink extrusion process has been accomplished through a single nozzle printhead with a rapid ink switching capability within the nozzle.[47] The developed system was driven pneumatically, allowing 3D pixelated printing to be created with a switching frequency up to 50 Hz.[47] This system used the specific property of Herschel-Bulkley type viscoelastic inks to achieve high-speed switching, but this approach and deemed not possible for viscous inks.[47] Therefore, there is a need to achieve rapid switching between different inks with synchronized deposition for a wide range of commercially available Newtonian inks, which can expand the number of applications benefits from pixelated 3D DIW printing.

### **1.1.3 Nonplanar DIW printing systems**

Developing multifunctional devices that require an interface with the biological components is essential for biomedical applications [48] and wearable electronics.[49] The

ability to directly print over topologically complex and non-planar surfaces using the DIW technique could potentially enable new functionality and applications. Various approaches have been developed for printing over nonplanar surfaces using DIW printing. One approach depends on the scanning technology, which detects the surface topology and then creates the toolpath based on the scanned target topology.[50, 51] However, it does not have an active feedback mechanism, and registration errors and alignment errors can affect printability. Alternatively, vision-based systems have been used that allow real-time tracing by providing instantaneous feedback of the topographical variations of the print substrate.[52] However, this approach is complicated and expensive to accomplish. Furthermore, environmental conditions such as lighting mist can influence the performance of vision-based systems. Therefore, the use of passive mechanisms might enable a more straightforward and robust operation. To conclude, DIW printing still requires a more elaborate design of controllable printheads to allow such rapid fabrication on complex surfaces.

This chapter presents a broad overview of the various methods that have been developed in the literature in addressing the emerging challenges associated with 3D multimaterial printing on planar and non-planar surfaces. From the existing challenges, it develops objectives and aims for this thesis. It then summarizes the main contributions that have been made to address some of those challenges. First, various additive manufacturing methods used to pattern silicone structures are discussed in detail, along with their limitations and resolution limits. In addition, the multimaterial approaches by different 3D printing techniques are also discussed. Next, the fundamental flow phenomenon inside a microfluidic channel for achieving mixing is described. After that, various 3D printing

applications were discussed with the use of multimaterial printing. Next, the motivation of the thesis is presented, which aims to research challenges in the mechanisms integrated inside the printhead to achieve high speed throughout 3d printing. Finally, the thesis objectives, main contributions, and outline are presented.

## **1.2 Literature review**

### **1.2.1 Soft polymer materials**

Soft materials have unique structures that allow them to be deformed under various forces such as mechanical and thermal stresses. Soft materials are a general term for different substances, including polymers, liquids, foams, gels, and granular materials.[53-57] By definition, any large molecule comprised of repeated subunits "monomers" to form chains can be called polymers. They typically have large molecular masses and high thermal resistance.[58, 59]

Polymers can be classified into natural polymers and synthetic polymers.[58, 59] Examples of natural polymers include rubber, amber, silk, and keratin. Natural polymers play crucial roles in organisms in different forms, such as energy storage particles, structural proteins, and functional proteins. On the other hand, synthetic polymers can be made using chemical reactions in a laboratory rather than a biological process. Many synthetic polymers, such as polystyrene, silicone, and nylon, have been used in industries for different reasons. For example, polymers have been used to create adhesives, mechanical arts, and paints. Synthetic polymers can be divided into thermoset and thermoplastic polymers. The general raw material forms for preparing thermoset plastic are liquid or solid substances. The curing process can be achieved by heating or radiation by crosslinking to form the thermoset plastic.[58, 59] The curing is irreversible, and the

monolith formed cannot be changed back to its uncured state. Many polymers can be grouped under the heading thermoset plastic, such as polyesters, silicones, and acrylic resins. On the contrary, thermoplastic polymers have large molecular weight and exist in the solid form at room temperature in an entangled state.[58, 59] Heating a thermoplastic polymer above its glass transition temperature can provide energy to the polymer chains to allow disentanglement, and it can be returned to its liquid state. Thermoplastic polymers have many examples, such as nylon, polypropylene, acrylic, and polyethylene.

Processing constraints, material structure, and system properties are greatly influenced by polymer type.[53-57] A wide range of polymers can be processed by traditional plastics processing methods, including extrusion, injection moulding, spinning, and casting. The most suitable polymers for 3D printing, particularly extrusion 3D printing, are thermoplastic polymers rather than thermosets polymers owing to the inherent risk of clogging of the thermoset materials in the printing mechanism due to inadvertent in-situ curing.[53-57] Therefore, certain 3D printing approaches are suitable for only specific polymers. In the 3D printing field, the material is chosen according to different reasons, including the printing validity, the final application, the exposure environment (e.g., temperature, humidity, and mechanical loads), and the market requirements.[58, 59] For instance, fused-deposition modelling (FDM) and selective laser sintering (SLS) use a thermoplastic material that is converted to a liquid state by melting to facilitate extrusion through a small nozzle and then cooled on the substrate to solidify into the printed shape. FDM and SLS have been used with a wide range of thermoplastic materials, including acrylonitrile butadiene styrene (ABS), polylactic acid (PLA), and nylon. For processing thermoset materials, different 3D printing methods have been used. For instance, the vat

polymerization method utilizes a light source to solidify the inks, which are typically photopolymer materials. This approach requires photocurability and therefore narrows the number of materials that can be processed using it.[60] The material jetting method can be used with thermoset polymers to create high-resolution patterns, but only low viscous inks can be used, which can lead to mechanically weak structures. Another 3D printing method that can process thermoset polymers is DIW printing. In material jetting and DIW printing methods, a pre-thermoset polymer is initially loaded in the liquid form and converted to solid-state upon curing.[61, 62] Polymers utilized by DIW printing should exhibit specific rheological properties to allow printed layers to retain their shape. One of the most important classes of thermoset polymers is silicones, which have been processed by several AM methods. Silicones are commercially significant, yet further investigation is required to determine suitable resin formulations for 3D printing as well as refine the 3D printing methods to enable functional multimaterial applications.[53-57]

### 1.2.1.1 Silicones

Silicones or polysiloxanes are made of a repeating backbone chain consisting of two main elements: silicon and oxygen. The general silicone formulation consists of the inorganic backbone --Si-O- and organic groups such as methyl, ethyl, or phenyl. Silicones come in different forms, including cyclic and linear.[21, 63] One commercially available and widely used silicone is linear polydimethylsiloxane (PDMS); the PDMS chemical structure is illustrated in **Figure 1-1**.

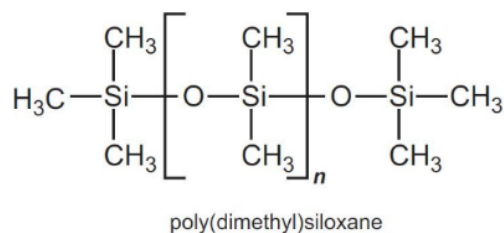


**Figure 1-1:** PDMS molecular structure in which n is several repeating monomers  $[\text{SiO}(\text{CH}_3)_2]$  unit.

Like other silicones, the main element of PDMS is the stable inorganic backbone consisting of Si-O bonds. Silicones are known for their flexibility and robustness. PDMS can be used in various applications due to its low thermal conductivity, low toxicity, high gas permeability, stability at high and low temperatures, and chemical stability.[21, 63] Further, the availability of other organic groups attached to the Si-O backbone makes chemical modifications possible. As a result, various forms of silicones such as liquid, resin, gel, and rigid elastomer are available based on their molecular mass and degree of polymerization.

Owing to silicone's different forms and properties, they have been utilized in many fields, including engineering, life science, adhesives, medicine, electronics, and the chemical industry. For instance, many silicone elastomers are biocompatible, making them used in the medical field to fabricate medical products such as testicle implants, breast implants, contact lenses, and soft tissue.[21, 63] Furthermore, silicone elastomers can be employed in moulding applications due to their flexibility and low interaction energy. Many moulding applications use silicone rubber as resins and foams. Also, silicone rubbers can be used as sealing material as they are resistant to moisture, dust, and electricity, making them good candidates for isolating electronic devices.[21, 63] Additionally, silicone's ability to replicate makes it suitable for different research fields, including microfluidic research for creating microfluidic devices.

3D printing requires the formation of solid silicone material through crosslinking. The pre-polymer ink used in 3D printing contains the base, crosslinker, catalyst or curing agent, as well as filler materials such as silica to improve structural and flow properties.[64]

There are various ways to induce cross-linking or curing of silicones. These include moisture curing, thermal curing, and photocuring.

#### *1.2.1.1.1 Silicone crosslinking techniques*

One method is moisture-induced curing, in which the silicone cures due to the exposure to humidity in the atmosphere. The uncured silicone is introduced as one component in an enclosed environment in the moisture-curing method, which simplifies the dispensing step for 3D printing.[64] The curing process is initiated after the one component-silicone is exposed to the atmosphere containing moisture due to humidity. Consequently, a chemical reaction between the water molecules and silicone components occurs, leading to cross-linking and hardening the silicone layer close to the surface. Depending on the pre-polymer resin type, by-products can be generated from that reaction, such as alcohol, acetic acid, or amine.[64, 65] The curing process starts from the outside surface and propagates into the inside of the uncured silicone. Therefore, curing large and thick layers is a challenge.[64, 65] In addition, the curing time is relatively large, and sometimes it takes several hours/days. The curing speed is controlled by three parameters: relative humidity, layer dimensions, and process temperature. The curing process can be accelerated using heating, which can speed the reaction. Although, at a high temperature above  $\sim 60$  °C, a degradation process can occur, which prevents the curing.[64, 65] The advantage of the moisture-curing silicone is in the use of a single component mixture and is used in applications where a thin film of silicone needs to be formed in applications as diverse as electronic, medical, and aerospace.

Other curing approaches require two components of silicone that need mixing prior to the curing process. The curing process in the case of a two-component silicone can be

induced chemically, thermally, or by the generation of free radicals.[63, 66] The chemical polymerization method starts when the two silicone components meet, and the chemical reaction is spontaneously initiated upon mixing. It should be highlighted that the catalyst component for light or thermal initiation is not needed. On the other hand, the thermally driven polymerization process consists of a platinum catalyst and curing agent to initiate the crosslinking process.[63, 66] Using different mixing ratios between the silicone components, the final cured silicone's stiffness, flexibility, and stretchability can be controlled. The polymerization process can be induced at room temperature, although the curing time will be relatively high on the order of hours. Therefore, heating can be introduced to accelerate the curing process and reduce the curing time significantly (sometimes within minutes). In addition, the polymerization process by chemical curing generates minimal by-products, unlike the moisture-driven process.[63, 66]

The last method is the radical-driven process that applies light to initiate the crosslinking reaction.[67, 68] The silicone properties change chemically and physically after exposure to light, such as ultraviolet light, "UV light", or lasers. A photocurable silicone often contains a combination of multifunctional monomers and oligomers depending on the desired physical features.[67, 68] When the silicone mixture is crosslinked after the light exposure, it creates a thermoset polymer network. It is essential to mention that the curing process in the photocure method is considered environmentally friendly, as it eliminates any volatile organic solvents, and by-products are reduced significantly.[67, 68] Further, the curing time can be very fast, in seconds, making photocurable silicone a reasonable replacement for the thermally curable silicone in many

applications. Examples of the industrial sectors benefit from the photo curable silicones: the optical industry, medical devices, and 3D printing technology.

Due to the silicone's various applications, many methods have been used to process, including injection moulding, extrusion, transfer moulding, and compression moulding.[1-4] Each method has certain specifications regarding the part size, the used material to create the final product, and the operation parameters.[1-4] The common advantage of these methods is producing many parts, which reduces the part price. However, each design requires special tools like dies, which are expensive to make and will need to be remade if any parameters have to change. Besides, the machine design is very complex and expensive, and the operation process needs a well-trained worker. On the other hand, 3D printing technology has many advantages. The structure fabricated by 3D printing can be easily customized, and it allows customization and rapid manufacturing, especially for biomedical applications where patient-specific devices or components are needed. In addition, the complexity of the design is not a restriction when it comes to 3D printing, which can be exploited to achieve functional properties that cannot be obtained by conventional manufacturing. Most importantly, many 3D printing methods are suitable for creating multimaterial structures that allow advanced functional devices to be built. For those reasons, 3D printing techniques have been considered in the thesis, and a detailed discussion of various methods of 3D printing is presented in the next section.

### **1.2.2 Additive manufacturing techniques**

The field of AM has experienced rapid growth in the past decade due to the rapid advancement in manufacturing, computer vision, material science, and active control

systems. It relies on the digital interpretation of a Computer-Aided Design (CAD) file with a printer controlled by a computer.[9, 69, 70] The 3D CAD file can be obtained by the 3D scan of the intended object to be reproduced or other topological data generated through design. After that, a discretized computer format is obtained from the CAD model like stereolithography CAD format such as Standard Triangle Language "STL." Next, The STL file is converted into layers in the computer numerical control (CNC) programming language as G-code. The G-code is used to drive the 3D printer to create the target shape in a layer-by-layer manner.[9, 69, 70] Each layer of the 3D structure is deposited or patterned by various means like extrusion through printheads or patterns using optical tools depending on the type of printed materials and the AM method used. The printed materials have different forms like powders, resins, filaments, or inks, which may require a curing step to retain the printed shape during or after the deposition.[9, 69-71] There are many AM techniques reported up-to-date that include sheet lamination Object Manufacturing (LOM), binder jetting, direct energy deposition, powder bed fusion (SLS), vat photopolymerization (stereolithography), material jetting (like inkjet), and extrusion printing (FDM and DIW).[72, 73] **Table 1-1** lists some AM techniques along with their capabilities, characteristics and limitations. Sheet lamination is an AM technique in which the 3D objects are built by binding patterned material sheets made of metals, papers or solid polymers. Binder jetting is another AM technique that deposits a binder selectively on the powder field (layer) then creates the solid object by building binder bound selective patterns layer by layer. It is primarily used to process ceramics, metals and powder plastics. Another AM technique used for printing metals is the direct energy deposition technique, as it utilizes concentrated heat energy to melt the metal during the material delivery in a

patterned manner on the print bed. The powder bed fusion method is an AM method in which the fusion process is achieved by melting the material powder together with an electron beam or laser in a pattern, layer by layer, and this process is used for printing a variety of materials such as metals, ceramics, and polymers. Vat photopolymerization involves a light-activated polymerization process where a laser is used to selectively polymerize photo resin in a vat layer by layer or volumetrically to define the 3D structure. It is usually used for printing polymers. The material jetting method is a process in which droplets of the required ink (such as photopolymer or thermoplastic inks) are selectively dropped and solidified layer by layer to build the required pattern with a wide range of materials, including polymers, ceramics, biologicals and composites. Finally, the material extrusion method is a printing process in which the ink is selectively dispensed through a nozzle as a continuous filament to create the 3D parts, and it is usually used for printing polymers and composites. Only the last four AM techniques are amenable for use with soft polymeric materials. The following section will highlight these four AM techniques, focusing on the working principle, performance parameters (resolution, multimaterial capability, speed), advantages, limitations, and applications.

**Table 1-1** AM approaches for polymers besides the advantages and disadvantages.

AM methods	Resolution	Materials	Pros	Cons
<b>Sheet lamination</b>	---	Papers, metal fibers, alumina	Fast, no support structures, ease of handling	Waste materials, bonding strength, not high finishes
<b>Binder Jetting</b>	Process deposits a selective binder on the powder bed, then bounding the selective areas.			

	100 $\mu\text{m}$	starch, PLA, ceramics	fast; allows multilateral AM low temperature	the limited strength of parts; rough surfaces
<b>Direct energy deposition</b>	The process concentrates heat energy to melt the metal during the material delivery.			
	---	Ex. Titanium and Titanium alloys, Stainless Steels	Fast, large parts, reduce waste, multimaterial range, repairing tasks	High cost, low resolution, no overhangs structures
<b>Powder Bed Fusion</b>	Process in which thermal source (provided, e.g., by a laser or an electron beam) selectively affects areas of a powder bed.			
- Polymer SLS	15-100 $\mu\text{m}$	PA12, PEEK	best mechanical properties; less anisotropy	rough surfaces; poor reusability of unsintered powder
<b>Vat photopolymerization (Stereolithography)</b>	A liquid photopolymer in a tank is selectively cured by light-stimulated polymerization.			
- exposure from top	50-100 $\mu\text{m}$	acrylates/epoxides	excellent surface quality and precision	limited mechanical properties
- Continuous Liquid Interface Production (CLIP)	75 $\mu\text{m}$	acrylates	high build speed	low-viscosity resins required
- exposure from bottom	25-100 $\mu\text{m}$	acrylates/epoxides	low initial vat volume; better surface quality	limited mechanical properties
- Multiphoton lithography	0.1-5 $\mu\text{m}$	acrylates	very high resolution	low build speed; limited materials
<b>Material Jetting</b>	Process in which droplets of build ink (such as photopolymer or thermoplastic inks) are selectively dropped.			
- Inkjet-Based Lithography	25 $\mu\text{m}$	acrylates	multilateral AM	low viscosity ink
- aerosol jet printing	10 $\mu\text{m}$	conductive inks/dielectrics	high resolution; low temp process	low viscosity ink
<b>Material Extrusion</b>	Material is selectively dispensed through a nozzle			
- FDM	100-150 $\mu\text{m}$	ABS, PLA, PC, HIPS	inexpensive machines moreover, materials	rough surfaces; high-temperature process
- 3D dispensing	100 $\mu\text{m}$ to 1 cm	thermo-plastics, composites, Photoresist, hydrogels.	broad range of materials	rough surfaces; narrow viscosity process window

### 1.2.2.1 Powder bed fusion

The powder bed fusion (PBF) process involves the melting and fusion of powdered materials using either a laser or an electron beam. In powder bed fusion, the temperature of powder material on the powder bed increases, resulting in melting and fusion into a solid monolith. A fused material pattern in a single layer is built by moving the energy source

(laser beam) over a pattern.[74, 75] Since powder bed fusion occurs via melting, it is also known as selective laser melting (SLM). To begin the process, a roller is used to spread the powders with diameters ranging from 1 to 10  $\mu\text{m}$  to create the first layer over the build platform (**Figure 1-2**). Next, a particular pattern on the powder bed corresponding to the sliced section from the CAD file is exposed to the laser in order to selectively fuse the powders with each other only in those regions, as indicated in **Figure 1-2**. After that, the platform is moved down by layer thickness to create the next layer (**Figure 1-2**), and the previous two steps are repeated. The printing process is completed by repeating the above steps until the entire 3D object is formed. One advantage of the SLM technique is that it does not require any supporting materials as the unsintered powder supports the printed shape. In addition, the unsintered powder can be reused after recycling, which reduces material waste significantly.[74, 75]

To achieve higher printing efficiency, the printed material is warmed by heating the process chamber at a high temperature below the tempering point. The higher the surrounding temperature, the higher the printed powder's rate of fusing and binding, and the higher the printing speed obtained.[76, 77] Another critical parameter for the SLM process is particle size. A lower printing resolution usually results from bigger particle size. Thus, to reach higher printing efficiency, smaller particle size is preferred. However, most commercially available powders have a particle size ranging from 20-50  $\mu\text{m}$  leading to a printing layer resolution of 15-100  $\mu\text{m}$  for the SLM process as reported in the literature.[78, 79] The powder material utilized in the SLM process should have favourable properties such as ageing stability, flowability, and thermal stability. These powder properties help achieve proper blending during the fusion process, obtain uniform solidified regions free

of porosity, and achieve good mechanical properties.[80] It is possible to use powder metal, plastics, or ceramics to construct the component, which provides a high degree of complexity. Recently, a few soft polymer materials have been printed using SLM, like thermoplastic elastomers (TPEs).[81] Yet, there are challenges to processing soft materials using SLM due to the particular requirements of the powder material properties. Hence, sometimes to improve the thermal stability and stiffness, inorganic fillers were utilized.[82] Another limitation of the SLM method is that it is challenging to achieve multimaterial printing, which is required in some applications such as soft robotics. The SLM method has been used with soft polymer materials, mostly for medical applications.[83]

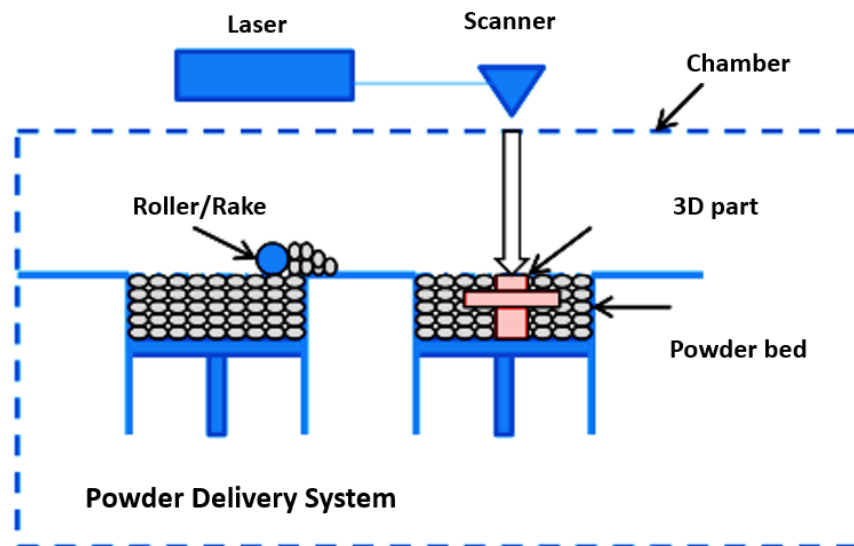


**Figure 1-2.** Schematic diagram of the Powder bed fusion technique.[84]

#### **1.2.2.2 VAT photopolymerization**

A light-activated polymerization process is employed in vat photopolymerization to cure a photoactive liquid resin in a pattern, layer by layer, to form the 3D object. Vat photopolymerization was one of the first 3D printing techniques developed in the 1980s, as stereolithography (SLA), and since then, many other vat photopolymerization techniques have been established. These newer techniques use different scanning

approaches for light or different light sources and include methods such as digital projection lithography (DLP),[85] continuous liquid interface production (CLIP),[86] two-photon /multi-photon polymerization (TPP),[87] and computed axial lithography (CAL).[88] The printer setup for vat photopolymerization is similar to SLM (**Figure 1-3**), with the exception of the energy source and the material form. The printing process can be divided into multiple steps; first, the photocurable polymer, which is in the form of a thin layer on the print substrate, is exposed to light in a pattern corresponding to that in the sliced section of the CAD file. The light exposure starts to crosslink the photopolymer in the pattern which is generated using a direct write approach (**Figure 1-3**) or parallelly through a mask forming the first patterned layer. Next, the support platform is moved down by layer thickness, to form the next photopolymerizable layer and the patterning step is repeated again with the pattern corresponding to the next sliced layer, as shown in **Figure 1-3**. By doing these steps repeatedly, the final 3D object is formed, and the unpolymerized ink in the vat is drained off. Sometimes, a post-treatment process like an auxiliary photocuring process is required to preserve the final product mechanical properties.

To improve patterning efficiency, different novel vat photopolymerization techniques have been developed. In a traditional vat photopolymerization technique, the exposure is through a direct-write technique where a laser spot is scanned across the printed bed in the regions that need to be photopolymerized. In newer methods such as digital projection lithography (DLP) and continuous liquid interface production (CLIP) methods, an entire layer can be exposed simultaneously via a digital mirror array or a patterned mask.[85] These approaches not only increase the throughput but also are capable of high resolution and complex geometries while maintaining a smooth surface.[89] Such novel

modifications increase the printing speed and reduce printing time from hours to mins. Another novel technique is the two-photon /multi-photon polymerization (TPP) technique, which improves the printing resolution to reach the highest printing resolution of 100 nm, as cited in the literature.[87] The TPP technique applies a light source in the form of ultrashort laser pulses. These laser pulses initiate the two-photon polymerization, which occurs only when a high density of photons are present, which is typically at the central part of the gaussian distribution profile of the light beam. This results in a high print resolution which is then determined by the spread function of the two-photon absorption as a function of the light wavelength  $\lambda$ . [87] Another recent technique is the computed axial lithography (CAL) technique, which is different from conventional vat photopolymerization techniques. It creates the 3D objects by providing the light source to a rotating volume of material in a sequence of 2D images. Each sequence of images is projected on the material volume rather than a layer, and the light goes through it based on the light projection angle, making the solidification process occurs on different locations of the whole 3D material volume simultaneously. Therefore, the printing speed in the CAL technique is much faster than other methods based on the layer-by-layer technique.[88, 90] There are trade-offs between printing speed, printing volume, and printing resolution in any vat polymerization approach. For instance, although the TPP technique can reach the highest resolution, the printed volume is limited to 1 cm<sup>3</sup>, and the printing speed is lower than CLIP.[91, 92] The CLIP technique can create complicated structures within a hundred cm<sup>3</sup> range, yet the output resolution is below 100  $\mu\text{m}$ . [91, 92] In the same vein, CAL is a volumetric fabrication process that allows high printing speed, but the printing resolution is in the low submillimeter range.

Two essential parameters define the printing material for vat polymerization: flowability and the ability to cure when exposed to light (photocurability).[93] The first parameter ensures that the photopolymer material spreads uniformly over the printing bed when a new layer is formed. More specifically, the photopolymer viscosity is an essential property that can affect the printing accuracy and be adjusted using diluents to improve the flowability. The other parameter is photocurability, which is related to the photopolymer components. The photopolymer can be classified based on the photoinitiator, type of light source, and other additives, which can reduce the variety of the photopolymers compared with the polymer family.[94] Other additives include light absorbers, which can significantly affect the curing depth. Various soft photopolymers have been processed using vat photopolymerization, such as silicone elastomers, hydrogels, and elastic resins.[94] To conclude, key parameters control the printing process, which involves the liquid resin viscosity, the photoinitiator intensity, exposed laser terms (e.g., laser wavelength, speed, exposure time), and the absorption of other additives such as pigments and UV absorbers. [94]

Similar to the SLM, it is difficult to integrate multiple materials in the construction of the 3D object in the vat photopolymerization method due to similarities in the way that the individual layers are formed and dispensed.[95] Apart from this, other limitations exist in the creation of composite structures. For example, adding particles to the photopolymer increases the viscosity, reducing the printing efficiency and photopolymer transparency.[96]

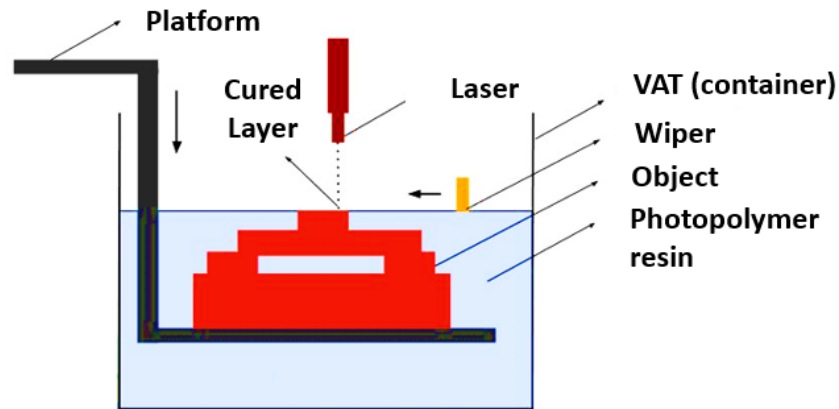


**Figure 1-3.** Schematic diagram of the vat photopolymerization technique.[97]

### 1.2.2.3 Material jetting

In material jetting, materials are deposited in droplets at a particular place to build the target shape. The inkjet printer setup consists of a moving platform in three directions (x, y, and z), a nozzle for jetting the material and curing devices such as a UV light source or heating stage (**Figure 1-4**). The inkjet technique utilizes a low viscosity ink by ejecting it from the printheads and the ejected droplets are delivered accurately on the print stage by controlling the platform motion, as shown in **Figure 1-4**. After the deposition step, the delivered material is cured to create a solid object (**Figure 1-4**). There are two types of inks that can be used: those made of photocurable polymers, which can be exposed to light for curing or droplets of molten material exposed to the thermal process for cooling and solidifying.[98]

To generate droplets, there are two inkjet approaches, continuous inkjet (CIJ)[99, 100] printing and drop-on-demand (DOD) printing.[101] In the CIJ method, a jet of droplets is ejected from the jetting nozzle continuously when the stream of fluid ejected breaks up under the capillary-driven Rayleigh-Plateau instability regime. Patterning can be achieved by the control of where the droplet stream is deposited through an electrical control mechanism. Charged droplets can be formed by applying a potential between the jetting heads and the ground and can be directed to a particular location on the print bed

using an electric field to ensure deposition accuracy. When the potential is off, the generated droplets are free from charges, do not respond to the applied electric field, and are instead deposited into a collection reservoir.

On the other hand, the DOD method generates droplets only when needed by inducing a pressure pulse in the jetting head. Droplets are pushed from the jetting head once the pressure exceeds a specific value. There are two actuation mechanisms to produce the time-dependent pressure pulses inside the jetting head: thermal DOD printing [102] and piezoelectric DOD printing.[103] The thermal DOD mechanism forms bubbles that collapse to produce the pressure pulse. In comparison, the piezoelectric DOD mechanism utilizes the piezoelectric effect to create the necessitated pressure pulse for ejecting the droplet. A trade-off exists between the printing speed and droplet size. CIJ mechanism has a high printing speed ( $>10\text{m/s}$ ) owing to the fast droplet production process (20-60 kHz) [104], yet the produced droplet size is bigger than the nozzle diameter, which leads to a lower resolution. By contrast, the printing speed of the DOD mechanism is around 5-8 m/s [105], and the droplet size is almost equal to the nozzle diameter, which means reaching a higher resolution. Besides, the ejection speed greatly influences the droplet impact, which affects the final surface finish and printing efficiency. In addition, the interaction between the droplet and the substrate has a significant impact on the printing resolution which is to some extent determined by the spreading of the droplet on the substrate. Generally, the highest printing resolution of the inkjet printing technique is usually in micrometers range,[106] and it can be enhanced by combining the inkjet technique with an electrohydrodynamic system for utilizing an electric field to stretch the fluid stream.[107, 108] Such a technique is called electrohydrodynamic inkjet printing (E-jet), in which E-jet

produces a much smaller droplet size of 50 nm.[109, 110] E-jet allows constructing micro/nano 3D structures. However, the E-jet suffers from the low print material options as the print fluid should be conductive, and the 3D structure's height is limited due to the electrostatic repulsion when additional layers need to be deposited.[111]

The inkjet printing technique requires two classes of inks for printing 3D objects, one is the building ink, and the other is the supporting ink. Both types of inks (building and supporting) should have proper fluid properties to allow the ink-jetting like low viscosity and the ability to cure for retaining the shape to achieve proper ejecting and deposition steps. Many factors affect the droplet generation process stability and define the printing resolution, such as material density, surface tension, material viscosity, droplet size, droplet pushing speed, and the nozzle tip diameter.[112] To achieve an optimal ejection process with different kinds of complex fluids is a challenge, especially with fluids containing filler particles (larger than 100 nm), limiting the printing material options whether the fluid cures thermally or chemically.[113] Due to these limitations, only a small number of soft polymers have been demonstrated using this method, such as hydrogels,[114, 115] PCL,[116] and silicone elastomers.[117] Nevertheless, the inkjet printing methods are highly adaptable for multimaterial printing as different nozzles can be used to print different materials at the same time or sequentially. Unlike SLM and vat photopolymerization techniques, 3D multimaterial architectures can be easily constructed with various properties using multiple jetting nozzles. Today, the most recent multimaterial inkjet printer has thousands of jetting heads that can eject droplets with a speed of around 100 million droplets/sec, which offers a significant capability to build complex 3D objects.[118]

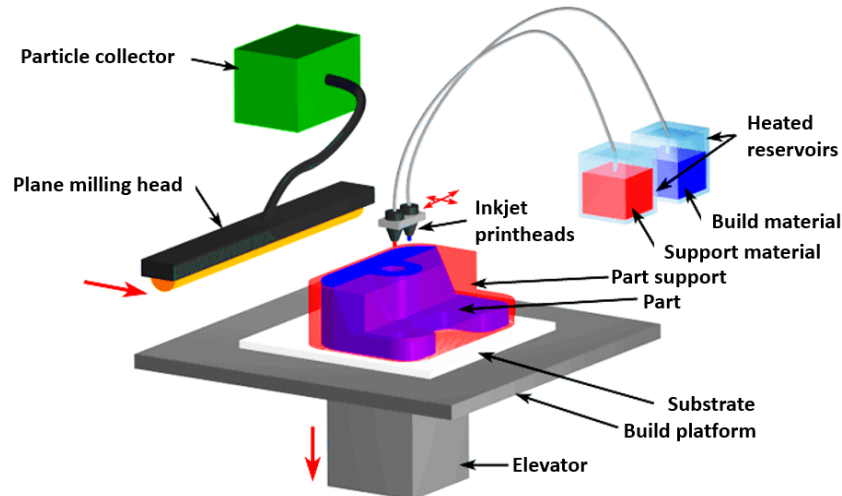


**Figure 1-4.** Schematic diagram of the inkjet printing technique.[119]

#### 1.2.2.4 Extrusion printing

Material extrusion is one of the most commonly used 3D printing techniques, where mechanical pressure is used to extrude the print material from a printhead tip as a continuous filament. The extruded filament is then delivered to the moving stage in a defined pattern to create the required 3D object. Like an inkjet printer, the material extrusion printer consists of a three-dimensional motion platform, a printhead for delivering the print material, and a curing source to help keep the printed pattern shape, as shown in **(Figure 1-5a)**. The ejected filament is delivered in a particular design based on the toolpath, which controls the stage movements to construct one layer at a time. Then the printhead moves up by a layer thickness in order to form the next layer. By repeating these steps, the entire 3D object is constructed. The printed feature's resolution depends on the nozzle cross-sectional diameter and the motion feed rate. There are two methods of extrusion printing, namely fused deposition modelling (FDM) and direct ink writing (DIW). [98]

The FDM technique, also known as fused filament fabrication (FFF), is an extrusion printing technique in which thermoplastic filaments are extruded through a

printhead adjusted at high temperature for melting the filament to a semi-molten state. The melted filament is deposited on the XY platform to print the entire structure layer by layer (**Figure 1-5a**).[120] The solidification process occurs with time as the printed materials cool under their glass transition temperature to solidify the printed pattern. The FDM process's resolution is usually on the order of 1 mm, owing to certain limitations.[121] These include the need to use larger diameter nozzles to accommodate high viscosity melts of polymers as well as post extrusion swelling of the polymer, which limit the resolution that can be achieved.[121] Nevertheless, the printing speed of the FDM can reach a value up to 500 mm/s after optimizing the printing parameters, including the nozzle temperature and the platform temperature.[122] Depending on the desired mechanical and rheological properties, various thermoplastic soft polymeric materials have been utilized, such as thermoplastic elastomers (TPEs).[123, 124] Although only a limited number of soft polymeric materials can be printed by FDM, the FDM technique has a remarkable ability to deposit both polymer composites [125] and multimaterial printing.[126, 127]

The other extrusion technique is the DIW technique, in which viscoelastic materials can be processed. In DIW, a low viscous material compared to the FDM method is extruded from tiny nozzles under controlled flow rates and deposited along digitally defined paths (**Figure 1-5b**) to fabricate the final 3D object.[27] Different mechanisms to extrude the print material include pressurized air, a mechanical piston-cylinder system, and a mechanical pushing screw.[1] The extruded material should be cured upon the deposition by exposure to a light source (e.g., UV light) for photopolymers or a heating source for thermally cured polymers.[1] The printing process in the DIW depends on the ink rheological properties required for achieving continuous printing. These properties involve

the ink viscosity, yielding point, shear-thinning behaviour, and recovery ability to keep the shape of the extruded filaments. One of the most well-suited inks for DIW printing is shear-thinning ink. Shear-thinning, in rheology, is a phenomenon in which fluid viscosity diminishes under shear strain. The pressure applied to start the ink flow from the printhead should surpass the material yielding stress to ensure ink recoverability; once the ink extrudes out of the outlet tip, the ink viscosity increases as it is no longer encountering shear strain due to the walls, which helps retain the entity shape. Additionally, an auxiliary curing devices such as UV light can be used to crosslink the printed filaments just after the deposition.[128] Alternatively, a coaxial printing approach has also been cured based on ionic crosslinking with hydrogels.[129] The curing step here needs to be optimized as excessive curing could weaken the interfacial bonding between layers, while inadequate curing leads to a loss of feature definition.

The DIW method has some restrictions. One of them is the ability to retain structural shape, especially with 3D parts printed using soft materials. However, this limitation can be significantly resolved using different approaches. One approach is using a printhead that is synchronized with curing devices (including UV lamps and heated chambers) to ensure the fast curing of the underlying printed layers.[130] An alternative solution is using a support material with particular properties like high Young's modulus to support the built material.[22, 131] Another limitation is its low printing speed, and the requirement of an accurate feed system as the flow rate determines the resolution. Unlike fast AM methods like vat photo-polymerization, the DIW printing speed is low and limited to 100 mm/s, as reported in the literature.[22] The DIW process can achieve a resolution of several micrometres after suitable optimization of the printing conditions.[22] It is

related to the effect of the printing speed on the print resolution due to the stretch and towing properties of the printed material.[132] To further enhance the printing resolution, some use an electric field and integrate that with conventional system leading to establish a new technique called electrohydrodynamic direct-writing (EHDP).[133] Due to the influence of the electric field, the extruded filament is stretched further, resulting in the formation of filament that reaches the order of nanometers in dimension, constrained by the electrostatic repulsion.[134] These methods can be used to create micro and nano 3D objects.

The DIW technique is compatible with a wide range of materials as rheological modifications using additives can be made to make several previously unprintable polymers printable. In addition, other approaches and modifications, including two-step crosslinking or printing inside a supporting structure like a gel (embedded printing), can also facilitate its use with a number of different materials. Thus, various soft polymer materials have been used to 3D print using DIW, including hydrogels,[25, 135] polyurethane (PU),[20] and silicone elastomers.[22, 132] The wide range of material choices, simple printer setup, multimaterial capability utilizing multiple nozzles,[136] composite inks,[18] or customized printheads[137] make it a versatile method for 3D printing of soft polymeric materials.

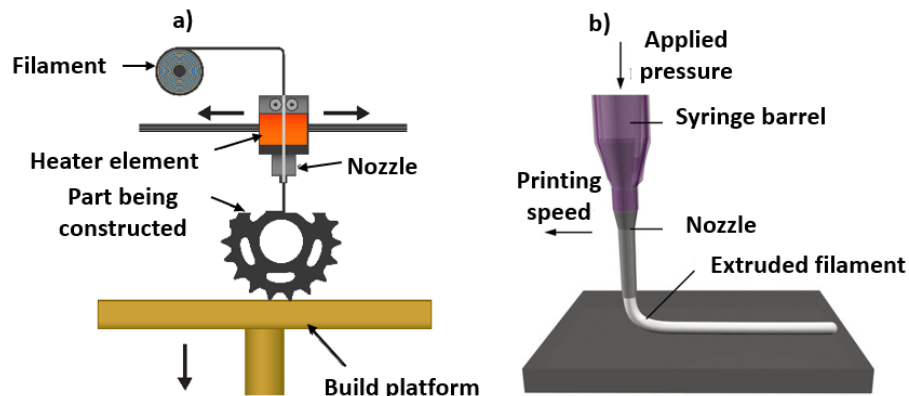


**Figure 1-5** Schematic view of extrusion 3D printing techniques: (a) FDM and (b) DIW.[138]

To sum up, many 3D printing techniques have been utilized to print soft polymers materials with various printing resolutions, speed, and complexity. However, in the coming section, we will focus only on the techniques used for printing silicone materials, namely vat polymerization, material jetting, and material extrusion.

### **1.2.3 Silicone 3d printing techniques**

Among the AM techniques, only vat polymerization, material jetting, and extrusion printing have been exploited to process silicones. The popularity of silicone-based materials comes from the diversity of their chemical and physical properties.[139] Nevertheless, there are numerous challenges associated with 3D printing silicone-based materials. This section will explore the AM techniques adapted for silicone-based materials, silicone compositions, and approaches to overcome fabrication limitations and expand their potential industrial applications.

#### ***1.2.3.1 Vat polymerization technique for silicones***

In the vat polymerization method, the liquid resin vats contain the following components: a photoinitiator, a photocurable monomer or oligomer, and other additives like UV exposures.[140] After the exposure, different photopolymerization mechanisms occur to solidify the exposed layer. Among the most common forms of photopolymerization mechanisms that have been used in silicone 3D printing is free radical polymerization, which depends on the photoinitiator type and photopolymer.[141, 142] Free radical polymerization occurs when the photoinitiator bond cleaves by homolytic action after the UV exposure. The FRP is composed of three phases: initiation, propagation, and termination.[141, 142] Firstly, the photoinitiator is added to the system, then it decomposes under a trigger source (UV light), which generates free radicals leading to have unpaired,

very active electrons. Therefore, free radical species react with monomers to start a radical chain. The propagation step begins after the initiating radical's chain has been formed by attacking another monomer to transfer the active centre to the attacked molecule. Ultimately, the polymer chain develops by repeating the propagation step. Once the macromolecules are grown, the active centre is disabled, leading to the termination of the polymerization step. The photoinitiators should have the following properties: the ability to dissolve in silicone, the strong absorption of UV light with a wavelength of UV-LED commercial projectors above 385 nm, the efficient production of free radicals. The most common photoinitiators used in silicone 3D printing can be classified into Type I and Type II. The first one produces free radicals through homolytic cleavage of specific one- or two-bonds. General chemical compositions are 2,4,6-trimethyl benzoyl diphenylphosphine oxide (TPO) and hydroxyacetophenone (HAP).[73] Type II's second category of photoinitiators requires activation by an alcohol, amine, or acrylate-based coinitiator. An example of a Type II chemical name is isopropyl-thioxanthone (ITX).[73] According to the target resolution, the layer thickness ranges between 50 and 200  $\mu\text{m}$  (z-resolution), depending on the concentration of the photoinitiator.[73] The other factor that significantly influences the polymerization mechanism is the photopolymer type. In principle, the essential requirements of the photopolymers include fast curability for retaining the cured shape, low toxicity, insensitivity to oxygen and water, and low viscosity. These requirements allow high-resolution printing with minor volume shrinkage and reliable mechanical property of the printed part.[143] Also, when the monomer is deposited on top of the crosslinked substrate during printing, a low viscosity resin helps to achieve good recoatability.[143] Currently, among the most commercially usable photopolymers are

Formlab flexible resins, Stratasys Tangoplus, and silicone elastomer (SIL).[141, 142] However, the UV curable silicone elastomer is more suitable for applications requiring sufficient stretchability, good optical properties, and tunable mechanical properties.[144] One of the most widely used silicone-based materials is PDMS due to its excellent transparency, flexibility, chemical resistance, and electric isolation.[143] The Sylgard 184 version of PDMS is a thermally cured material when used in soft lithography. However, in vat photopolymerization, a chemical group called thiolene has been utilized to allow the polymerization process under direct UV light. The thiolene chemistry enhances the chain network uniformity based on its unique abilities, including high curing rates, by-products free process, and not being sensitive to water and oxygen.[149] The remaining section reviews various methods used to fabricate 3D structures using silicone-based materials in different applications.

An SLA technique that uses a femtosecond laser to crosslink the PDMS resin has been developed by *Rekšytė et al.* to construct 3D micro-objects.[145] The developed technique reached a resolution of 5  $\mu\text{m}$  and a printing speed of 720  $\mu\text{m}^3/\text{s}$ . [145] In another work by *Sirrine et al.*, two groups of amorphous PDMS along with a thiol-functional PDMS crosslinker and 0.5% photoinitiator were mixed and used to construct high aspect ratios architectures regarding their fast curing of <5 seconds.[146] In addition, PDMS is used in many membrane applications which involve nanofiltration and oxygenation owing to its gas permeability.[146] For example, a novel sacrificial lithography method using a DLP printer and a rapid curing photoresist has been established by Femmer and Wessling. In their work, a photopolymerization reaction was initiated through a functionalized PDMS copolymer by adding a photoinitiator, namely 2 wt% ethyl (2,4,6-trimethylbenzoyl) phenyl

phosphinate (TPO-L).[146] The developed method was utilized to construct a 3D membrane depending on a triple-periodic minimal surface (TPMS) structure with unique high strength and lightweight properties.[146] The fabricated TPMS-PDMS membrane showed an excellent interface that can be considered suitable for various applications such as gas exchangers, blood oxygenators, and catalysis.[147] A mixture consisting of PDMS, TPO-L photoinitiator, and photo absorber (ITX) has been adapted by *Bhattacharjee et al.*[148] Interestingly, the developed method used a DLP printer and achieved a lateral resolution of 150  $\mu\text{m}$ . Besides, the printed structures were transparent, biocompatible, flexible, and gas-permeable.[148]

In summary, vat photopolymerization is a highly valuable technique for fabricating silicone-based materials, even with its limitations related to the desired mechanical and optical properties. These limitations have been resolved by integrating an efficient photoinitiator, a dye absorber, or other additives. However, the main drawback of vat photopolymerization is associated with the ability to fabricate composites and multimaterial 3D printed parts. Vat photopolymerization methods have some restrictions with printing composites. These restrictions are related to the additive particles, which can easily influence the fluid properties like viscosity and the curing process leading to have uneven and unstable printed objects. In addition, the additive particles can affect the light scattering or ink transparency, leading to imperfections within the printing. As for multimaterial printing using vat photopolymerization, many attempts have been established to achieve multiple materials using switchable vats manually or mechanically.[149, 150] Although switching vats allow printing of multimaterial structures, they are slow, complicated in their setup, may not work with entrapped

materials, and might have issues with adhesion between surfaces leading to have low resolution.[149] Recently, a possible alternative to printing multiple materials with vat photopolymerization has been demonstrated by some researchers [149, 151] who have used chemoselective wavelength-control to selectively cure different components of a single resin formulation located in one vat to create multimaterial objects directly. This approach is much faster than the switchable vats, and the printer setup is similar to the one used for single printing material. The chemoselective wavelength-control approach requires more control of the ink formulation to allow phase separation, and an advanced wavelength light source is needed. However, the developed approaches to allow multimaterial via vat photopolymerization are not able to achieve fast switching between different inks to allow pixelated printing patterns or in situ mixing between different materials while printing. Moreover, vat photopolymerization is not an ideal method to 3D print over an existing nonplanar topography or part.

### ***1.2.3.2 Inkjet technique for silicones***

Several additive manufacturing processes have been based on material jetting, including Ink jetting, Binder Jetting, and Aerosol Jetting. As mentioned earlier, Binder jetting is not applicable for silicone-based materials since it is mainly used for processing ceramics and metals. While Aerosol Jetting method involves an aerodynamic process in which the generated aerodynamic flow is focused on accurately delivering the inks onto the printed.[152] The inks were loaded into an atomizer which is responsible for generating a dense mist of the print ink and creating droplets in the range of 1-5 microns diameter.[152] A sheath gas covers the aerosol mist as an annular ring to focus the deposited aerosol mist. As opposed to Aerosol Jetting, which is less developed, Ink Jetting

is the more advanced and widely used technique for additive manufacturing. Thus, the inkjet technique is our focus in this section to process silicone-based materials.

In Inkjet 3D printing, the printing resolution depends on the final diameter of the droplets after the impact. The relation between the droplet diameters before and after impact is greatly influenced by the drop contact angle( $\theta$ ) on the substrate.[104] Hence, to achieve high resolution, it is preferred to use high contact angle substrates. In the case of silicone-based materials, it has a good recoatability property, resulting in a smaller contact angle that can lead to greater spreading over substrates. To retain the printed pattern fidelity, the deposited ink should be solidified. For some of the thermoplastic materials, the solidification step occurs through solvent evaporation. However, such a solidification method could leave a thicker edge and a non-uniform deposited pattern after the evaporation process, which results in the classical coffee ring effect. Commonly used silicone inks have very little solvents and therefore do not solidify by evaporation and require other curing mechanisms such as thermal, UV, or chemical curing to be employed during or after printing.[117, 153]

#### *1.2.3.2.1 Thermally cured silicone ink*

Thermally initiated silicones come as two components that require mixing prior to high-temperature exposure to achieve curing. Thermally cured silicones are a good choice for 3D printing applications, especially when the aspect ratio of the printed structure is low. The inkjet method usually uses a single or multi-nozzle to create the required pattern. The single nozzle configuration requires mixing the silicones components before loading them in the ejecting system. Such configuration has lower throughput of the material and requires inks with a long pot life as they should not solidify inside the nozzle head. By

using the multi-nozzle scheme, the two components can be deposited separately. Consequently, they are alternately printed on a heated print bed at the same location, one after another.[153] After the deposition of the silicone components, one on the top of another, mixing between them occurs by diffusion along with some reaction and solidification. Next, they are subjected to high temperatures to complete the curing process and create a solid silicone structure. *Sturgess et al.* have developed two printing strategies, namely layer strategy and line strategy, as shown in **Figure 1-6**. The first strategy is depositing one layer with each ink at a time, each ink from a different nozzle, after which the curing was initiated. While the second strategy is depositing both inks to build the pattern line by line, followed by curing. The first component includes polysiloxanes with hydride side groups (ink A), while the second ink comprises polysiloxanes along with vinyl terminal groups and the platinum catalyst (ink B).[153] Next, the two inks were deposited in a two-layer/line strategy in order to make the printed pattern curable. In order to facilitate mixing between the two ink elements and finally initiate the solidification process, the substrate temperature must be elevated to 80 °C. The mixing time was 2 min (for creating 4mm square area) when the printing was created by the first strategy and the mixing time was reliant on the printing geometry and nozzle printing speed. On the other hand, the second strategy reduced the deposition time to 0.3s because the mixing time was not dependent on the print structure and only relied on nozzle print speed. Notably, thermally initiated silicone has been successfully printed using full reactive inkjet printing (FRIJP) to fabricate a 3D entity but with a very small aspect ratio. Using a prepared substrate, it was possible to achieve features with a spatial resolution of up to  $48\pm 2 \mu\text{m}$ . [153]

Due to the thermal insulating properties of silicone, this method can construct only thin objects (a few hundred microns), as too little heat is transferred to the upper layers after a few printed layers.[153] This means that the thermally cured silicone is not proper to create 3D structures using the inkjet method.

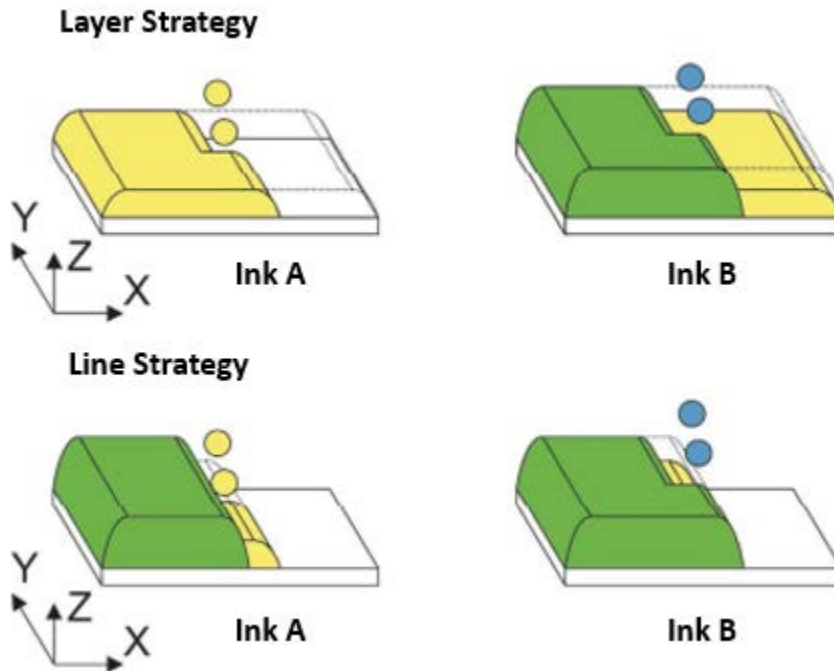


**Figure 1-6** Deposition strategies of ink; first is layer strategy, and the second is line strategy. Ink A is yellow, and Ink B is blue. After the mixing and curing processes, the printed lines turn to green.[153]

#### 1.2.3.2.2 UV-curable silicone ink

A UV curable inks for silicones contain all the ingredients in a single ink, which is then printed on a substrate followed by UV exposure that initiates the polymerization process and solidifies the material.[117] In that technique, one has to be careful to ensure that the UV light does not reflect into the nozzle or the ink reservoir, as such exposure can cause inadvertent curing and clogging. However, delays in post printing exposure to UV also lead to the spread of the ink on the substrate affecting the resolution. To allow the initiation of the UV curing at the nozzle tip (in-situ curing) or after it is deposited at the substrate,

*McCoul et al.* was able to have in-situ printing with UV curable silicone by applying a small time delay between the deposition and the light exposure of each droplet, which allow curing on the fly in seconds.[117] In their work, they used a DOD technique for constructing silicone elastomers. A 3D structure and membrane were fabricated for dielectric elastomer actuators, reaching a resolution of 2 $\mu$ m in thickness and a mechanical failure under a tensile strain of 727% using a dilated UV curable silicone.[117]

UV curable silicones have not been used widely due to the need for a more complex printer setup as well as the issue of inadvertent exposure of the ink to stray light reflected of the part or the substrate causing clogging at the nozzle. In addition, it is necessary to conduct a postprocessing stage to continue irradiating the printed part to UV light until its crosslinking is complete after printing.

#### *1.2.3.2.3 Chemically initiated silicone ink*

Chemically initiated silicone inks come in two part formulations in which the polymerization method starts when the two silicone components interact, and the chemical reaction is spontaneously initiated upon mixing. Chemically initiated silicones can easily be processed using the inkjet 3D printing technique and are primarily done through two approaches. The first method is by depositing the first ink component above the other ink component located in a bath.[154] Once the two components interact, the curing process occurs, and the printed layer solidifies. After that, the platform moves downwards by the desired layer thickness, and the cured layer merged in the bath contains the second component. It is essential to use low viscosity liquid in the bath to ensure free flow, as the crosslink reaction occurs in the order of seconds. The above method can reach high accuracy depending on the droplet size with relatively fast speed. On the other hand, post-

processing takes a long time with no ability of multimaterial printing. The second method includes printing low viscous inks by depositing the individual silicone components from different nozzles onto a dry print bed. After that, the chemical reaction occurs when the two droplets meet on the platform. This method does not require auxiliary devices other than the material distributor's assembly, including print heads and positioners. Many researchers have used the printing then mixing procedure to process reactive material like two-components silicone.[155] To achieve that, they interlace the jets or droplets to deposit different components at the same location using the inkjet printing technique.[155] The intersecting jets printing technique has been used to reach high printing resolution for 2D patterns.[156] *Śliwiak et al.* adapted a new inkjet 3D printing approach by ejecting two reactive droplets simultaneously from two dispensers, merged and mixed in free space outside the nozzle, and deposited upon a substrate in a pattern based on the interaction between the two droplets.[157] This approach was applied to create 2D patterns and high aspect ratio 3D structures with a resolution of a few micrometres.[157]

The inkjet printing approach has several advantages, including the ability to print multiple materials simultaneously by using multiple printheads (thousands of small nozzles per printhead), the high printing resolution, and the ability to print over a large area. Yet, there are significant limitations. One of these limitations is the limited material selection, as the inkjet systems are customized to certain materials that can be printed at low viscosities. Another limitation associated with the mechanical strength of the printed objects by the inkjet approach is low, compared to traditional techniques with similar structures. The substrate topography is another limitation. When printing over nonplanar substrates, the ink can spread away from the defined pattern path leading to inaccurate

printing. Despite those limitations, some works have been printed over nonplanar substrates by applying a slight offset between the layer and the following one. These limitations can present an obstacle for constructing pixelated structures with inks that have relatively high viscosity or shear thinning properties.

### 1.2.3.3 Extrusion-based techniques for silicones

Extrusion-based printing can be used for 3D printing a variety of thermoplastics, elastomers, and other flexible materials.[158] Silicone is one material that can be printed with extrusion-based techniques. However, extrusion-based printing generally has a lower resolution than other AM methods like inkjet printing or vat photopolymerization, but it can be easily adapted. Within extrusion-based printing, there are two leading techniques: FDM and DIW.

In FDM, as shown in **Figure 1-5a**, thermoplastic materials are usually used because the FDM method requires the material to be melted and extruded.[118] This means that traditionally chemical polymerized silicones, which can not be remelted after solidification, can not be utilized as the solid filaments with the FDM technique.[118] Silicone-based materials like PDMS usually exist as viscous ink before the polymerization step. There are two ways to modify PDMS for printing using the FDM technique. The first way is modifying the PDMS structure to contain hard and soft components, subsequently forming a copolymer with phase separation that crosslinks physically. As such, PDMS copolymers were prepared by adding a hard aliphatic isocyanate with pure PDMS (>90%).[159] Hence, the hard component can be cured at room temperature forming solids, and the melting point is around 170 °C. Such an approach was used by *Calcagnile et al.* to create solid filament using the PDMS copolymer.[159] Likewise, *Liaw et al.* formulated

poly(siloxane-co-imide) copolymers by decoupling amine-terminated PDMS with 2,20-bis[4-(3-aminophenoxy)phenyl]sulfone using pyromellitic dianhydride.[160] As a result, a microphase separation occurred between the hard polyimide domains and the flexible PDMS chains and the copolymerized PDMS can be similar to a thermoplastic material for extrusion printing.[160] The other way to create thermoplastic like PDMS is to develop compositions where the temperature can be used to reversibly bind and unbind polymer chains.[161-163] Yet, the bond recovery responsible for retaining the 3D structures at high temperatures is slower than the case in thermoplastic materials, which is considered a big challenge.[161-163] Due to these reasons, the FDM technique has not found favour in the fabrication of silicone-based materials. The focus in the coming section will be on the DIW technique due to the compatibility of the DIW technique with silicone-based materials.

#### *1.2.3.3.1 DIW technique for silicone*

Silicone-based materials are most commonly processed through the DIW method for 3D printing. As silicone-based materials exist as a liquid at room temperature, extruding it pneumatically is feasible. However, maintaining the shape of the extruded material post extrusion is a challenge. Direct ink writing commonly uses silicone-based materials mixed with the appropriate crosslinking agents to build the required structures that exhibit sufficient mechanical rigidity and strength. The pressure applied to extrude should be higher than the material yield stress to induce the flow of such materials from the printhead. One approach that has been attempted has been the use of shear-thinning materials that are typically highly viscous but can become less viscous when they encounter high shear stresses. When extruded pneumatically, these materials encounter higher shear stress than the yield stress at the nozzle and therefore extrude easily. However, when they pass the

nozzle, the shear stress is significantly reduced, and they revert to a highly viscous configuration which provides higher mechanical rigidity and strength to the extruded and printed structure. [164, 165] A curing step can be included either after the printing or during the printing. In non-shear-thinning behaviour, other techniques can be used to provide mechanical rigidity to the extruded material. These include modifying the ink itself, or adjusting the surrounding ambient around the deposited materials, and finally using an in-situ curing technique depending on the initiator agents.

#### 1.2.3.3.1.1 Rheology modification methods of silicone

When working with silicone, it is common to employ rheological additives, such as silica nanoparticles. The silica particle size is chosen so that the nozzle will not be clogged by the additive, allowing for a smooth material flow. Two mechanisms have been used to adapt the material to be printable by the DIW technique, one through attraction (networking) and the other by utilizing repulsion (jamming).[164, 165]

In the first mechanism, a network is formed as polymers interact, but the network falls apart when the forces are relaxed. For instance, the addition of silica can make the silicone material shear-thinning through non-covalent interactions.[166-168] A suitable rheological property can be tuned depending on the concentration of silica particles in the mixture along with the molecular weight. A drawback of using hydrophilic silica within the polysiloxane chain is the possibility to have a stiff material due to the presence of silanol groups after the reaction between the earlier components.[169] Using the networking mechanism, *Roh et al.* mixed PDMS microbeads and uncured liquid precursors along with water to create a capillary suspension ink that could be 3D printed.[21] Capillary attraction caused by the liquid precursor holds the PDMS microbeads together in a gel state, creating

a network chain, leading to exhibit shear-thinning behaviour. Their work developed a 3D printable ink that can be cured, and the water can be removed subsequently to form 3D porous PDMS structures with high flexibility and elasticity.[21]

Alternatively, for the second mechanism, liquid flow is hindered by adding solid particles; thus, it is also named the repulsion mechanism. For example, a treated silica particle anchored with nonpolar organic groups can be used as an additive to PDMS to use this mechanism. Fillers that are treated cannot serve as crosslinkers to connect PDMS chains. On the other hand, they act as barriers in the PDMS fluid flow. The rheological mixture properties will be modified depending on the amount of filler.[170, 171] As the filler amount increases, the mixture will behave as non-Newtonian fluid and exhibit shear-thinning properties. That is related to the increase in the collisions between particles relatively linked with the filler amount. Hence, the friction results from the collisions will require more shear force.[170, 171] Compared to the networking approach, this mechanism usually requires more functionalized silica fillers. For instance, *Ly et al.* reported an approach for fabricating PDMS-based mesh structures with good shape retention. In this work, they created a mixture between PDMS and silica particles with different weight ratios. [170] Using 15-20% silica that had yield stress of 20 - 320 Pa, they demonstrated the printing of microporous mesh structures that can be used for oil/water separation applications.[170] *Jindal et al.* used silica loaded PDMS to print maxillofacial prostheses that could be customized for the patients as well as functionally to provide tissue-like mechanical properties.[172, 173]

#### 1.2.3.3.1.2 Silicone 3D printing using environmental modifications

A couple of methods have been developed where the environment around the printed pattern has been adapted to enable silicone printing. One of these methods which has been used with the DIW technique is embedded printing.

In embedded printing, the printing occurs in the DIW format into a bath of particulate or solid like support matrix instead of air. [64] The particulate or solid-like matrix replaces the need for any other supporting structure and is designed to hold the shapes of the extruded DIW pattern in it. The matrix should exhibit both strength and elasticity to support the printed object's weight while allowing the nozzle to pass freely through it. Ideal materials are shear-thinning materials that allow free movement of the print nozzle through them due to their viscoelastic behaviour but behave like a solid to support the printed material in 3D space. [174] The matrix should also have thixotropic properties to recover its original structure after being pushed out of the way by the nozzle during printing. This preserves the dimensional integrity of the structure to be printed.[175] There are different curing mechanisms that have been used with embedded printing. One of these mechanisms is to use a moist environment as the curing initiator.[64] As mentioned previously, such a technique takes too long (hours) until the print is totally cured. Therefore, achieving high printing resolution is very challenging using this method. Another mechanism is using elevated temperature to initiate the curing. In this mechanism, premixed silicone components are cured at high temperatures to act as a solid. Usually, the heating process is introduced after the printing. Alternatively, the heating can be initiated during the printing. However, clogging at the printhead outlet might occur.[176] As an example for the embedded printing, *Hinton et al.* used a self-standing Carbopol gel as the

support matrix, while the printed material was hydrophobic PDMS prepolymer.[175] The printed structure takes around 72 hours to cure at room temperature or 2 hours at 65°C. After that, the support matrix was dissolved by using phosphate-buffered saline (PBS) solution. They managed to print a range of overhang 3D structures with a printing speed of 20 mm/s, such as a helical tube (1.2 cm in diameter) and a perusable tube (1.6 cm in diameter).

To summarize, embedded 3D printing strategy has a significant advantage in building overhang structures because of the supporting medium, which allows ink deposition to occur at any place inside the supporting environment. This advantage can allow some strategies of multimaterial printing by embedded 3D printing like overlapping multiple surfaces. However, there are still some limitations within the embedded 3D printing strategy. The most critical problem is the needle deformation that results when an extremely long and slender needle (needed not to affect the rest of the bath) is dragged in a thixotropic medium, resulting in inaccurate printing. Moreover, the needle size and particles inside the support matrix can affect the printing resolution significantly.

#### 1.2.3.3.1.3 In-situ curing technique of silicone

As stated previously, non-Newtonian fluids, composed of particles of different sizes and/or different types of fillers, can be printed using DIW techniques. Hence, a rapid curing technique should be employed for printing materials with low viscosity as well as a flow controlling system. The first requirement is achieved using the radical curing technique, which can reach fast curing time in the order of seconds. One of the most widely used radical curing methods is high-intensity UV light, which produces rapid curing.[177, 178] Once the UV light is introduced to the photocurable silicone, the silicone layer is partially

cured, allowing the deposition of a second layer. After the complete formation of the structure, it is also exposed to a post-cure. The exposure time during the printing is typically much lower than the postprocessing exposure time to enable faster processing time. Printing low viscous inks with on-the-fly curing can enhance the printing resolution. In order to form free hang structures using low viscous ink, the embedding printing method can be utilized.[179]. When using UV curing, it should be noted that the shear-thinning support material has to be transparent to allow curing by UV light. Photosensitive silicone can be printed from a single nozzle where the ink blends the reaction mixture and is exposed to light as it is extruded.

As a such, *Zheng et al.* developed a family of fast-curing low viscous silicone inks composed of the crosslinker, polymers containing the chain extender, and thiol-ene click chemistry.[180] They utilized a pneumatic system as the flow control system in their work. The curing speed was less than 2 sec which enabled the creation of 3D structures.[180] As opposed to existing techniques, the system enables 3D extrusion printing of low-viscosity silicone materials without the need for support structures. This is achieved with a single nozzle and silicone ink with the following formulation: the liquid base material, the chain-extender, and the cross-linker “photoinitiator”. The liquid-crystal monomer is polymerized by UV light. In this study, the ability to use a single nozzle to 3D print overhanging structures and discrete/continuous structures using least two distinct materials was presented. **Table 1-3** summarizes the AM techniques available for silicone 3d printing with their features. One of the potential techniques to expand the ability of 3D printing is multimaterial capabilities. Therefore, the multi-ink 3D printing techniques will be the focus of the following section.

### 1.2.4 Multimaterial 3D printing approaches for silicones

Traditionally, 3D printing has been used to fabricate early-stage prototypes that have been used primarily for visual inspection and interim functionality. Nevertheless, with 3D printing's advancement, printing multiple materials is increasingly desirable to enhance the printed device functionality. In contrast to single 3D printing, multimaterial 3D printing is able to print more complex objects that are not possible with single 3D printing. Multi-ink printing enables incorporating several different materials with potentially different mechanical, optical or chemical properties into a single object.[59] Many 3D printing approaches have been adapted for multimaterial printing, including vat polymerization, inkjet printing, and extrusion-based 3D printing. Several strategies have been developed to introduce multiple inks through these 3D printing approaches for silicones-based polymers.

**Table 1-2** Comparison of the silicone 3d printing features for available AM techniques.

AM Technique	Materials	Curing Mechanism	Feed Mechanism	Curing Time	Size feature	Applications	Multi-material printing	Ref.
<i>Extrusion 3d printing</i>								
	one-part oxime cure silicone elastomer	Moisture-cured	progressive cavity pump with 340 KPa, and tapered nozzle 22G	24 hours	Rough around 600 µm	Pneumatic finger and sphere balloons	No	[64]
	-----	The chemical reaction between gel remains in the bath and extruded ink	----	Between hours to days.	Between 200-400 µm	-----	No	[181]
Chemical Direct Ink Writing (DIW)	PDMS	Thermally cured	Two Syringe pump	----	400 – 500 µm	3D architectures	Yes (2 Inks)	[182]
	Biocompatible polysiloxane (RTV 800-400)	UV curable	Pneumatic micro-syringe deposition system	3 secs	300 µm	-----	No	[177]
	poly(acrylamide) (PAAm) hydrogel and (PDMS)-	UV curable and thermal curing at 60 °C	syringe pumps	6 hours	sub-millimeter	Soft Ionic device	No	[178]

	KER-4690 Block copolymer (UV curable silicone) dispersed in mineral oil	UV Curable	syringe pumps	20 min	30 $\mu\text{m}$	organic microgel system	No	[179]
	Mercapto-functional silicones	UV curable	Pneumatic deposition system	<20 s	600 $\mu\text{m}$	-----	Yes (2 Inks)	[180]
<b><i>Vat Polymerization</i></b>								
One photon	UV curable silicone + Photo initiator	UV curable	-----	-----	100-400 $\mu\text{m}$	Bio-compatible scaffolds	No	[145]
Two photon & Mask projection	PDMS	UV curable	-----	-----	1-5 $\mu\text{m}$	-----	No	[183, 184]
<b><i>Material Jetting</i></b>								
Fully reactive inkjet printing (FRIJP)	Polytek PlatSil 71-Silliglass	Chemical reaction	-----	0.3 sec	50-100 $\mu\text{m}$	-----	Yes	[153]
<b><i>Hybrid Jetting and Extrusion printing</i></b>								
DIW	UV-curable silicone	UV/Moisture curable mechanism	Pneumatic and solenoid actuation	-----	500-600 $\mu\text{m}$ for extrusion , 300-400 $\mu\text{m}$ for jetting	-----	No	[185]

These strategies include the use of multiple nozzles,[182, 186-189] multiple vats,[150, 190-192] and core-shell/coaxial configurations.[129, 193-198] 3D printing using a multi-nozzle strategy is often employed in applications using multiple materials. Each nozzle distributes a different type of material, as they are independent. Multiple nozzle strategy has been employed in inkjet printing and extrusion printing. In the vat photopolymerization method, switchable vats make it possible to print multiple materials simultaneously. The exchange of materials has been achieved through either manual or automated approaches. Another method for multimaterial printing is the use of coaxial flow

that is used to form a core-shell type arrangement of materials. Coaxial techniques are a unique approach to the extrusion-based 3D printing method. This method positions two independent inks close to each other along the same axis along the shank of the extrusion printhead. Inks with different compositions and functional properties can be positioned in a radially stacked fashion, and the low Reynolds number ensures that they remain stable in this configuration as they are deposited on the printbed.

Rapid prototyping for a wide range of applications could be made possible by these multimaterial printing strategies. Among all AM processes, only material jetting and material extrusion have demonstrated promising results for silicone multimaterial 3D printing. Specifically, the DIW method has been the most widely used one to create multimaterial structures formulated from silicones. The reason behind that is the versatility and compatibility of the DIW method with the rheological nature of different types of silicones. Following section, we will discuss the multimaterial printing progress for silicone-based materials using the DIW method.

#### ***1.2.4.1 DIW multimaterial techniques for silicones***

Multimaterial DIW enables the creation of soft/hard structures made of silicones as well as other materials and has the ability to combine different compositions and rheology to create distinct formulations. Recently, there has been considerable use of the direct ink writing technique to develop multi-material 3D printing in a precise, robust, and rapid manner. The main focus of the research to shift from single to multi-ink printing has been in the introduction of modifications to microfluidic printheads, which allow switching or mixing of different materials in just one step. With DIW technology, different formulations can be

combined in complex structures through approaches such as co-extrusion of inks and multiple inks containers.

Co-extrusion of inks is often performed using concentrically oriented nozzles to dispense coaxial filaments (composed of a core and a shell of different materials). Co-extrusion technology has previously been used to print polymer-based core-shell structures. For example, *Frutiger et al.* reported a multicore-shell fiber structure printed by an aligned coaxial printhead composed of four cylindrical nozzles (**Figure 1-7a**).[193] The developed multicore-shell fiber comprises a dielectric layer (silicone elastomer) sandwiched between two conductive layers (ionically conductive ink). This printed geometry was used as a capacitive soft strain sensor in which the thickness changes as a result of applying a deformation can be sensed (**Figure 1-7a**).[193] The fabricated multicore-shell fiber had a core diameter of  $335 \pm 6 \mu\text{m}$ , the silicone layers thickness ranged from  $135 - 277 \mu\text{m}$ , and the fiber diameter was around 1.5 mm.[193] After curing at elevating the temperature, the fabricated fiber can function up to 700% strain.[193] The authors also integrated the developed soft strain sensor with textile substrates to detect human motion. Similarly, *Mueller et al.* reported an innovative method for constructing lattices through a core-shell printing approach to obtain stiff and durable structures (**Figure 1-7b**).[199] A 3D printed tapered coaxial printhead was fabricated using a commercial stereo-lithography to allow printing the required 3D core-shell structures (**Figure 1-7b**).[199] Three different viscoelastic inks were used, including flexible epoxy as the core, hard but brittle epoxy as the shell and the interface resin was silicone elastomer. In order to ensure adequate separation between the core and the shell, the printed silicone layer thickness was about  $34 \mu\text{m}$ . [199] Another demonstration presented by *Chortos et al.*

exploited the multicore-shell 3D printing approach to develop dielectric elastomer fibers and bundles (**Figure 1-7c**).[200] The fabricated tapered printhead with three inputs allows coaxial printing of insulating dielectric matrices (composed of fumed silica nanoparticles dispersed in silicone elastomers) and conductive electrodes (composed of Carbon black nanoparticles dispersed into silicone elastomers), as shown in **Figure 1-7c**. [200] The printing process had the ability to switch between core, sheath and shell inks (through a start and stop process) dynamically, which enabled different core-shell material configurations in the same print. The minimum electrode layer thickness obtained was about 15  $\mu\text{m}$ , while the fibre diameter was around 730  $\mu\text{m}$  with maximum strain of 100%. [200] The developed multimaterial multicore shell printing structures were utilized as novel soft active materials to be used as soft actuators with predefined electrode patterns. Co-axial printing is limited by the specific radial orientation of the material stacking that it can create and therefore is limited to a small subset of applications where such features can be used. Furthermore, nozzle diameter has to be increased to accommodate larger number of materials co-axially and switching could also be a problem.

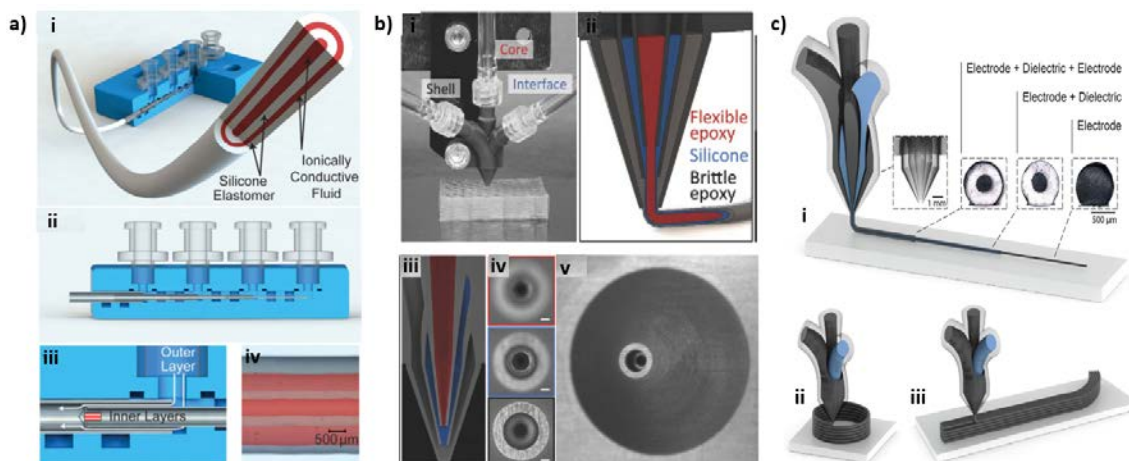


**Figure 1-7** a) Illustrations of the printhead configuration with a magnified view of the outlet region.[193] b) Multicore-shell nozzles and ink rheology. Optical image of the coaxial printhead connected to the core, interface, and shell ink reservoirs, and a schematic cross-sectional view of

the C-S printhead.[199] e) Multicore-shell 3D printing illustration with a cross-sectional view of nozzle-based printhead and core-shell dielectric elastomer fiber (DEF).[200]

The most widely used approach in DIW for multiple material printing is to use multiple ink containers, which can hold the different inks and either switch between them or mix them in various proportions to create a palette of ink combinations. To achieve mixing, a single nozzle is used to extrude multiple materials via a common printhead in which all inks meet and mix, then dispense from the single nozzle to allow the gradual change of the ink compositions. [201-206] While, in the case of switching between various inks, a multiple nozzles outlet,[43, 207-209] or single nozzle outlet [182, 210] have been utilized. Thus, the discussion will be divided into two sections; one is related to the mixer printhead, and the other is related to switching between inks.

On-the-fly mixing has been achieved using different approaches of the DIW method by designing a customizable printhead. Mixing in DIW printing, especially with silicones inks, is a challenge due to the low Reynolds number flow regime that they operate in. Therefore, different attempts have been developed to overcome this constraint by using various mixing techniques. For example, *Thomas et al.* developed an active mixing printhead for viscoelastic inks printing such as silicone elastomer (DOWSIL™ SE 1700 Adhesive) and lubricant gel[201] by incorporating a rotating impeller inside the printhead. Their printhead consisted of two inlets that merged together at the mixing chamber and a small rotating impeller located inside the mixing chamber (**Figure 1-8**). The mixing impeller (2.7 mm in diameter and 30 mm in length) was ground down to fit into the nozzle diameter, and it was connected to a stepper motor for speed control. The designed mixer volume was around 150  $\mu\text{L}$ , allowing switching time between different ink compositions of 30 sec.[201] That allows mixing of multiple high-viscosity inks using the impeller setup,

and the mixing efficiency was not dependent on the flow rate and the mixer volume.[201] However, the incorporation of a large impeller into the printhead increased the priming volume (range of hundred microliters), resulting in high switching time obtained between different compositions as well as the limitation of the number of inks that can be mixed (only three).[205, 206] It also needed active control of the mixer through an external power supply.

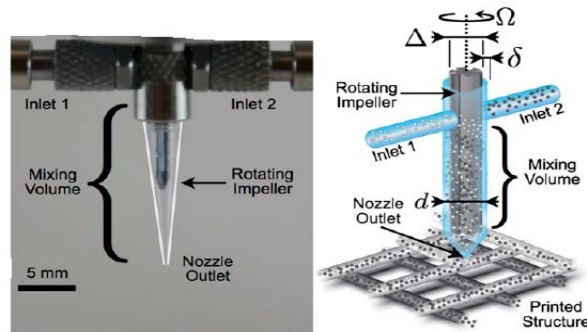


**Figure 1-8** Optical image of the impeller-based active mixer, and schematic illustration of the mixing nozzle in operation for 3D printing of two inks with particles of a different colour.[201]

The other approach involves on the fly switching of containers and/or nozzles during the ink delivery, which can be considered a “true” multi-material printing. The challenge associated with this approach is in achieving fast switching between different inks combined with accurate printing. This challenge has not been overcome through the use of multiple nozzle outlets due to the incompatibility of such design with fast start-stop operations, which has led to a loss of precision in printing. More recently, some attempts have been made using the single nozzle outlet attached with multiple inlet ink reservoirs to achieve multimaterial printing. For example, *Hardin et al.* demonstrated the ability to 3D print multi-material using a single nozzle printhead by utilizing a microfluidic technique to control the material rapidly. A microfluidic printhead, shown in **Figure 1-9a**, was designed based on an analytical model of viscoelastic ink flow.[182] The scaling laws were

derived through this model for optimizing the ink switch ( $\sim 1\text{Hz}$ ) between the two inks relying on the small dimensions of the developed design (the priming volume was in the nanoliters range). Multiple 3D architectures were patterned with silicone-based materials (DOWSIL™ SE 1700 Adhesive) to demonstrate the application of this method of switching to produce 2D and 3D parts with varying mechanical properties embedded in them.[182] However, the developed system was not scalable to more than two inks and used a syringe pump-driven DIW system that is not suitable for fast start-stop operations required for 3D pixelated printing due to the compliance and thread backlash during printing.[182] Alternatively, another attempt made by *Zheng et al.* was reported in which different 3D multimaterial structures were formulated from silicone polymers.[180] The printhead comprised three inks reservoirs connected to a 3-way junction connector and extrusion needle (25 gauge) at the outlet tip (**Figure 1-9b**).[180] The reservoirs were connected to three solenoid valves separately, and the flow was initiated pneumatically by a pneumatic system with air pressure up to 8 bar. The printhead was designed with a priming volume of  $130\ \mu\text{m}$ , which allows switching. However, due to the large priming volume, the printhead should be dispensed from the nozzle far from the printing zone (for 40 sec) while switching to remove excess ink before continuing the printing with the new one.[180] Although the developed printer setup was utilized by a pneumatic system that allows more flow control, the switching was very slow, and the design was not scalable. Recently, *Skylar et al.* reported a novel DIW system with a scalable printhead that can rapidly switch between up to 8 viscoelastic inks.[47] The printhead was fabricated using a high-resolution stereolithography printer to allow the scalability of the printhead channels (**Figure 1-9c**). The authors used a pneumatic driven system to allow more controlling of

the flow for continuous extrusion during the start-stop operations. The minimum pixelated resolution they could reach was around 0.5 mm. The developed switching printhead can reach up to a switching speed of 50 Hz, allowing them to fabricate various pixelated structures such as foldable origami patterns and soft robots.[47] However, this system cannot be used without special shear-thinning inks (Herschel - Bulkley) that allow accurate switching by preventing undesirable backflow (due to static yield resistance). If such fast switching can be achieved with Newtonian inks it can potentially widen the application of pixelated 3D DIW printing to many more industrially significant materials. **Table 1-4** summarized different DIW multimaterial approaches with the output features, limitations, and applications. To better understand the physics behind achieving fast switch ability and mixing, the rheological behaviour of the used inks in literature and the mixing technique in microfluidic devices have been summarized.

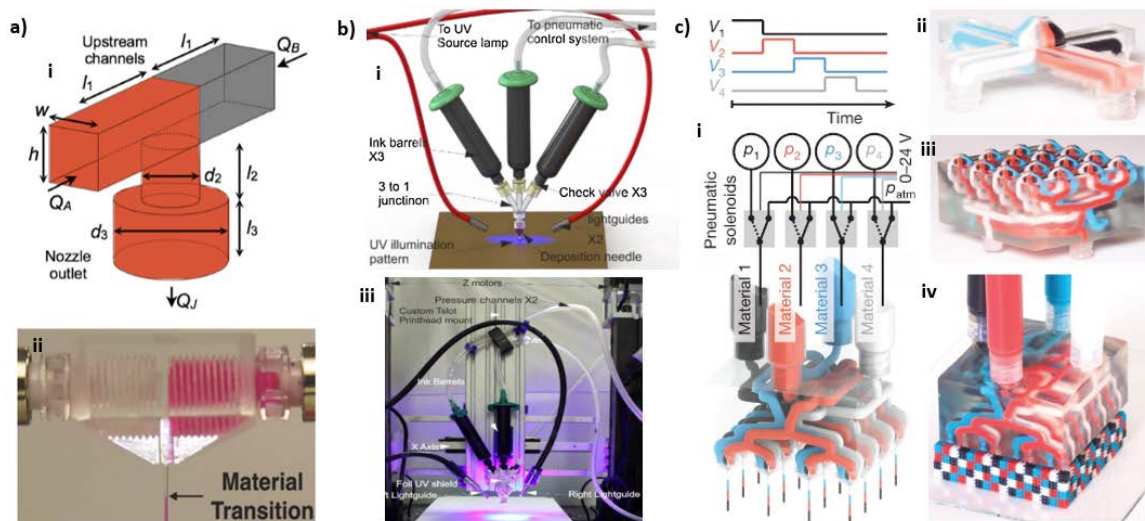


**Figure 1-9** a) Multi-material microfluidic printhead. Illustration of the nozzle outlet with dimensions. [182] b) Illustration of the 3D printing system with all connections joined to the junction and needle.[180] c) Schematic of switching printheads that control the extrusion pressures  $p_1$ – $p_4$  for materials 1–4, with a Voxelated matter created using a  $4 \times 4$ -nozzle, four-material, 2D printhead.[47]

**Table 1-3** Comparison of multi-ink printing approaches for silicones.

AM technology	Materials	No. of inks	Mixing technique	Features	Limitations	Applications	Ref.
---------------	-----------	-------------	------------------	----------	-------------	--------------	------

DIW	PDMS elastomers of varying composition	2	Switching between two inks from the same nozzle, no mixing	High switching rate with prim volume 12.6 nl.	Low aspect ratio and a maximum of two inks.	1 D, 2 D, 3D architectures with two inks	[182]
DIW	Polyurethane acrylate (PUA) oligomers,	3	Static mixing using two magnetic, up to 4 inks from the separate nozzle	Building blocks used to control the orientation of anisotropic particles by applying low magnetic fields	More than one nozzle, supporting material for overhang structure	Soft mechanical fasteners, complex heterogeneous composite with intricate shape	[211]
DIW	Polyurethane Acrylate Ink:	2	Static disposable mixer with max mixing ratio 1:5	Dual-mixing extrusion for fabrication of polymer-based heterogeneous materials.	Limited no. of inks	Artificial Hand	[212]
Extrusion printing	Nonvolatile ionic fluid, silicone	2	No mixing, coaxial printing	Custom-designed printhead composed of four cylindrical nozzles aligned coaxially	Limited no. of inks	Multicore-shell fibre strain sensor	[193, 202]
DIW	Silver ink, Pluronic solution, Carbon ink, an aqueous polymer lubricant	2	Active mixing	On-the-fly active mixing using a rotating impeller of concentrated viscoelastic inks.	Limited no. of inks	-----	[201]
DIW	photosensitive resin, and water-glycerol mixture	2	Passive droplet mixing	Multi-material microfluidic 3D printing for fabricating textured composites with fluid inclusions of programmable distribution.	Limited no. of inks	Self-healing composites	[213]
Extrusion printing	Calcium chloride, water, Alginate	4	No mixing, switching with active check valve	Coaxial-flow focusing technique to precisely dispense and build heterogeneous hydrogel structures	Switching rate prolonged, no mixing	-----	[214]
Extrusion printing	Acylated urethane UV-curable adhesive &	2	A disposable static chaotic mixer	Fabricate a range of composite materials	Limited no. of inks	gradient printing human tendon muscle	[215]

	alginate/poly(acrylamide)						
Extrusion printing	Flexible and Brittle epoxy and Silicone	3	No mixing, coaxial printing	Creating architected lattices composed of core-shell struts	Limited no. of inks	Architected lattices	[199]
Extrusion bio-printing	Shear-thinning bio links	7	No mixing, bio-inks switching	It is continuously extruding multiple coded bio-inks with fast and smooth switching.	No mixing	cell-laden structures	[207]
DIW	Concentrated silver nanoparticle ink	1	-----	Printing on standard three-dimensional Surfaces	Printing on Freeform surfaces, no. of inks	3D electrically small antennas	[216]

#### 1.2.4.1.1 Material rheological behaviour

In extrusion 3D printing, fluid flow inside the printhead not only depends on the channel's dimensions but also on the material rheology. A 3D multimaterial printing with switching and mixing capabilities needs to be integrated within the printhead design to create multifunctional devices. One of the most important ink properties that greatly influences this operation is viscosity. This is especially true for complex rheology fluids, which is used more frequently in practical applications.

In general, fluids can be classified into two groups: Newtonian and non-Newtonian fluids.[217, 218] Newtonian fluids have a linear relationship between the shear rate and shear stress (**Figure 1-10**). Viscosity represents this relationship and is the ratio of the shear stress to the shear rate. In Newtonian fluids, the viscosity is independent of shear rate, and the relation between viscosity and shear rate can be plotted as a horizontal line. The relation between the shear rate and shear stress is nonlinear in the case of non-Newtonian fluids, which are also known as time-dependent fluids (**Figure 1-10**). Among non-Newtonian fluids, shear-thinning fluids are the most commonly used type in extrusion 3D printing in

which the viscosity decreases as the shear rate increases.[217, 218] In the DIW method, the ink should exhibit a low viscosity to facilitate the flow through the printhead throughout. In addition, the ink should have the ability to maintain the printed shape after the deposition. The shear-thinning materials meet such requirements to print with high fidelity and be used as support materials owing to their unique rheological properties. Shear thinning fluids at very low shear rates zero-shear exhibits very high viscosity,  $\mu_0$ , which means the resistance to initiate flow increases significantly. Therefore, the shear thinning materials also allow achieving fast switching like described in the previous section due to static yield resistance.[47] On the other hand, Newtonian ink rheology limits the ability to achieve fast and reliable switching. Next, we will discuss the mixing techniques in literature for achieving proper mixing during printing.

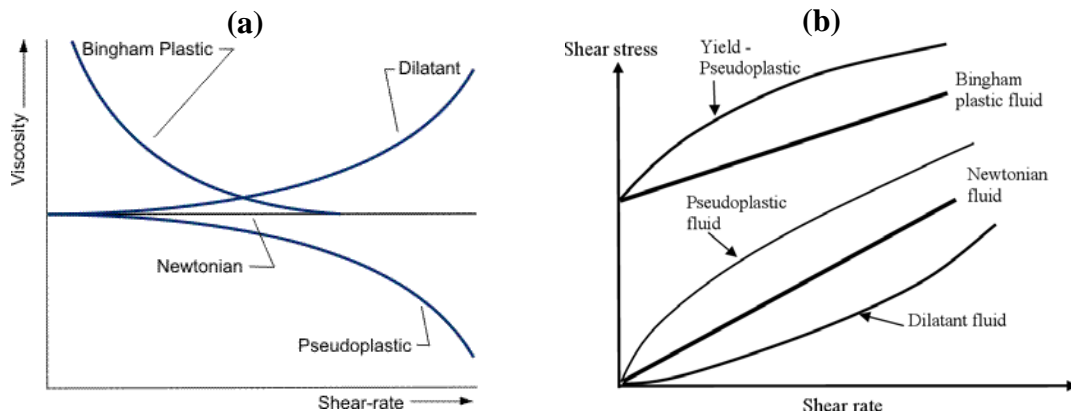


**Figure 1-10** Fluid types with the influence of shear rate on (a) viscosity and (b) shear stress. [217, 218]

#### 1.2.4.1.2 Mixing techniques for microfluidic devices

Microfluidic devices and printheads operate under a flow regime where viscosity dominates over inertial flow. This regime is known as the low Reynolds number regime, where the Reynolds number can be defined as follows.[30]

$$Re = \frac{U D_h}{\nu} \quad 2$$

Where  $\nu$  is the kinematic viscosity ( $\text{m}^2 \text{s}^{-1}$ ),  $D_h$  is the hydraulic diameter (m),  $U$  is the average flow velocity ( $\text{m s}^{-1}$ ).  $Re$  represents the ratio between inertia and viscous friction. In most cases of microfluidics, a low Reynolds number and a laminar flow can be expected.  $D_h$  can be determined by this relation  $4 \times \text{Area (cross-section area) / wetted perimeter (of channel cross-section)}$ . In a low Reynolds number regime, mixing is difficult as the fluid layers slide past one another, and mixing is by diffusion alone. For many bioassays to material synthesis procedures, [30, 219] mixing at small Reynolds is essential. Several techniques have been developed in microfluidics to mix fluids at this scale and can be categorized as passive and active mixers. Passive mixers - also known as static micromixers - are simple and work without moving parts, but their mixing efficiency is strongly associated with flow velocity, and internal channel structure mixing is achieved mainly through diffusion or chaotic advection. Significant research has been conducted to develop microfluidic systems that passively blend tiny quantities of liquid through chaotic advection or secondary flow [30, 31]. A passive micromixer can be classified into three-dimensional (3D) or two-dimensional (2D) micromixers based on its design dimensions. Several designs of passive micromixers based on the T-type [220], Zigzag [221], and Serpentine [222] have been developed. However, since passive mixers require complex geometry to introduce chaotic advection in the flowing fluid, they are challenging to manufacture. On the other hand, active micromixers utilize the disturbance created by an external force for the mixing operation, such as electrical, magnetic, and sound fields. The mixing effect is enhanced by adding different external forces to disturb the fluids, improve the contact area, or induce chaotic advection. Active micromixers are distinguished based

on the type of external energy source they are driven by, such as electrical [223, 224] and magnetic fields,[225] sound fields,[226], and thermal fields [227]. Micromixers with active mixing are often simpler in their design, and their control is less complicated, but they require external energy sources, making them more challenging to fit inside the micromixer structure. **Table 1-5** and **Figure 1-11** compare the passive and active micromixers approaches with advantages and limitations along with the working conditions.

Several non-dimensional groups have been used to evaluate the micromixer performance. one of these non-dimensional groups is the Peclet number, which is vital to evaluate the mixing process:[30]

$$Pe = \frac{U L}{D} = \frac{Q}{D_h D} = Re Sc \quad 3$$

Where  $D$  is the diffusion coefficient ( $m^2 s^{-1}$ ),  $L$  is the mixing path (m),  $Pe$  represents the ratio between the mass transport due to convection and that of diffusion. For materials with high viscosity (high  $Pe$ ), very long channels are required, leading to significant pressure drops. Hence, a flow regime with lower  $Pe$  will have better mixing efficiency. The dimensionless parameter is the Schmidt number,  $Sc = \nu/D$ . Convection is dominant at higher Peclet numbers. For an active mixer, another important non-dimensional group is the Strohal number:

$$St = \frac{f D_h}{U} \quad 4$$

Where  $f$  is the disturbance frequency (Hz),  $St$  represents the ratio between the residence time of a species and the period of its disturbance in an active micromixer. When examining the unsteady flow, a valuable criterion for evaluating how closely the flow approaches its fully developed state is based on the following combination of the Reynolds and Strouhal numbers.

$$\frac{v t}{L^2} = \frac{1}{St Re} \quad 5$$

Micromixers are able to mix different fluid streams at very small scales due to the dominance of molecular diffusion at channel sizes of only a few tens of microns. However, in most DIW 3D printing printheads, the channel dimensions are several hundred microns or more, which means that the diffusion of molecules can take a long time. In addition, the DIW method mostly uses shear-thinning inks or viscous inks in which the flow regime is low Re. A large-scale mixing can only be achieved in a reasonable amount of time if both interfacial surface areas are increased massively, and the diffusion path is decreased, thereby enhancing molecular diffusion. This reasoning indicates that the minimum residence time scale of a fluid element in the mixer must exceed the mixing time  $t_{\text{mix}}$  needed for the species to diffuse over a characteristic distance set by the flow dynamics within the mixer in order to mix these liquids. Additionally, mixing inside micromixer printheads can also be enhanced by introducing features to stretch and fold the layers of fluids, which can be achieved by a different breakup and rejoining mixing mechanisms.

Many approaches have been used to incorporate a micromixer in a DIW printhead. In particular, some of these have focused on mixer sub-assemblies that can enable disassembly and cleaning in the complex geometries that allow passive mixing in the case when the ink solidifies inside the printhead, and it clogs. One of the suitable passive mixers that can achieve on the fly mixing is a static mixer which can be integrated inside the mixing junction.[205, 206] However, the priming mixing volume is large, leading to a large switching time between different compositions. In addition, the mixing efficiency is entirely dependent on the channel dimension and the flow rate. Therefore, an active mixer can make the mixing efficiency independent of the channel dimensions and flow rate by

initiating instabilities inside the mixing chamber and enhancing mixing. Some recent works have used microstirrers based on a rotating impeller to achieve that decoupling.[201-204] However, this mixer design is more complex, and the mixing chamber volume is larger, making the switching between different formulations still not fast enough. Therefore, an existing challenge in the field is developing a versatile technique to allow mixing and fast switching during printing independent of flow characteristics.

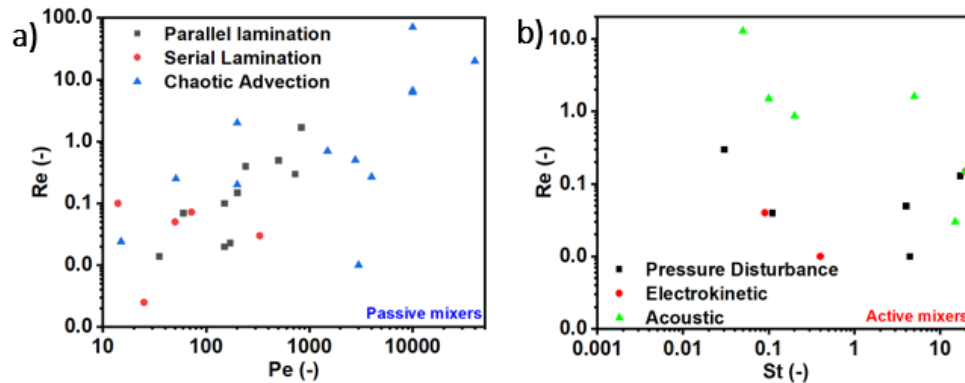


Figure 1-11 Typical operation ranges of micromixers, a) Passive mixer, b) Active mixers.

Table 1-4 Passive and active mixing techniques comparison in the microfluidic field.

Type	Categories	Channel dim. (µm)	Velocity (mm.S <sup>-1</sup> )	Re*10 <sup>-2</sup>	Pe	Mixing Index	Mix Time (ms)	Materials	Advantages	Limitations	Operation Principle	Ref.	
Passive Micromixer	<i>Parallel lamination micromixers</i>												
	T-mixer "molecular diffusion."	550* 25	6	30	72 5	---- --	2000/--	SI-Glass	Low fabrication cost and simple design	Long mixing path and high t <sub>mix</sub>	Transport phenomena studies on a microscale	[220]	
	Y-Mixer "molecular diffusion"	900* 50	0.27	2	15 0	---- --	2400/--	PMMA				[228]	
	<i>Serial Lamination Micromixers</i>												
	Join-Split-Join	300* 30	1-22	3- 6.6	15- 33 0	---- ---	~/ 100- 300	Si-glass 3- stages	Basic, but more effective than pure diffusive mixing	Long/complex micromixer network	Electro-osmosis flows between the multiple intersect.	[229]	
	Split-Split-Join	600* 100	0.5	5	50	0.98	3400/--	Mylar 6 stages				[230]	
	Multiple Intersecting	100* 10	0.25	0.2 5	25	1	100- 1000/-	Quartz 1 stage				[231]	
	<i>Injection Micromixers</i>												
	400 Nozzles (330 µm)	2000* 15	1.2	1.8	18	---	---- /1200	Silicon-glass	Increase contact surface/ reduce the mixing path.	High fabrication cost with complexity in fluids distribute.	Splits solute flow and injects them into the solvent flow.	[232]	
	1 Nozzle (7 µm)	820* 70	15	10	10 5	----	9400/3 700	Silicon-glass				[233]	

Type	Categories	Channel dim. (µm)	Velocity (mmS-1)	ω <sub>c</sub> (Hz)	Re*10 <sup>-2</sup>	Pe	St	Materials	Mixing Index	Advantages	Limitations	Ref.
<b>Chaotic Advection</b>												
	Cylindrical obstacles	100*100	20	20	200	0.55	1200/--	Silicon-glass	uniform mixing over the whole channel.	The difficulty of fabrication.	Clear evidence of stretching-folding action.	[234]
	Zig-zag shaped	100*48	1.3	26	130	0.81	2000/--	Mylar				[221]
	3D Serpentine	100*70	1-20	10-200	10-200	0.99	1200/--	PDMS	Easy to fabricate (no moving parts)	Requires adjust level of mixing	Precise control is not needed.	[222]
	Slanted Grooves	200*70	15	1	3000	---	---	PDMS				[235]
<b>Droplet Micromixers</b>												
	Pressure driven	100*150	--	--	--	--	--	PDMS/P MMA 10 nl drop size	Droplet takes an isolated form. Mixing created by a meandering channel.	The carrier fluid and the target samples should be immiscible.	Chaotic Advection, Surface-tension effect is existing. Ca is significant as it reduces.	[236]
	Electrowetting-Hydrophobicity/ Surface Modification	600-1000	---	---	---	---	-- /1700-1490	Glass 1600 nl drop size	Additional mixing enhancement.	Complicated for surface modification zones	The merged droplet transported around using electrowetting.	[237]
	Multiple Phase	(20-100)	--	--	--	--	--/800	PDMS 75-150 nl drop size	Low fabrication cost.	Purification step as immiscible carrier liquids.	Shear force between carrier liquid and the sample increased the mixing process in the droplet.	[238]
<b>Acoustic Disturbance</b>												
	Acoustically driven sidewall-trapped microbubbles	240*155	---	---	---	---	---	PDMS	0.975 with 120 ms	Nearly instantaneous mixing easy to operate	Need a bubble and temperature rise caused by acoustic energy.	[226]
	Acoustic streaming induced by surface acoustic wave	6000*60	0.5	60 K	3	30	---	Si-glass				-----
<b>Dielectrophoretic disturbance</b>												
	Chaotic advection based on Linked Twisted Map	50*25	0.5	1	3	25	0.1	Si-SU8-glass	0.85	Mixing time is reduced. very simple design	Need non-uniform electrical field	[240]
<b>Thermal Disturbance</b>												
	Thermal enhancement	200*50	0.11 µl/s	200	--	---	---	Si-glass	0.95	Simple to integrate into a device	Requires heaters	[227]
<b>Electrokinetic disturbance</b>												
	Low Reynolds number	500*35	1	0.17	3	509	0.09	PDMS-glass	0.98	Effectively at low voltages. short mixing lengths.	Requires integrated electrodes	[223]
	Electro-osmotic flow	1000*300	0.5	10	15	1050	20					[224]
<b>Magneto-hydrodynamic disturbance</b>												

High operating frequency	100*50	1.756	17.56	--	---	1	-----	0.977 at 1100 ms	An external magnetic field generate Lorentz forces	only works with an electrolyte solution.	[225]
<i>Electrohydrodynamic disturbance</i>											
Staggered herringbone structure	50*20	---	---	30	---	---	Si-PDMS	≈ 1	Achieving good mixing by adjusting voltage and freq.	Needs series of electrodes. Complex design.	[241]
Electrohydrodynamic	250*250	4.2	0.5	2	1050	0.03	-----	0.85 at 0.1 s			[242]
<i>Pressure field Disturbance</i>											
Microstirrers- for 3d printing application	750*70	---	600 rpm	--	--	--	Si	0.82	Versatile; excellent mixing with control	Complex shape (moving parts); need multiple-stirrers	[201, 243]
Flow pulsation/ serial segmentation	1000*150	--	--	5.5	59300	---	Si-glass	0.68			[244]
Chaotic electric fields	50	---	---	---	---	---	---	0.95 at 100 ms	Easy to implement using micropumps or electric fields	Requires fine-tuning to achieve optimal mixing	[245]
Periodic electro-osmotic flow	200*50	----	2	18	104	0.54	PDMS	0.88			[246]
Pressure disturbance along the mixing channel	200*26	1.6	0.85	4	321	0.11	PDMS	-----			[247]

Another challenge of 3D printing techniques is the ability to construct structures over nonplanar substrates or geometries. Therefore, we will discuss different techniques used for achieving such advanced capability.

### 1.2.5 Printing silicones patterns over non-planar morphology

Due to their origins in prototyping, additive manufacturing techniques have been generally developed for printing on planar surfaces. Adapting many of them to printing on non-planar geometries and surfaces is challenging. For instance, flexible electronic and wearable devices need to be printed directly on natural non-planar geometry. Due to a lack of direct approaches, alternate ones such as printing on flexible and elastic thin films that can be bonded to curved surfaces have been developed.[248, 249] In light of this challenge, processes for fabricating 3D functional objects directly on irregular surfaces with customizable, 3D conformable, and flexibly mountable on the target surfaces are highly

sought after.[249, 250] There have been several recent methods for manufacturing functional devices on non-planar topography, including transfer printing, conformal inkjet printing, aerosol jet printing, and extrusion 3D printing.[248, 249] For instance, transfer printing is the most commonly used method due to its size and quality advantages. A textile transfer printing process involves printing a design on a planar substrate and later transferring it to a nonplanar substrate via a separate process. Transfer printing allows high precision fabrication, can be operated at room temperature and is compatible with various sizes and shapes of substrates. In terms of manufacturing accuracy and performance, transfer printing has an excellent property, but they cannot be used on large surfaces. Also, the design of the stamps for transfer printing is difficult to achieve for non-planar geometries.[248, 249] In contrast, direct fabrication methods such as additive 3D printing have the potential to be adaptable to printing on non-planar substrates [248, 249]

Several attempts have been made to incorporate the extrusion 3D printing technique for printing on nonplanar topography. For instance, 6 DOF mechanical arm robots equipped with material deposition printheads have been used to 3D print on complex curved surfaces. Nevertheless, there are still several challenges to overcome. It is computationally challenging for 6-DOF robots to plan collision-free trajectories along complex curved surfaces. It is vital to continuously adjust process parameters as the deposition is performed along curved surfaces to achieve defect-free parts. For this reason, we need to construct a model relating process parameters to deposition. Additionally, multimaterial printing could be integrated to produce support structures over curvatures and facilitate creating geometries with more complex characteristics.

Alternative techniques have been developed by creating an algorithm that makes it easy to produce a printing trajectory as a sequence of points projected on a triangle-tessellated non-planar surface.[51] In this algorithm, prepared points of the 2D path are processed, along with STL files of the target layer and predicted direction. Next, the printer receives G-code instructions for the new trajectory on the target surface.[51] Similarly, in the curved layer manufacture (CLM) technique, the layers of material are built up along a curve rather than along a planar surface. Using this approach, a process of fabrication on non-planar lattices along parametric surfaces has been developed.[251] The method was utilized to fabricate a variety of lattices on Bézier surfaces, showing its promise and demonstrating its zero-waste output when reusable mandrels are used.[251] Further work describes how to design and build a four-axis 3D printer that uses Direct Ink Writing techniques to extrude a thixotropic silicone into any irregularly shaped substrate accurately.[252] 3D scan of the target surface was used as the input to a parametric software to transform the 3D object to be printed along that surface.[252, 253] After that, the print path of the computed substrate was generated to create the 3D printer toolpath. These approaches, however, completely relied on the nonplanar surface of interest to create a path without real-time feedback and at a relatively high cost.

To be able to print on the fly on unknown surface topologies, the 3D printing system should include more capable scanning technology and a calibration process.[254] A prototype was developed for depositing over unknown 3D subjects by first scanning the 3D objects then generating a toolpath on the fly.[254] Further investigation also developed a new methodology for combining 3D scanning techniques with multiple axis 3D printing to create layers at different deposition angles and print on uneven substrates.[255] All the

techniques mentioned above are open-loop systems that do not have instantaneous feedback from the surface to correct any errors that may have crept in during printing. Alternatively, combining a close-loop system with the 3D printer can allow real-time feedback, facilitating printing on a complex surface or even freeform surfaces like skin.[256] A hybrid manufacturing process was developed using this method by integrating the automatic pick-and-placing method with 3D DIW printing to allow printing on freeform surfaces like live mice.[256] Nevertheless, this approach needs more development to reduce printing time and allow multimaterial printing required to create multifunctional devices like wearable electronic components. In addition, such active closed-loop control requires a complex computer visioned automation system to produce the freeform G-code path with real-time response. Therefore, identifying lower cost and more reliable passive control system is of significant interest.

### **1.2.6 Multimaterial 3D printing applications for silicones**

Soft matter can now be fabricated with high complexity using 3D printing. This section will explore these applications in detail while emphasizing the powerful role that 3D printing techniques have played in them.[59] In particular, the focus is on applications including flexible electronics,[132, 257, 258] soft robots,[259, 260] and energy harvesting devices.[261-272] One of the relatively new applications among those mentioned earlier is the energy harvesting field.[4] Energy harvesting devices collect energy from the surroundings and use it for generating electricity for use in other electrical appliances. Many energy harvesting approaches have used 3D printing technology such as solar cells,[261, 273-275] piezoelectric energy harvesting devices,[262, 263, 276] and triboelectric nanogenerator devices.[263, 266-272, 277] For the use of silicone based

material, triboelectric nanogenerator (TENG) may be consider the most appropriate technology to utilize and integrate materials like silicone-based materials within the fabricated device.

TENGs can convert mechanical energy and the corresponding electrostatic induction to electricity through the triboelectric effect. A triboelectric effect results in a potential being created in this power generation unit. This is created by the charge transfer between two thin organic/inorganic films exhibiting opposite tribo-polarities. To balance the potential, electrons are drawn between two electrodes attached to the backside of the films in the outer circuit. Since the common structures of any TENG device are multilayer structures, thus adapting a multimaterial technique to fabricate such device in one step will be timesaving and enhance the contact interface between the layers. Many attempts have been developed to use silicone-based material in TENG devices. For example, *Li et al.* reported an adaptable TENG created through the DIW method.[278] The DIW printing approach has been used to print the triboelectric layer formulated from silicone elastomer viscoelastic ink, and the substrate was an aluminium foil to be used as an electrode layer.[278] The DIW allows the creation of a micro-sized tribo-layer (the thickness range of the triboelectric film was from 150  $\mu\text{m}$  - 400  $\mu\text{m}$ ), enhancing the surface textures by optimizing the extruding process and subsequently enhancing the TENG output.[278] On the other hand, the TENG can sustainably drive 51 LEDs and a 3.25-in. display through vibration energy harvesting operation. In another attempt, *Qian et al.* reported an all printed biocompatible cellulose TENG to work as self-powered mechanical and humidity sensors.[279] The TENG device consisted of a cellulose nanofiber aerogel (CNF) as the first tribo-layer, a PDMS layer as the second tribo-layer, an AG layer as an electrode, and

PET as a substrate.[279] A direct-write printing method was used to print the Ag electrode on the prepared PET substrate rendering to the design. Next, on the Ag/PET substrate, respectively, the PDMS and CNF layers were printed. To create hierarchically patterned 3D micro/nano microarchitectures, CNF based 3D layers are freeze dried and then annealed. Through the assembly of positive and negative friction layers, the desired TENG was obtained.[279] In comparison to traditional molded TENGs, the developed TENG yields a higher voltage output thanks to its hierarchical micro/nano 3D structure which increases the contact area. A set of 88 LEDs and a humidity sensor can be driven by the 3D printed TENG, which can collect mechanical energy. Despite the various attempts to use 3D printing to create energy harvesting devices, their fabrication still requires many assemblies' processes after printing the functional layer. Thus, more work still needs to be able to create an energy harvesting device like TENG using only the 3D printing method without the need for adhering the electrode layers to the functional layer.

In summary, various multimaterial printing methods that have been discussed in this introduction do not seem to be designed optimally to print silicones and PDMS, especially in multimaterial combinations. Even so, extrusion DIW has a few advantages over other AM processes. The setup is simple and low cost. It can also be applied to a wide variety of materials with different curing mechanisms. Nevertheless, it is hard to find printing methods that can work with UV-curable silicones and highly reactive silicones. Moreover, the high reactivity of the resin makes it challenging to use extrusion printing since there can be no pre-mixing, which would ensure that the two components are homogeneous, and the dispensing device is not clogged. Despite this, DIW methods appear more appropriate for multimaterial printing, as they can handle different viscosities and curing mechanics,

but they may require some modifications. In order to overcome the limitations of printing with DIW inks, this thesis develops a new printhead design that can print inks of low/high viscosity and high reactivity with functional features.

### **1.3 Thesis Motivation**

The characteristics of silicone compounds are outstanding, including their biocompatibility, elasticity, heat, chemical resistance, and UV resistance. They are used extensively in automotive, aircraft, medical devices, and microfluidic applications. Silicone objects can be manufactured using extrusion, injection moulding, compression moulding, or several other methods. The methods mentioned above are more suitable for volume production, while newer Additive Manufacturing (AM) techniques allow rapidly and accurately fabrication of customized architectures in silicone. The stereolithography process, extrusion-based printing, and inkjet printing are the three most widely held AM techniques for silicones. Each of these methods produces fabricated objects of different sizes and resolutions. Despite the extensive research work, there are several challenges in printing multi-material combinations of silicones, and it is still under investigation and development. In particular, the use of microfluidic printheads to sequence and mix compositional variations from base inks is still in its infancy. Although microfluidic geometry is practically suitable for studying the ability of printing/mixing various soft materials, they are not tested to high throughput printing (HTP). Combining extrusion 3D printing research with microfluidic printheads can allow new multimaterial 3D printing capabilities such as fast switching, producing compositional gradients dynamically, and using many commercially available materials. Therefore, the proposed research aims to

develop a novel microfluidic printhead to regulate the deposition with a feedback control system for multi-material ink printing in extrusion 3D printing.

## 1.4 Research Objectives

The main goal of this thesis is to develop a controlled deposition printhead for silicones and demonstrate its use in smart sensing, actuators, and functionally graded materials. In addition, this printhead will facilitate controlling direct printing on freeform surfaces. To pursue this goal, the following objectives are defined:

1. Developing microfluidic printheads with integrated hybrid mixing by sequential injection for multimaterial 3D Printing
2. Developing a microfluidics printhead with deposition-controlled features for rapid continuous multi-material extrusion viscoelastic and viscous materials.
3. Developing direct ink writing technique for multimaterial printing over complex surfaces with a mechanically passive control system.

## 1.5 Thesis Outline

The thesis consists of six chapters. The first chapter (this one) introduces the literature review, thesis motivation, objectives, and the main contributions. The other chapters are summarized as follows:

**Chapter 2** details the application of 3D extrusion printing of silicones for application in energy generation. A previously developed 3D printing system in our lab was extended to fabricate the first all-printable TENG “triboelectric nanogenerator” that was used to generate power from snow. The 3D extrusion multimaterial printing approach for manufacturing the snow TENG was exploited not only to ensure low price and scalable fabrication but also to allow manufacture adaptability. In this procedure, the snow TENG

device is built by printing consecutive thin layers of PEDOT: PSS as an electrode and UV curable silicone as the triboelectric active layer. Owing to the energy harvesting ability of the snow-TENG, it can be used in cold regions as an automated weather station that generates its own electricity using nothing but the snow above it. Interestingly, it is able to measure snowfall rate, wind speed, and snow depth. The Snow-TENG can also be utilized as a renewable energy source for wearable devices and tracking equipment to monitor human activities. This means that mechanical energy harvested from the snow friction with the snow-TENG can be used for biomedical purposes in cases where possible hazards in snow-related sports are detected. Despite this demonstration, our previously developed DIW system had a few limitations. In this 3D printing process, mixing was not possible during the printing process. Moreover, the ink switching took considerably longer than desired because it had a large priming volume. Additionally, this printer could not print on non-planar topography. These problems are common to many other 3D printing techniques as well. Thus, to expand the capabilities of this and other extrusion printing systems, new enhancements were sought. The following chapters will discuss the enhancements developed during my PhD to fulfil the mentioned objectives.

**Chapter 3** presents our new microfluidic printhead that can mix together several different inks to create a palette of different ink combinations. In order to achieve fast mixing with a low priming volume, pulsatile injection of different inks is combined with a static mixing element. Computer simulations and experiments were conducted to help identify the range of conditions for optimal mixing using UV curable silicone inks. The simulation findings were validated by experiments with UV curable silicone inks. In order to achieve rapid mixing, the mixing efficiency was decoupled from the flow rate and

volume of the mixer. The results also revealed the ability to switch between different types of inks. Being able to quickly switch from one ink to another enabled sharp, clear interfaces when printing. The print head's switching time, measured as the time it takes for the print head to change ink colors, is the fastest ( $< 4$  seconds) among all cartridge-type DIW printheads used to print high viscosity inks. 2D and 3D objects such as a 2D color map and a 3D Rubik's cube were printed using inks of various viscosities to demonstrate its capability. This easy-to-assemble printhead can be used with a variety of liquid materials, including silicones and epoxies, allowing users to print flexible electronics and tissues on soft robotics.

**Chapter 4** details a versatile multimaterial printhead that can switch between viscous or viscoelastic inks to create pixelated patterns. Using an innovative combination of the pressure-driven flow behaviour of various inks and pressure-adjustable pressure, Segmented filaments were printed continuously, and with high quality through the use of multiple viscous or viscoelastic Based on numerical simulations of both fluid flow in the printhead's nozzle and its extrusion, the pressure generated at the junction between the ink inlets has been measured under various conditions of printing speed, extrusion frequency, and inlet pressure. It has been found that providing backpressure to ink reservoirs that are not in use can neutralize the pressure gradient that causes the ink to encroach into a channel that's meant for another ink. Our analysis found that the required backpressure depends on the switching frequency, so it needs to be dynamically adjusted based on the switching frequency correlated with pixelated printing. Upon determining the conditions needed for a particular combination of inks, they can be easily incorporated into the software that simultaneously controls nozzle movement and ink pressure. To show the tunability of this

method, we printed pixelated 2D patterns in up to 4 colours and 3D patterns in only 2 colours. It was possible to attain resolutions of 500  $\mu\text{m}$ . Using the same printhead and viscoelastic inks, soft robotic actuators were fabricated as an application that utilizes the co-printing of hard and soft materials in order to operate pneumatically powered gripping devices. This study demonstrated that pixelated 3D extrusion printing is possible under a narrow range of conditions with fast and reliable switching of viscous inks.

**Chapter 5** presents a system for tracing nonplanar topography profiles and printing multimaterial structures. With changing topography under the printhead, it becomes increasingly difficult to maintain the gap between the printhead and the target nonplanar surface. The developed printhead tracker maintained the gap between the printhead and the nonplanar plane through self-adapting mechanical feedback. The developed approach employed simple mechanical components such as roller bearings, which allowed smooth tracking, and spring-loaded structures, which allowed ball bearings to stay in contact with surface shapes that are not flat. It was possible to define the gap spacing for the tracker by constructing it with a defined distance between the nozzle tip and the ball bearings. Contrary to other approaches, the developed system is simple, elegant, and compatible with a wide variety of 3D printer platforms. Further optimization of the tracker design was accomplished by conducting numerical simulations of modal and transient motion. After that, two-dimensional architectures were printed on different non-planar surfaces, such as a human hand, inclined surfaces, and dome surfaces. It is also interesting to note that the developed tracker can be used in conjunction with a conventional extrusion printhead to achieve high aspect ratio structures over nonplanar surfaces. Additionally, we combined the tracker printhead with the mixer printhead used in chapter 3 to print multimaterial

structures over a Bézier surface and dome substrate with very sharp interfaces between coloured segments. As a result of this technique, the printhead can now track topology in real-time, making it possible to embed and print a broader range of features over complex objects.

**Chapter 6** summarizes all achievements in this thesis and the research contributions.

Finally, recommendations for future work are discussed.

## References

- [1] L.-Y. Zhou, J. Fu, and Y. He, "A Review of 3D Printing Technologies for Soft Polymer Materials," *Advanced Functional Materials*, vol. 30, no. 28, p. 2000187, 2020.
- [2] T. J. Fleck, A. K. Murray, I. E. Gunduz, S. F. Son, G. T. C. Chiu, and J. F. Rhoads, "Additive manufacturing of multifunctional reactive materials," *Additive Manufacturing*, vol. 17, pp. 176-182, 2017/10/01/ 2017.
- [3] K. L. Sampson *et al.*, "Multimaterial Vat Polymerization Additive Manufacturing," *ACS Applied Polymer Materials*, vol. 3, no. 9, pp. 4304-4324, 2021/09/10 2021.
- [4] G. L. Goh, H. Zhang, T. H. Chong, and W. Y. Yeong, "3D Printing of Multilayered and Multimaterial Electronics: A Review," *Advanced Electronic Materials*, vol. 7, no. 10, p. 2100445, 2021.
- [5] W. Oropallo and L. A. Piegler, "Ten challenges in 3D printing," *Engineering with Computers*, vol. 32, no. 1, pp. 135-148, 2016/01/01 2016.
- [6] ISO, "ISO/ASTM 52900: Additive manufacturing—General principles—Terminology," ed: ISO Genebra, 2016.
- [7] M. Cianchetti, C. Laschi, A. Menciasci, and P. Dario, "Biomedical applications of soft robotics," *Nature Reviews Materials*, vol. 3, no. 6, pp. 143-153, 2018/06/01 2018.
- [8] D. Rus and M. T. Tolley, "Design, fabrication and control of soft robots," *Nature*, vol. 521, no. 7553, pp. 467-475, 2015/05/01 2015.
- [9] J. Shintake, V. Cacucciolo, D. Floreano, and H. Shea, "Soft robotic grippers," *Advanced Materials*, vol. 30, no. 29, p. 1707035, 2018.
- [10] C. Laschi, B. Mazzolai, and M. Cianchetti, "Soft robotics: Technologies and systems pushing the boundaries of robot abilities," *Science Robotics*, vol. 1, no. 1, p. eaah3690, 2016.
- [11] C. Zhu, C. Ninh, and C. J. Bettinger, "Photoreconfigurable Polymers for Biomedical Applications: Chemistry and Macromolecular Engineering," *Biomacromolecules*, vol. 15, no. 10, pp. 3474-3494, 2014/10/13 2014.
- [12] K. M. Weerakoon-Ratnayake, C. E. O'Neil, F. I. Uba, and S. A. Soper, "Thermoplastic nanofluidic devices for biomedical applications," *Lab on a Chip*, 10.1039/C6LC01173J vol. 17, no. 3, pp. 362-381, 2017.
- [13] A. Góra, R. Sahay, V. Thavasi, and S. Ramakrishna, "Melt-Electrospun Fibers for Advances in Biomedical Engineering, Clean Energy, Filtration, and Separation," *Polymer Reviews*, vol. 51, no. 3, pp. 265-287, 2011/07/01 2011.

- [14] J. S. Heo, J. Eom, Y.-H. Kim, and S. K. Park, "Recent Progress of Textile-Based Wearable Electronics: A Comprehensive Review of Materials, Devices, and Applications," *Small*, vol. 14, no. 3, p. 1703034, 2018.
- [15] Y. Liu, M. Pharr, and G. A. Salvatore, "Lab-on-Skin: A Review of Flexible and Stretchable Electronics for Wearable Health Monitoring," *ACS Nano*, vol. 11, no. 10, pp. 9614-9635, 2017/10/24 2017.
- [16] Y. Yang and W. Gao, "Wearable and flexible electronics for continuous molecular monitoring," *Chemical Society Reviews*, 10.1039/C7CS00730B vol. 48, no. 6, pp. 1465-1491, 2019.
- [17] L. Hao *et al.*, "Direct Ink Writing of Mineral Materials: A review," *International Journal of Precision Engineering and Manufacturing-Green Technology*, vol. 8, pp. 665-685, 2021.
- [18] V. G. Rocha, E. Saiz, I. S. Tirichenko, and E. García-Tuñón, "Direct ink writing advances in multi-material structures for a sustainable future," *Journal of Materials Chemistry A*, vol. 8, no. 31, pp. 15646-15657, 2020.
- [19] L. del-Mazo-Barbara and M.-P. Ginebra, "Rheological characterisation of ceramic inks for 3D direct ink writing: a review," *Journal of the European Ceramic Society*, 2021.
- [20] Q. Chen, P.-F. Cao, and R. C. Advincula, "Mechanically Robust, Ultraelastic Hierarchical Foam with Tunable Properties via 3D Printing," *Advanced Functional Materials*, vol. 28, no. 21, p. 1800631, 2018.
- [21] S. Roh, D. P. Parekh, B. Bharti, S. D. Stoyanov, and O. D. Velev, "3D printing by multiphase silicone/water capillary inks," *Advanced Materials*, vol. 29, no. 30, p. 1701554, 2017.
- [22] Y. Kim, H. Yuk, R. Zhao, S. A. Chester, and X. Zhao, "Printing ferromagnetic domains for untethered fast-transforming soft materials," (in eng), *Nature*, vol. 558, no. 7709, pp. 274-279, Jun 2018.
- [23] C. B. Highley, C. B. Rodell, and J. A. Burdick, "Direct 3D Printing of Shear-Thinning Hydrogels into Self-Healing Hydrogels," *Advanced Materials*, vol. 27, no. 34, pp. 5075-5079, 2015.
- [24] D. M. Kirchmayer, R. Gorkin Iii, and M. in het Panhuis, "An overview of the suitability of hydrogel-forming polymers for extrusion-based 3D-printing," *Journal of Materials Chemistry B*, 10.1039/C5TB00393H vol. 3, no. 20, pp. 4105-4117, 2015.
- [25] T. Jiang, J. G. Munguia-Lopez, S. Flores-Torres, J. Kort-Mascort, and J. M. Kinsella, "Extrusion bioprinting of soft materials: An emerging technique for biological model fabrication," *Applied Physics Reviews*, vol. 6, no. 1, p. 011310, 2019.
- [26] A. Shahzad and I. Lazoglu, "Direct ink writing (DIW) of structural and functional ceramics: Recent achievements and future challenges," *Composites Part B: Engineering*, p. 109249, 2021.
- [27] J. A. Lewis, "Direct ink writing of 3D functional materials," *Advanced Functional Materials*, vol. 16, no. 17, pp. 2193-2204, 2006.
- [28] D. Behera and M. Cullinan, "Current Challenges and Potential Directions Towards Precision Microscale Additive Manufacturing—Part I: Direct Ink Writing/Jetting Processes," *Precision Engineering*, 2020.
- [29] P. Jiang, Z. Ji, X. Zhang, Z. Liu, and X. Wang, "Recent advances in direct ink writing of electronic components and functional devices," *Progress in Additive Manufacturing*, vol. 3, no. 1-2, pp. 65-86, 2018.
- [30] N.-T. Nguyen and Z. Wu, "Micromixers—a review," *Journal of micromechanics and microengineering*, vol. 15, no. 2, p. R1, 2004.

- [31] Y. K. Suh and S. Kang, "A review on mixing in microfluidics," *Micromachines*, vol. 1, no. 3, pp. 82-111, 2010.
- [32] A. D. Stroock, S. K. Dertinger, A. Ajdari, I. Mezić, H. A. Stone, and G. M. Whitesides, "Chaotic mixer for microchannels," *Science*, vol. 295, no. 5555, pp. 647-651, 2002.
- [33] D. Therriault, S. R. White, and J. A. Lewis, "Chaotic mixing in three-dimensional microvascular networks fabricated by direct-write assembly," *Nature materials*, vol. 2, no. 4, p. 265, 2003.
- [34] A. Groisman and V. Steinberg, "Efficient mixing at low Reynolds numbers using polymer additives," *Nature*, vol. 410, no. 6831, p. 905, 2001.
- [35] A. M. Golobic *et al.*, "Active mixing of reactive materials for 3D printing," vol. 21, no. 8, p. 1900147, 2019.
- [36] J. M. Ortega *et al.*, "Active mixing of disparate inks for multimaterial 3D printing," vol. 4, no. 7, p. 1800717, 2019.
- [37] K. Cheng, H. Lan, S. Zou, L. Qian, and D. J. S. S. T. Li, "Research on active mixing printhead for multi-material and multi-scale 3D printing," vol. 47, no. 2, pp. 149-162, 2017.
- [38] H. Lan, "Active mixing nozzle for multi-material and multi-scale 3d printing," in *International Manufacturing Science and Engineering Conference*, 2017, vol. 50732, p. V002T01A024: American Society of Mechanical Engineers.
- [39] P. Arratia, J. Kukura, J. Lacombe, and F. Muzzio, "Mixing of shear-thinning fluids with yield stress in stirred tanks," *AIChE journal*, vol. 52, no. 7, pp. 2310-2322, 2006.
- [40] H. Lipson and M. Kurman, *Fabricated: The new world of 3D printing*. John Wiley & Sons, 2013.
- [41] C. Xu, B. Quinn, L. L. Lebel, D. Therriault, and G. L'Espérance, "Multi-material direct ink writing (DIW) for complex 3D metallic structures with removable supports," *ACS applied materials & interfaces*, vol. 11, no. 8, pp. 8499-8506, 2019.
- [42] O. D. Yirmibesoglu *et al.*, "Multi-material direct ink writing of photocurable elastomeric foams," *Communications Materials*, vol. 2, no. 1, pp. 1-14, 2021.
- [43] T. K. Merceron *et al.*, "A 3D bioprinted complex structure for engineering the muscle-tendon unit," *Biofabrication*, vol. 7, no. 3, p. 035003, 2015.
- [44] S. Khalil, J. Nam, and W. Sun, "Multi-nozzle deposition for construction of 3D biopolymer tissue scaffolds," *Rapid Prototyping Journal*, vol. 11, no. 1, pp. 9-17, 2005.
- [45] J. Campbell, I. McGuinness, H. Wirz, A. Sharon, and A. F. Sauer-Budge, "Multimaterial and multiscale three-dimensional bioprinter," *Journal of Nanotechnology in Engineering and Medicine*, vol. 6, no. 2, p. 021005, 2015.
- [46] H.-W. Kang, S. J. Lee, I. K. Ko, C. Kengla, J. J. Yoo, and A. Atala, "A 3D bioprinting system to produce human-scale tissue constructs with structural integrity," *Nature biotechnology*, vol. 34, no. 3, p. 312, 2016.
- [47] M. A. Skylar-Scott, J. Mueller, C. W. Visser, and J. A. Lewis, "Voxelated soft matter via multimaterial multinozzle 3D printing," *Nature*, vol. 575, no. 7782, pp. 330-335, 2019.
- [48] R. A. Johnson, J. J. O'Neill, R. L. Dockter, and T. M. Kowalewski, "Toward Inkjet Additive Manufacturing Directly Onto Human Anatomy," in *Frontiers in Biomedical Devices*, 2017, vol. 40672, p. V001T11A016: American Society of Mechanical Engineers.
- [49] N. Matsuhisa *et al.*, "Printable elastic conductors with a high conductivity for electronic textile applications," *Nature communications*, vol. 6, no. 1, pp. 1-11, 2015.
- [50] D. Ahlers, F. Wasserfall, N. Hendrich, and J. Zhang, "3D printing of nonplanar layers for smooth surface generation," in *2019 IEEE 15th International Conference on Automation Science and Engineering (CASE)*, 2019, pp. 1737-1743: IEEE.

- [51] A. V. Shembekar, Y. J. Yoon, A. Kanyuck, and S. K. Gupta, "Trajectory planning for conformal 3d printing using non-planar layers," in *International Design Engineering Technical Conferences and Computers and Information in Engineering Conference*, 2018, vol. 51722, p. V01AT02A026: American Society of Mechanical Engineers.
- [52] A. V. Shembekar, Y. J. Yoon, A. Kanyuck, and S. K. Gupta, "Generating robot trajectories for conformal three-dimensional printing using nonplanar layers," *Journal of Computing and Information Science in Engineering*, vol. 19, no. 3, 2019.
- [53] C. Creton and M. Ciccotti, "Fracture and adhesion of soft materials: a review," *Reports on Progress in Physics*, vol. 79, no. 4, p. 046601, 2016/03/23 2016.
- [54] N. Elango and A. A. M. Faudzi, "A review article: investigations on soft materials for soft robot manipulations," *The International Journal of Advanced Manufacturing Technology*, vol. 80, no. 5, pp. 1027-1037, 2015/09/01 2015.
- [55] Z. Liu, W. Toh, and T. Y. Ng, "Advances in Mechanics of Soft Materials: A Review of Large Deformation Behavior of Hydrogels," *International Journal of Applied Mechanics*, vol. 07, no. 05, p. 1530001, 2015.
- [56] B. Li, Y.-P. Cao, X.-Q. Feng, and H. Gao, "Mechanics of morphological instabilities and surface wrinkling in soft materials: a review," *Soft Matter*, 10.1039/C2SM00011C vol. 8, no. 21, pp. 5728-5745, 2012.
- [57] D. T. N. Chen, Q. Wen, P. A. Janmey, J. C. Crocker, and A. G. Yodh, "Rheology of Soft Materials," *Annual Review of Condensed Matter Physics*, vol. 1, no. 1, pp. 301-322, 2010.
- [58] M. Doi, *Soft matter physics*. Oxford University Press, 2013.
- [59] L. Y. Zhou, J. Fu, and Y. He, "A review of 3D printing technologies for soft polymer materials," *Advanced Functional Materials*, vol. 30, no. 28, p. 2000187, 2020.
- [60] S. Zakeri, M. Vippola, and E. Levänen, "A comprehensive review of the photopolymerization of ceramic resins used in stereolithography," *Additive Manufacturing*, vol. 35, p. 101177, 2020/10/01/ 2020.
- [61] Y. L. Yap, S. L. Sing, and W. Y. Yeong, "A review of 3D printing processes and materials for soft robotics," *Rapid Prototyping Journal*, 2020.
- [62] J. Herzberger, J. M. Serrine, C. B. Williams, and T. E. Long, "Polymer design for 3D printing elastomers: Recent advances in structure, properties, and printing," *Progress in Polymer Science*, vol. 97, p. 101144, 2019.
- [63] O. D. Yirmibesoglu *et al.*, "Direct 3D printing of silicone elastomer soft robots and their performance comparison with molded counterparts," in *2018 IEEE International Conference on Soft Robotics (RoboSoft)*, 2018, pp. 295-302: IEEE.
- [64] J. Plott and A. Shih, "The extrusion-based additive manufacturing of moisture-cured silicone elastomer with minimal void for pneumatic actuators," *Additive Manufacturing*, vol. 17, pp. 1-14, 2017.
- [65] F. B. Albuquerque and H. Shea, "Effect of humidity, temperature, and elastomer material on the lifetime of silicone-based dielectric elastomer actuators under a constant DC electric field (Conference Presentation)," in *Electroactive Polymer Actuators and Devices (EAPAD) XXII*, 2020, vol. 11375, p. 113751E: International Society for Optics and Photonics.
- [66] S. Abdollahi, E. J. Markvicka, C. Majidi, and A. W. Feinberg, "3D Printing Silicone Elastomer for Patient-Specific Wearable Pulse Oximeter," *Advanced healthcare materials*, vol. 9, no. 15, p. 1901735, 2020.
- [67] G. Jeong *et al.*, "Photocurable Elastomer Composites with SiO<sub>2</sub>-Mediated Cross-Links for Mechanically Durable 3D Printing Materials," *ACS Applied Polymer Materials*, vol. 2, no. 11, pp. 5228-5237, 2020.

- [68] K. Pooput, S. Channasanon, P. Tesavibul, P. Pittayavinai, and W. Taweelue, "Photocurable elastomers with tunable mechanical properties for 3D digital light processing printing," *Journal of Polymer Research*, vol. 27, no. 10, pp. 1-10, 2020.
- [69] T. D. Ngo, A. Kashani, G. Imbalzano, K. T. Nguyen, and D. Hui, "Additive manufacturing (3D printing): A review of materials, methods, applications and challenges," *Composites Part B: Engineering*, vol. 143, pp. 172-196, 2018.
- [70] M. N. Nadagouda, M. Ginn, and V. Rastogi, "A review of 3D printing techniques for environmental applications," *Current Opinion in Chemical Engineering*, vol. 28, pp. 173-178, 2020.
- [71] M. Cianchetti, C. Laschi, A. Menciasci, and P. Dario, "Biomedical applications of soft robotics," *Nature Reviews Materials*, vol. 3, pp. 143-153, 2018.
- [72] S. C. Ligon, R. Liska, J. r. Stampfl, M. Gurr, and R. Mülhaupt, "Polymers for 3D printing and customized additive manufacturing," *Chemical reviews*, vol. 117, no. 15, pp. 10212-10290, 2017.
- [73] J. W. Stansbury and M. J. Idacavage, "3D printing with polymers: Challenges among expanding options and opportunities," *Dental Materials*, vol. 32, no. 1, pp. 54-64, 2016/01/01/ 2016.
- [74] I. S. Kinstlinger *et al.*, "Open-source selective laser sintering (OpenSLS) of nylon and biocompatible polycaprolactone," *PLoS one*, vol. 11, no. 2, p. e0147399, 2016.
- [75] M. Brandt, "Laser additive manufacturing: materials, design, technologies, and applications," 2016.
- [76] J. P. Kruth, P. Mercelis, J. Van Vaerenbergh, L. Froyen, and M. Rombouts, "Binding mechanisms in selective laser sintering and selective laser melting," *Rapid prototyping journal*, 2005.
- [77] J. Kruth, G. Levy, and F. Klocke, "Childs THC," *Ann CIRP.–2007.–56 (2).–730–59*, 2007.
- [78] S. C. Ligon, R. Liska, J. Stampfl, M. Gurr, and R. Mülhaupt, "Polymers for 3D Printing and Customized Additive Manufacturing," (in eng), *Chemical reviews*, vol. 117, no. 15, pp. 10212-10290, 2017/08// 2017.
- [79] F. Caballero, Ed. *Encyclopedia of Materials: Metals and Alloys*. Elsevier, 2021, p. 2492.
- [80] F. Calignano, D. Manfredi, E. P. Ambrosio, L. Iuliano, and P. Fino, "Influence of process parameters on surface roughness of aluminum parts produced by DMLS," *The International Journal of Advanced Manufacturing Technology*, vol. 67, no. 9, pp. 2743-2751, 2013/08/01 2013.
- [81] M. A. Dechet, I. Baumeister, and J. Schmidt, "Development of polyoxymethylene particles via the solution-dissolution process and application to the powder bed fusion of polymers," *Materials*, vol. 13, no. 7, p. 1535, 2020.
- [82] S. R. Athreya, K. Kalaitzidou, and S. Das, "Mechanical and microstructural properties of Nylon-12/carbon black composites: Selective laser sintering versus melt compounding and injection molding," *Composites science and technology*, vol. 71, no. 4, pp. 506-510, 2011.
- [83] S. F. S. Shirazi *et al.*, "A review on powder-based additive manufacturing for tissue engineering: selective laser sintering and inkjet 3D printing," *Science and Technology of Advanced Materials*, vol. 16, no. 3, p. 033502, 2015/06/20 2015.
- [84] D. Dev Singh, T. Mahender, and A. Raji Reddy, "Powder bed fusion process: A brief review," *Materials Today: Proceedings*, vol. 46, pp. 350-355, 2021/01/01/ 2021.
- [85] Y. Lu, G. Mapili, G. Suhali, S. Chen, and K. Roy, "A digital micro-mirror device-based system for the microfabrication of complex, spatially patterned tissue engineering scaffolds," (in eng), *J Biomed Mater Res A*, vol. 77, no. 2, pp. 396-405, May 2006.

- [86] J. R. Tumbleston *et al.*, "Additive manufacturing. Continuous liquid interface production of 3D objects," (in eng), *Science*, vol. 347, no. 6228, pp. 1349-52, Mar 20 2015.
- [87] T. Baldacchini, *Three-dimensional microfabrication using two-photon polymerization: fundamentals, technology, and applications*. William Andrew, 2015.
- [88] B. E. Kelly, I. Bhattacharya, H. Heidari, M. Shusteff, C. M. Spadaccini, and H. K. Taylor, "Volumetric additive manufacturing via tomographic reconstruction," *Science*, vol. 363, no. 6431, pp. 1075-1079, 2019.
- [89] Y. Pan, Y. Chen, and Z. Yu, "Fast mask image projection-based micro-stereolithography process for complex geometry," *Journal of Micro and Nano-Manufacturing*, vol. 5, no. 1, 2017.
- [90] P. N. Bernal *et al.*, "Volumetric bioprinting of complex living-tissue constructs within seconds," *Advanced materials*, vol. 31, no. 42, p. 1904209, 2019.
- [91] B. Zhang *et al.*, "Highly stretchable hydrogels for UV curing based high-resolution multimaterial 3D printing," *Journal of Materials Chemistry B*, 10.1039/C8TB00673C vol. 6, no. 20, pp. 3246-3253, 2018.
- [92] H. Gong, B. P. Bickham, A. T. Woolley, and G. P. Nordin, "Custom 3D printer and resin for 18  $\mu\text{m}$   $\times$  20  $\mu\text{m}$  microfluidic flow channels," *Lab on a Chip*, 10.1039/C7LC00644F vol. 17, no. 17, pp. 2899-2909, 2017.
- [93] X. Wang, M. Jiang, Z. Zhou, J. Gou, and D. Hui, "3D printing of polymer matrix composites: A review and prospective," *Composites Part B: Engineering*, vol. 110, pp. 442-458, 2017.
- [94] B. Husár, S. C. Ligon, H. Wutzel, H. Hoffmann, and R. Liska, "The formulator's guide to anti-oxygen inhibition additives," *Progress in Organic Coatings*, vol. 77, no. 11, pp. 1789-1798, 2014/11/01/ 2014.
- [95] J. Borrello, P. Nasser, J. Iatridis, and K. D. Costa, "3D Printing a Mechanically-Tunable Acrylate Resin on a Commercial DLP-SLA Printer," (in eng), *Additive manufacturing*, vol. 23, pp. 374-380, 2018.
- [96] J. J. Schwartz and A. J. Boydston, "Multimaterial actinic spatial control 3D and 4D printing," *Nature Communications*, vol. 10, no. 1, p. 791, 2019/02/15 2019.
- [97] A. Medellin, W. Du, G. Miao, J. Zou, Z. Pei, and C. Ma, "Vat photopolymerization 3d printing of nanocomposites: a literature review," *Journal of Micro-and Nano-Manufacturing*, vol. 7, no. 3, p. 031006, 2019.
- [98] Q. Yan *et al.*, "A review of 3D printing technology for medical applications," *Engineering*, vol. 4, no. 5, pp. 729-742, 2018.
- [99] M. Rosello, G. Maîtrejean, D. C. D. Roux, P. Jay, B. Barbet, and J. Xing, "Influence of the Nozzle Shape on the Breakup Behavior of Continuous Ink Jets," *Journal of Fluids Engineering*, vol. 140, no. 3, 2017.
- [100] M. Junfeng, M. R. Lovell, and M. H. Mickle, "Formulation and processing of novel conductive solution inks in continuous inkjet printing of 3-D electric circuits," *IEEE Transactions on Electronics Packaging Manufacturing*, vol. 28, no. 3, pp. 265-273, 2005.
- [101] Y. Wang, J. Bokor, and A. Lee, *Maskless lithography using drop-on-demand inkjet printing method* (Microlithography 2004). SPIE, 2004.
- [102] M. Romagnoli, M. Lassinantti Gualtieri, M. Cannio, F. Barbieri, and R. Giovanardi, "Preparation of an aqueous graphitic ink for thermal drop-on-demand inkjet printing," *Materials Chemistry and Physics*, vol. 182, pp. 263-271, 2016/10/01/ 2016.
- [103] Y.-J. Kim, S. Kim, J. Hwang, and Y.-J. Kim, "Drop-on-demand hybrid printing using a piezoelectric MEMS printhead at various waveforms, high voltages and jetting

- frequencies," *Journal of Micromechanics and Microengineering*, vol. 23, no. 6, p. 065011, 2013/04/29 2013.
- [104] B. Derby, "Inkjet Printing of Functional and Structural Materials: Fluid Property Requirements, Feature Stability, and Resolution," *Annual Review of Materials Research*, vol. 40, no. 1, pp. 395-414, 2010.
- [105] Y. Guo, H. S. Patanwala, B. Bognet, and A. W. K. Ma, "Inkjet and inkjet-based 3D printing: connecting fluid properties and printing performance," *Rapid Prototyping Journal*, vol. 23, pp. 562-576, 2017.
- [106] B. W. An *et al.*, "High-Resolution Printing of 3D Structures Using an Electrohydrodynamic Inkjet with Multiple Functional Inks," *Advanced Materials*, vol. 27, no. 29, pp. 4322-4328, 2015.
- [107] P.-A. Mouthuy, L. Groszkowski, and H. Ye, "Performances of a portable electrospinning apparatus," *Biotechnology Letters*, vol. 37, no. 5, pp. 1107-1116, 2015/05/01 2015.
- [108] V. D. Nguyen and D. Byun, "Mechanism of electrohydrodynamic printing based on ac voltage without a nozzle electrode," *Applied Physics Letters*, vol. 94, no. 17, p. 173509, 2009.
- [109] P. Galliker, J. Schneider, H. Eghlidi, S. Kress, V. Sandoghdar, and D. Poulikakos, "Direct printing of nanostructures by electrostatic autofocussing of ink nanodroplets," *Nature Communications*, vol. 3, no. 1, p. 890, 2012/06/12 2012.
- [110] L. Qian, H. Lan, and G. Zhang, "A theoretical model for predicting the feature size printed by electrohydrodynamic jet printing," *Applied Physics Letters*, vol. 112, no. 20, p. 203505, 2018.
- [111] E. Sutanto *et al.*, "A multimaterial electrohydrodynamic jet (E-jet) printing system," *Journal of Micromechanics and Microengineering*, vol. 22, no. 4, p. 045008, 2012/03/15 2012.
- [112] B. Derby, "Inkjet printing ceramics: From drops to solid," *Journal of the European Ceramic Society*, vol. 31, no. 14, pp. 2543-2550, 2011/11/01/ 2011.
- [113] T. Wang, R. Patel, and B. Derby, "Manufacture of 3-dimensional objects by reactive inkjet printing," *Soft Matter*, 10.1039/B807758D vol. 4, no. 12, pp. 2513-2518, 2008.
- [114] A. Negro, T. Cherbuin, and M. P. Lutolf, "3D Inkjet Printing of Complex, Cell-Laden Hydrogel Structures," (in eng), *Sci Rep*, vol. 8, no. 1, p. 17099, Nov 20 2018.
- [115] G. Gao *et al.*, "Improved properties of bone and cartilage tissue from 3D inkjet-bioprinted human mesenchymal stem cells by simultaneous deposition and photocrosslinking in PEG-GelMA," (in eng), *Biotechnol Lett*, vol. 37, no. 11, pp. 2349-55, Nov 2015.
- [116] Y. He *et al.*, "A new photocrosslinkable polycaprolactone-based ink for three-dimensional inkjet printing," (in eng), *J Biomed Mater Res B Appl Biomater*, vol. 105, no. 6, pp. 1645-1657, Aug 2017.
- [117] D. McCoul, S. Rosset, S. Schlatter, and H. Shea, "Inkjet 3D printing of UV and thermal cure silicone elastomers for dielectric elastomer actuators," *Smart Materials and Structures*, vol. 26, no. 12, p. 125022, 2017.
- [118] R. L. Truby and J. A. Lewis, "Printing soft matter in three dimensions," *Nature*, vol. 540, no. 7633, pp. 371-378, 2016/12/01 2016.
- [119] N. Scoutaris, M. R. Alexander, P. R. Gellert, and C. J. Roberts, "Inkjet printing as a novel medicine formulation technique," *Journal of Controlled Release*, vol. 156, no. 2, pp. 179-185, 2011/12/10/ 2011.

- [120] B. N. Turner, R. J. Strong, and S. A. Gold, "A review of melt extrusion additive manufacturing processes: I. Process design and modeling," *Rapid Prototyping Journal*, vol. 20, pp. 192-204, 2014.
- [121] B. N. Turner and S. A. Gold, "A review of melt extrusion additive manufacturing processes: II. Materials, dimensional accuracy, and surface roughness," *Rapid Prototyping Journal*, 2015.
- [122] J. Go and A. J. Hart, "Fast Desktop-Scale Extrusion Additive Manufacturing," *Additive Manufacturing*, vol. 18, pp. 276-284, 2017/12/01/ 2017.
- [123] "High-Force Soft Printable Pneumatics for Soft Robotic Applications," *Soft Robotics*, vol. 3, no. 3, pp. 144-158, 2016.
- [124] P. Awasthi and S. S. Banerjee, "Fused deposition modeling of thermoplastic elastomeric materials: Challenges and opportunities," *Additive Manufacturing*, vol. 46, p. 102177, 2021/10/01/ 2021.
- [125] R. D. Farahani, M. Dubé, and D. Therriault, "Three-Dimensional Printing of Multifunctional Nanocomposites: Manufacturing Techniques and Applications," *Advanced Materials*, vol. 28, no. 28, pp. 5794-5821, 2016.
- [126] J. Yin, C. Lu, J. Fu, Y. Huang, and Y. Zheng, "Interfacial bonding during multi-material fused deposition modeling (FDM) process due to inter-molecular diffusion," *Materials & Design*, vol. 150, pp. 104-112, 2018/07/15/ 2018.
- [127] D. Espalin, J. A. Ramirez, F. Medina, and R. Wicker, "Multi-material, multi-technology FDM: exploring build process variations," *Rapid Prototyping Journal*, 2014.
- [128] "Additive Manufacturing with Ultraviolet Curable Silicones Containing Carbon Black," *3D Printing and Additive Manufacturing*, vol. 5, no. 1, pp. 73-86, 2018.
- [129] Q. Gao, Y. He, J.-z. Fu, A. Liu, and L. Ma, "Coaxial nozzle-assisted 3D bioprinting with built-in microchannels for nutrients delivery," *Biomaterials*, vol. 61, pp. 203-215, 2015/08/01/ 2015.
- [130] R. Farahani, L. Lebel, and D. Therriault, "Processing parameters investigation for the fabrication of self-supported and freeform polymeric microstructures using ultraviolet-assisted three-dimensional printing," *Journal of Micromechanics and Microengineering*, vol. 24, no. 5, p. 055020, 2014.
- [131] A. K. Grosskopf, R. L. Truby, H. Kim, A. Perazzo, J. A. Lewis, and H. A. Stone, "Viscoplastic matrix materials for embedded 3D printing," *ACS applied materials & interfaces*, vol. 10, no. 27, pp. 23353-23361, 2018.
- [132] L.-y. Zhou *et al.*, "Multimaterial 3D Printing of Highly Stretchable Silicone Elastomers," *ACS Applied Materials & Interfaces*, vol. 11, no. 26, pp. 23573-23583, 2019/07/03 2019.
- [133] Y. Huang *et al.*, "Electrohydrodynamic direct-writing," *Nanoscale*, 10.1039/C3NR04329K vol. 5, no. 24, pp. 12007-12017, 2013.
- [134] J. Zheng *et al.*, "Electrohydrodynamic direct-writing orderly pattern with sheath gas focusing," *AIP Advances*, vol. 6, no. 11, p. 115304, 2016.
- [135] C. B. Highley, C. B. Rodell, and J. A. Burdick, "Direct 3D printing of shear-thinning hydrogels into self-healing hydrogels," *Advanced Materials*, vol. 27, no. 34, pp. 5075-5079, 2015.
- [136] M. H. Ali, N. Mir-Nasiri, and W. L. Ko, "Multi-nozzle extrusion system for 3D printer and its control mechanism," *The International Journal of Advanced Manufacturing Technology*, vol. 86, no. 1, pp. 999-1010, 2016/09/01 2016.
- [137] C. Xu, B. Quinn, L. L. Lebel, D. Therriault, and G. L'Espérance, "Multi-Material Direct Ink Writing (DIW) for Complex 3D Metallic Structures with Removable Supports," *ACS Applied Materials & Interfaces*, vol. 11, no. 8, pp. 8499-8506, 2019/02/27 2019.

- [138] J. A. Lewis, J. E. Smay, J. Stuecker, and J. Cesarano, "Direct ink writing of three-dimensional ceramic structures," *Journal of the American Ceramic Society*, vol. 89, no. 12, pp. 3599-3609, 2006.
- [139] E. G.-C. Luis, H. Liu, J. K. Song, and W. Y. Yeong, "A Review of Medical Silicone 3 D-Printing Technologies and Clinical Applications", 2018.
- [140] W. L. Ng *et al.*, "Vat polymerization-based bioprinting—process, materials, applications and regulatory challenges," *Biofabrication*, vol. 12, no. 2, p. 022001, 2020.
- [141] J. Yeo, J. J. Koh, F. Wang, Z. Li, and C. He, "3D Printing Silicone Materials and Devices," *Silicon Containing Hybrid Copolymers*, pp. 239-263, 2020.
- [142] C. He and Z. Li, *Silicon Containing Hybrid Copolymers*. John Wiley & Sons, 2020.
- [143] Z. Weng, Y. Zhou, W. Lin, T. Senthil, and L. Wu, "Structure-property relationship of nano enhanced stereolithography resin for desktop SLA 3D printer," *Composites Part A: Applied Science and Manufacturing*, vol. 88, pp. 234-242, 2016/09/01/ 2016.
- [144] D. K. Patel, A. H. Sakhaei, M. Layani, B. Zhang, Q. Ge, and S. Magdassi, "Highly Stretchable and UV Curable Elastomers for Digital Light Processing Based 3D Printing," *Advanced Materials*, vol. 29, no. 15, p. 1606000, 2017.
- [145] S. Reškštytė, M. Malinauskas, and S. Juodkazis, "Three-dimensional laser micro-sculpturing of silicone: towards bio-compatible scaffolds," *Optics Express*, vol. 21, no. 14, pp. 17028-17041, 2013/07/15 2013.
- [146] J. M. Sirrine *et al.*, "3D Printing Amorphous Polysiloxane Terpolymers via Vat Photopolymerization," *Macromolecular Chemistry and Physics*, vol. 220, no. 4, p. 1800425, 2019.
- [147] T. Femmer, A. J. C. Kuehne, J. Torres-Rendon, A. Walther, and M. Wessling, "Print your membrane: Rapid prototyping of complex 3D-PDMS membranes via a sacrificial resist," *Journal of Membrane Science*, vol. 478, pp. 12-18, 2015/03/15/ 2015.
- [148] Y. T. Kim, K. Castro, N. Bhattacharjee, and A. Folch, "Digital Manufacturing of Selective Porous Barriers in Microchannels Using Multi-Material Stereolithography," *Micromachines*, vol. 9, no. 3, p. 125, 2018.
- [149] K. L. Sampson *et al.*, "Multimaterial vat polymerization additive manufacturing," *ACS Applied Polymer Materials*, vol. 3, no. 9, pp. 4304-4324, 2021.
- [150] J. Borrello, P. Nasser, J. C. Iatridis, and K. D. Costa, "3D printing a mechanically-tunable acrylate resin on a commercial DLP-SLA printer," *Additive manufacturing*, vol. 23, pp. 374-380, 2018.
- [151] J. Schwartz and A. Boydston, "Multimaterial actinic spatial control 3D and 4D printing," *Nature communications*, vol. 10, no. 1, pp. 1-10, 2019.
- [152] N. Wilkinson, M. Smith, R. Kay, and R. J. T. I. J. o. A. M. T. Harris, "A review of aerosol jet printing—a non-traditional hybrid process for micro-manufacturing," vol. 105, no. 11, pp. 4599-4619, 2019.
- [153] C. Sturgess, C. J. Tuck, I. A. Ashcroft, and R. D. Wildman, "3D reactive inkjet printing of polydimethylsiloxane," *Journal of Materials Chemistry C*, 10.1039/C7TC02412F vol. 5, no. 37, pp. 9733-9743, 2017.
- [154] T. Boland *et al.*, "Drop-on-demand printing of cells and materials for designer tissue constructs," *Materials Science and Engineering: C*, vol. 27, no. 3, pp. 372-376, 2007.
- [155] R. Xiong, Z. Zhang, W. Chai, Y. Huang, and D. B. Chrisey, "Freeform drop-on-demand laser printing of 3D alginate and cellular constructs," *Biofabrication*, vol. 7, no. 4, p. 045011, 2015/12/22 2015.

- [156] K. Christensen, A. Compaan, W. Chai, G. Xia, and Y. Huang, "In situ printing-then-mixing for biological structure fabrication using intersecting jets," *ACS Biomaterials Science & Engineering*, vol. 3, no. 12, pp. 3687-3694, 2017.
- [157] M. Śliwiak, R. Bui, M. A. Brook, and P. R. Selvaganapathy, "3D Printing of Highly Reactive Silicones Using Inkjet Type Droplet Ejection and Free Space Droplet Merging and Reaction," *Additive Manufacturing*, p. 102099, 2021.
- [158] J. Plott, "Extrusion-based additive manufacturing of silicone elastomer parts," 2017.
- [159] P. Calcagnile, G. Cacciatore, C. Demitri, F. Montagna, and C. Esposito Corcione, "A Feasibility Study of Processing Polydimethylsiloxane–Sodium Carboxymethylcellulose Composites by a Low-Cost Fused Deposition Modeling 3D Printer," *Materials*, vol. 11, no. 9, p. 1578, 2018.
- [160] W.-C. Liaw, J. Chang-Chien, H. Kang, Y.-L. Cheng, and L.-W. Fu, "A Straightforward Synthesis and Characterization of a New Poly(imide siloxane)-based Thermoplastic Elastomer," *Polymer Journal*, vol. 40, no. 2, pp. 116-125, 2008/02/01 2008.
- [161] J. Zhao, R. Xu, G. Luo, J. Wu, and H. Xia, "A self-healing, re-moldable and biocompatible crosslinked polysiloxane elastomer," *Journal of Materials Chemistry B*, 10.1039/C5TB02036K vol. 4, no. 5, pp. 982-989, 2016.
- [162] J. Lao *et al.*, "A Deep Learning-Based Radiomics Model for Prediction of Survival in Glioblastoma Multiforme," *Scientific Reports*, vol. 7, no. 1, p. 10353, 2017/09/04 2017.
- [163] S. Tazawa, A. Shimojima, T. Maeda, and A. Hotta, "Thermoplastic polydimethylsiloxane with l-phenylalanine-based hydrogen-bond networks," *Journal of Applied Polymer Science*, vol. 135, no. 24, p. 45419, 2018.
- [164] A. Z. Nelson and R. H. Ewoldt, "Design of yield-stress fluids: a rheology-to-structure inverse problem," *Soft Matter*, 10.1039/C7SM00758B vol. 13, no. 41, pp. 7578-7594, 2017.
- [165] A. Z. Nelson, R. E. Bras, J. Liu, and R. H. Ewoldt, "Extending yield-stress fluid paradigms," *Journal of Rheology*, vol. 62, no. 1, pp. 357-369, 2018.
- [166] A. S. Wu *et al.*, "3D Printed Silicones with Shape Memory," *Scientific Reports*, vol. 7, no. 1, p. 4664, 2017/07/05 2017.
- [167] Z. Gao, Z. Jia, J. Zhang, A. Feng, Z. Huang, and G. Wu, "Tunable microwave absorbing property of LaxFeO3/C by introducing A-site cation deficiency," *Journal of Materials Science: Materials in Electronics*, vol. 30, no. 14, pp. 13474-13487, 2019/07/01 2019.
- [168] M. M. Durban *et al.*, "Custom 3D Printable Silicones with Tunable Stiffness," *Macromolecular Rapid Communications*, vol. 39, no. 4, p. 1700563, 2018.
- [169] P. Vondráček and M. Schätz, "Bound rubber and "crepe hardening" in silicone rubber," *Journal of Applied Polymer Science*, vol. 21, no. 12, pp. 3211-3222, 1977.
- [170] J. Lv *et al.*, "3D printing of a mechanically durable superhydrophobic porous membrane for oil–water separation," *Journal of Materials Chemistry A*, 10.1039/C7TA02202F vol. 5, no. 24, pp. 12435-12444, 2017.
- [171] J. J. Stickel and R. L. Powell, "FLUID MECHANICS AND RHEOLOGY OF DENSE SUSPENSIONS," *Annual Review of Fluid Mechanics*, vol. 37, no. 1, pp. 129-149, 2005.
- [172] S. K. Jindal, M. Sherriff, M. G. Waters, J. E. Smay, and T. J. Coward, "Development of a 3D printable maxillofacial silicone: Part II. Optimization of moderator and thixotropic agent," *The Journal of Prosthetic Dentistry*, vol. 119, no. 2, pp. 299-304, 2018/02/01/ 2018.
- [173] S. K. Jindal, M. Sherriff, M. G. Waters, and T. J. Coward, "Development of a 3D printable maxillofacial silicone: Part I. Optimization of polydimethylsiloxane chains and cross-

- linker concentration," *The Journal of Prosthetic Dentistry*, vol. 116, no. 4, pp. 617-622, 2016/10/01/ 2016.
- [174] J. T. Muth *et al.*, "Embedded 3D printing of strain sensors within highly stretchable elastomers," (in eng), *Adv Mater*, vol. 26, no. 36, pp. 6307-12, Sep 2014.
- [175] T. J. Hinton, A. Hudson, K. Pusch, A. Lee, and A. W. Feinberg, "3D Printing PDMS Elastomer in a Hydrophilic Support Bath via Freeform Reversible Embedding," *ACS Biomaterials Science & Engineering*, vol. 2, no. 10, pp. 1781-1786, 2016/10/10 2016.
- [176] J. O. Hardin, T. J. Ober, A. D. Valentine, and J. A. Lewis, "3D printing: microfluidic printheads for multimaterial 3D printing of viscoelastic inks (Adv. Mater. 21/2015)," *Advanced Materials*, vol. 27, no. 21, pp. 3278-3278, 2015.
- [177] F. Liravi, R. Darleux, and E. Toyserkani, "Nozzle dispensing additive manufacturing of polysiloxane: dimensional control," *International Journal of Rapid Manufacturing*, vol. 5, no. 1, pp. 20-43, 2015.
- [178] K. Tian *et al.*, "3D printing of transparent and conductive heterogeneous hydrogel-elastomer systems," *Advanced Materials*, vol. 29, no. 10, p. 1604827, 2017.
- [179] C. S. O'Bryan *et al.*, "Self-assembled micro-organogels for 3D printing silicone structures," *Science advances*, vol. 3, no. 5, p. e1602800, 2017.
- [180] S. Zheng, M. Zlatin, P. R. Selvaganapathy, and M. A. Brook, "Multiple modulus silicone elastomers using 3D extrusion printing of low viscosity inks," *Additive Manufacturing*, vol. 24, pp. 86-92, 2018.
- [181] S. P. Scott and C. Sutcliffe, "Additive manufacturing apparatus and method," ed: Google Patents, 2015.
- [182] J. O. Hardin, T. J. Ober, A. D. Valentine, and J. A. Lewis, "Microfluidic printheads for multimaterial 3D printing of viscoelastic inks," *Advanced materials*, vol. 27, no. 21, pp. 3279-3284, 2015.
- [183] N. Bhattacharjee, C. Parra-Cabrera, Y. T. Kim, A. P. Kuo, and A. Folch, "Desktop-Stereolithography 3D-Printing of a Poly (dimethylsiloxane)-Based Material with Sylgard-184 Properties," *Advanced materials*, vol. 30, no. 22, p. 1800001, 2018.
- [184] T. Femmer, A. J. Kuehne, and M. Wessling, "Print your own membrane: direct rapid prototyping of polydimethylsiloxane," *Lab on a Chip*, vol. 14, no. 15, pp. 2610-2613, 2014.
- [185] F. Liravi and E. Toyserkani, "A hybrid additive manufacturing method for the fabrication of silicone bio-structures: 3D printing optimization and surface characterization," *Materials & Design*, vol. 138, pp. 46-61, 2018.
- [186] J. U. Lind *et al.*, "Instrumented cardiac microphysiological devices via multimaterial three-dimensional printing," *Nature materials*, vol. 16, no. 3, pp. 303-308, 2017.
- [187] D. B. Kolesky, K. A. Homan, M. A. Skylar-Scott, and J. A. Lewis, "Three-dimensional bioprinting of thick vascularized tissues," *Proceedings of the national academy of sciences*, vol. 113, no. 12, pp. 3179-3184, 2016.
- [188] E. MacDonald and R. Wicker, "Multiprocess 3D printing for increasing component functionality. Science 353: aaf2093," ed, 2016.
- [189] Y. F. Zhang *et al.*, "Soft Robots: Fast-Response, Stiffness-Tunable Soft Actuator by Hybrid Multimaterial 3D Printing (Adv. Funct. Mater. 15/2019)," *Advanced Functional Materials*, vol. 29, no. 15, p. 1970098, 2019.
- [190] K. Kowsari, S. Akbari, D. Wang, N. X. Fang, and Q. Ge, "High-efficiency high-resolution multimaterial fabrication for digital light processing-based three-dimensional printing," *3D Printing and Additive Manufacturing*, vol. 5, no. 3, pp. 185-193, 2018.

- [191] X. Ma *et al.*, "Deterministically patterned biomimetic human iPSC-derived hepatic model via rapid 3D bioprinting," *Proceedings of the National Academy of Sciences*, vol. 113, no. 8, pp. 2206-2211, 2016.
- [192] Z. Ji, C. Yan, B. Yu, X. Wang, and F. Zhou, "Multimaterials 3D printing for free assembly manufacturing of magnetic driving soft actuator," *Advanced Materials Interfaces*, vol. 4, no. 22, p. 1700629, 2017.
- [193] A. Frutiger *et al.*, "Capacitive soft strain sensors via multicore-shell fiber printing," *Advanced Materials*, vol. 27, no. 15, pp. 2440-2446, 2015.
- [194] L.-Y. Zhou, Q. Gao, J.-F. Zhan, C.-Q. Xie, J.-Z. Fu, and Y. He, "Three-dimensional printed wearable sensors with liquid metals for detecting the pose of snakelike soft robots," *ACS applied materials & interfaces*, vol. 10, no. 27, pp. 23208-23217, 2018.
- [195] M. Costantini *et al.*, "Microfluidic-enhanced 3D bioprinting of aligned myoblast-laden hydrogels leads to functionally organized myofibers in vitro and in vivo," *Biomaterials*, vol. 131, pp. 98-110, 2017.
- [196] Q. Pi *et al.*, "Digitally tunable microfluidic bioprinting of multilayered cannular tissues," *Advanced Materials*, vol. 30, no. 43, p. 1706913, 2018.
- [197] L. Shao *et al.*, "Fiber-based mini tissue with morphology-controllable GelMA microfibers," *Small*, vol. 14, no. 44, p. 1802187, 2018.
- [198] L. Shao, Q. Gao, C. Xie, J. Fu, M. Xiang, and Y. He, "Coaxial Bioprinting: Bioprinting of Cell-Laden Microfiber: Can It Become a Standard Product?(Adv. Healthcare Mater. 9/2019)," *Advanced Healthcare Materials*, vol. 8, no. 9, p. 1970040, 2019.
- [199] J. Mueller, J. R. Raney, K. Shea, and J. A. Lewis, "Architected Lattices with High Stiffness and Toughness via Multicore-Shell 3D Printing," *Advanced Materials*, vol. 30, no. 12, p. 1705001, 2018.
- [200] A. Chortos, J. Mao, J. Mueller, E. Hajiesmaili, J. A. Lewis, and D. R. Clarke, "Printing Reconfigurable Bundles of Dielectric Elastomer Fibers," *Advanced Functional Materials*, vol. 31, no. 22, p. 2010643, 2021.
- [201] T. J. Ober, D. Foresti, and J. A. Lewis, "Active mixing of complex fluids at the microscale," *Proceedings of the National Academy of Sciences*, vol. 112, no. 40, pp. 12293-12298, 2015.
- [202] J. M. Ortega *et al.*, "Active Mixing of Disparate Inks for Multimaterial 3D Printing," *Advanced Materials Technologies*, vol. 4, no. 7, p. 1800717, 2019.
- [203] A. M. Golobic *et al.*, "Active Mixing of Reactive Materials for 3D Printing," *Advanced Engineering Materials*, vol. 21, no. 8, p. 1900147, 2019.
- [204] H. Lan, "Active Mixing Nozzle for Multi-Material and Multi-Scale 3D Printing," in *ASME 2017 12th International Manufacturing Science and Engineering Conference collocated with the JSME/ASME 2017 6th International Conference on Materials and Processing*, 2017: American Society of Mechanical Engineers Digital Collection.
- [205] B. K. Deuser, L. Tang, R. G. Landers, M. C. Leu, and G. E. Hilmas, "Hybrid extrusion force-velocity control using freeze-form extrusion fabrication for functionally graded material parts," *Journal of Manufacturing Science and Engineering*, vol. 135, no. 4, 2013.
- [206] L. Ren *et al.*, "3D printing of materials with spatially non-linearly varying properties," *Materials & Design*, vol. 156, pp. 470-479, 2018.
- [207] W. Liu *et al.*, "Rapid continuous multimaterial extrusion bioprinting," *Advanced materials*, vol. 29, no. 3, p. 1604630, 2017.
- [208] D. B. Kolesky, R. L. Truby, A. S. Gladman, T. A. Busbee, K. A. Homan, and J. A. Lewis, "3D bioprinting of vascularized, heterogeneous cell-laden tissue constructs," *Advanced materials*, vol. 26, no. 19, pp. 3124-3130, 2014.

- [209] C. J. Hansen *et al.*, "High-throughput printing via microvascular multinozzle arrays," *Advanced Materials*, vol. 25, no. 1, pp. 96-102, 2013.
- [210] !!! INVALID CITATION !!! {Skylar-Scott, 2019 #1391;Zheng, 2018 #1459}.
- [211] D. Kokkinis, M. Schaffner, and A. R. Studart, "Multimaterial magnetically assisted 3D printing of composite materials," *Nature communications*, vol. 6, p. 8643, 2015.
- [212] D. Kokkinis, F. Bouville, and A. R. Studart, "3D Printing of Materials with Tunable Failure via Bioinspired Mechanical Gradients," *Advanced Materials*, vol. 30, no. 19, p. 1705808, 2018.
- [213] X. Li, J. M. Zhang, X. Yi, Z. Huang, P. Lv, and H. Duan, "Multimaterial microfluidic 3D printing of textured composites with liquid inclusions," *Advanced Science*, vol. 6, no. 3, p. 1800730, 2019.
- [214] S. Beyer, T. Mohamed, and K. Walus, "A Microfluidics Based 3D Bioprinter with On-The-Fly Multimaterial Switching capability," in *17th International Conference on Miniaturized Systems for Chemistry and Life Sciences*, 2013.
- [215] S. E. Bakarich, R. Gorkin III, R. Gately, S. Naficy, M. in het Panhuis, and G. M. Spinks, "3D printing of tough hydrogel composites with spatially varying materials properties," *Additive Manufacturing*, vol. 14, pp. 24-30, 2017.
- [216] J. J. Adams *et al.*, "Conformal printing of electrically small antennas on three-dimensional surfaces," *Advanced Materials*, vol. 23, no. 11, pp. 1335-1340, 2011.
- [217] Y. Gan, *Continuum mechanics: progress in fundamentals and engineering applications*. BoD—Books on Demand, 2012.
- [218] G. Degré, P. Joseph, P. Tabeling, S. Lerouge, M. Cloitre, and A. Ajdari, "Rheology of complex fluids by particle image velocimetry in microchannels," *Applied Physics Letters*, vol. 89, no. 2, p. 024104, 2006.
- [219] N.-T. Nguyen, M. Hejazian, C. Ooi, and N. Kashaninejad, "Recent advances and future perspectives on microfluidic liquid handling," *Micromachines*, vol. 8, no. 6, p. 186, 2017.
- [220] A. E. Kamholz and P. Yager, "Molecular diffusive scaling laws in pressure-driven microfluidic channels: deviation from one-dimensional Einstein approximations," *Sensors and Actuators B: Chemical*, vol. 82, no. 1, pp. 117-121, 2002.
- [221] V. Mengeaud, J. Josserand, and H. H. Girault, "Mixing processes in a zigzag microchannel: finite element simulations and optical study," *Analytical chemistry*, vol. 74, no. 16, pp. 4279-4286, 2002.
- [222] H. Chen and J.-C. Meiners, "Topologic mixing on a microfluidic chip," *Applied Physics Letters*, vol. 84, no. 12, pp. 2193-2195, 2004.
- [223] Z. Tang *et al.*, "Electrokinetic flow control for composition modulation in a microchannel," *Journal of Micromechanics and Microengineering*, vol. 12, no. 6, p. 870, 2002.
- [224] M. Oddy, J. Santiago, and J. Mikkelsen, "Electrokinetic instability micromixing," *Analytical chemistry*, vol. 73, no. 24, pp. 5822-5832, 2001.
- [225] Y. Wang, J. Zhe, B. T. Chung, and P. Dutta, "A rapid magnetic particle driven micromixer," *Microfluidics and Nanofluidics*, vol. 4, no. 5, pp. 375-389, 2008.
- [226] D. Ahmed, X. Mao, B. K. Juluri, and T. J. Huang, "A fast microfluidic mixer based on acoustically driven sidewall-trapped microbubbles," *Microfluidics and nanofluidics*, vol. 7, no. 5, p. 727, 2009.
- [227] J.-H. Tsai and L. Lin, "Active microfluidic mixer and gas bubble filter driven by thermal bubble micropump," *Sensors and Actuators A: Physical*, vol. 97, pp. 665-671, 2002.

- [228] Z. Wu, N.-T. Nguyen, and X. Huang, "Nonlinear diffusive mixing in microchannels: theory and experiments," *Journal of Micromechanics and Microengineering*, vol. 14, no. 4, p. 604, 2004.
- [229] J. Branebjerg, P. Gravesen, J. P. Krog, and C. R. Nielsen, "Fast mixing by lamination," in *Proceedings of Ninth International Workshop on Micro Electromechanical Systems*, 1996, pp. 441-446: IEEE.
- [230] M. S. Munson and P. Yager, "Simple quantitative optical method for monitoring the extent of mixing applied to a novel microfluidic mixer," *Analytica Chimica Acta*, vol. 507, no. 1, pp. 63-71, 2004.
- [231] B. He, B. J. Burke, X. Zhang, R. Zhang, and F. E. Regnier, "A picoliter-volume mixer for microfluidic analytical systems," *Analytical chemistry*, vol. 73, no. 9, pp. 1942-1947, 2001.
- [232] R. Miyake, T. S. Lammerink, M. Elwenspoek, and J. H. Fluitman, "Micro mixer with fast diffusion," in *[1993] Proceedings IEEE Micro Electro Mechanical Systems*, 1993, pp. 248-253: IEEE.
- [233] J. Voldman, M. L. Gray, and M. A. Schmidt, "An integrated liquid mixer/valve," *Journal of Microelectromechanical Systems*, vol. 9, no. 3, pp. 295-302, 2000.
- [234] H. Wang, P. Iovenitti, E. Harvey, and S. Masood, "Optimizing layout of obstacles for enhanced mixing in microchannels," *Smart materials and structures*, vol. 11, no. 5, p. 662, 2002.
- [235] A. D. Stroock and G. M. Whitesides, "Controlling flows in microchannels with patterned surface charge and topography," *Accounts of chemical research*, vol. 36, no. 8, pp. 597-604, 2003.
- [236] K. Hosokawa, T. Fujii, and I. Endo, "Droplet-based nano/picoliter mixer using hydrophobic microcapillary vent," in *Technical Digest. IEEE International MEMS 99 Conference. Twelfth IEEE International Conference on Micro Electro Mechanical Systems (Cat. No. 99CH36291)*, 1999, pp. 388-393: IEEE.
- [237] P. Paik, V. K. Pamula, and R. B. Fair, "Rapid droplet mixers for digital microfluidic systems," *Lab on a Chip*, vol. 3, no. 4, pp. 253-259, 2003.
- [238] H. Song, M. R. Bringer, J. D. Tice, C. J. Gerdtts, and R. F. Ismagilov, "Experimental test of scaling of mixing by chaotic advection in droplets moving through microfluidic channels," *Applied Physics Letters*, vol. 83, no. 22, pp. 4664-4666, 2003.
- [239] G. Yesiloz, M. S. Boybay, and C. L. Ren, "Effective thermo-capillary mixing in droplet microfluidics integrated with a microwave heater," *Analytical chemistry*, vol. 89, no. 3, pp. 1978-1984, 2017.
- [240] J. Deval, P. Tabeling, and C.-M. Ho, "A dielectrophoretic chaotic mixer," in *Technical Digest. MEMS 2002 IEEE International Conference. Fifteenth IEEE International Conference on Micro Electro Mechanical Systems (Cat. No. 02CH37266)*, 2002, pp. 36-39: IEEE.
- [241] Y. Du, Z. Zhang, C. Yim, M. Lin, and X. Cao, "A simplified design of the staggered herringbone micromixer for practical applications," *Biomicrofluidics*, vol. 4, no. 2, p. 024105, 2010.
- [242] A. O. El Moctar, N. Aubry, and J. Batton, "Electro-hydrodynamic micro-fluidic mixer," *Lab on a Chip*, vol. 3, no. 4, pp. 273-280, 2003.
- [243] L.-H. Lu, K. S. Ryu, and C. Liu, "A magnetic microstirrer and array for microfluidic mixing," *Journal of microelectromechanical systems*, vol. 11, no. 5, pp. 462-469, 2002.

- [244] H. Y. Gan, Y. C. Lam, N. T. Nguyen, K. C. Tam, and C. Yang, "Efficient mixing of viscoelastic fluids in a microchannel at low Reynolds number," *Microfluidics and Nanofluidics*, vol. 3, no. 1, pp. 101-108, 2007.
- [245] C.-C. Cho, "Electrokinetically driven flow mixing utilizing chaotic electric fields," *Microfluidics and nanofluidics*, vol. 5, no. 6, pp. 785-793, 2008.
- [246] C. Y. Lim, Y. C. Lam, and C. Yang, "Mixing enhancement in microfluidic channel with a constriction under periodic electro-osmotic flow," *Biomicrofluidics*, vol. 4, no. 1, p. 014101, 2010.
- [247] F. Okkels and P. Tabeling, "Spatiotemporal resonances in mixing of open viscous fluids," *Physical review letters*, vol. 92, no. 3, p. 038301, 2004.
- [248] H. Wu, Y. Tian, H. Luo, H. Zhu, Y. Duan, and Y. Huang, "Fabrication techniques for curved electronics on arbitrary surfaces," *Advanced Materials Technologies*, vol. 5, no. 8, p. 2000093, 2020.
- [249] Y. Huang *et al.*, "Programmable robotized 'transfer-and-jet' printing for large, 3D curved electronics on complex surfaces," *International Journal of Extreme Manufacturing*, vol. 3, no. 4, p. 045101, 2021.
- [250] J. Huang, H. O. T. Ware, R. Hai, G. Shao, and C. Sun, "Conformal Geometry and Multimaterial Additive Manufacturing through Freeform Transformation of Building Layers," *Advanced Materials*, vol. 33, no. 11, p. 2005672, 2021.
- [251] J. C. McCaw and E. Cuan-Urquizo, "Curved-layered additive manufacturing of non-planar, parametric lattice structures," *Materials & Design*, vol. 160, pp. 949-963, 2018.
- [252] F. B. Coulter, B. S. Coulter, E. Papastavrou, and A. J. Ianakiev, "Production techniques for 3D printed inflatable elastomer structures: part II—four-axis direct ink writing on irregular double-curved and inflatable surfaces," *3D Printing Additive Manufacturing*, vol. 5, no. 1, pp. 17-28, 2018.
- [253] C. Rodriguez-Padilla, E. Cuan-Urquizo, A. Roman-Flores, J. L. Gordillo, and C. Vázquez-Hurtado, "Algorithm for the Conformal 3D Printing on Non-Planar Tessellated Surfaces: Applicability in Patterns and Lattices," *Applied Sciences*, vol. 11, no. 16, p. 7509, 2021.
- [254] N. Bausch, D. P. Dawkins, and R. Frei, "InSPIREd-advances in Conformal Printing: 3D printing onto unknown uneven surfaces," in *2017 IEEE International Conference on Advanced Intelligent Mechatronics (AIM)*, 2017, pp. 430-435: IEEE.
- [255] N. Bausch, D. P. Dawkins, R. Frei, and S. Klein, "3D printing onto unknown uneven surfaces," *IFAC-PapersOnLine*, vol. 49, no. 21, pp. 583-590, 2016.
- [256] Z. Zhu *et al.*, "3D printed functional and biological materials on moving freeform surfaces," *Advanced Materials*, vol. 30, no. 23, p. 1707495, 2018.
- [257] A. Valentine, T. Busbee, J. Boley, J. Raney, A. Chortos, and A. Kotikian, "JD 1204 Berrigan, MF Durstock, JA Lewis," *Advanced Materials*, vol. 29, no. 40, p. 1703817, 2017.
- [258] J. T. Muth *et al.*, "Embedded 3D printing of strain sensors within highly stretchable elastomers," *Advanced Materials*, vol. 26, no. 36, pp. 6307-6312, 2014.
- [259] G. Haghiashtiani, E. Habtour, S.-H. Park, F. Gardea, and M. C. McAlpine, "3D printed electrically-driven soft actuators," *Extreme Mechanics Letters*, vol. 21, pp. 1-8, 2018.
- [260] N. W. Bartlett *et al.*, "A 3D-printed, functionally graded soft robot powered by combustion," *Science*, vol. 349, no. 6244, pp. 161-165, 2015.
- [261] S. H. Kim, K. Hong, K. H. Lee, and C. D. Frisbie, "Performance and Stability of Aerosol-Jet-Printed Electrolyte-Gated Transistors Based on Poly(3-hexylthiophene)," *ACS Applied Materials & Interfaces*, vol. 5, no. 14, pp. 6580-6585, 2013/07/24 2013.
- [262] M. Ali, D. Prakash, T. Zillger, P. K. Singh, and A. C. Hübler, "Printed Piezoelectric Energy Harvesting Device," *Advanced Energy Materials*, vol. 4, no. 2, p. 1300427, 2014.

- [263] X. Zhou and P. S. Lee, "Three dimensional printed nanogenerators," *EcoMat*, vol. 3, no. 3, p. e12098, 2021.
- [264] S. Gatz *et al.*, "19.4%-efficient large-area fully screen-printed silicon solar cells," *physica status solidi (RRL) – Rapid Research Letters*, vol. 5, no. 4, pp. 147-149, 2011.
- [265] W. Deng *et al.*, "22.61 % Efficient Fully Screen Printed PERC Solar Cell," in *2017 IEEE 44th Photovoltaic Specialist Conference (PVSC)*, 2017, pp. 2220-2226.
- [266] H.-J. Yoon *et al.*, "3D-printed biomimetic-villus structure with maximized surface area for triboelectric nanogenerator and dust filter," *Nano Energy*, vol. 63, p. 103857, 2019/09/01/ 2019.
- [267] R. Cao *et al.*, "Rotating-Sleeve Triboelectric–Electromagnetic Hybrid Nanogenerator for High Efficiency of Harvesting Mechanical Energy," *ACS Nano*, vol. 11, no. 8, pp. 8370-8378, 2017/08/22 2017.
- [268] X. Du *et al.*, "Ultra-robust triboelectric nanogenerator for harvesting rotary mechanical energy," *Nano Research*, vol. 11, no. 5, pp. 2862-2871, 2018/05/01 2018.
- [269] W. Yang, Y. Wang, Y. Li, J. Wang, T. Cheng, and Z. L. Wang, "Integrated flywheel and spiral spring triboelectric nanogenerator for improving energy harvesting of intermittent excitations/triggering," *Nano Energy*, vol. 66, p. 104104, 2019/12/01/ 2019.
- [270] C. Yan *et al.*, "A linear-to-rotary hybrid nanogenerator for high-performance wearable biomechanical energy harvesting," *Nano Energy*, vol. 67, p. 104235, 2020/01/01/ 2020.
- [271] J. P. Lee, B. U. Ye, K. N. Kim, J. W. Lee, W. J. Choi, and J. M. Baik, "3D printed noise-cancelling triboelectric nanogenerator," *Nano energy*, vol. 38, pp. 377-384, 2017.
- [272] G. Nasti and A. Abate, "Tin Halide Perovskite (ASnX<sub>3</sub>) Solar Cells: A Comprehensive Guide toward the Highest Power Conversion Efficiency," *Advanced Energy Materials*, vol. 10, no. 13, p. 1902467, 2020.
- [273] C. Yang, E. Zhou, S. Miyanishi, K. Hashimoto, and K. Tajima, "Preparation of Active Layers in Polymer Solar Cells by Aerosol Jet Printing," *ACS Applied Materials & Interfaces*, vol. 3, no. 10, pp. 4053-4058, 2011/10/26 2011.
- [274] A. Mette, P. L. Richter, M. Hörteis, and S. W. Glunz, "Metal aerosol jet printing for solar cell metallization," *Progress in Photovoltaics: Research and Applications*, vol. 15, no. 7, pp. 621-627, 2007.
- [275] H. Cui *et al.*, "Three-dimensional printing of piezoelectric materials with designed anisotropy and directional response," *Nature Materials*, vol. 18, no. 3, pp. 234-241, 2019/03/01 2019.
- [276] N. Chandrasekharan and L. L. Thompson, "Increased power to weight ratio of piezoelectric energy harvesters through integration of cellular honeycomb structures," *Smart Materials and Structures*, vol. 25, no. 4, p. 045019, 2016/03/14 2016.
- [277] N. J. Vickers, "Animal Communication: When I'm Calling You, Will You Answer Too?," *Current Biology*, vol. 27, no. 14, pp. R713-R715, 2017/07/24/ 2017.
- [278] H. Li *et al.*, "3D printed flexible triboelectric nanogenerator with viscoelastic inks for mechanical energy harvesting," *Nano Energy*, vol. 58, pp. 447-454, 2019/04/01/ 2019.
- [279] C. Qian *et al.*, "All-printed 3D hierarchically structured cellulose aerogel based triboelectric nanogenerator for multi-functional sensors," *Nano Energy*, vol. 63, p. 103885, 2019/09/01/ 2019.

## 2 Chapter 2

### All Printable Snow-Based Triboelectric Nanogenerator

**Complete Citation:**

Ahmed, A., Hassan, I., Mosa, I.M., Elsanadidy, E., Phadke, G.S., El-Kady, M.F., Rusling, J.F., Selvaganapathy, P.R. and Kaner, R.B., 2019. All printable snow-based triboelectric nanogenerator. *Nano Energy*, 60, pp.17-25.

**Copyright:**

Reproduced with permission from Nano Energy, 2019.

**Contribution:**

The main 3D printer system was developed priorly by our lab, and had been used to create the current TENG device.

Ahmed, A and Hassan, I.: Designed and performed all experiments, interpretation and analysis of data, wrote the manuscript draft, and Ahmed, I was responsible for paper submission.

Mosa, I.M., Elsanadidy, E., Phadke, G.S., El-Kady, M.F., Rusling, J.F.: Revised and edited P. R. Selvaganapathy and Kaner, R.B.: Supervised Ahmed, A and Hassan, I and provided guidance, revised and edited the manuscript.

## 2.1 Abstract

The development of power generators that function in harsh snowy environments and by contact with snow can be beneficial but challenging to accomplish. Herein we introduce the first snow-based triboelectric nanogenerator (snow TENG) that can be used as an energy harvester and a multifunctional sensor based on the principle of snow-triboelectrification. In this work, we used a 3D printing technique for the precise deposition of the electrode and triboelectric layer, leading to flexible, stretchable and metal-free triboelectric generators. Based on the single electrode mode, the device can generate instantaneous output power density as high as  $0.2 \text{ mW/m}^2$ , open circuit voltage up to  $8 \text{ V}$ , and current density  $40 \text{ }\mu\text{A/m}^2$ . In addition, the snow TENG can function as a self-powered multifunctional weather station in cold climates to measure snowfall rate, snow depth, wind direction, and speed in snowy and/or icy environments. In addition, the snow-TENG can be used as a wearable power source and biomechanical sensor to detect human body motions, which may prove useful for snow-related sports. Unlike conventional sensor platforms, the proposed design works without the need for batteries or image processing systems. We envision these devices could potentially be integrated with solar panels to ensure continuous power supply during harsh weather conditions.

## 2.2 Introduction

Access to green, renewable power sources, including solar energy and wind turbines, in areas with frequent snowfall, poses a major challenge. Severe weather conditions, such as prolonged cloud cover, short daylight periods, heavy snow accumulation, and sub-zero temperatures, can affect energy generation.[1, 2] Alternate methods that exploit local weather conditions in these settings could offer a more viable energy generation strategy.

concurrently, continuous meteorological observation is also essential in these cold or snowy environments for all forms of daily activities. However, typical weather stations and meteorological sensors have several limitations, such as their ability to function with snow accumulation, large form factor, cost, complexity and most importantly a need for a sustainable power source to operate effectively in such severe environment.[3, 4] In this scenario, a self-powered multifunctional weather station is a logical choice, but one which does not yet exist. This issue is complicated by snow cover that comprises the largest area of the cryosphere, an average of 46 million square kilometers of the Earth's surface each year.[5]

The natural phenomenon of snow particles carrying electrical charges (i.e., snow electrification) during snowfall was previously observed, but has remained a curiosity and has not been effectively exploited for useful purposes. [6-11] The Snow electrification is based on ordering of the electrical dipoles of water molecules as they crystallize into snowflakes and also can be generated frictionally due to the relative motion between the sliding layer and snow. [6-11] In frictional snow electrification, the charge density at the surface as well as the triboelectric potential of snow as compared to the surface that it rubs against determining the amount of contact electrification and charge transfer that occur. [6-11] Snow electrification is significantly affected by the temperature.[12, 13] For instance, it has been noted that the snow layer is charged positively at temperatures of  $-5^{\circ}\text{C}$  and  $-10^{\circ}\text{C}$  and negatively at  $-15^{\circ}\text{C}$  and  $-20^{\circ}\text{C}$ . [12, 13] Triboelectric Nanogenerators (TENGs) have been reported as promising devices for harvesting energy from mechanical vibration induced by ocean waves, raindrops and wind by converting it into electrical energy through contact electrification.[14-30] Among these, water waves and waterfalls, can be excellent

sources of energy with potential for large-scale applications. While there have been many research efforts to extract this water-based energy [16, 23, 31-36], none have been directed at extracting energy from snow.

Here, we present, for the first time, a snow-triboelectric nanogenerator (snow-TENG) that is designed to harvest energy originating from the contact/friction with snow. The device, operating in a single electrode mode, is designed to utilize both contact electrification and electrostatic induction during a snowfall event. This is made possible by exploiting various kinds of relative motions including snow falling on the surface of the device as well as sliding of snow particles past the device. The snow-TENG output can reach a voltage of up to 8 V with a crest current density of  $40 \mu\text{A}/\text{m}^2$ . Snow-TENG, connected to a load resistor of  $50 \text{ M}\Omega$ , produces output power density as high as  $0.2 \text{ mW}/\text{m}^2$ . This device not only functions as an energy generator but also serves as a self-powered multifunctional sensor with various applications. We also demonstrate the utility of this device as a self-powered cold region multimodal atmospheric weather station that can measure different meteorological parameters, such as snowfall rate and its direction, wind speed, and depth of snow accumulation. Such a compact and self-powered sensors could also find applications in performance monitoring for winter sports such as skating and skiing where currently unwieldy video analysis equipment are used to assess and improve athlete's kinematics[37, 38]. Furthermore, taking advantage of its lightweight and stretchability, we successfully demonstrate the ability of the snow-TENG as a wearable power source and as a self-powered device for monitoring biomechanical physical activity. Subsequently, we can track various kinds of human activity, such as running, walking, jumping and marching by attaching snow-TENG onto a pair of shoes. Given its low cost,

mechanical durability, and ease of fabrication, this wearable snow-based TENG shows potential in a wide range of applications including wearable and environmental sensors and as a sustainable power source in cold climates.

## 2.3 Materials and Methods

### Materials

Poly (3,4-ethylene dioxythiophene)-poly (styrene sulfonate) 1.1% in H<sub>2</sub>O, neutral pH, high-conductivity grade (PEDOT: PSS) and dimethyl sulfate ((DMS, (CH<sub>3</sub>)<sub>2</sub>SO<sub>4</sub>), 99.8% purity) were purchased from Sigma Aldrich. Mercapto-functionalized silicones, specifically 13-17% (mercaptopropyl) methylsiloxane-dimethylsiloxane copolymer 1 (SMS-142, 100-200cSt), 2-3% (mercaptopropyl) methylsiloxane-dimethylsiloxane copolymer 2 (SMS-022, 100cSt), and  $\alpha,\omega$ -Vinyl-terminated poly(dimethylsiloxane) copolymers 4 (DMS-V31, MW 21500, viscosity of 1000 cSt) were purchased from Gelest. Photoinitiator TPO-L (ethyl (2,4,6-trimethylbenzoyl) phenyl phosphinate) was received as a gift from IGM Resins, Inc.

**Preparation of the microstructure pattern:** First, a 2 mm thick (100) Si wafer was covered by thermally grown photoresist layer (40  $\mu\text{m}$ ) using spin coating technique on the Si wafer upper surface. Secondly, using photolithography, a square pattern of side length 25  $\mu\text{m}$  x 25  $\mu\text{m}$  is patterned.[39, 40] KOH solution was utilized to complete the etching process and produce the recessed structures of a square. The patterned silicon wafer was used as a mold and was treated with trimethylchlorosilane (Sigma Aldrich) by gas phase silanization to reduce adhesion to the subsequent layers.[25, 41] This functionalized Si mold has been used as a substrate for the extrusion printing of silicone, thus decorating the triboelectric layer with the square patterns. The silicone layer was initially exposed to UV

curing with a light intensity of 20 W. After post-curing at a UV intensity of 76 W for 6 min, the micropatterned silicone layer was peeled off from the mold. This silicone layer was used as the tribo-functional layer.

**3D Printing of PEDOT: PSS layer:** An aqueous dispersion of PEDOT: PSS was used as an ink for the 3D extrusion printing of the electrode layer. The conductive polymer was treated by an inorganic dopant, DMS, in an attempt to enhance the polymer conductivity without compromising its excellent mechanical properties and visible light transparency. The weight ratio of the two components was set at 1:25 to achieve the best conductivity (estimated at 100 S/cm).[42] This solution was subsequently heated at 100°C for 2 hours to adjust the viscosity of the ink before performing extrusion printing on the stretchable silicone substrate with squared patterns.

**3D Printing of silicone layer:** A customized print head system was used for the direct printing of the silicone layer. This system takes advantage of a pneumatic pump (up to 90 psi) with switchable solenoid valves for applying positive pressure to control the flow of the ink through the print head. The speed in x and y directions was adjusted at 500 mm/min, while a commercial extrusion nozzle (25-gauge needle) was connected to the ink reservoir with a blunt tip diameter of 215  $\mu\text{m}$ .

The ink consists of the cross-linkers and receptors indicated in the materials section, combined with TPO-L as a photoinitiator. This silicone layer was printed on top of the PEDOT: PSS and used as the substrate of the snow-TENG. Exposure of this layer to UV light leads to polymer crosslinking and eventually results in a mechanically strong, yet flexible and stretchable, silicone layer. This was achieved using a controllable Omnicure S1000 (Lumen Dynamics) light source that was positioned at a 45° angle to the surface, 4

cm from the extrusion nozzle, producing a light intensity of  $2.3 \text{ W cm}^{-2}$ . This light source has a broad UV wavelength spectrum in the range of 275–500 nm, and strong intensity of 100 Watts. The printing setup utilized two of these light sources, which has the potential for shortening the cure time and increasing the production efficiency.

**Electrical measurements:** The output current and voltage were recorded using a voltage preamplifier (Keithley 6514 System Electrometer) that was interfaced with a custom LabVIEW program.

## 2.4 Results and Discussion

### 2.4.1 TENG Fabrication Process

We utilized a 3D extrusion printing approach for fabricating the snow-TENG not only to ensure low-cost and scalable manufacturing but also to allow a high degree of customization in the size and shape of the devices. In this process, the snow-TENG device is constructed by deposition of successive thin films of PEDOT: PSS as an electrode and UV curable silicone as a triboelectrification layer, as illustrated in **Figure 2-1**. The extrusion printing relies on the properties of the inks, which tend to have a considerable influence on the structure and performance of the printed subject. These inks should have high viscosity and shear-thinning behavior to enable controlled flow through nozzles. Considering its flexibility and environmental stability, PEDOT: PSS should be an excellent electrode for transparent snow-TENGs. This conductive polymer is commercially available as a dispersion in water, but lacks reasonable electronic conductivity. The addition of dimethyl sulfate (DMS) ensures higher electronic conductivity of up to  $100 \text{ S/cm}$  (see methods section). Increased viscosity has been achieved by evaporating extra water. After adjusting its viscosity, this ink is extruded into a thin electrically conductive film on a

printed silicone substrate (**Figure 2-1(a-i)**) and is subsequently thermally cured. Then, a thin film of silicone is printed on the cured electrode layer (**Figure 2-1(a-ii)**).

Here, pendent thiol propyl silicones are utilized as cross-linkers and telechelic vinyl-substituted silicones as receptors, while TPO-L is added as a photo-initiator in the formulation. This layer can be cured at low temperatures using UV light, leading to mechanically strong, yet flexible and stretchable, silicone-based triboelectric generators. **Figure 2-1b** shows a schematic illustration of the device structure. The surface of silicone has been patterned with an array of microscopic squares/cubes to increase the efficiency of the nanogenerator by increasing the surface area of the contact. SEM analysis of the resulting patterned array shows uniform microstructures with a feature size of 25  $\mu\text{m}$  (see methods section). The device creates electricity through the principle of snow triboelectrification when the falling airborne snow particles come in contact with the silicone surface, as schematically illustrated in **Figure 2-1c**. It is worth noting that the different layers of the device are highly transparent (**Figure 2-1d**). With further developments, this device could be printed directly onto the surface of solar panels to create electricity during snow seasons without compromising the efficiency of the solar cells. It is also interesting to realize that the snow-TENG device is highly stretchable, as demonstrated in **Figure 2-1e**, achieving maximum stretchability of approximately 125 %.

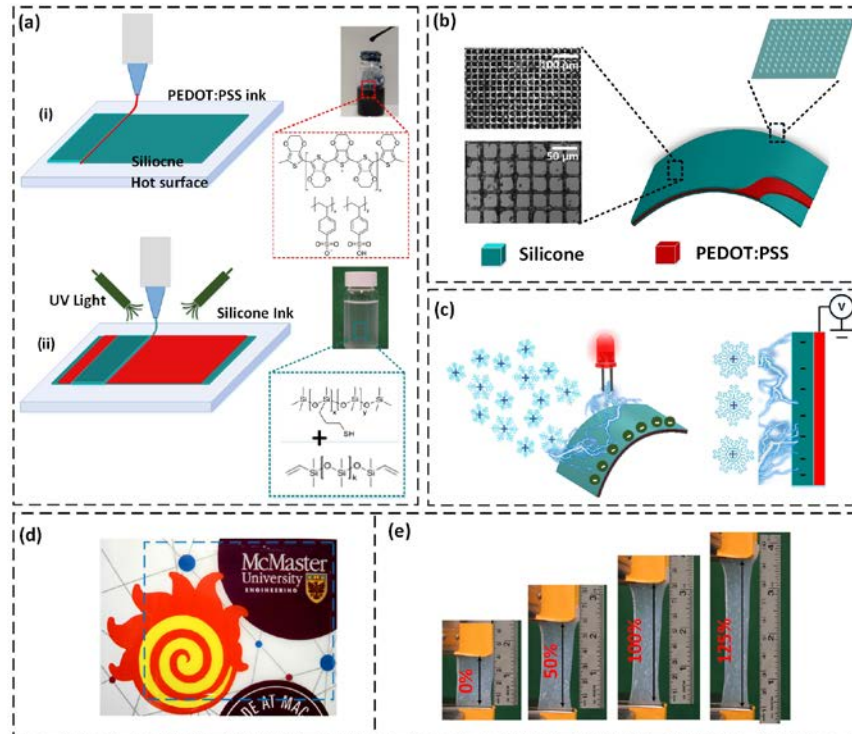


**Figure 2-1** 3D printing process, architecture along with optical and mechanical properties of the snow TENG. (a) Schematic illustration of the printing process of the snow TENG, (a-i) printing of a conductive polymer electrode; inset shows the chemical composition of the PEDOT:PSS ink, (a-ii) Printing of the triboelectrification layer based on UV curable silicone ink; inset reveals the chemical composition of the silicone ink. (b) Schematic illustration of the structure of the device, featuring micropatterned surface of the UV curable silicone. SEM images on the left showing the micropattern at different magnifications. Scale bars are 100µm and 50µm, respectively. (c) The working principle of the device based on snow triboelectrification. (d) A photograph showing the high transparency of the silicone layer; the logo of McMaster University shown in the background can be clearly recognized through the silicone layer. (e) Exposure of the snow TENG to different stretching conditions.

#### 2.4.2 Evaluation of Snow-TENG Electrical Performance

To investigate the electrical output of a snow-TENG, a “triboelectric series” of four different triboelectric materials were selected based on their ability to gain or lose electrons and tested in contact with the snow. This includes some materials at the negative scale of the triboelectric series, such as silicone, polytetrafluoroethylene (PTFE), others at the middle section, such as Kapton, and finally, some positive tribo-materials, such as

aluminum (Al).[43] Open circuit voltage  $V_{oc}$  and current density  $J_{sc}$  between the snow layer and selected tribomaterials are recorded, as seen in **Figure 2-2a**. Results indicate that  $V_{oc}$  and  $J_{sc}$  increase steadily depending on the position of the material in the triboelectric series while achieving maximum performance with the most tribo-negative materials. For instance, the contact of snow particles and silicone produced the maximum  $V_{oc}$  (8 V), and  $J_{sc}$  ( $24 \mu\text{A}/\text{m}^2$ ), whereas snow and Al produced the minimum  $V_{oc}$  (1 V), and  $J_{sc}$  ( $2 \mu\text{A}/\text{m}^2$ ). Based on the difference in output signals, the snow can be defined as a tribo-positive material.

While the selection of the proper triboelectric material is critical, fine-tuning of its surface structure, surface charges, and other physical properties is also necessary for ensuring high-performance TENGs. This was achieved by exploring the effect of curing conditions, such as UV intensity and curing time, on the snow-TENG performance. It was previously discovered that UV light intensity could help in the production of negative charges on the surface of silicone.[44] However, if the UV-exposure time exceeds a specific critical value (6 min as reported), the local charge distribution declines rapidly, and the surface potential in the entire zone slowly achieves a saturation state.[45] It was also reported that UV light irradiation could increase the contact angle of silicone, leading to surfaces with anti-icing properties.[45-47] Therefore, we systematically studied the influence of UV light intensity and curing time on the performance of a snow-TENG. Results in **Figure 2-2(b, c)**, indicate that the exposure of the silicone layer to a UV light with an intensity of 76 W for 6 min delivers the best performance for the snow-TENG.

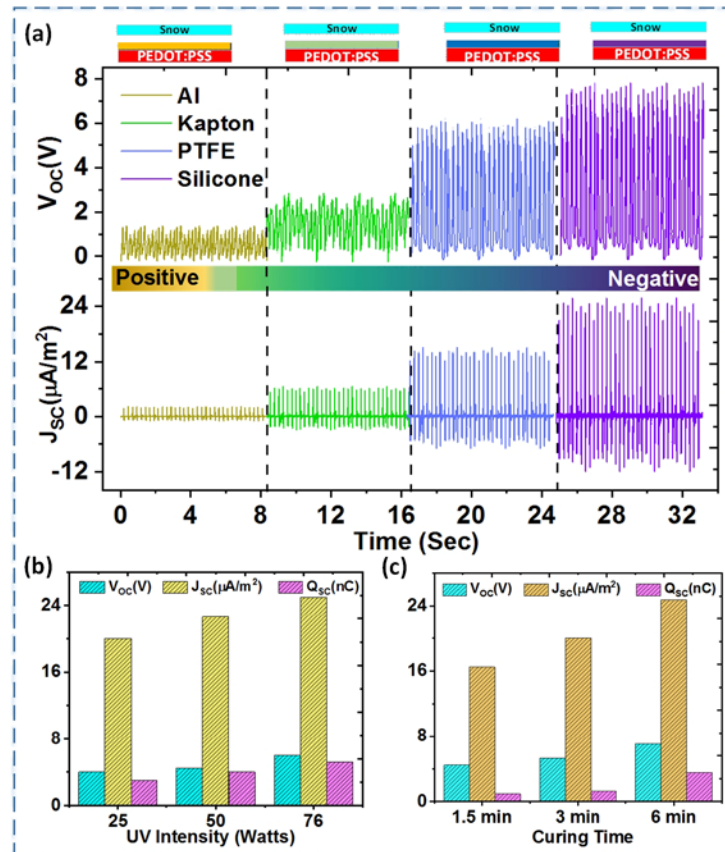


**Figure 2-2** Evaluation of the electrical performance of snow TENG for harvesting energy from falling snow. (a)  $V_{oc}$  and  $J_{sc}$  define the triboelectrification performance of snow TENG using different positive and negative triboelectric materials. (b, c) Influence of the UV light intensity and curing time of the triboelectrification layer (silicone) on the electrical output of the device. The plots compare open circuit voltage, short-circuit current, and short circuit charge under different conditions.

### 2.4.3 Snow-TENG Working Mechanisms

The fabricated single electrode snow-TENG can operate through various modes of triboelectrification, such as tapping, sliding and snowfall. In the tapping scenario, as shown in **Figure 2-3a**, the silicone layer does not exhibit a surface charge prior to contact with the snow. Surface groups on the silicone layer will be ionized as the contact event occurs, causing the development of a net negative charge on the silicone surface and a net positive charge on the snow surface (to maintain electrical neutrality). The negative charges remain on the silicone surface as it moves away from the snow, creating a potential difference

between the ground and the silicone electrode. Alternatively, the snow-TENG can also generate contact electrification in the sliding scenario, as shown in **Figure 2-3b**. Here too, no charge transfer occurs unless silicone comes in contact with the snow. As silicone slides on the snow, surface groups on the silicone develop negative charges, while electrical neutrality is maintained by the generation of positive charges on the snow surface. The negative charges remain on the surface of silicone as the snow slides off, creating a potential difference between the ground and the silicone layer.

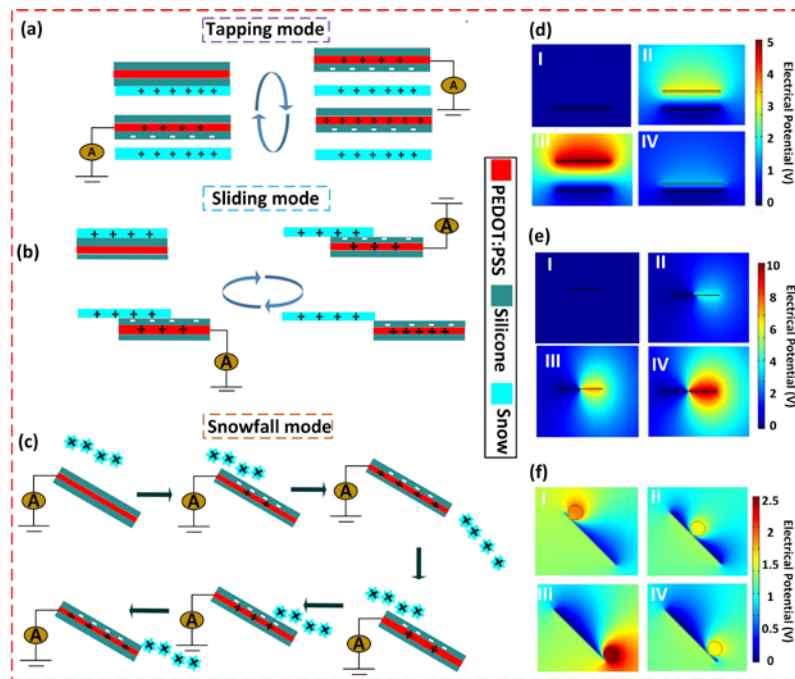


**Figure 2-3** The working mechanisms and FEM simulations of snow TENG. (a, b, c) Schematic illustration showing the working mechanism of snow TENG utilizing three different operating modes including tapping, sliding, and snowfall. (d, e, f) FEM simulation results for the corresponding operation modes.

Finally, triboelectric charges can also be generated when snow falls on the silicone thin film, as shown in **Figure 2-3c**. As snow/ice slides on the silicone layer, triboelectricity is produced, resulting in the formation of charged snow particles and a charged silicone surface. When the falling snow comes into contact with the thin film of silicone, the film

becomes negatively charged due to ionization of surface groups. As the snow leaves the silicone layer, a potential difference develops between the ground and the electrode. This potential difference results in an instantaneous negative current flow when the electrode is connected to the ground through a load resistor, as illustrated in **Figure 2-3c**. Further contact with additional snowfall on the surface of the silicone film leads to an increasing amount of electrification and thus, charge density on the surface continues to increase. This increased charge density leads to a corresponding increase in the charges on the electrode that could be measured. This cycle can be repeated as long as snow particles continue to fall, touch, and leave the surface of the snow-TENG device.

A finite element method (FEM) analysis was carried out to show the electrical potential distribution of the snow-TENG in case of three proposed configurations, i.e., tapping, sliding, and snowfall scenarios. The snow-TENG was connected to ground and was assigned a uniform  $50 \mu\text{C}\cdot\text{cm}^2$  triboelectric charge density. Using COMSOL software, the charge transfer between the snow-TENG electrode and ground was modulated by changing the relative distance between the snow and the silicone layer in the case of tapping mode or relative lateral distance in the case of sliding mode. At the contact area, the electrical potential approaches zero (**Figure 2-3d, e**). When the two materials are separated, the electrical potential difference increases dramatically, reaching a maximum of 5 V at a distance of 10 mm (in the case of tapping, **Figure 2-3d**) and 10 V at a distance 15 mm (in case of sliding, **Figure 2-3e**). On the other hand, simulated results for the snow-TENG in snowfall scenarios show an increasing electrical potential difference between the silicone layer and the snow (**Figure 2-3f**). When the snow particle leaves the silicone layer, the electrical potential difference increases dramatically, reaching a maximum of 2 V.

The testing setup for the tapping scenario is presented in **Figure 2-4a**, revealing the snow layer and the TENG attached to a vertical linear motor whereby the release and loading cycles produces consistent electrical output. Because of induced capacitance at the contact area, the snow-TENG has relatively good electrical output with matched external resistance. In the tapping scenario, at a frequency of 3 Hz, the snow-TENG registers a  $V_{oc}$  of  $\sim 6$  V and  $I_{sc}$  of  $20 \mu\text{A}/\text{m}^2$  (**Figure 2-4b, c**). The power output of the device depends on the load resistance, with instantaneous power reaching a peak value of approximately  $0.06 \text{ mW}/\text{m}^2$  at a load resistance of  $100 \text{ M}\Omega$ , **Figure 2-4d**. **Figure 2-4e** shows the charging behavior of  $1 \mu\text{F}$  capacitor using the output from the snow-TENG. Results show that the capacitor can charge to 2 V in almost 4 minutes. Interestingly, there is no apparent degradation in voltage profiles for the designed snow-TENG even after about 8000 cycles of repeated loading and unloading at a frequency of 3 Hz, as seen in **Figure 2-4f**. This confirms that snow-TENG is a durable and stable device, even with long-term usage.

To demonstrate snow-TENG's capability for scavenging unused friction energy, such as from rolling tires on the snow (**Figure 2-4g**), the device is attached on a rubber bicycle wheel, and its friction energy scavenging performance was experimentally examined. The experimental setup is shown in **Figure 2-4h** where the snow-TENG has been attached to a bicycle tire and the sliding contact between snow and the device during cycling produces an electrical signal that can be harvested. In this sliding mode triboelectric generation, an  $V_{oc} \sim 8$  V and  $I_{sc}$  of  $40 \mu\text{A}/\text{m}^2$  (see **Figure 2-4i, j**) were obtained. The power output of the snow-TENG device is higher by almost two times in the sliding scenario than with tapping, with instantaneous power reaching a peak of approximately  $0.2 \text{ mW}/\text{m}^2$  at a load resistance of  $50 \text{ M}\Omega$  (**Figure 2-4k**).

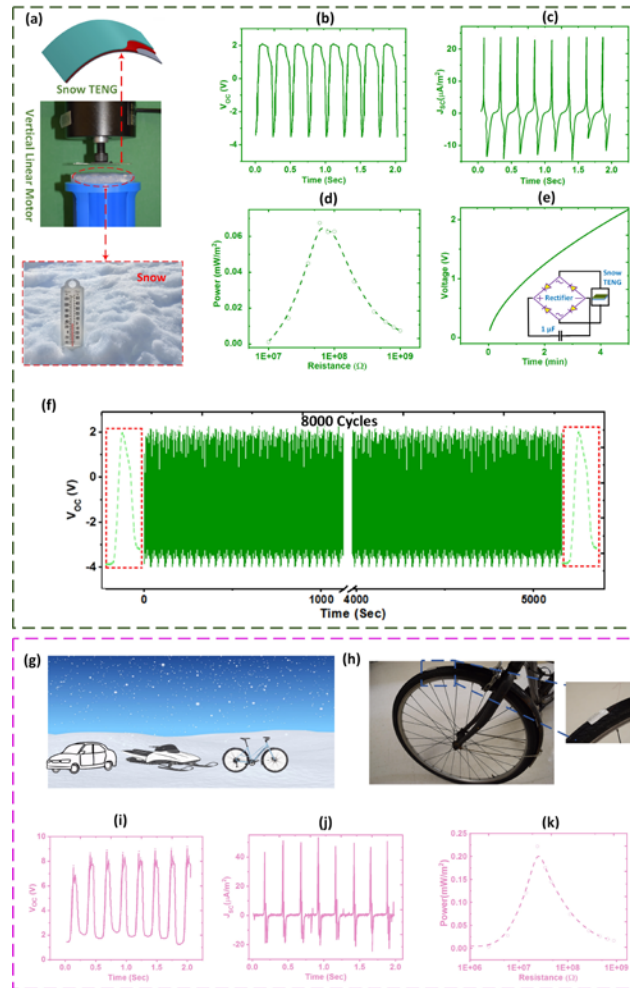


**Figure 2-4** Characterization of the electrical properties of snow TENG in tapping and sliding scenarios. (a) The testing setup showing a vertical linear motor, snow layer, and the fabricated snow TENG. (b) Open circuit voltage,  $V_{oc}$ , (c) Short circuit current  $J_{sc}$ , and (d) External load dependent peak power in tapping scenario. (e) The charging profile of  $1 \mu\text{F}$  capacitor. (f)  $V_{oc}$  during 8000 cycles of repeated loading and unloading, reflecting the stability of the snow TENG device. (g) A visionary scene for a snowy location where the snow TENG can be used for harvesting energy of moving bicycles or cars. (h) A photograph of an energy-harvesting unit attached to a bicycle. Inset: Actual snow TENG device on the wheel. (i) Measured  $V_{oc}$ , (j) measured  $J_{sc}$ , and (k) external load dependent peak power in the sliding scenario.

#### 2.4.4 Snow-TENG as a Self-Powered Arctic Weather Station

Given its capability for detecting and harvesting energy from falling snow, the snow-TENG has a huge potential as a self-powered multifunctional cold weather station. This includes measurement of different meteorological parameters, such as snowfall rate and

accumulation depth. For example, after adjusting the experimental setup towards the direction of snowfall, we found that the output signal depends on the angle of the falling snow. This is manifested by **Figure 2-5a**, in the snowfall mode, where the snow-TENG can detect snowfall angles of  $0^\circ$ ,  $45^\circ$ , and  $90^\circ$  at a constant wind speed of 10.8 km/h and a falling snow rate of 1 cm/min. The increase of the output signal occurs as a larger effective surface area is exposed to the snowfall as the angle increases. For instance, as the device angle increases up to  $90^\circ$  (normal to the direction of the snowfall), the snow impacts a larger surface area of the snow- TENG leading to higher output. In addition, as shown in **Figure 2-5b, c**, the snow-TENG can be used to measure other meteorological parameters such as the snowfall rate as well as the wind speed. While sensing the snowfall rate at a constant angle of  $90^\circ$  and wind speed of 10.8 km/h, the generated electrical signal increases with a higher falling rate as more snow impacts the exposed area of the device. However, measuring the speed of wind depends on the snow impact. The wind increases the impact force of snow particles on the surface of the device, which increases the electrical output as a result (**Figure 2-5c**). It is worth mentioning that all wind speed measurements are recorded at a snowfall rate of 1 cm/min and device angle of  $45^\circ$ .

Using the sliding mode, as shown in **Figure 2-5d**, snow-TENG can also measure the depth of snow accumulation when inserted into a snow precipitate on the ground. As the accumulated snow depth increases from 1.0 cm to 3.0 cm, the contact area of snow with the device also increases, and this is reflected in the increase in electric output. The snowfall rate and wind speed data were obtained from the reported values on the weather network on the day of the measurements. All the measurements were conducted outdoors, using the snowfall scenario, under the following conditions: Temperature of  $-6^\circ\text{C}$ ,

humidity of 60%, and snow particle diameters less than 1 cm. Electrical output measurements yield a clear correlation with the measured parameters, indicating the snow-TENG's ability to measure parameters of meteorological significance (**Figure 2-5a-d**). This multi-parametric snow-TENG sensing platform can be developed to measure multiple parameters simultaneously with the help of signal-processing techniques for analyzing the time-domain signal to separate the contribution of each stimulus.

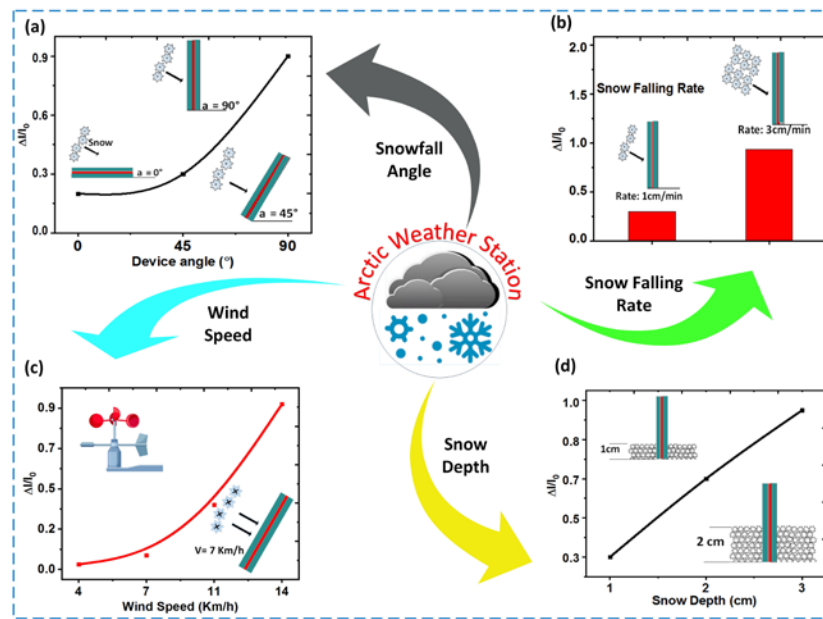


**Figure 2-5** Snow TENG as a Self-powered arctic weather station. Snow TENG can be used as a multifunctional weather station for measuring several functions including (a) Snowfall angles or the direction of falling snow. (b) Snowfall rate. (c) The speed of the wind. (d) The snow accumulation depth.

#### 2.4.5 Snow-TENG as a Self-Powered Biomechanical Monitor

Thanks to its stretchability, lightweight, and conformability, the as-fabricated snow-TENG has big potential for wearable electronics, as illustrated in **Figure 2-6a**.

When attached to clothing, snow-TENG can be used not only as wearable energy

harvester for charging electronic devices but also as an active, self-powered

multifunctional tracking platform (**Figure 2-6b, c**). Here, the performance of the device

depends on the impact force, which in turn depends on the exact location where it is integrated. For example, the potential difference generated under real snowfall conditions depends on whether the snow-TENG device is attached to the shoulder, wrist or knee area. In these experiments, the electrical outputs from the snow-TENG devices worn on these body parts were obtained in the snowfall mode, where both impact and sliding are responsible for the signal generation. In addition, **Figure 2-6(c)** shows that a snow-TENG device attached to the sole of a shoe and in direct contact with snow can generate signals that could be used to identify various activities performed by the wearer. The results show that the output signal of the snow-TENG can be used to capture the intensity of motion and its type. This is mainly due to the dependence of the shape of the waveform on the type of activity, as illustrated in **Figure 2-6c(ii)**. All the results were measured outdoor, under the following conditions: Temperature of  $-6^{\circ}\text{C}$ , humidity of 60%, wind speed of 15 Km/h and snow particles diameter lower than 1 cm.

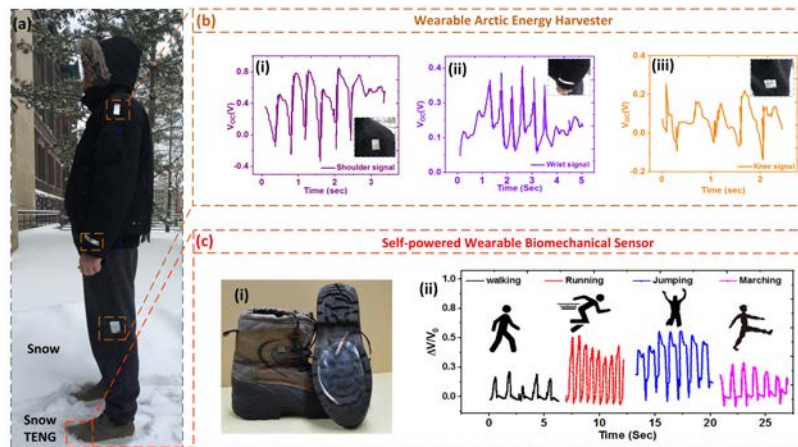


**Figure 2-6** Investigation of snow TENG as a wearable energy harvester and self-powered biomechanical monitor. (a) Harnessing and sensing biomechanical movements by attaching snow TENG to different locations of the human body. (b) Measurement of the electrical output from a snow TENG device that uses a snowfall mode when attached on the (i) shoulder, (ii) wrist, and (iii) knee. (c-i) A photograph of the snow TENG device assembled and attached to the bottom of a snow boot as a self-powered biomechanical sensor. (c-ii) Electrical outputs from the snow TENG as the wearer performs different movements – running, jumping, walking, and marching.

## 2.5 Conclusions

In summary, a new all-printable TENG, based on snow-triboelectrification, is presented with UV curable silicone as the triboelectric material and PEDOT: PSS as electrodes, fabricated using a facile 3D printing method. The developed metal-free snow-TENG has been used as an energy harvesting and multifunctional sensing device for snow-related applications. Upon friction/impact with the snow, the snow-TENG device in a single electrode mode yields output peak-to-peak  $V_{oc}$  and output  $J_{sc}$  of 8 V and  $40 \mu\text{A}/\text{cm}^2$ , respectively. Instantaneous output power density from the snow-TENG achieved  $0.2 \text{ mW}/\text{m}^2$  when connected to a load resistor of  $50 \text{ M}\Omega$ . Unlike traditional weather stations in cold regions, the snow-TENG has a simple design, low cost, and is maintenance-free. This gives the snow-TENG the ability to be used as a self-powered, sensitive snow-related meteorological monitoring station to measure critical weather parameters, such as snowfall rate, snow depth, wind direction, and speed. In addition, the proposed snow-TENG can be utilized as a sustainable power source for wearable electronics and biomechanical tracking sensors to monitor different human movements, such as running, jumping, walking and marching. This opens to the door to a new generation of self-powered wearable devices for tracking athletes and as an effective detector for avoiding hazard in snow-related sports.

## Acknowledgements

This research is partially funded by the Canada Research Chairs Program, Canada First Research Excellence Program through Global Water Futures Program and the Natural Science and Engineering Research Council of Canada through the Strategic Grant Program. The authors thank Dr. Michael A. Brook and Ms. Sijia Zheng for providing us with the inks.

## References

- [1] R. W. Andrews, A. Pollard, and J. M. Pearce, "The effects of snowfall on solar photovoltaic performance," *Solar Energy*, vol. 92, pp. 84-97, 2013/06/01/ 2013.
- [2] N. Dalili, A. Edrissy, and R. Carriveau, "A review of surface engineering issues critical to wind turbine performance," *Renewable and Sustainable Energy Reviews*, vol. 13, no. 2, pp. 428-438, 2009/02/01/ 2009.
- [3] M. Free, B. Sun, and H. L. Yoo, "Comparison between total cloud cover in four reanalysis products and cloud measured by visual observations at US weather stations," *Journal of Climate*, vol. 29, no. 6, pp. 2015-2021, 2016.
- [4] F. Sabatini, "Setting up and Managing Automatic Weather Stations for Remote Sites Monitoring: From Niger to Nepal," in *Renewing Local Planning to Face Climate Change in the Tropics*: Springer, 2017, pp. 21-39.
- [5] (2018, 23 October). <https://nsidc.org/cryosphere/snow/climate.html>.
- [6] O. Buser and A. Aufdermaur, "Electrification by collisions of ice particles on ice or metal targets," in *Electrical processes in atmospheres*: Springer, 1976, pp. 294-301.
- [7] W. Hutchinson, "Ice-crystal contact electrification," *Quarterly Journal of the Royal Meteorological Society*, vol. 86, no. 369, pp. 406-407, 1960.
- [8] V. F. Petrenko and S. C. Colbeck, "Generation of electric fields by ice and snow friction," *Journal of applied physics*, vol. 77, no. 9, pp. 4518-4521, 1995.
- [9] J. Drake, "Electrification accompanying the melting of ice particles," *Quarterly Journal of the Royal Meteorological Society*, vol. 94, no. 400, pp. 176-191, 1968.
- [10] W. Gaskell and A. Illingworth, "Charge transfer accompanying individual collisions between ice particles and its role in thunderstorm electrification," *Quarterly Journal of the Royal Meteorological Society*, vol. 106, no. 450, pp. 841-854, 1980.
- [11] J. Latham, "The electrification of snowstorms and sandstorms," *Quarterly Journal of the Royal Meteorological Society*, vol. 90, no. 383, pp. 91-95, 1964.
- [12] J. Caranti, A. Illingworth, and S. Marsh, "The charging of ice by differences in contact potential," *Journal of Geophysical Research: Atmospheres*, vol. 90, no. D4, pp. 6041-6046, 1985.
- [13] E. Jayaratne and C. Saunders, "Thunderstorm electrification: The effect of cloud droplets," *Journal of Geophysical Research: Atmospheres*, vol. 90, no. D7, pp. 13063-13066, 1985.
- [14] F.-R. Fan, L. Lin, G. Zhu, W. Wu, R. Zhang, and Z. L. Wang, "Transparent triboelectric nanogenerators and self-powered pressure sensors based on micropatterned plastic films," *Nano letters*, vol. 12, no. 6, pp. 3109-3114, 2012.
- [15] X.-S. Zhang *et al.*, "Frequency-multiplication high-output triboelectric nanogenerator for sustainably powering biomedical microsystems," *Nano letters*, vol. 13, no. 3, pp. 1168-1172, 2013.
- [16] L. Zong-Hong, C. Gang, L. Sangmin, P. K. C., and W. Z. Lin, "Harvesting Water Drop Energy by a Sequential Contact-Electrification and Electrostatic-Induction Process," *Advanced Materials*, vol. 26, no. 27, pp. 4690-4696, 2014.
- [17] G. Zhu *et al.*, "Harvesting water wave energy by asymmetric screening of electrostatic charges on a nanostructured hydrophobic thin-film surface," *ACS nano*, vol. 8, no. 6, pp. 6031-6037, 2014.

- [18] Z. H. Lin, G. Cheng, L. Lin, S. Lee, and Z. L. Wang, "Water–Solid Surface Contact Electrification and its Use for Harvesting Liquid-Wave Energy," *Angewandte Chemie*, vol. 125, no. 48, pp. 12777-12781, 2013.
- [19] J. Chen *et al.*, "Networks of triboelectric nanogenerators for harvesting water wave energy: a potential approach toward blue energy," *ACS nano*, vol. 9, no. 3, pp. 3324-3331, 2015.
- [20] T. Jiang, Y. Yao, L. Xu, L. Zhang, T. Xiao, and Z. L. Wang, "Spring-assisted triboelectric nanogenerator for efficiently harvesting water wave energy," *Nano Energy*, vol. 31, pp. 560-567, 2017.
- [21] A. Ahmed *et al.*, "Self-powered wireless sensor node enabled by a duck-shaped triboelectric nanogenerator for harvesting water wave energy," *Advanced Energy Materials*, vol. 7, no. 7, p. 1601705, 2017.
- [22] A. Ahmed, I. Hassan, M. Hedaya, T. A. El-Yazid, J. Zu, and Z. L. Wang, "Farms of triboelectric nanogenerators for harvesting wind energy: A potential approach towards green energy," *Nano Energy*, vol. 36, pp. 21-29, 2017.
- [23] A. Ahmed *et al.*, "Environmental life cycle assessment and techno-economic analysis of triboelectric nanogenerators," *Energy & Environmental Science*, vol. 10, no. 3, pp. 653-671, 2017.
- [24] A. Ahmed *et al.*, "Self-adaptive Bioinspired Hummingbird-wing Stimulated Triboelectric Nanogenerators," *Scientific reports*, vol. 7, no. 1, p. 17143, 2017.
- [25] A. Ahmed *et al.*, "A washable, stretchable, and self-powered human-machine interfacing Triboelectric nanogenerator for wireless communications and soft robotics pressure sensor arrays," *Extreme Mechanics Letters*, vol. 13, pp. 25-35, 2017.
- [26] F.-R. Fan, Z.-Q. Tian, and Z. L. Wang, "Flexible triboelectric generator," *Nano energy*, vol. 1, no. 2, pp. 328-334, 2012.
- [27] A. Ahmed, I. Hassan, and J. Zu, "Design Guidelines of Stretchable Pressure Sensors-Based Triboelectrification," *Advanced Engineering Materials*, p. 1700997, 2018.
- [28] F. Yi *et al.*, "A highly shape-adaptive, stretchable design based on conductive liquid for energy harvesting and self-powered biomechanical monitoring," *Science advances*, vol. 2, no. 6, p. e1501624, 2016.
- [29] Q. Zhang *et al.*, "Service behavior of multifunctional triboelectric nanogenerators," *Advanced Materials*, vol. 29, no. 17, 2017.
- [30] Q. Zhang *et al.*, "Electromagnetic shielding hybrid nanogenerator for health monitoring and protection," *Advanced Functional Materials*, vol. 28, no. 1, p. 1703801, 2018.
- [31] G. Romain, C. Jean-Jacques, J. Thomas, and D. Ghislain, "Harvesting raindrop energy: experimental study," *Smart Materials and Structures*, vol. 17, no. 1, p. 015039, 2008.
- [32] G. W. Taylor, J. R. Burns, S. A. Kammann, W. B. Powers, and T. R. Welsh, "The Energy Harvesting Eel: a small subsurface ocean/river power generator," *IEEE Journal of Oceanic Engineering*, vol. 26, no. 4, pp. 539-547, 2001.
- [33] L. Zong-Hong, C. Gang, L. Long, L. Sangmin, and W. Z. Lin, "Water–Solid Surface Contact Electrification and its Use for Harvesting Liquid-Wave Energy," *Angewandte Chemie*, vol. 125, no. 48, pp. 12777-12781, 2013.
- [34] Q. Liang *et al.*, "Highly transparent triboelectric nanogenerator for harvesting water-related energy reinforced by antireflection coating," *Scientific reports*, vol. 5, p. 9080, 2015.
- [35] X. Jiaqing, L. Meng-Fang, W. Jiangxin, G. S. Long, P. Kaushik, and L. P. See, "Wearable All-Fabric-Based Triboelectric Generator for Water Energy Harvesting," *Advanced Energy Materials*, vol. 7, no. 21, p. 1701243, 2017.

- [36] Q. Zhang *et al.*, "An Amphiphobic Hydraulic Triboelectric Nanogenerator for a Self-Cleaning and Self-Charging Power System," *Advanced Functional Materials*, vol. 28, no. 35, p. 1803117, 2018.
- [37] F. Marsland, K. Lyons, J. Anson, G. Waddington, C. Macintosh, and D. Chapman, "Identification of cross-country skiing movement patterns using micro-sensors," *Sensors*, vol. 12, no. 4, pp. 5047-5066, 2012.
- [38] R. Chambers, T. J. Gabbett, M. H. Cole, and A. Beard, "The use of wearable microsensors to quantify sport-specific movements," *Sports medicine*, vol. 45, no. 7, pp. 1065-1081, 2015.
- [39] Y. Zhu *et al.*, "A flexible and biocompatible triboelectric nanogenerator with tunable internal resistance for powering wearable devices," *Scientific reports*, vol. 6, p. 22233, 2016.
- [40] S. Wang, L. Lin, and Z. L. Wang, "Nanoscale triboelectric-effect-enabled energy conversion for sustainably powering portable electronics," *Nano letters*, vol. 12, no. 12, pp. 6339-6346, 2012.
- [41] L. Dhakar, P. Pitchappa, F. E. H. Tay, and C. Lee, "An intelligent skin based self-powered finger motion sensor integrated with triboelectric nanogenerator," *Nano Energy*, vol. 19, pp. 532-540, 2016.
- [42] M. Reyes-Reyes, I. Cruz-Cruz, and R. López-Sandoval, "Enhancement of the Electrical Conductivity in PEDOT:PSS Films by the Addition of Dimethyl Sulfate," *The Journal of Physical Chemistry C*, vol. 114, no. 47, pp. 20220-20224, 2010/12/02 2010.
- [43] Z. L. Wang, "Triboelectric nanogenerators as new energy technology for self-powered systems and as active mechanical and chemical sensors," *ACS nano*, vol. 7, no. 11, pp. 9533-9557, 2013.
- [44] F. R. Fan *et al.*, "Highly transparent and flexible triboelectric nanogenerators: performance improvements and fundamental mechanisms," *Journal of Materials Chemistry A*, vol. 2, no. 33, pp. 13219-13225, 2014.
- [45] J. H. Kim, B. K. Yun, J. H. Jung, and J. Y. Park, "Enhanced triboelectrification of the polydimethylsiloxane surface by ultraviolet irradiation," *Applied Physics Letters*, vol. 108, no. 13, p. 133901, 2016.
- [46] M. J. Kreder, J. Alvarenga, P. Kim, and J. Aizenberg, "Design of anti-icing surfaces: smooth, textured or slippery?," *Nature Reviews Materials*, vol. 1, no. 1, p. 15003, 2016.
- [47] T. Trantidou, Y. Elani, E. Parsons, and O. Ces, "Hydrophilic surface modification of PDMS for droplet microfluidics using a simple, quick, and robust method via PVA deposition," *Microsystems & Nanoengineering*, vol. 3, p. 16091, 2017.

### **3 Chapter 3**

## **A Microfluidic Printhead with Integrated Hybrid Mixing by Sequential Injection for Multimaterial 3D Printing**

#### **Complete Citation:**

I. Hassan and P. R. Selvaganapathy, " A Microfluidic Printhead with Integrated Hybrid Mixing by Sequential Injection for Multimaterial 3D Printing," *Additive Manufacturing*, 2021 Dec 16:102559.

#### **Copyright:**

Reproduced with permission from Additive Manufacturing, 2021.

#### **Contribution:**

I. Hassan: Designed and performed all experiments, interpretation and analysis of data, wrote the manuscript draft.

P. R. Selvaganapathy: Supervised I. Hassan and provided guidance, revised and edited the manuscript, was responsible for the manuscript submission.

### 3.1 Abstract

Extrusion-based 3D printing is often performed using a single ink or switching between two or more inks. The ability to create compositional variation in-situ by rapid mixing of two different inks inside the printhead with dynamically changing ratios can produce a broad palette of material composition that is useful in making functionally graded materials for applications in soft robotics or integrated sensors. However, rapid mixing of high viscosity polymer inks in low Reynolds number flows has been a challenge. Here, we demonstrate a multimaterial microfluidic printhead mixer (MM-PHM) that is capable of mixing dynamically controllable ratios of different silicone inks to print graded materials. The MM-PHM uses a pulsatile injection of multiple inks pneumatically inside a mixing junction combined with a free-floating static mixer to produce various compositions from up to four different base inks. The performance of the MM-PHM when dissimilar inks are used has been assessed using both experimental and computational (fluids dynamics) methods. To illustrate the versatility of this method, a 2D colored gradient map, and 3D Rubix cube have been fabricated using four-color inks to produce nine different material combinations. This scalable method expands the palette of multimaterial 3D printing materials that can be fabricated and constructed in complex shapes and varying properties.

**Keywords:** Multimaterial 3D-printing, Silicone elastomer, graded materials, and microfluidic mixing

### 3.2 Introduction

3D extrusion printing is becoming a mainstream manufacturing method, and the technology is evolving to accommodate multiple materials and compositions.[1-3] One approach to increasing the palette of compositions that can be printed would be to

incorporate a mixer in the print head that can dynamically combine multiple inks in various ratios. However, mixing, especially at a low Reynolds number, is still a significant challenge [4-8]. Nevertheless, dynamically changeable ink compositions are essential in producing functionally graded materials and structures for various applications including, but not limited to, robotics with soft or partly soft forms, integrated sensors, electronics, and multimaterial gradient interfaces with complex shapes, that are believed as safer and more adaptable for human interaction[9-17]. Among the different additive manufacturing methods, Direct Ink Writing (DIW), based on extrusion to deposit complex "inks" in a layer-by-layer manner, is well suited for multi-material printing. This is due to its ability to produce subtle composition gradations, utilizing more than one ink, and at a relatively low cost [1, 2, 18-26]. One approach that has been taken is to switch between two ink channels that connect to the extrusion channel in a passive printhead by using computer control of positive displacement pumps to force a particular ink without mixing through the extrusion nozzle [6]. This approach cannot produce a broad palette of inks combinations and is limited to ~1 Hz switching frequency due to thread backlash from the positive displacement pumps. However, using a pneumatic system for controlling different inks was able to reach high-frequency switching (~50 Hz).[27] Alternatively, various types of mixer printheads, with active mixing based on externally powered rotational impeller [7, 28-30], have been developed to exploit the advantage of decoupling mixing efficiency from the mixer size and the flow rate. Nevertheless, such externally powered active mixers are more complex and bulkier due to the rotational element volume and the connection to the external power source. More straightforward static mixers have been incorporated to mix up to two different inks [8, 18, 31-34], but their mixing efficiency is intimately tied to

size and flow rate. They also require a large priming volume for complete mixing and more complex geometries that are difficult to manufacture and maintain. They have high mixing times ( $> 6$  sec) and are not scalable beyond three inks.[35, 36] An ideal multimaterial print head should have a small form factor, rapid mixing of inks, scalable to accommodate a large number of inks, fast switching between compositions, ability to handle a range of viscosities of the inks, and independent control of mixing efficiency from flow rate.

Here, we demonstrate a multimaterial microfluidic printhead mixer (MM-PHM) that has several of these properties. It enables real-time, fast switching with the ability to mix a wide range of compositions on the fly. The approach is highly scalable to many inks, and up to four inks producing 9 nine different compositions has been demonstrated. The mixer printhead incorporates a unique combination of a floating mixing element combined with pneumatic control of ink injection into the mixer to produce a hybrid combination that can dynamically change compositions near instantaneously, mix rapidly, produce continuous or discrete variations in compositions with high switching frequency, and low latency due to its small priming volume. Most importantly, the MM-PHM device can be easily disassembled to maintain clean and quickly reassembled. Using this approach, we show that the MM-PHM is able to reach a high degree of mixing up to 99% with a low mixing time ( $\leq 4$  sec) which controlled the time to switch between compositions. The effect of process parameters such as pulse frequency, duty cycle, inlet pressure, and phase difference on mixing was investigated using a computational model and validated through experiments. Previously, switching of inks has been demonstrated, but they are limited in the different compositions that can be printed. Our advance expands the application of extrusion 3D printing to produce inks of any composition dynamically using software

control directly at the printed and therefore enables printed of compositionally varied parts that were not possible before.[27] To demonstrate the scalability of this approach, four inks were used to produce nine compositional combinations dynamically, in real-time to print various features such as 2D colored gradient map and 3D Rubix cube using multiple UV curable silicone elastomer inks. By enabling real-time, in-situ mixing in the printhead in a scalable manner, this approach vastly expands the palette of properties that can be embedded into 3D printed objects.

### 3.3 Experimental details and methods

#### 3.3.1 Materials

UV curable Silicone inks with different combinations have been used, as mentioned in **Table 3-1**. Functional silicones: vinylsilicones: vinyl terminated polydimethylsiloxane, DMS-V31, and DMS-V35 with molecular weights of 3853, 21500, 42300 g.mol<sup>-1</sup>, respectively and [13-17% (mercaptopropyl)methylsiloxane] – dimethylsiloxane copolymer (SMS-142) were purchased from Gelest, Inc, US. Photoinitiator TPO-L 6 was gotten as a gift from IGM Resins, Inc. Red, blue, yellow, and green silicone pigments were acquired from Smooth-On. Aerosil-150 was bought from Evonik Industries.

In the current study, photoinitiated polymerization was chosen due to its fast reaction time, ideal for low viscosity inks. Two PDMS inks (**Table 3-1**) were prepared using a combination of different reagents. Pendent thiopropylsilicones behaved as crosslinkers, while telechelic vinyl-substituted silicones were picked as the base polymers.[37] The silicone elastomers' young's modulus can be tuned by controlling the chemical crosslink density and fillers (typically silica). As for initiation, the curing process under UV light irradiation (in our work wavelength was 365 nm), a type- one photoinitiator

TPO-L [37] was used within the formulation (**Table 3-1**). Moreover, the rheological behavior of the used UV curable inks under steady shear after using a rotational rheometer was assessed. Inks V31 and V35 showed a Newtonian response with a constant viscosity of 1.6 and 5 Pa.s.

### **3.3.2 Fabrication of MM-PHM Devices**

The MM-PHM devices were designed using CAD software (SolidWorks, Dassault Systèmes, Inc). The CAD files were converted to STL (Stereolithography) files, and 3D printed using ProJet 2500 Plus 3D printer set to the XHD (Xtreme High Definition) printing configuration with high resolution, up to 1600 x 900 x 790 DPI.[38] The MM-PHM devices were printed at 20–28 °C using a transparent VisiJet M3 Crystal resin (for visualization of the internal channel) along with a VisiJet S300 support wax material. While in the case of actual printing, a VisiJet SL impact "opaque, white" has been used to prevent clogging from occurring inside the channels. Following printing, post-processing involves warming the part in an oven to ~60 °C and holding the devices there to melt off the majority of the wax support, and then running it in a heated ultrasonic bath filled with special support cleaning fluid to clean the channels. Add to that, wax from the internal microstructures was cleaned by 30 min perfusion of corn oil (heated to ~70°C). We can repeat these processes and/or try running them at higher temperatures and/or longer times if there is leftover support material in the channels. The only caveat is that this could cause some amount of warpage to the part. We use the settings that we do to try and keep deformations during post-processing to a minimum. After that, the MM-PHM devices were submerged in soap and sonicated water "DI water" for 20 min to remove any wax or oil inside the microchannels.

In addition, a metal needle (25 gauge) was attached at the end of the outlet, which prevented any inadvertent polymerization of the extruding ink at the mixer due to the reflection of the illuminating UV light from the print-bed. In addition, the MM-PHM was designed to be disassembled and cleaned in case the ink mixtures polymerized and cured inside the print head. To eliminate leakage, two O-rings have been used to ensure that no leakage will happen with eight bolts. The size and number of bolts were calculated to secure the connection, guaranteeing no ink leakage. As for the barrel connection with the printhead, the ink barrels are attached to the printhead, using a heating insert with internal thread (M5). Firstly, the brass insert should be heated to  $\sim 60$  °C, then pressed inside the printhead. After that, a structural adhesive Epoxy (Loctite® M-121hp, 1.69 oz, McMaster-Carr) was added around the insert and left for one day to be cured to secure the connection. Finally, the check valve (Female Luer Lock Inlet, Male Luer Lock Outlet, Qosina) was attached above the threaded insert using a threaded/male Luer lock connection.

Afterward, we tested the chemical compatibility of the printhead material with the printing ink using ASTM D543 “Evaluating the Resistance of Plastics to Chemical Reagents.”[39] In this test, plastic materials are evaluated for their durability against chemical reagents based on simulations of potential environments in which they may be used. As a chemical reagent, lubricants, cleaning agents, inks, foods, or whatever may be encountered by the test material can be used. Tests are conducted to measure weight, dimensions, appearance, and strength. Weigh and measure the printhead before it contacts the chemical reagent. Immersion testing was used to test the ink exposure. The printheads are then sealed in a container for five days at room temperature in a dark environment. After an agreed-upon period, we remove and evaluate the printhead to determine whether

it has changed in weight or appearance. According to the results, the printhead was not damaged by the printing ink, and after proper cleaning, it was used to print.

### 3.3.3 Experimental Setup

The available test setup is shown in **Figure 3-1**. A motion control platform based on a commercially available UNI-PRINT-3D FDM 3D printer purchased from 'The Cool 'Tool' GmbH company. An opaque syringe barrels 10 ml and 50 ml (Model Optimum by Nordson EFD) pressurized to  $340\pm 30$  kPa, which feeds the printhead cavities with silicone material while preventing the introduction of air bubbles into the silicone. An external air pressure supply can provide air pressure up to 100 psi. The pressure supply was attached through a filter to three control channels, each containing a regulator and solenoid 3-way pneumatic valve (S15MM-30-12-3B, Pneumadyne, Inc), which can link each ink barrel to a preselected pressure (by the regulator) or atmosphere. The control system can individually regulate each solenoid valve. For curing purposes, the UV source that could initiate the reaction should be a strong UV source such as a metal halide lamp, which produces a broader spectrum UV, with peaks distribution typically between 300nm-400nm (varies by lamp design and filtering). An 'S1000 'Omniure' curing system from 'Lumen Dynamics' (elaborated in printer design) which provides a broad spectrum UV of up to 100W with two light guides or four light guides (**Figure 3-1**) which produce a narrow cone of  $\sim 30^\circ$  was used as the light source. In addition, Frontend control was provided by the 'MachineFace' networked GUI interface for the machine kit developed by 'The Cool Tool'<sup>TM</sup> to enable synchronous control of the XYZ positioner, the solenoid valves, and the UV lamp. The solenoid valves were controlled through a driver, which was synchronized over an i2c communication bus. The interaction between the control system and the

solenoids is faster than ~50 Hz, which is the mechanical response time of the solenoid valves. Once an ink barrel gets pressurized through its control channel, the pressure on the ink starts pushing it down into the channel. Then, the pressure difference opens the check valve (there is a minimum opening pressure head of the check valve below 5 Psi) and enables the flow of that ink into the junction. The pressure rise in the junction then seals the other check valves, preventing any backflow, and forces the ink to flow through the extrusion needle. The extruded ink is then deposited onto the print surface.

The movement of the printer (XYZ) was synchronized with the valve control and the switch controlling the on/off state of the lamp through a central G-code machine interface controller. Therefore, the sequence of inks flowing through the nozzle and its spatial deposition can be synchronized. Also, when it is required to stop the flow of the ink, it can be instantaneously stopped, and simultaneously the UV light is switched off so that there is no unwanted crosslinking at the tip.

### **3.3.4 Rheological Measurements**

The ink viscosity was evaluated using a rotational rheometer (AR2000, TA Instruments). A 40 mm, 2° cone and plate geometry is used for shear rate up to 1 S-1.[40] At values larger than shear rate 1 S-1 up to 100 S-1, we used the Cox-Merz transformation. The Cox-Merz transformation was utilized using the TRIOS pc-program by TA instruments using oscillation frequency data to obtain viscosity at a higher shear rate. It was noticed that an overlap between the frequency sweep and the Cox-Merz rule. The shear rate range is 0.1 to 0.6 S-1, which was validated using the Cox-Merz method.[41]

### **3.3.5 Numerical model Governing Equations**

The computational model used in this proposal to simulate the Y-junction micromixer is shown in **Figure 3-3**. The convergence of the flow begins at the intersection point of the inlets; then, the mixing fluid goes in a narrow channel. To determine mixing efficiency, the component concentration at the printhead outlet will be observed. The velocity, pressure, and concentration components will be numerically investigated relying on the continuous and Navier-Stokes (N-S) equations to solve incompressible fluid flow as follows:[42, 43]

$$\text{Continuity equation} \quad \nabla \cdot U = 0 \quad (1)$$

$$\text{Momentum equation} \quad \frac{\partial \rho U}{\partial t} + \rho U \cdot \nabla U = -\Delta p + \mu \nabla^2 U + \nabla \cdot \tau_p \quad (2)$$

where  $U$  represents the flow velocity vector;  $p$  is the pressure;  $\rho$  is the density,  $\mu$  is the dynamic viscosity of the fluid and  $\tau_p$  is the elastic stress (in case of Newtonian fluid put as zero).

For  $d_i \ll L$ ,  $|\frac{\partial^2 v_x}{\partial x^2}|/|\frac{\partial^2 v_x}{\partial y^2}| \sim (d_i/L)^2$  and the momentum equation in the flow, in dimensionless form, is approximated as

$$StRe \frac{\partial v_x}{\partial t} = -\frac{\partial p}{\partial x} + \frac{\partial^2 v_x}{\partial y^2} + \gamma^2 \frac{\partial^2 v_x}{\partial z^2} \quad (3)$$

where  $\gamma = \frac{d_i}{d_m}$ ,  $St = \frac{f d_i}{U}$  is the Strouhal number and  $Re = \frac{U l}{\nu}$  is the Reynolds number;  $\nu = \eta/\rho$  is the kinematic viscosity.

As for the mass transfer equation, it can be expressed in non dimensionless form as follows:

$$St \frac{\partial c}{\partial t} + \theta v_x \frac{\partial c}{\partial x} = \frac{1}{Pe} \left( \frac{\partial^2 c}{\partial y^2} + \gamma^2 \frac{\partial^2 c}{\partial z^2} \right) \quad (4)$$

where  $c$  is the species concentration,  $\theta = d_i/L$ , and Peclet number  $Pe = Ud_i/D$  may be expressed as the product of Reynolds and Schmidt number  $Pe = Sc \cdot Re$ , with  $Sc = \nu/D$ . Moreover, to determine the field concentration in the flow, the convection-diffusion equation can be used (Eq.4):[42-44]

$$\frac{\partial C}{\partial t} + U \cdot \nabla C = D \nabla^2 C \quad (5)$$

Where  $C$  is the element concentration of the ink and  $D$  is the fluid diffusion coefficient.

### 3.4 Results and Discussion

#### 3.4.1 Printer Design

A custom-built 3D printer system, as shown in **Figure 3-1**, was designed to dispense and print UV curable silicone inks after in-situ mixing between them (**Table 3-1, see experimental section for more details**). The ultraviolet-aided direct writing (UV-DW) system consists of an XYZ positioner stage, a syringe barrel holding the uncured ink, assembled with a multi-material microfluidic printhead mixer (MM-PHM) extrusion nozzle having a defined circular cross-section. In addition, the system includes a pneumatic control system and integrated computer control to synchronize the printhead motion with the pneumatic system, as shown in **Figure 3-1**(**See experimental section for more details**). The pneumatic system allows the switching between different inks at high frequency and reduced latency compared with a positive pressure pump-driven system. The extruded ink filament was exposed to UV illumination by four optical fiber bundles positioned in a circular pattern around the printhead nozzle. The UV light was directed to a position just below the tip of the nozzle so that the polymerization process induced by the exposure does not adversely affect the flow through it. The UV illumination system

was mounted with the MM-PHM so that curing of the deposited ink occurs in the same manner irrespective of the 3D position of the print head (see **Figure 3-1-i**). The in-situ cure chemistry is rapid and allows sufficient structural rigidity to deposit further material on top and build a multilayer structure (see *Appendix 1 Figures 7-1:3*). To concurrently print and mix multiple thermoset inks through a single nozzle, we custom-engineered an MM-PHM illustrated schematically in **Figure 3-1-ii**. Briefly, four opposed pneumatic solenoid valves alternately drive and control the ink pressure and injection through input channels (with diameter " $d_i$ ") that are located around the central nozzle. The injected inks are mixed in the mixing chamber and pushed through the end to the extrusion nozzle (with diameter " $d_o$ "). Pressure on the ink chamber was applied through pneumatic lines that connected a pressure source to the ink chambers and mediated using the solenoid valves (**Figure 3-1**). During printing, the tool path is deconstructed so that nozzle was moved only in the z-direction, while the substrate was moved using a 2-axis, motion-positioning stage. The flow rate of the current system ranged from 100  $\mu\text{l/s}$  to 500  $\mu\text{l/s}$ . Additionally, the printing speed used in the applications was 10 mm/s.

**Table 3-1** UV curable silicone inks formulations used in this work given in weight percentage

<b>Inks</b>	<b>Vinyl Terminated PDMS</b> MW "g/mol" (wt %)	<b>SMS-142</b> MW "g/mol" (wt%)	<b>Photoinitiator TPO-L</b> wt (%)	<b>Silicone pigment</b> wt%	<b>Viscosity Pa.s</b>
<b>V31H</b>	21500 (90)	578 (7)	1	2	1.6
<b>V35H</b>	42300 (93)	578 (4)	1	2	5

a: Stoichiometry (vinyl/SMS-142) =1:1.4TPO-L 10 mol% (164 mg)

b: UV radiation supply: Black-Ray B-100SP, 365nm UV, 1.27 W/cm<sup>2</sup>.

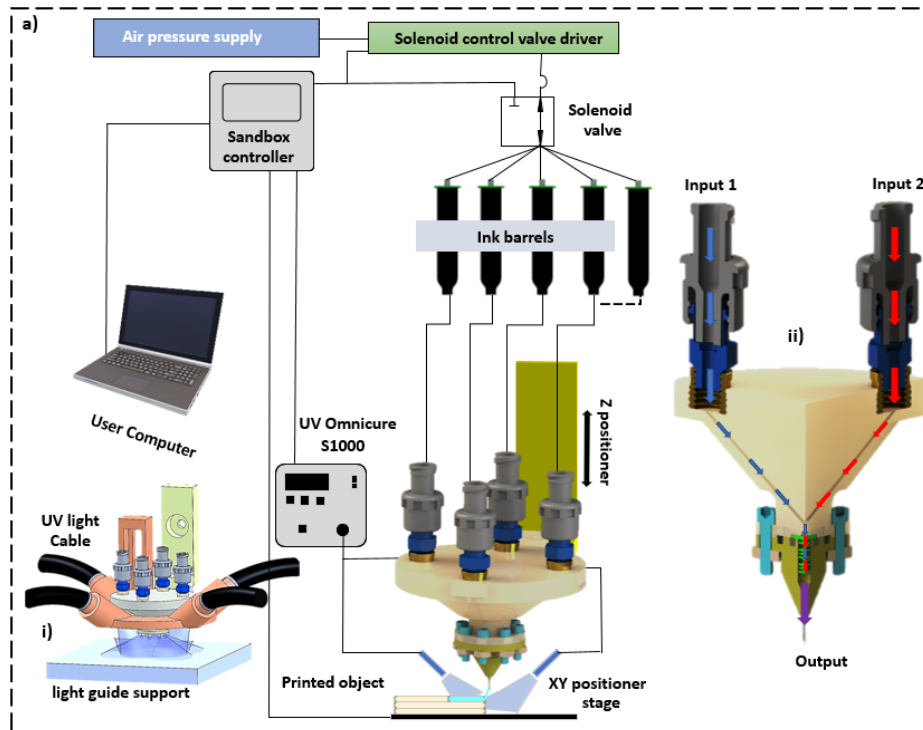


**Figure 3-1** Direct ink writing 3d printing platform. A schematic diagram of the customized printhead mixer is attached to the ink barrels connected to pressure regulators. **i)** Schematic description of the UV-aided mixing printhead. The UV-curable silicone is deposited through a micronozzle and exposed to UV radiation using a set of optical fibers synchronized with the extrusion printhead mixer. The rapid curing lets the production of a 3D-shaped structure along the path of the UV-direct writing mixing tool. **ii)** A CAD model of the microfluidics printhead mixer consisting of the four independently actuated pneumatic flow circuits controlled the inlet pressure of each material through a metal needle 25 gauge and heat threaded inserts/ check valves on the top. Red and blue arrows are UV curable silicone liquids fed into the microfluidic printhead mixer from the pneumatic barrel syringes and exited from the output.

### 3.4.2 Active Mixing MM-PHM for Multimaterial 3D Printing

Highly viscous inks are typically used in 3D extrusion printing to preserve the shape of the extruded filament as it is printed and maintain the structure's integrity. High viscosity inks are challenging to mix due to low Reynolds number and the laminar flow regime they are operating in, where diffusion is the only mechanism of mixing. In low Reynolds number ( $Re$ ) regime, the inertial forces play only a minimal role in the flow dynamics while viscous and capillary forces are more dominant. The entrance length in this regime is fairly small (*Appendix 1 Figure 7-1c*), and the flow is fully developed with no turbulence or secondary

flow. Therefore, adequate mixing can only be achieved by maximizing the interfacial area between the co-flow streams. Another design requirement for multimaterial 3D printing is the minimization of the priming volume of the mixing chamber so that the switching between various ink compositions can be achieved quickly. Passive micromixing using grooved patterns on the walls of the mixing chamber can be used to mix a co-flowing stream of viscous liquids [45, 46], but require the residence time of the fluids ( $t_{res}$ ) to be greater than the mixing time constant ( $t_{mix}$ ). For passive micromixers, this condition leads to the following relationship [29, 45].

$$\frac{t_{res}}{t_{mix}} > 1 \rightarrow \frac{l}{d} \geq \frac{1}{Re} \quad (6)$$

When highly viscous polymers are used, such as in our case, where the Reynolds numbers are  $\sim 10^{-5}$ , it requires an inordinately long length ( $\sim$  several meters) for effective mixing to occur. Such large priming volume of the mixing chamber can produce significant latency in the switching between different ink compositions, which is undesirable. An alternate approach is to introduce plugs of the two different fluids to be mixed into the mixing chamber so that the interface between them is stretched continuously due to the parabolic flow profile in pressure-driven fluid flow.

Our strategy is to use a hybrid approach combining active and passive micromixing elements to develop an integrated micromixer printhead that achieves both highly efficient mixing and minimizes priming volume for fast switchability, as shown in **Figure 3-2a**. The micromixer is capable of operation in two modes. The first mode (mode 1) is a simple pneumatically controlled active mixer where the various inks can be injected into a central mixing chamber using pulsatile pneumatic pressure on the ink sources to inject alternate plugs (see **Figure 3-2a-i**). These injected plugs are stretched laterally using an expanding

section to maximize the interfacial area and then stretched axially due to the parabolic flow profile as they flow down the mixing section. For a given nozzle diameter " $d_o$ ", a low  $l/d$  is desirable to reduce its "dead" volume, in that way permitting rapid switching between different material compositions.

Similarly, a low aspect ratio is necessary to reduce the pressure drop across the mixing chamber for a fixed mixer chamber volume. In addition, the frequency of the disturbance (pulses) is an independent variable that can be used to control the degree of mixing. The Strouhal number " $St$ " represents the ratio of the unsteadiness inertial force due to the disturbance of the flow to the inertia of the flow field due to changes in velocity in an active micromixer ( $fd/U$ ), where  $f$  is the pulse frequency[47, 48]. In this mode, three different mixing chamber diameters (DI, DII, DIII) with the corresponding volume of 10, 22, 45  $\mu\text{L}$  were considered based on the required mixing time and the desired mixing performance (see **Figure 3-2a-i**). In addition, a hybrid mixing approach (see **Figure 3-2a-ii**) where a floating static mixer element was inserted into the mixing chamber to provide passive mixing was combined with the active mixing (mode 2) using pneumatic pulses in order to introduce secondary flows and further decrease the priming volume while providing high efficiency of mixing and reduce the mixing time.

The multi-material microfluidic printhead mixer (MM-PHM) comprises three major components: an inlet manifold, a mixing chamber, and an outlet nozzle, as shown in **Figure 3-2b**. The printhead was 3D printed using the ProJet 2500 Plus 3D printer set to the XHD (Xtreme High Definition) with white VisiJet M3-X (MJP) for actual printing and clear VisiJet Armor (M2G-CL) (MJP) for visualization designed for easy disassembly and cleaning, which is important for long term operation. The inlet manifold was designed to

accommodate four ink inputs that merge into an expanding conical section. The expanding section allows the plugs of ink injected to expand laterally and increase its contact area with the next incoming plug. The mixing chamber is cylindrical with varying diameters and contains an insert in the form of a central static micromixer element that contains the grooves to introduce chaotic advective flow (**Figure 3-2b-i**). The central micromixer element can be easily removed and replaced, while the cylindrical mixing chamber can be easily cleaned. Finally, a metal microneedle inserted at the downstream end of the mixing chamber and positioned flush to the end served as the printhead nozzle. The flow geometry was constructed without sharp edges or dead zones for cleanability, easy maintenance, and reducing pressure drop inside the inlet channels. A CAD model was also created to simulate the mixing process, as shown in **Figure 3-2b-ii**. Images of the 3D printed MM-PHM are shown in **Figure 3-2c**. As shown in **Figure 3-2c-i**, the nozzle tip had an inner diameter of 230  $\mu\text{m}$  (25 Gauge) and a priming volume of 0.166  $\mu\text{L}$ . The static mixer, shown in **Figure 3-2c-ii**, had a cross shape element at its base in order to snugly fit onto the mixing chamber (**Figure 3-2c-iii**) in an aligned manner. The priming volume of the MM-PHM after the insertion of the static mixing element was 15  $\mu\text{L}$  without the static mixer. The assembled mixing chamber with the static mixing element is shown in **Figure 3-2c-iv**.

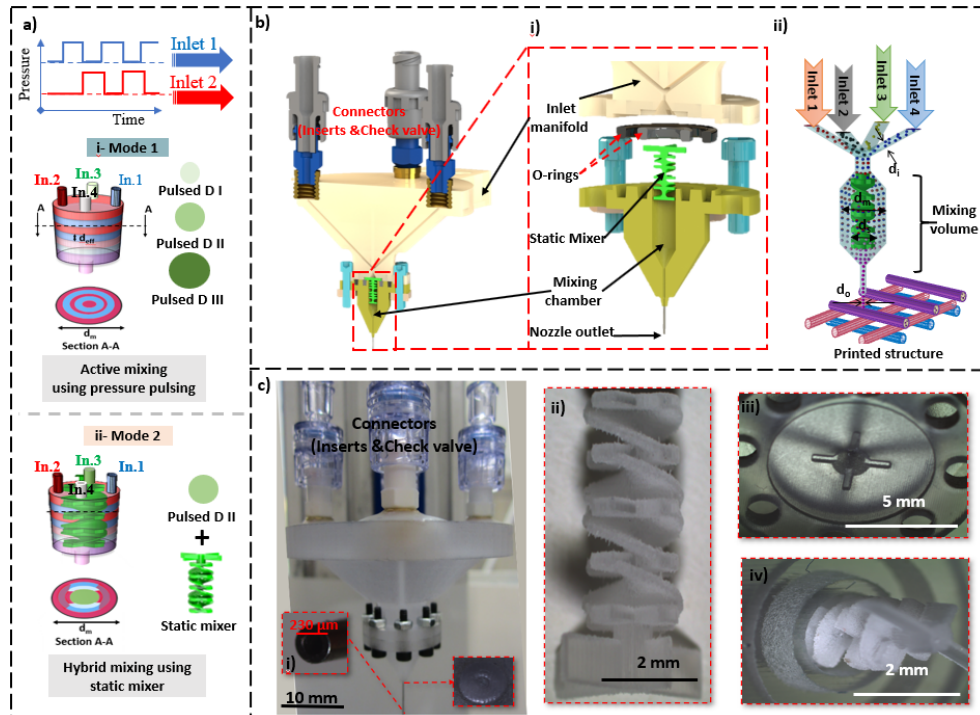


**Figure 3-2** MM-PHM configurations. **a)** Two modes have been used for mixing **i-** active mixing mode using pressure segmentation with three different configurations, **ii-** hybrid mixing routine using static mixer along with pressure segmentation pulses. **b)** Schematic illustration of the section views of the MM-PHM nozzle, **i-** The exploded 3D model of the MM-PHM, **ii-** Schematic illustration of the Fluid volume in operation for 3D printing of four inks with different particles color. Each ink enters the mixing chamber of diameter  $d_i$  through a separate inlet and is homogenized in a mixing chamber of width  $d_m$  by a static mixer of diameter  $d_s$  with outlet diameter of  $d_o$ . **c)** Optical image of the MM-PHM, **i-** outlet needle diameter, **ii-** an actual image of the static mixer, **iii-** end of inlet chamber body, **iv-** the top of mixing chamber body.

### 3.4.3 Simulation of The Mixing Process

A computational model was developed to simulate the fluid dynamics of the pulsatile flow and the mixing process. Unsteady Navier–Stokes, species transport equations for laminar flows in three-dimensional coordinates were solved using FLOW-3D (see **Experimental method section-Numerical model Governing Equations**). Such a simulation allowed visualization of the mixing process inside the micromixer and could be used to determine operating parameters for optimized and efficient mixing in the printhead for fluids of various viscosity. The input pressure into the individual ink channels was modeled as a

square wave as shown in **Figure 3-3a** and represented mathematically as pulsatile pressure input of the form

$$P_1(t) = \frac{A}{2} + \frac{2A}{\pi} \sum_{n=1}^{\infty} \left\{ \frac{1}{2n-1} \right\} \sin (2\pi(2n-1)ft) \quad (7)$$

$$P_2(t) = \frac{A}{2} + \frac{2A}{\pi} \sum_{n=1}^{\infty} \left\{ \frac{1}{2n-1} \right\} \sin ((2\pi(2n-1)ft) + \Phi)$$

Where A is the pulse amplitude,  $f$  is the signal frequency, T is the cycle period,  $\Phi$  is the phase shift between the signals, and  $D_c$  is the duty cycle defined as the active pulse time over the total cycle period. By changing these parameters and calculating the mixing efficiency at the outlet nozzle, optimal conditions for efficient mixing can be determined. This study was conducted using a simplified two-channel input configuration as shown in **Figure 3-3b**, where  $l$  is the mixing channel length,  $d_m$  is the mixing channel diameter. The length of inlet channels ( $l_i$ ) was set as 2 mm, and the angle at which they converge ( $\alpha$ ) was set as  $108^\circ$  to correspond to dimensions in the actual printhead as they were found suitable to minimize priming volume will also produce smooth corners and edges prevent ink accumulation and stagnation. The flow was considered laminar, Newtonian, and the fluid as incompressible with a viscosity around 1.6 Pa.s. The flow simulation also extended beyond the extrusion nozzle, and the flow onto the print substrate was also simulated. For this purpose, the surface tension measurement using the pendant drop method was used as an input into the simulation.

The boundary conditions used in the simulations are shown in **Figure 3-3c-i** for both the input into the print head as well as the output from the print nozzle and the moving print substrate, which was set as 100 mm/sec in the x-direction. The pulsatile input injects an alternative plug of different inks into the central mixing chamber, and the effect of the

frequency of the pulsatile input and their offset on the flow disturbances introduced as well as on the mixing index was evaluated. In addition, these conditions were also experimentally determined using the printhead configuration whose schematic is shown in **Figure 3-3c-ii** to validate the model using V31 ink (see **Table 3-1**) doped with different colors.

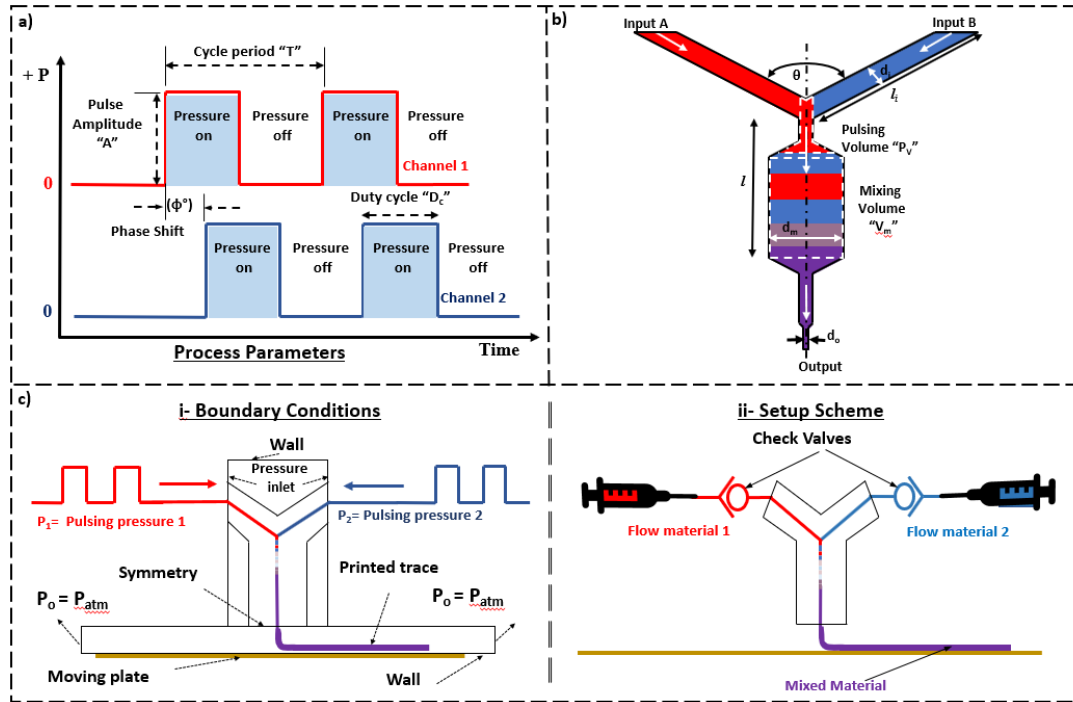


**Figure 3-3** Operating scheme of the multi-material mixer printhead in case of simulation and experimental process. **a)** An illustration depicting the process parameters of the inlet pressure pulses, including cycle period, pulse amplitude, phase shift, and duty cycle. **b)** Principle of MM-PHM operation. Inks A and B enter the MM-PHM and are combined within the mixer (volume  $\approx 10\text{-}45\ \mu\text{L}$ ). The pneumatic pressure signal applied to the ink input inlets (input A, B) determines the volume of plugs injected ( $P_v$ ) and its sequence. The length of this pulsing volume region was determined by the pulsing frequency of the inlet pressure signal. Expanding the diameter of the mixer volume chamber further enhanced the mixing. **c)** The simulation setup and boundary conditions applied for simulating flow through the printhead geometry to optimize the mixing process. **i)** The computational model of the multi-material mixer printhead consists of two central regions; the first is the channel structure with pressure inlet regime, and the second is the printing trace block along with the boundary conditions for both regions. **ii)** A schematic illustration for the experimental scheme for mixing using the pulsing technique.

### 3.4.4 Optimization of Mixing in the Printhead

In order to optimize the mixing within the print head, the mixing index was obtained numerically and experimentally at various Strouhal numbers. Specifically, tracers were introduced in the simulation model, and their concentration at each location along the printhead was used to determine the mixing of the fluid. Both flow velocity and mass fraction of each channel were assessed in each simulation cell over time. The degree of mixing (represented by the mixing index) at the outlet was calculated by taking the standard deviation of the concentration at all meshed points in outlet cross-section, which is represented mathematically by the following equation:[42, 43]

$$M\% = \left(1 - \frac{\sqrt{\sum_{i=1}^N \frac{(c_i - c_c)^2 V_i}{N V_{mean}}}}{c_c}\right) \times 100 \quad (8)$$

Where N is the number of meshed points in the cross-section,  $c_i$  is the concentration at the point I,  $c_c$  is the complete mixing concentration (0.5),  $V_i$  is the velocity at the mesh point, and  $V_{mean}$  is the average velocity in outlet cross-section. Therefore,  $M = 100\%$  indicates full mixing, while  $M = 0\%$  when no mixing occurs. The mixing index was also determined experimentally from the images of the traces obtained from the printed lines using the same input parameters as in the simulations. ImageJ software was used to generate normalized concentration profiles of the printed line, and the standard deviation of the concentration profile at each pixel of the line from that of the completely mixed situation was evaluated using the equation below[49, 50].

$$M\% = \left(1 - \frac{\sqrt{\frac{1}{N} \sum_{i=1}^N (R - \bar{R})^2}}{\sqrt{\frac{1}{N} \sum_{i=1}^N (R_i^o - \bar{R})^2}}\right) \times 100 \quad (9)$$

Where  $N$  is the total number of examined points at the printed line, and  $R_i$  is the local intensity at each location,  $R_i^o$  is the intensity of non-mixing fluid for the same number of examined points (by measuring RGB intensity of the first color based on the tracking ink), and  $\bar{R}$  is the intensity of a completely mixed case.

Simulations were carried out for various pulsation frequencies (from 1 Hz to 20 Hz) to compare them with experimental results performed at the same operating conditions, which were represented by the non-dimensional Strouhal ( $St$ ) number in order to both validate the simulation as well as study the effect of it on mixing characteristics. In all cases, the operating conditions were  $P = 6$  bar,  $d_i = 500 \mu\text{m}$ ,  $\phi = 180$ , and  $Re = 0.02$ . Another parameter called expansion ratio (ER), defined as the ratio between the mixing chamber diameter and the inlet channel diameter, was used to investigate mixer configurations. For the first mode, three different ER (2, 4, 6) were used. As for the second mode, the static mixer was designed with dimensions that fit into the chamber configuration with ER = 4 with a 2.2 mm diameter mixing chamber. These various configurations of the mixer with different ER values expansion ratios (ER) of 2,4,6 as well as mode 2 with ER of 4 (hybrid mode) were simulated and experimentally tested. The results (**Figure 3-4a**) indicate the close congruence of the mixing index obtained experimentally with that obtained numerically, which validates the simulation. It also shows that the mixing index increases with pulsation frequency (and Strouhal number) in all configurations. Some of these configurations have an optimal range of  $St$  where the mixing is highest. At higher frequencies, the flow from each nozzle does not have sufficient time for complete injection leading to stratification and insufficient mixing. At lower frequencies, the plug injected into the mixing chamber is larger than necessary. The optimal range represents the

maximization of the interfacial surface area to the volume injected to produce efficient mixing under the operating conditions. The variation in the mixing index obtained experimentally decreased at higher Strouhal numbers due to more homogeneity of the composition of the extruded material at higher frequencies. In the case of hybrid mixing, the static mixer placed at the center introduces secondary flow that enhances mixing and achieves 100% mixing after a certain frequency.

Transient simulations were also performed to understand the fluid dynamics of the mixing process. Here an initial state was used by filling the half of the mixing channel with ink defined by red color (mass fraction 0) and the other half with blue color (mass fraction 1) with the same ink properties. A well-mixed sample will have a green color and a mass fraction of 0.5. Sequential injection of the two inks into the mixing chamber ( $ER=6$ ) at various frequencies was simulated, and the composition of the chamber after 12 sec (sufficient to achieve steady-state) is shown in **Figure 3-4b**. The driving pressure was 6 bar, and switching frequencies ranging from 2 to 20 Hz corresponding to various St numbers were selected. **Figure 3-4b** also shows the simulated and experimentally obtained compositional profile of the ink extruded from the nozzle section at various frequencies. It can be seen that when the applied pulsation frequency is small (2 Hz), the alternative plugs of inks injected into the mixing chamber are significant, and it produces a striated pattern, as shown in **Figure 3-4b-i**. In this case, the size of the injected plugs was much larger than the volume of the inlet to the mixing chamber ( $P_v \gg d_i^3$ ). Due to the thickness of the injected plugs, the inks were not entirely mixed by diffusion even when they emerged at the nozzle, as shown both in the simulation (section A-A) as well as the closeup view of the printed trace.

The increase in frequency makes the injected plug smaller and close to the volume of the inlet to the mixing chamber ( $P_v \sim d_i^3$ ). In this case, sequential plugs are formed, and the surface to volume ratio is maximum which reduces the time constant for diffusional mixing. Therefore, complete mixing of the extruded fluid is observed at a frequency of 9 Hz (**Figure 3-4b-iii**) in the current case (mode 1, ER 6). However, when the frequency is increased even further, the volume of the plug injected is so small ( $P_v \ll d_i^3$ ) that a clear plug filling the entire volume of the neck region of the inlet into the mixing chamber is not filled. These results in a stratified flow pattern that continues into the mixing chamber. The interfacial length is smaller than the case where plugs are formed, resulting in poorer mixing (**Figure 3-4b-iv**). In terms of pulsation frequency, one can consider the situation where  $f \sim U/d_i$  is the optimal frequency for operation for rapid mixing.

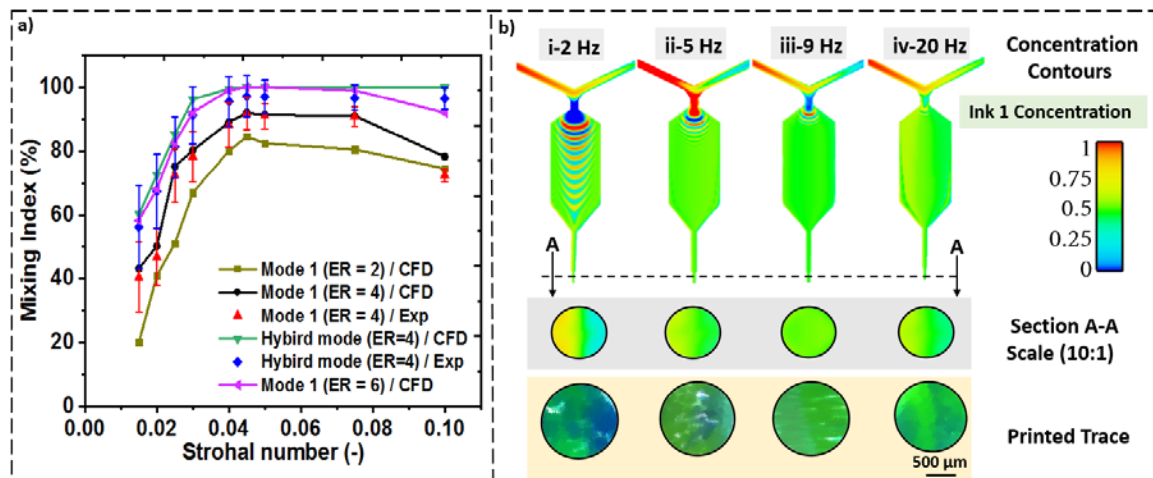


**Figure 3-4** Simulation and experimental validation of mixing in the printhead. **a)** Numerical and experimental evaluations of mixing index at different Strouhal number "St" at low Reynolds number 0.017 with different proposed configurations. **b)** CFD inks concentration distribution contours generated from simulation analysis under modulating driving pressure "6 bar" at the inlet 1 and 2 with different frequencies (2, 5, 9, and 20 Hz) at steady state (after 12 sec). The images also show the cross-section of the extruded ink at the nozzle (section A-A) and its comparison with the actual printed trace of the filaments extruded under the same conditions.

### 3.4.5 Optimization of Mixing in the Printhead

Although pulsatile plug injection and expansion result in good mixing, dynamic switching of the ink composition and achieving steady-state takes considerable time. Therefore, an additional insert in the form of a free-floating static mixer was introduced into the mixing chamber to reduce the time to achieve a steady state after a switch of composition. Fluid dynamic transient simulations were performed for printhead designs with different expansion ratios as well as for those with a hybrid configuration where a static mixer was included. A driving pressure of 6 bar, a pulsing frequency of 9 Hz, and an expansion chamber length of 6 mm were set for the simulation. Initially, the mixing chamber was filled with half of each ink, and then the pulsatile injection started. The time to achieve steady-state (defined as the switching time) and the mixing index were determined. **Figure 3-5a** shows that the increase in the expansion ratio (ER) of the mixing chamber increased the mixing index but also resulted in an increase in switching time. An increase in ER results in enhanced stretching of the incoming inks, resulting in greater interfacial area and enhanced mixing. However, with the increase in ER, the mixing chamber volume also increases, resulting in a higher switching time to mix the ink in the chamber thoroughly. When the static mixing element was introduced into the mixing chamber, the switching time was substantially reduced to under 4 sec while achieving a very high mixing index (~99%). The static mixing element provides a way to use chaotic advection to create additional interfaces that enhance the diffusional mixing of inks. It also reduces the volume of the mixing chamber (to ~ 15  $\mu$ L), thereby decreasing the switching time, which is also related to the time needed to empty the chamber of the mixed inks.

The evolution of the concentration distribution within the mixing chamber in various configurations (first and second mode) is shown in **Figure 3-5b** for a printhead with ER=4. Immediately after the start of pulsatile injection of the inks, the mixing within the chamber was initiated. In the case of mode 1, the mixing is solely due to an expansion geometry (chamber diameter of 2.2 mm and ER of 4) which stretches the interface between the injected plugs of different inks. Nevertheless, the entire chamber (26  $\mu\text{L}$ ) was completely filled with well-mixed inks within 10 sec (**Figure 3-5b-i**), and the extruded trace also was homogeneous. It represents the switching time for this configuration. The presence of the static mixing element in Mode 2 reduces the chamber volume to 15  $\mu\text{L}$ . The composition evolution within the change (**Figure 3-5b-ii**) was much faster. Complete mixing was achieved within 4 sec after initiation of the pulsatile inputs, indicating the faster response time of the hybrid mixer design to changes in composition or composition of the start-stop operations that may be required. The faster response time is both due to the reduction in volume and also due to the radial recirculatory flows that are enabled by the geometry of the static mixer. To elaborate our work with other published mixing system, we did a comparison between the current work and the published mixing technique showing the mixing performance and printing features (see *Appendix 1 Table 7-1*).

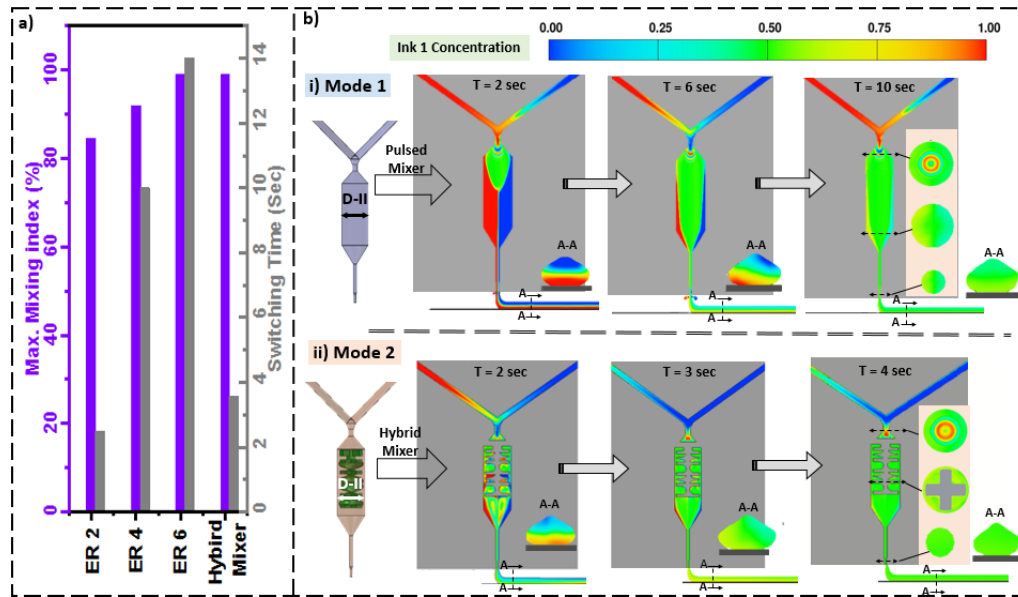


**Figure 3-5** a) Comparison between the proposed configurations showing the degree of mixing obtained and switching time for each case. b) Transient simulation of inks concentration contours at 9 Hz and the mixing chamber diameter 2 mm for the mixing junction and printed trace with sections at different locations, i) mode 1: without a static mixer, and ii) mode 2: with a static mixer.

### 3.4.6 Pneumatic Control of Mixing

Since the injection of the inks into the mixing chamber is pneumatic, various parameters such as the amplitude of applied pressure signal, its frequency, duty cycle, and phase difference between the pneumatic signals between two different injection channels can be used exquisitely to control the mixing within the printhead. Higher applied pressure results in a higher flow rate into the mixing chamber, which the non-dimensional  $Re$  can represent. The mixing was simulated at various Reynolds numbers ( $8 \times 10^{-4}$  to  $2.21 \times 10^{-3}$ ) for pulsed DII mixer design (ER 4) with  $St$  ranging from 0.005-0.12 and expansion chamber length  $l$  of 6 mm. The results shown in **Figure 3-6a** indicate that the maximum mixing efficiency was obtained at a lower Reynolds number in this regime as the residence time within the chamber was larger, allowing more diffusional mixing. For the low  $Re$  of  $8 \times 10^{-4}$  and  $St$  (0.02), the two inks were thoroughly mixed along the axial flow direction, with the mixing index of 0.972 at the exit cross-section (**Figure 3-6a**). An increase in  $Re$  results in larger

plugs being injected, which consequently reduces the mixing index. The  $St$  at which peak mixing index was obtained (inset in **Figure 3-6a**) is shifted to higher values as the  $Re$  increases. This corresponds the optimal condition where the mixing is best if the size of the injected plugs is about the size of the inlet into the expanding section of the mixing chamber. Interestingly, over a large range of  $St$ , the increased amplitude of the pulses (higher  $Re$ ) produces a stable mixing index. Compared with smaller  $Re$  where the peak mixing index is obtained only for a small range of  $St$ . The results indicate that when a higher driving pressure (higher  $Re$ ) is applied, a higher  $St$  (switching frequency) is required if maximum mixing performance is required to be attained.

We also investigated the effect of the phase difference between the pulsatile inputs into the two inlets on the mixing efficiency. Various phase differences ( $20$ - $340^\circ$ ) were used with a pulsing frequency of  $9$  Hz, an expansion ratio of  $6$ , a duty cycle of  $50\%$ , the pressure applied of  $6$  bar, and the expansion chamber length  $l$  of  $6$  mm. As shown in **Figure 3-6b**, the simulation results indicate that the optimal phase difference was  $180$ - $200^\circ$ . Interestingly, a broad range of phase differences was suitable for complete mixing even though the theoretical expectation would be an optimal point of  $180^\circ$ . At a very small or large phase difference (close to  $0$  or  $360^\circ$ ), both inlets were injected at nearly the same time leading to a stratified flow of the inks into the expansion chamber. The flow stratification reduces as the phase difference in the signals grows closer to the optimal region between  $120$ - $240^\circ$ . In this region, plug-type injection occurs for the majority of the time from one or other of the inlets resulting in optimal mixing characteristics.

A key parameter that can be modulated to obtain various mixing ratios is the duty cycle ( $D_c$ ). The duty cycle represented the proportion of time within each cycle when the

pressure was on. A 50% duty cycle in each inlet with a phase difference of  $180^\circ$  will represent a mixing ratio of 1:1 between the two inks. However, by proportionally changing the duty cycles between the two inlets, one can introduce any ratio of ink composition into the mixing chamber. Simulations of the ink compositional ratios obtained with various duty cycles are shown in **Figure 3-6c**. Duty cycles between 0.4 and 0.6 were found to be optimal to produce a linearly varying composition of inks. At duty cycles below 0.4 and above 0.6, predominantly one type of ink was injected, resulting in non-linear variation in composition that could not be easily controlled. Therefore, duty cycles between 0.4-0-0.6 are recommended.

The capability of the MM-PHM to dynamically change the composition of the ink extruded and to create a wide variety of ink compositions for printing was demonstrated with UV curable silicone inks. The V31H ink (Table I) was doped with blue and yellow colored dyes to obtain two distinguishable inks (V31H blue, V31H yellow). The MM-PHM in the hybrid mixing model was used. A toolpath for continuous extrusion where the printhead is raster-scanned to cover a region was used. The ink compositions are dynamically changed from purely yellow ink (1:0) to purely blue (0:1) with three different compositions in between by controlling the duty cycle of each of the ink injected. Each composition was printed over a region of (4 x 2 cm). The printing of this geometry and the final printed feature is shown in **Figure 3-6d**. The total print time was only 4 min, similar to printing using a single-color ink, indicating the pulsatile injection was fast enough and did not slow down the process. The results show that the composition of the ink can be dynamically changed using this approach. The colors obtained in each region were homogenous. For characterizing the homogeneity of the printed structure, an RGB analysis

was performed, and the results were presented in *Appendix 1 Figure 7-4* and *Figure 7-5*. Followed by evaluating the RGB intensities by calculating the homogeneity index. It can be seen that the lowest homogeneity index of 0.911 was found at the mixed green zone. While the unmixed printed zones have a better homogeneity, and it was around 0.94 for the blue zone and 0.97 for the yellow zone. By using different duty cycles, the composition can be tuned to any percentage between the inks used. The range of composition (palette) can further be enhanced by increasing the number of ink inputs. It should be noted that the MM-PHM has a priming volume of 15  $\mu\text{l}$  without the static mixer.

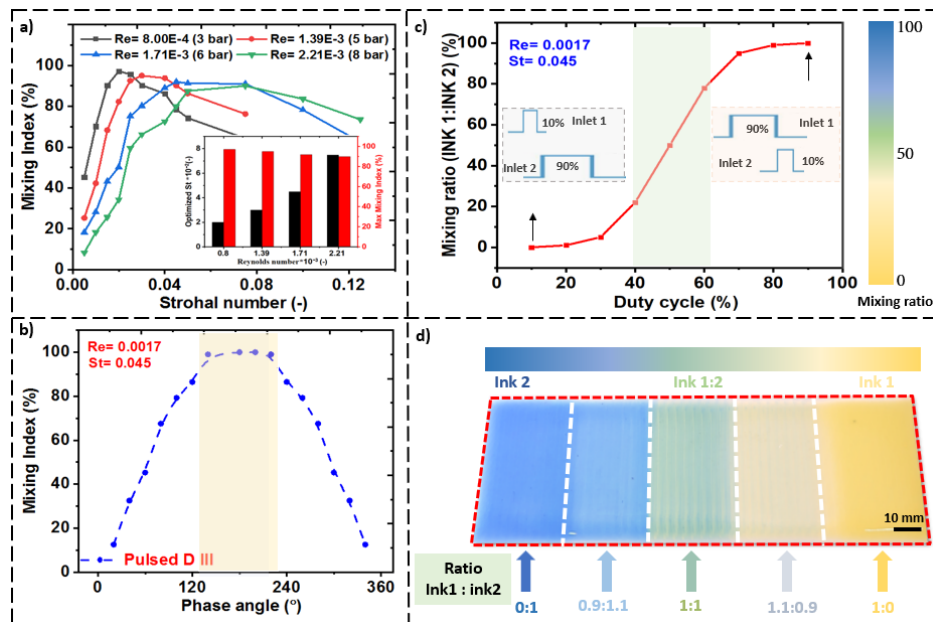


**Figure 3-6** a) Numerically calculated mixing index for different Reynolds number "Re" ranging from 0.00025 to 0.0025 illustrating the effect of pulse amplitude on the mixing index by examining the mixing index at each Re for different St ranging from 0.005 to 0.12, inset is showing the optimized St at each Re with the corresponding maximum mixing index obtained. b) Numerically calculated mixing index for phase shift angles ranging from 0 to 360°. The middle blue region shows the best mixing range. c) The plot of duty cycle (pulse duration /total cycle time) at mixing ratio (Ink 1: Ink 2) at satisfied Re 0.0017 and St 0.045. The green zone is the range of duty cycles over which composition can be controlled linearly. d) Image of a 2D carpet structure showing the effect of mixing ratio on the printed color area, the color changing from yellow at the right to the blue at the left of the 2D carpet—the color gradient rectangle on the top showing the color gradient fill.

Therefore, this volume has to be extruded out to switch the ink composition and represents the minimum resolution obtained when switching inks. Typically, by coordinating the pneumatic control with the tool path, this extra volume can be accommodated except for those prints where extremely small patterns with a different ink have to be printed with high resolution.

### 3.4.7 Printing Compositionally Graded 2D and 3D Objects using MM-PHM

In order to demonstrate the capability of this print head, 2D and 3D objects were 3D printed with regions of different compositions embedded in them. As a first demonstration, we printed a 2D color map consisting of 9 colors using a printhead with four ink (color) inlets. The inks were composed of UV curable silicone materials "V31H, V35H" doped with different colors (cyan and yellow – V31H and magenta and green - V35H), and the printhead used the hybrid mixing mode (**Figure 3-7a**). Different ratios of these inks can produce up to 9 different colors, which were demonstrated. To cover the region where the 2D map was printed, a toolpath was created for continuous extrusion with instantaneously mixing and switching the compositions. **Figure 3-7b-i** shows the printing scheme of the printhead setup, the inset on the left shows the printhead optical image, and the right image presents the printing process with UV light radiation in operation. The ink compositions are dynamically altered from one purely color (on the corners), including the magenta, yellow, green, and blue colors, to mixed colors with five different compositions in between by controlling the mixing inlets colors of each of the ink injected using a duty cycle of 0.5. Each composition was printed over a region of (2 x 2 cm). Under the used print conditions, the residence time within the MM-PHM nozzle was 4 s, ensuring a sharp interface between each color region and reducing the wasted material (**Figure 3-7b-ii**) significantly. The

printing process took only 18 min to print four layers for each composition region which was no different from the time to print the same features in a single color. Using the hybrid mixing approach, the color groups printed in each composition area were homogenous with a sharp interface between color regions (with a layer resolution of  $0.25 \pm 0.04$  mm). As a second demonstration, we used the mixing printhead to print a 3D Rubix cube from UV curable silicone materials (V31H and V35H) with different viscosity (**Figure 3-7c**). A printed 3D Rubix cube (3x3x3 cm) was created from four inlet printhead with different inks (V31 cyan, V31 yellow, V35 red, V35 gray) (**Figure 3-7c-i**). The printing process needed only 125 min for printing 40 layers for each color region, and the time was identical to printing the same volume using a single color without switching. Using the hybrid mixing approach, the color combinations printed in each cube region were homogenous with a sharply defined border between color surfaces in 3D.

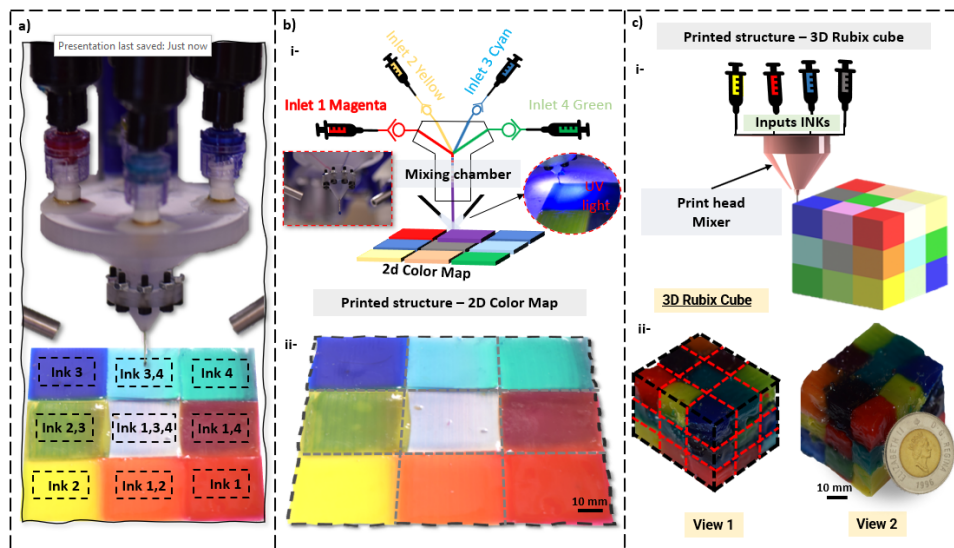


**Figure 3-7** a) Gradient-colored model printed along with the actual image of the printhead mixer with four different inlets. b) 2D printed color map. i) A schematic illustration of the 2D color map, including the four inlets inks with different colors magenta, yellow, cyan, and green. Insets are "on-left" the bottom of the actual printhead mixer image, and "on-right" 3d printing process under UV light for instant curing. ii- The actual 2D color map, printing nine different colors using four inlet colors by mixing between different colors. c) 3D printed Rubix cube. i) A schematic illustration of the 3D Rubix cube. ii) The actual image of the 3D Rubix cube, showing the capabilities of 3d printing structure.

This ability to compositionally tune and produce a multitude of compositions from a few base inks can be used to produce various compositional graded materials and objects with applications in soft robotics, flexible electronics, and biomedical devices.

### **3.5 Conclusions**

In summary, we have developed a new multimaterial microfluidic printhead that is capable of mixing several inks simultaneously to produce a multitude of compositions. The unique printhead combines pulsatile injection of different inks with a static mixing element to achieve fast mixing with low priming volume. Simulations of the flow dynamics provided a suitable range of parameters for optimal mixing and compositional tuning. These were validated using experiments with UV curable silicone inks. By decoupling the mixing efficiency from the flow rate and volume of the mixer, the ability to achieve rapid mixing was achieved. It further provided the ability to rapidly switch between compositions enable sharp and clear interfaces when printing. The print head has the fastest switching time (< 4 sec) of all mixers used for highly viscous inks. In order to demonstrate its capability, 2D and 3D objects such as a 2D color map and 3D Rubix cube were printed. The simple and versatile printhead demonstrated here is of broad application to 3D print a variety of UV curable materials such as silicones, epoxies, or hydrogels and produce compositionally graded objects that can be used for soft robotics, flexible electronics, and even tissue engineering applications.

In the future, the mixing evaluation of the printed structures can be enhanced by analyzing the printed image by converting it to HSB colour space. Colour space HSB divides an image into three channels, each representing a pixel's hue, saturation, and brightness. The colour harmony is created by the colour saturation and hue, called

chromaticity. Therefore, a colour can be defined according to its chromaticity and intensity. Different colour model techniques have been used to check colour homogeneities, such as RGB, CMY, and HSI. The HSI model could have an advantage over the prior model mentioned, as it considers a combination of hue, saturation, and intensity rather than the amount of combination between red, green or blue components in the RGB model. Furthermore, the international commission on illumination has characterized a colour space called CIELAB colour space ( $L^*a^*b$ ), in which the image is analyzed based on the distance's scales rather than the perceived colour difference. Such a technique can be helpful in the case of colourant mixtures. Alternatively, the printed mixing coefficient of variation can be obtained through micro-CT images to check the mixing on a molecular scale. The cross-sections of the printed structure are scaled proportionally to the grayscale pixel intensity. As another method for quantification, the spatial probability density functions of the intensity image may be used in case the standard deviation of the intensity values can not differentiate between regions in the image. On the other hand, measuring a chemical reaction's fluorescent product is another way of quantifying the mixing. It is typically an acid-base reaction with a dye whose quantum yield depends on the pH. The colour analysis techniques mentioned are handy for estimating the mixing index in microfluidic devices and can be adapted in 3D printing.

## **Acknowledgements**

We acknowledge the financial support of the Natural Sciences and Engineering Research Council of Canada. PRS also thanks the Canada Research Chair Program for support. We are very grateful for the gift of a photoinitiator from IGM Resins, Inc. We are very grateful for the academic license of flow-3d software from flow science, Inc.

## References

- [1] D. Han and H. Lee, "Recent advances in multi-material additive manufacturing: methods and applications," *Current Opinion in Chemical Engineering*, vol. 28, pp. 158-166, 2020.
- [2] V. G. Rocha, E. Saiz, I. S. Tirichenko, and E. García-Tuñón, "Direct ink writing advances in multi-material structures for a sustainable future," *Journal of Materials Chemistry A*, vol. 8, no. 31, pp. 15646-15657, 2020.
- [3] G. L. Goh, H. Zhang, T. H. Chong, and W. Y. Yeong, "3D Printing of Multilayered and Multimaterial Electronics: A Review," *Advanced Electronic Materials*, vol. 7, no. 10, p. 2100445, 2021.
- [4] N. Jones, "Science in three dimensions: the print revolution," *Nature News*, vol. 487, no. 7405, p. 22, 2012.
- [5] C. Colosi *et al.*, "Microfluidic bioprinting of heterogeneous 3D tissue constructs using low-viscosity bioink," *Advanced Materials*, vol. 28, no. 4, pp. 677-684, 2016.
- [6] J. O. Hardin, T. J. Ober, A. D. Valentine, and J. A. Lewis, "Microfluidic printheads for multimaterial 3D printing of viscoelastic inks," *Advanced materials*, vol. 27, no. 21, pp. 3279-3284, 2015.
- [7] T. J. Ober, D. Foresti, and J. A. Lewis, "Active mixing of complex fluids at the microscale," *Proceedings of the National Academy of Sciences*, vol. 112, no. 40, pp. 12293-12298, 2015.
- [8] D. Kokkinis, F. Bouville, and A. R. Studart, "3D Printing of Materials with Tunable Failure via Bioinspired Mechanical Gradients," *Advanced Materials*, vol. 30, no. 19, p. 1705808, 2018.
- [9] Z. X. Khoo *et al.*, "3D printing of smart materials: A review on recent progresses in 4D printing," *Virtual and Physical Prototyping*, vol. 10, no. 3, pp. 103-122, 2015.
- [10] A. S. Gladman, E. A. Matsumoto, R. G. Nuzzo, L. Mahadevan, and J. A. Lewis, "Biomimetic 4D printing," *Nature materials*, vol. 15, no. 4, pp. 413-418, 2016.
- [11] M. M. Durban *et al.*, "Custom 3D printable silicones with tunable stiffness," *Macromolecular rapid communications*, vol. 39, no. 4, p. 1700563, 2018.
- [12] J. R. Raney, B. G. Compton, J. Mueller, T. J. Ober, K. Shea, and J. A. Lewis, "Rotational 3D printing of damage-tolerant composites with programmable mechanics," *Proceedings of the National Academy of Sciences*, vol. 115, no. 6, pp. 1198-1203, 2018.
- [13] K. H. Matlack, A. Bauhofer, S. Krödel, A. Palermo, and C. Daraio, "Composite 3D-printed metastructures for low-frequency and broadband vibration absorption," *Proceedings of the National Academy of Sciences*, vol. 113, no. 30, pp. 8386-8390, 2016.
- [14] B. G. Compton and J. A. Lewis, "3D Printing: 3D-Printing of Lightweight Cellular Composites (Adv. Mater. 34/2014)," *Advanced Materials*, vol. 26, no. 34, pp. 6043-6043, 2014.
- [15] F. Ilievski, A. D. Mazzeo, R. F. Shepherd, X. Chen, and G. M. Whitesides, "Titelbild: Soft Robotics for Chemists (Angew. Chem. 8/2011)," *Angewandte Chemie*, vol. 123, no. 8, pp. 1765-1765, 2011.
- [16] A. Russo, B. Y. Ahn, J. J. Adams, E. B. Duoss, J. T. Bernhard, and J. A. Lewis, "Pen-on-paper flexible electronics," *Advanced materials*, vol. 23, no. 30, pp. 3426-3430, 2011.
- [17] S. B. Walker and J. A. Lewis, "Reactive silver inks for patterning high-conductivity features at mild temperatures," *Journal of the American Chemical Society*, vol. 134, no. 3, pp. 1419-1421, 2012.

- [18] A. Frutiger *et al.*, "Capacitive soft strain sensors via multicore–shell fiber printing," *Advanced Materials*, vol. 27, no. 15, pp. 2440-2446, 2015.
- [19] S. Beyer, T. Mohamed, and K. Walus, "A Microfluidics Based 3D Bioprinter with On-The-Fly Multimaterial Switching capability," in *17th International Conference on Miniaturized Systems for Chemistry and Life Sciences*, 2013.
- [20] S. E. Bakarich, R. Gorkin III, R. Gately, S. Naficy, and G. M. Spinks, "3D printing of tough hydrogel composites with spatially varying materials properties," *Additive Manufacturing*, vol. 14, pp. 24-30, 2017.
- [21] J. Mueller, J. R. Raney, K. Shea, and J. A. Lewis, "Architected Lattices with High Stiffness and Toughness via Multicore–Shell 3D Printing," *Advanced Materials*, vol. 30, no. 12, p. 1705001, 2018.
- [22] R. Sochol *et al.*, "3D printed microfluidic circuitry via multijet-based additive manufacturing," *Lab on a Chip*, vol. 16, no. 4, pp. 668-678, 2016.
- [23] W. Liu *et al.*, "Rapid continuous multimaterial extrusion bioprinting," *Advanced materials*, vol. 29, no. 3, p. 1604630, 2017.
- [24] J. Liu, Y. Guo, C. Weng, H. Zhang, and Z. Zhang, "High thermal conductive epoxy based composites fabricated by multi-material direct ink writing," *Composites Part A: Applied Science and Manufacturing*, vol. 129, p. 105684, 2020.
- [25] S. Tagliaferri, A. Panagiotopoulos, and C. Mattevi, "Direct ink writing of energy materials," *Materials Advances*, vol. 2, no. 2, pp. 540-563, 2021.
- [26] K. E. Neely, K. C. Galloway, and A. M. Strauss, "MULTI-MATERIAL ADDITIVELY MANUFACTURED COMPOSITE REACTIVE MATERIALS VIA CONTINUOUS FILAMENT DIRECT INK WRITING," *Additive Manufacturing*, vol. 35, p. 101332, 2020.
- [27] M. A. Skylar-Scott, J. Mueller, C. W. Visser, and J. A. Lewis, "Voxelated soft matter via multimaterial multinozzle 3D printing," *Nature*, vol. 575, no. 7782, pp. 330-335, 2019.
- [28] J. M. Ortega *et al.*, "Active Mixing of Disparate Inks for Multimaterial 3D Printing," *Advanced Materials Technologies*, vol. 4, no. 7, p. 1800717, 2019.
- [29] A. M. Golobic *et al.*, "Active Mixing of Reactive Materials for 3D Printing," *Advanced Engineering Materials*, vol. 21, no. 8, p. 1900147, 2019.
- [30] H. Lan, "Active Mixing Nozzle for Multi-Material and Multi-Scale 3D Printing," in *ASME 2017 12th International Manufacturing Science and Engineering Conference collocated with the JSME/ASME 2017 6th International Conference on Materials and Processing*, 2017: American Society of Mechanical Engineers Digital Collection.
- [31] S. E. Bakarich, R. Gorkin III, R. Gately, S. Naficy, M. in het Panhuis, and G. M. Spinks, "3D printing of tough hydrogel composites with spatially varying materials properties," *Additive Manufacturing*, vol. 14, pp. 24-30, 2017.
- [32] J. Ramsay, M. Simmons, A. Ingram, and E. Stitt, "Mixing performance of viscoelastic fluids in a Kenics KM in-line static mixer," *Chemical Engineering Research and Design*, vol. 115, pp. 310-324, 2016.
- [33] D. Kokkinis, M. Schaffner, and A. R. Studart, "Multimaterial magnetically assisted 3D printing of composite materials," *Nature communications*, vol. 6, no. 1, pp. 1-10, 2015.
- [34] D. Therriault, S. R. White, and J. A. Lewis, "Chaotic mixing in three-dimensional microvascular networks fabricated by direct-write assembly," *Nature materials*, vol. 2, no. 4, pp. 265-271, 2003.
- [35] B. K. Deuser, L. Tang, R. G. Landers, M. C. Leu, and G. E. Hilmas, "Hybrid extrusion force-velocity control using freeze-form extrusion fabrication for functionally graded material parts," *Journal of Manufacturing Science and Engineering*, vol. 135, no. 4, 2013.

- [36] L. Ren *et al.*, "3D printing of materials with spatially non-linearly varying properties," *Materials & Design*, vol. 156, pp. 470-479, 2018.
- [37] S. Zheng, M. Zlatin, P. R. Selvaganapathy, and M. A. Brook, "Multiple modulus silicone elastomers using 3D extrusion printing of low viscosity inks," *Additive Manufacturing*, vol. 24, pp. 86-92, 2018.
- [38] Materials Guide, Address the most demanding prototyping and production applications with an advanced plastics materials portfolio, 333 Three D Systems Circle, Rock Hill, SC 29730: 3D Systems Corporation, 2021, p. 47. [Online]. Available.
- [39] A. Standard, "D543," *Standard Practices for Evaluating the Resistance of Plastics to Chemical Reagents*. ASTM International, West Conshohocken, PA, 2006.
- [40] R. Tanner and M. Keentok, "Shear fracture in cone-plate rheometry," *Journal of Rheology*, vol. 27, no. 1, pp. 47-57, 1983.
- [41] J. M. Krishnan, A. P. Deshpande, and P. S. Kumar, *Rheology of complex fluids*. Springer, 2010.
- [42] J. M. Ottino and S. Wiggins, "Introduction: mixing in microfluidics," ed: The Royal Society, 2004.
- [43] H. A. Stone, A. D. Stroock, and A. Ajdari, "Engineering flows in small devices: microfluidics toward a lab-on-a-chip," *Annu. Rev. Fluid Mech.*, vol. 36, pp. 381-411, 2004.
- [44] F. M. White and I. Corfield, *Viscous fluid flow*. McGraw-Hill New York, 2006.
- [45] S. Gambhire, N. Patel, G. Gambhire, and S. Kale, "A review on different micromixers and its micromixing within microchannel," *International Journal of Current Engineering and Technology*, vol. 4, no. 4, 2016.
- [46] N.-T. Nguyen and Z. Wu, "Micromixers—a review," *Journal of micromechanics and microengineering*, vol. 15, no. 2, p. R1, 2004.
- [47] F. Cheaib, G. Kekejian, S. Antoun, M. Cheikh, and I. Lakkis, "Microfluidic mixing using pulsating flows," *Microfluidics and Nanofluidics*, vol. 20, no. 5, p. 70, 2016.
- [48] M. Zhang *et al.*, "High mixing efficiency by modulating inlet frequency of viscoelastic fluid in simplified pore structure," *Processes*, vol. 6, no. 11, p. 210, 2018.
- [49] J. T. Coleman, J. McKechnie, and D. Sinton, "High-efficiency electrokinetic micromixing through symmetric sequential injection and expansion," *Lab on a Chip*, vol. 6, no. 8, pp. 1033-1039, 2006.
- [50] H. Song, M. R. Bringer, J. D. Tice, C. J. Gerds, and R. F. Ismagilov, "Experimental test of scaling of mixing by chaotic advection in droplets moving through microfluidic channels," *Applied Physics Letters*, vol. 83, no. 22, pp. 4664-4666, 2003.

## **4 Chapter 4**

### **Microfluidic Printheads for Highly Switchable**

### **Multimaterial 3D Printing of Soft Materials**

#### **Complete Citation:**

I. Hassan and P. R. Selvaganapathy, " Microfluidic Printheads for Highly Switchable Multimaterial 3D Printing of Soft Materials", *Advanced Materials Technologies* (2022): 2101709.

#### **Contribution:**

I. Hassan: Designed and performed all experiments, interpretation and analysis of data, wrote the manuscript draft.

P. R. Selvaganapathy: Supervised I. Hassan and provided guidance, revised and edited the manuscript.

## 4.1 Abstract

Extrusion-based three-dimensional printing uses multiple printing nozzles to produce multimaterial combinations. It requires complex alignment and accuracy control as well as an effective start-stop procedure to print intermittently, which has so far proven difficult to achieve. A recently developed simpler approach is to sequence the multimaterial inks through a single nozzle that will avoid both of these requirements. Although it has been successfully demonstrated for viscoelastic inks, adapting it to more widely available viscous inks is a challenge. Here we demonstrate a dynamically-controllable multi-material single-nozzle 3D printing (MSN3D) printhead that is capable of printing both viscous and viscoelastic materials. It uses pneumatically-pulsed injection of multiple viscous inks into a central nozzle for printing. We show through simulations and experiments that a crucial but narrow range active reverse pressure in static reservoir(s) is essential to provide accurate switching in viscous inks, which is unlike viscoelastic inks that have a wider operating range and do not require a backflow control. Using this approach, we demonstrate high frequency and fast switching between four different viscous materials for pixelated printing of different materials which can be used to embed different functional properties in a variety of 2D and 3D shapes using commercially available polymers.

## 4.2 Introduction

Additive manufacturing of polymers through extrusion-based direct ink writing (DIW) or inkjet printing has advanced considerably over the past decade to include techniques to combine multiple materials in a 3D pixelated manner and fabricate complex 3D structures.[1-5] A 3D pixel object can be described as a unit volume in three-dimensional space with specific material, shape, and features. Inkjet-based 3D printing is an additive

manufacturing method that is exquisitely suited for multimaterial 3D pixelated printing at high resolution [6-9] but is limited by the tight restriction on ink properties which confine its use to a small set of printable inks[10, 11]. On the other hand, DIW has greater flexibility in the incorporation of different materials but is limited in its resolution and ability to perform pixelated prints. In a typical DIW system, the material is extruded from tiny nozzles under controlled flow rates and deposited along digitally defined paths.[12-14] Recently, multimaterial DIW systems have been developed that use mixing and switching at the nozzle to continuously co-print multiple inks.[15-18] Alternatively, multinozzle based multimaterial DIW systems have also been developed that divides the print into multiple parts depending on the ink to be printed and use a different nozzle for each ink to print them.[19-22] However, the use of multi-nozzle arrays for multimaterial printing has some limitations. For instance, syringe pump-driven DIW systems are suitable for continuous printing, and the start-stop operations required for 3D pixelated printing from multiple nozzles can create inaccuracies due to the compliance and thread backlash.[23] Recently, an innovative DIW system with a switching printhead that can sequence multiple materials through a single nozzle for continuous extrusion has been developed using a pneumatic/hydraulic driving system, that is capable of switching at high frequency (around 50 Hz), providing a possible way to perform pixelated 3D printing.[24] Yet, this system is limited by the need for special shear-thinning inks that allow precise switching capability (by preventing unwanted backflow) due to the static yielding resistance.[24] In particular, it is limited to inks that have a Herschel- Bulkley nature. Expanding the capability of such pneumatically driven switching printheads to accommodate more widely and

commercially available Newtonian inks can potentially widen the use of pixelated 3D DIW printing to a number of applications.

Here, we have designed a multi-material single nozzle 3D printing (MSN3D) printhead that can print both viscous and viscoelastic inks with the capability for rapid multimaterial switching for pixelated 3D printing. Due to the MSN3D nanoscale-priming volume and the integration of a unique pressure-controlled ink injector system, the MSN3D can deliver multiple compositions continuously or discretely with high switching frequency. Through numerical modeling, we determine a narrow range of critical parameters that enable precise switching of viscous Newtonian inks. We have demonstrated the applicability by producing pixelated multimaterial complex patterns. MSN3D switching dynamics have been optimized using computational fluid dynamics for viscous material and validated experimentally. The current approach reaches a high switching frequency up to 50 Hz with various ink rheology. This methodology has been shown to be highly scalable by printing a variety of 2D and 3D architectures with different silicone and epoxy inks. A vital aspect of this approach is its ability to allow ultrarapid switching in the printhead during printing on a scalable basis, expanding the attribute set available for 3D printed objects.

### **4.3 Materials and Methods**

#### **4.3.1 Materials**

*UV curable Silicone inks:* A variety of combinations have been used, as shown in *Appendix 2 Table 8-1*. Silicones with functional properties: vinylsilicones: vinyl terminated polydimethylsiloxane, DMS-V31, and DMS-V35 with molecular weights of 21500, 42300 g.mol<sup>-1</sup>, respectively, 2-3% (mercaptopropyl)methylsiloxane-dimethylsiloxane copolymer

2 (SMS-022), and [13-17% (mercaptopropyl)methylsiloxane]– dimethylsiloxane copolymer (SMS-142) were bought from Gelest, Inc, US. As a gift from IGM Resins, Inc., we received Photoinitiator TPO-L. Rubberized silicone pigments in red, blue, yellow, and green were purchased from Smooth-On. Aerosil-150 “Silica” was acquired from Evonik Industries.

As a result of its fast reaction time, photoinitiated polymerization was chosen for this study, which suits low viscosity inks best. A combination of reagents was utilized to prepare two PDMS inks (**Table 8-1**). [15]

The crosslinkers were derived from incompatibility thiopropylsilicones, while the primary polymers were turned into telechelic vinyl-substituted silicones.[1] A rotational rheometer was used to assess the rheological behavior of the UV curable inks under steady shear. Inks V31 and V35 show a Newtonian response with constant viscosities of 1.6 and 5 Pa.s (Appendix 2 **Figure 8-1**).

*Heat curable materials:* Stiff silicone material, a 10:1 balance of SE 1700 base, and catalyst is used as a controller to add 2% w/w pigment (Silc-Pig) in a Mini vortexer mixer for 10 min. However, the flexible silicone ink for using the soft robotic was first mixed with SE 1700 base (80 wt%), catalyst (3 wt%), pigments (2 wt%), then added Sylgard 527 Parts A and B (each 7.5 wt%) and stirred again (10 min) (*Appendix 2 Table 8-2*).

*Adhesive inks:* NOA68 Norland adhesive is a UV cure glue that elongates by 5000 cps. The toughness-shore is 60 psi, but it is an elastic adhesive.

#### **4.3.2 Fabrication of MSN3D Printhead**

We used SolidWorks (Dassault Systems, Inc.) to design the MSN3D devices, which were converted into STL files using a ProJet 2500 Plus 3D printer with XHD settings, up to 1600

x 900 x 790 DPI.[25] It was printed using VisiJet M3 Crystal resin and VisiJet S300 support wax material at 20–28 °C, and a transparent VisiJet M3 Crystal resin. As for actual printing, to avoid any clogging in the channels, VisiJet SL impact in "opaque, white" has been used. A post-processing technique involves warming the part to 60 °C in an oven and then heat-surfing it in an ultrasonic bath. The following step removes most of the wax support and cleans the channels. Furthermore, we used a 30min perfusion of corn oil at a temperature of 70°C to remove wax from the internal microstructures. There may be leftover support in the channels used to operate these procedures at higher temperatures for longer times. We use these settings to make sure deformations during post-processing are to a minimum. However, we can cause some amount of warpage to the part in this case. The MSN3D devices were then submerged in soap and sonicated water for 20 minutes to remove any wax.

Also, to prevent polymerization of the extruding ink at the mixer site due to light reflections from the print bed when printing viscous inks, a metal needle (25 gauge) was attached at the end of the outlet. Then, using an internal thread with internal threads, the ink barrels were attached to the printhead through a heating insert. Before pressing the brass insert into the printhead, the brass insert must be heated up to 60 °C. In the second step, mechanical adhesive epoxy (Loctite® M-121hp, 1.69 oz, McMaster-Care) has been put in and left to cure the bond for one day.

### **4.3.3 Experimental Setup**

In **Figure 4-1**, you can see the existing test setup. One way to control objects with motion control is a 3D printer made by UNI-PRINT-3D, commercially available from its manufacturer, 'The Cool Tool' GmbH company. The syringe barrels are opaque (Model

Optimum by Nordson EFD) and have a pressure of 34030 kPa over the passageway, which helps feed silicone into the printhead cavities without introducing air bubbles. External air pressure provides pressure up to 100 psi.

Several control channels consisting of three valves and a regulator were attached to the high-pressure pressure supply. Each channel is connected to a 3-way solenoid valve (S15MM-30-12-3B, Pneumadyne, Inc) to tie each barrel to atmospheric pressure. The control system can individually control each solenoid valve. To instigate the reaction, the UV source used for curing purposes must be a vital UV source, such as a metal halide lamp. These lamps generate a broad spectrum of UV with peaks typically between 300nm and 400nm. A 'Lumen Dynamics' 'S1000 Omniture' UV curing system (which combines two light guides with the light guide series of three) that produces a narrow cone of 30° when illuminated with ultraviolet was used. Furthermore, synchronized control of the XYZ positioner, solenoid valves, and UV lamp was gained using the machine interface developed by 'The Cool Tool'<sup>TM</sup>. Controlling the solenoid valves was conducted over an i2c communication bus via a driver programmed using I2C protocols.

Moreover, Controls and solenoid valves are active in sequence with a mechanical response of at least 100 Hz. A pressurized ink barrel's control channel pushes ink down into the channel as it is pressured over its air channel. With a central G-code machine interface controller, the printer moved synchronized with the valve's control and switch that controlled the lamp's on-off state. It is possible to instantly stop the ink flow when required so that there is no crosslinking at the tip and turn off the UV light immediately. GCode can be either programmed manually or created routinely from bitmap files using a custom script (MATLAB, Mathworks) for more complex patterns. By hand or using paint

software, bitmaps could be made or created from a .stl file. With the help of the custom MATLAB script, the bitmap file was read to determine a print path while simultaneously altering the material on the fly. By printing a uniform distribution of vertical lines bidirectionally to the left and right, a fixed offset variable as shown in *Appendix 2 Figure 8-1* was controlled to control the exact switching location.

#### 4.3.4 Rheological Measurements

*For viscous inks:* An ink viscosity was determined using an AR2000 rheometer (TA Instruments). Shear rate up to  $1 \text{ S}^{-1}$  is achieved using a 40 mm,  $2^\circ$  cone and plate geometry.[26] We used the Cox-Merz transformation up to shear rates greater than  $1 \text{ S}^{-1}$  and up to  $100 \text{ S}^{-1}$ . TA instruments used a Cox-Merz transformation using the TRIOS PC Software to obtain viscosity at higher shear rates. The cox-merz method was validated using Cox-Merz methodology that the shear rate ranged from 0.1 to  $0.6 \text{ S}^{-1}$  based on the frequency sweep (appendix 2 **Figure 8-1a**). [27]

*For Viscoelastic inks:* With a conical–plate geometry ( $8^\circ$  rotational angle and cone cylinder diameter), the rheology of the ink was measured by a controlled stress rheometer with a diameter of 40 mm and  $2^\circ$ . The excess ink was removed using a spatula after the ink was loaded into the cone–plate gap. By taking shear-rate sweeps at  $20^\circ \text{C}$  using shear rates in the range of  $1 \text{ s}^{-1}$  to about  $100 \text{ s}^{-1}$ , apparent viscosities were determined. Ink consistency, flow index, and shear yield stress were determined using the Herschel-Bulkley model by fitting the data to a Herschel–Bulkley model. Various oscillation frequencies (0.1 Hz to 10 Hz) and shear stresses (10 Pa) were applied to the static yield stresses “silicone” inks to determine the storage and loss moduli. We then conducted oscillations using strains of

0.01% to 1,000% for 1 Hz at an oscillation rate. Experimental results were obtained within 30 min after ink preparation “appendix 2 **Figure 8-1b**”.

#### 4.3.5 Stress-Strain Curve Measurements

A Universal Test System (INSTRON 3366, 50 N load cell) was used to measure the tensile strength of silicone for creating soft robotics. We prepared rectangular samples of 5 cm x 1.5 cm x 1.5 mm. The pieces were printed with a printing speed of 10 mm/s after mixing in a Mini Vortexer mixer (VWR.tm Inc.). Tests on tensile strength used a crosshead speed of 5mm.min<sup>-1</sup> to stretch the elastomers' ends. An electronic digital micrometer (Mitutoyo, Japan) was used to measure the dimensions of the tested elastomer specimens at three random positions.

#### 4.3.6 Numerical model Governing Equations

Simulation of a Y-junction channel's flow with a computational model used in this proposal. At the intersection of the two inlets, the flow begins to merge. The constant and Naiver-Stokes equations will be used to solve the fluid flow as follows by applying the velocity, pressure, and concentration components simultaneously:[28, 29]

$$\textit{Continuity equation} \quad \nabla \cdot U = 0 \quad (1)$$

$$\textit{Momentum equation} \quad \frac{\partial \rho U}{\partial t} + \rho U \cdot \nabla U = -\Delta p + \mu \nabla^2 U + \nabla \cdot \tau_p \quad (2)$$

The following formula represents U as the flow velocity vector; p is the pressure; d is the density; e is the dynamic viscosity, and a is the elasticity (in Newtonian fluid put equal to zero).

For  $d_i \ll L$ ,  $|\frac{\partial^2 v_x}{\partial x^2}| / |\frac{\partial^2 v_x}{\partial y^2}| \sim (d_i/L)^2$  and the momentum equation in the flow, in

dimensionless form, is approximated as

$$StRe \frac{\partial v_x}{\partial t} = -\frac{\partial p}{\partial x} + \frac{\partial^2 v_x}{\partial y^2} + \gamma^2 \frac{\partial^2 v_x}{\partial z^2} \quad (3)$$

where  $\gamma = \frac{d_i}{d_m}$ ,  $St = \frac{fd_i}{U}$  is the Strouhal number and  $Re = \frac{Ul}{\nu}$  is the Reynolds number;  $\nu = \eta/\rho$  is the kinematic viscosity.

It is possible to express the mass transfer equation in nondimensional form as follows:

$$St \frac{\partial c}{\partial t} + \theta v_x \frac{\partial c}{\partial x} = \frac{1}{Pe} \left( \frac{\partial^2 c}{\partial y^2} + \gamma^2 \frac{\partial^2 c}{\partial z^2} \right) \quad (4)$$

where  $c$  is the species concentration,  $\theta = d_i/L$ , and Peclet number  $Pe = Ud_i/D$  may be expressed as the product of Reynolds and Schmidt number  $Pe = Sc \cdot Re$ , with  $Sc = \nu/D$ .

Moreover, to determine the field concentration in the flow, the convection-diffusion equation can be used (**Eq.4**):[28-30]

$$\frac{\partial C}{\partial t} + U \cdot \nabla C = D \nabla^2 U \quad (5)$$

With  $C$  is the ink's element concentration while  $D$  is its fluid diffusion coefficient.

## 4.4 Results and Discussion

### 4.4.1 Printer Design

Direct ink wiring 3D printing platform, shown in **Figure 4-1a**, was designed and developed to enable multimaterial printing by high frequency switching of viscous or viscoelastic inks. The platform employs an XYZ stage whose movement is synchronized with the sequence of inks injected through a single nozzle through pneumatic control of the ink reservoirs in order to produce any designed multimaterial architecture with a 3D form. The MSN3D used to sequence the ink was fabricated by stereolithography using a ProJet 2500 Plus 3D printer (*see Methods for further information*). The MSN3D printhead was designed to deposit up to four inks (**Figure 4-1a-i**), each of which streams through a straight channel (with constant diameter of 500  $\mu\text{m}$ , and length of 6 mm) that merges into a single ink stream directly before the MSN3D outlet nozzle (**Figure 4-1ai**). The ink channels are connected to a bank of ink reservoirs (syringes with pneumatic seals)

containing various viscous or viscoelastic inks. The ink reservoirs are in turn connected upstream through pneumatic lines to a bank of fast-cycling pneumatic solenoids (response time 10 msec) that modulate the pressure in the ink reservoir between a set high (to enable flow) or low (to prevent backflow) pressure to enable high-frequency switching. The design is extensible to additional inks by the introduction of additional channels and appropriate connections to the ink reservoir (**Figure 4-1a**). Images of the 3D printed MSN3D printheads are shown in **Figure 4-1b**. The extruded ink stream dimension is controlled by the diameter of the nozzle tip which was made of a stainless-steel tube with an inner diameter of  $230\ \mu\text{m}$  (25 Gauge) and a priming volume of  $42\ \text{nL}$  (**Figures 4-1b (i, ii)**). The image of four different inks loaded inside the printhead is shown in **Figure 4-1b-iii**.

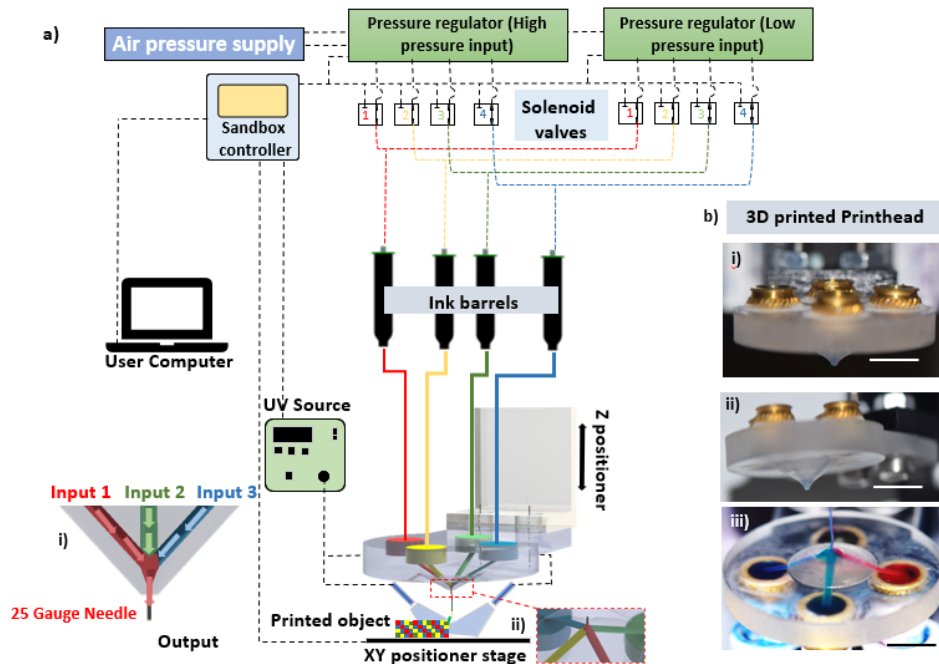


**Figure 4-1** Direct ink writing 3d printing platform for multimaterial highly switchable nozzle 3D printhead (MSN3D). **a)** Schematic of the MSN3D design. Both the MSN3D movements and UV optical fibers are synchronized to cure the deposited ink of the micro-single nozzle by exposure to UV radiation. **i)** A schematic of the MSN3D half-section shows red, green, and blue indicators for different inks supplied into the MSN3D pneumatically, with channel diameter of  $500\ \mu\text{m}$  and length of  $6\ \text{mm}$ , printhead outlet diameter of  $230\ \mu\text{m}$ . **b)** Images of the fabricated printhead **i-** the top (top) and side (**ii-** middle and **iii-** bottom side) views of a single nozzle, four-material MSN3D printhead, Scale bars,  $5\ \text{mm}$ .

#### 4.4.2 Simulation and Optimization of Multimaterial Switching of Viscous Inks

The key benefit of pneumatic operation as compared with syringe pump-driven positive pressure operation is faster start-up times and the ability to switch between inks near instantaneously. It is imperative for pneumatic extrusion that the ink rheology, internal channels inside the printhead, and flow pressure are designed to prevent the interaction of ink from one channel with that in the adjacent channel. This is especially important after switching between the inks in different channels where the transient local pressures can induce backflow resulting in the entrainment of inks or unpredictable composition of the resultant extruded ink, temporarily. In the case when viscoelastic inks are used, their nonlinear flow response to applied pressure can aid in maintaining minimal or zero-backflow conditions as long as the generated back-pressure is not higher than a critical yield stress,  $p_{cr}$ . [24] Thus, the backflow will not happen when the back pressure is lower than a predefined pressure value (depends on the channel geometry and ink rheology). [24] However, with Newtonian inks (as used here), transient pressure fluctuations during switching will introduce some backflow of ink from one channel to another, contaminating the inks in those channels that are static and are not inducing flow into the nozzle at that time, making digital pixelated printing challenging to achieve. In the current work, we determine the baseline positive static pressure that is needed in the non-flowing channels in order to prevent backflow for viscous inks that can enable high frequency switching possible (**Figure 4-2a**). The fluid dynamics of the pulsatile flow and the switching process of a Newtonian fluid were examined numerically using the FLOW-3D numerical software (*see Experimental Methods section-Numerical Model Governing Equations*). This simulation provided a way to visualize the switching process inside the nozzle and define

operating parameters for achieving zero backflow conditions when using Newtonian fluids. In particular, the transient pressure fluctuations, as well as the changes in the interface between the two inks, were easily visualized by the CFD simulations. A laminar flow was considered along with Newtonian properties and a viscosity of 5 Pa.s for the viscous fluid. In addition, the fluid flow simulations were also conducted beyond the extrusion nozzle and extended down to the substrate (see the boundary conditions in **Figure 4-2b**). By simulating the zone after the inks are extruded from the nozzle tip, the interface area between the two extruded inks can be visualized to evaluate the quality of the printing. We evaluated the effect of the frequency of input inks, lower pressure value  $P_L$ , and the substrate speed  $U$  on the switching process.

The initial condition for the simulations was defined as the left channel of the printhead filled with red ink (mass fraction 1) and the right channel filled with blue ink (mass fraction 0) with identical ink properties. Pulsatile pressure with a high-level  $P_H$  and low baseline level  $P_L$  were introduced into the respective ink reservoirs (**Figure 2a**). The effect of two parameters, the lower baseline pressure  $P_L$  and switching frequency  $f$ , on the resulting backflow was examined as shown in **Figure 4-2(c-f)**. At a particular operating frequency, the difference between the pressure at the intersection ( $P_{int}$ ) and the lower baseline pressure determines the pressure drop in the inlet channel for a particular ink and the extent of the recession of the interface between the two inks into that channel (**Figure 4-2c**). Simulations were performed at various lower baseline pressures  $P_L$  (3, 4, and 5.2 bar) with the switching frequency  $f$ , the high-pressure  $P_H$ , and the substrate speed  $U$  set to be 9 Hz, 6 bar, and 40 mm/s, respectively. It can be visually seen in **Figure 4-2d-i** (taken after 1 sec which is sufficient for steady-state development) that when the  $P_L$  was 4 bar

there was no backflow while a lower baseline pressure such as 3 bar resulted in the recession of the interface into the inlet channel. This indicates that the critical pressure value  $P_{cr}$  was close to 4 bar for this operating condition. Interestingly a slightly higher baseline pressure (5.2 bar) than the value at interface resulted in co-flow of both inks and its stratification in the printed line. The pressure distribution shown in **Figure 4-2d-ii** also demonstrate that at close to critical pressure conditions of  $P_L$  the pressure gradient in the static inlet channels is low indicating that there will be no recession of the interface. It should be noted that the determination of appropriate critical pressure to prevent backflow is dependent on ink properties such as viscosity as well as the printhead such as channel length, and channel diameter. After using different ink viscosities within the simulations, we found that the relationship was linear between the viscosity and the critical pressure which can affect the amount of recession accordingly. This allows us to predict and characterize the appropriate pressure setting during printing different Newtonian inks.

In addition to the lower baseline pressure, another parameter that can be controlled is the switching frequency. The effect of frequency on the relationship between the backflow and the difference in pressure between the lower baseline ( $P_L$ ) and the pressure at the intersection is shown in **Figure 4-2e**. The pressure difference predicted from the simulation showed a small variation at different frequencies with the other conditions being similar. For instance, the pressure at the intersection at higher frequencies tends to be lower than the applied  $P_L$ , while it tends to slightly increase at the lower frequency range. Therefore, the behaviour of the flow out of the nozzle is dependent on the applied frequency and the pressure applied in both channels. There are two regimes of operation. At low frequency, any pressure difference between the  $\Delta(P_L - P_{int})$  and  $P_{crit}$  (dependent on ink

parameters such as viscosity difference) results in a significant and steady recession of the interface between the two fluids into the corresponding inlet. At higher frequencies, this recession is small while complete switching from one ink to another occurs at the intersection point. At even higher frequencies, coflow of the two ink ensues, and complete switching does not occur. Therefore, there is an optimal region for operation (3 Hz up to 20 Hz) at  $P_L$  around 4 bar **Figure 4-2e** (pink rectangle) where there is complete switching and minimal recession that is ideal for operation of the printhead with viscous inks. Within this narrow range of operation, one can obtain complete switching with clear interfaces between the different inks for pixelated printing as shown in **Figure 4-2f**. In this case, the lower-pressure  $P_L$  (selected so that  $\Delta(P_L - P_{int}) \sim P_{crit}$ ), the higher-pressure  $P_H$ , and the substrate speed  $U$  were set to be 4 bar, 6 bar, and 40 mm/s, respectively. It can be seen that the printed segments were smaller with increasing the switching frequency. An increase in frequency resulted in deviation from the zero backflow condition as the frequency changes the  $P_{int}$  and that changes the balance between  $\Delta(P_L - P_{int})$  and  $P_{crit}$  (**Figure 4-2f**). Therefore printing at a much higher frequency, say at 50 Hz, will require that the  $P_L$  be changed accordingly to 3.5 bar to compensate for the reduction in  $P_{int}$  and balance  $P_{crit}$ . Therefore, the operational frequency of switching has an effect on the resolution of the print that must be compensated for and the simulation allows one to characterize this process for particular sets of inks that can be implemented into the printing software to get an accurate build. We also investigated the effect of substrate speed on the segment composition width, as shown in **Figure 4-2j**. Different substrate speeds were used (30 mm/s and 60 mm/s), while switching frequency, the higher-pressure, and the lower pressure were set to be 9 Hz, 6 bar, and 4 bar, respectively. It can be seen that the length of the printed segments was increased

with increasing the substrate velocity (**Figure 4-2j**). This can be used as another strategy to control the resolution of the pixelation.

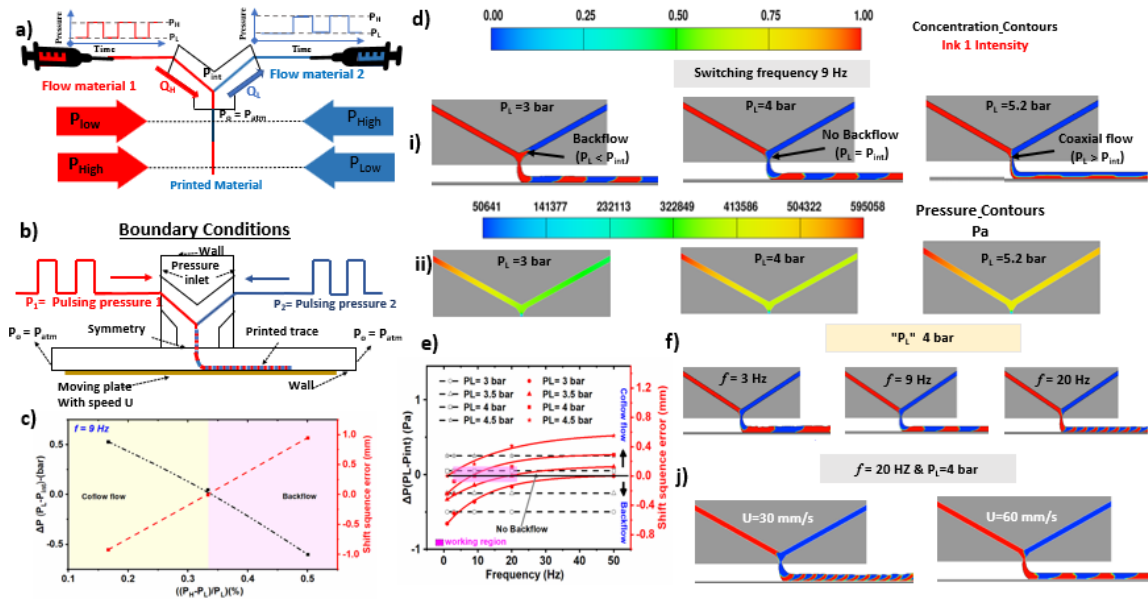


**Figure 4-2 Operating scheme of viscous ink flow through the MSN3D printhead.** a) Schematic of the MSN3D printhead operation, where  $P_H$ – $P_L$  represents the extrusion pressures for materials 1–2. The low-pressure  $P_L$  has to be defined to eliminate any backflow in the low-pressure channel. Below is an illustration representing the process parameters of the inlet pressure pulsations, including cycle period, pulse amplitude, and phase shift. b) CFD simulation to optimize the switching process for backflow elimination. The MSN3D printhead computational model includes two core regions: the channel structure with pressure inlet regime, the printing trace block, and boundary conditions for both areas. c) The corresponding pressure difference between the intersection pressure and lower pressure  $P_L$  with different lower pressure percentages presented on the left y-axis, while the on the right axis, the corresponding backflow shift (zero means no backflow, a positive value means coaxial filament, negative value mean backflow) with lower pressure percentage. d) CFD distribution contours. i) CFD inks concentration, to find the  $P_L$  value at which backflow vanishes,  $P_H$  kept at “6 bar” at the inlets, and  $P_L$  changed from 3-5.2 bar with frequency 9Hz at steady state (after 1 sec). ii) CFD pressure contours, to show the pressure difference on the printhead channels at different  $P_L$  values (3-5.2 bar). e) The corresponding pressure difference and backflow shift with different frequencies at different lower pressure values. f) To show the effect of the frequency on the backflow at the critical  $P_L$ ,  $P_H$  kept at “6 bar” at the inlets and  $P_L$  kept at “4 bar” with different frequencies (3, 9, and 20 Hz) at a steady-state (after 1 sec). j) CFD inks concentration distribution contours at 20 Hz,  $P_L$  4 bar,  $P_H$  6 bar with different feeding rates, showing the effect of feed rates on the printed segment length.

#### 4.4.3 2D Printing with Switching

Next, the performance of the MSN3D printhead was demonstrated by printing several 2D patterns with different materials and architectures. First, the MSN3D was operated at a

number of different switching frequencies to determine its range of operation and the fidelity of the patterns produced. Switching up to 50 Hz was possible and produced alternating and clearly defined segments of the two inks that were switched (**Figure 4-3a**). Next, different patterns presented in **Figure 4-3** were printed with a print speed of 40 mm s<sup>-1</sup>. Multimaterial patterns can be printed using either a vector or a raster scanning approach. In patterns that have relatively large segments of contiguous regions of the same ink, vector scanning is useful as it requires minimal switching (*Appendix 2 Figure 8-1*). The raster scanning approach is more general and applicable for all patterns but requires an ability to switch inks fast to obtain clear spatial resolution. We demonstrate both vector and raster printing with the MSN3D printhead. When we co-printed at high speeds with silicone V35H ‘viscosity of 5 Pa.s’ and silicone V31H ‘viscosity - 1.6 Pa.s’ inks, the ‘more viscous’ silicone ink recessed into the low silicone ink channel inlet. In order to handle inks with different viscosities, we used different lower pressure  $P_L$  ( $P_{L, V35H}$  “3 Pa.s” <  $P_{cr, V31H}$  “4 Pa.s”) for actuation of the respective ink. Using the actuation scheme, we performed vector printing of continuous spiral circle patterns with the transition from a red ink (V35H) to a blue ink (V31H) in the middle of the feature (**Figure 4-3b-i**). The same technique was used to create the same pattern with four different colors and all the used inks had the same viscosity “V35H” (**Figure 4-3b-ii**). The printed design was close to the design and the transition from one ink to the next was smooth topographically. The compositional transition (based on the color) showed a clear interface but was different in different sections of the print. For instance, at the middle of the spiral pattern (**Figure 4-3b-i**) the interface was straight and perpendicular to the print direction while in the outer extreme of the spiral pattern it was stretched over a distance of ~ 10 mm along the direction of the

print even though the interface was clear. This may be attributed to the radius of curvature of the shape being printed and the way that the fluid can be stretched as it is printed. This study shows that only a tiny window of conditions exists where fast and reliable transitions between viscous inks for precise pixelated extrusion printing are possible. It also indicates that the switching frequency is a crucial parameter for defining the operating conditions and the pneumatic system, which requires more enhancement to allow more controllability of the printing and switching parameters. Another issue could happen during switching associated with the interface between the ink flow and the inner wall printhead outlet. A surface treatment may be a solution for having perfectly continuous flow during printing without any residual ink remaining at the printhead outlet tip, which can cause that transitional residue of the blue ink can be found in each line of the red ink or verses verse.

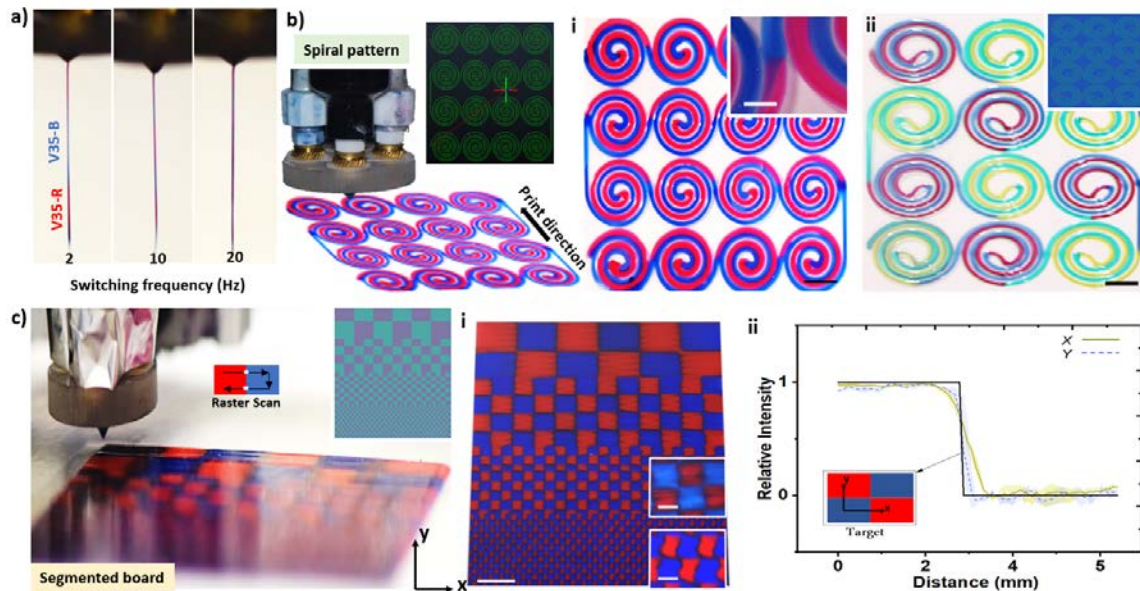


**Figure 4-3 Printing segmented objects with equal distances.** a) One continuous filament output with increased switching frequencies from a two-material nozzle. b) A multi-material MSN3D printhead with a circular print path using silicone inks (V35H). **i-** two inks, **ii-** four inks. Scale bars in b, 10 mm. c) A multi-material MSN3D printhead with a segmented printed board using silicone inks (V35H) with the target printed board. **i-** The printed segmented board with different segments width, scale bar 16mm. Two magnified photos of for the segmented board, the upper one with a scale bar, 4 mm, lower one with a scale bar, 2 mm. **ii-** The relative intensity of the red and blue colors from the transition zones in both X and Y directions, the shaded area is the standard deviation from  $n=4$  measurements.

A raster scanning approach to printing can avoid interfacial stretching and may be suitable for all designs.[24] For this reason, the raster scan technique had been used to print segmented boards with different segment widths (ranging from 16 mm to 2 mm), as shown in **Figure 4-3c**. To get the relative intensity, the intensity values were normalized according to the RGB intensity of red and blue regions close to the transition zone ( $> 3$  mm “segment width”), where the colored area represents the standard deviation based on 4 four measurements (**Figure 4-3c-ii**). The print fidelity was high, and the printed features were similar to the design. Relatively smooth transition between the two-colored regions was observed when the pattern sizes were large. The line separating the two regions was close to a straight line when 16 mm features (4% deviation from straightness) were printed and became more jagged as the feature size was reduced to 2 mm (18% deviation from straightness). The deviations from straightness were calculated using the least-squares reference line method (LSL), which is commonly utilized in industrial applications.[31] These results show that the MSN3D printheads can be used to produce multimaterial 2D patterns with a resolution of  $\sim 2$ mm pixel size using viscous silicone materials when operating under narrow conditions with carefully calibrated applied backpressure to prevent the ingress of other inks into the inlet channels. This approach can also be extended to other ink materials such as UV-curable epoxy, which exhibits a Newtonian behavior (appendix 2 **Figure 8-1d**).

In order to demonstrate the capability of this MSN3D printhead to print a pattern with multiple segment sizes, we designed complex patterns with an assortment of segment widths. The first demonstration was printing our lab logo “CAMEF”, which included regions of different segments widths “ranging from 3 mm to 20 mm” (**Figure 4-4a**). For

CAMEF logo printing, V35H black and V35H white inks were used with a printing speed of 20 mm/s. Moreover, the same technique and inks used to print the word “McMaster”, shown in **Figure 4-4b**. As a second demonstration, a periodic and complex triangular-patterns G-code was rapidly extracted from a bitmap image and then printed using MSN3D printhead (**Figure 4-4c**). All of the prints faithfully reproduced the patterns generated by the G-code and have the same transition points. During material switch points, the two-dimensional transition segments were measured to be around 500  $\mu\text{m}$  in length (4 times the resolution obtained in the segmented board pattern) “with printing speed 20  $\text{mm}\cdot\text{s}^{-1}$ ”, resulting in a switch time of 20 ms and an actual switching frequency of about 40 Hz. The sloped line that forms the triangular pattern in **Figure 4-4c** had a 4-20% variation from straightness at various print sections. The obtained resolution depends on the printhead's priming volume and the printing process conditions. To enhance the obtained resolution, the printhead's priming volume can be designed with lower dimensions, yet that may limit the choice of the ink as higher viscous ink might not be possible to proceed. The required pressure increases significantly as the channel dimension decreases, especially with high viscosity inks. Therefore, it is a trade-off problem between the material availability and the printhead dimensions. In addition, the more control of the printing process conditions like the pressure flow, the more possibility to obtain greater printing precision and reliability.

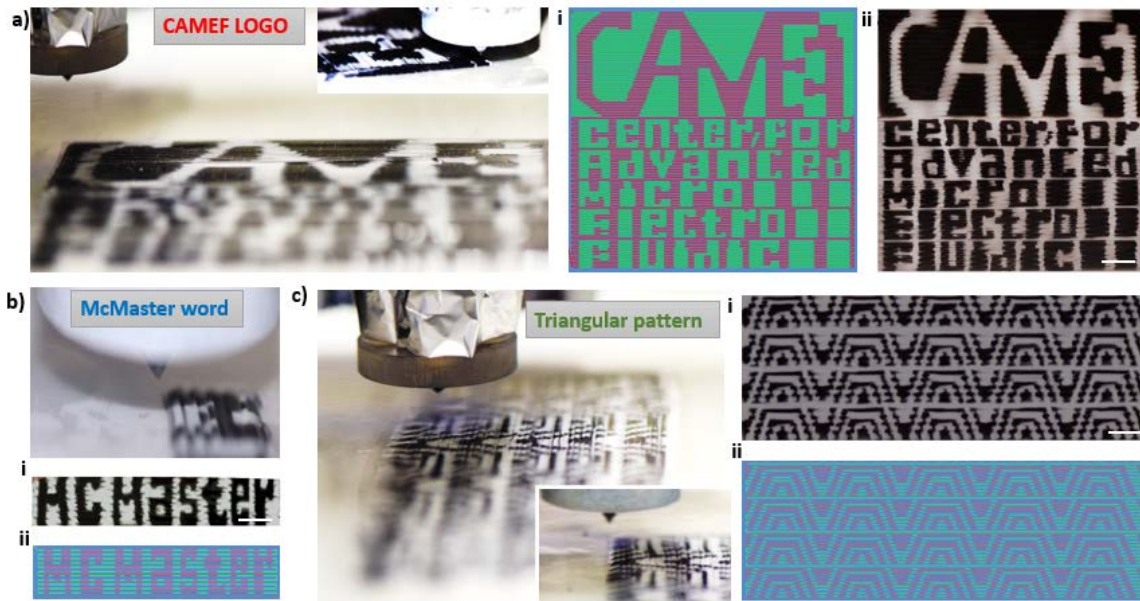


**Figure 4-4 Printing segmented objects with random distances.** a) Printing a two-material pattern using a single nozzle printhead by switching between two materials (V35H black, V35H white) for creating CAMEF logo word. **i-** The target pattern created by the G-code, **ii-** The actual printed pattern, Scale bar, 10 mm. b) Printing a 2D pattern McMaster word. **i-** The actual printed pattern, Scale bar, 10 mm, **ii-** The target pattern created by the G-code. c) Raster scan printing of a random triangular pattern in silicone V35H (black) and silicone V35H (white) using an MSN3D printhead. **i-** The actual printed pattern, Scale bar, 10 mm, **ii-** The target pattern created by the G-code.

#### 4.4.4 3D Printing of Actuators

Finally, to demonstrate that 3D multimaterial printing to embed structural intelligence is possible, an actuator was printed where a combination of rigid and soft elastomeric materials was switched to produce defined 3D patterns that, when pneumatically actuated, will result in bending in certain pre-defined direction. The 3D patterns used and the periodic arrangement of the rigid and soft elastomers are shown in *Appendix 2 Figure 8-3*. First, we used UV curable viscoelastic inks (*Appendix 2 Table 8-1*) to build 3D structures like a triangular prism with a stiff internal wall surrounded by a sloping and flexible external wall. The printing was performed such that two independently actuatable chambers were formed on either side of the stiff internal wall at the centre of the prism (*Appendix 2 Figure 8-3(b-d)*). By applying a vacuum to one chamber and positive pressure

to the other, the tip of the prism can be actuated in either direction. (*Appendix 2 Figure 8-3b*). We show that not only can this structure be actuated, placing two prisms adjacent to each other can be used synergistically to close the gap between the tips of the adjacent prisms or expand it and function like grippers. We tested the printed prism with different cyclic vacuum frequencies, and the response was the same at low frequencies lower than 1 Hz with an actuation distance of 10 mm. To further show the capabilities of our MSN3D printhead, we fabricated different 3D patterns like fingers using the UV curable silicones (*Appendix 2 Figure 8-3f*). For realistic applications in robotics, a soft actuator was also made of rigid and soft heat-curable elastomers in the form of fingers with the soft material printed in locations where bending was required. These were also printed with actuation chambers that can be pressurized to actuate, as shown in **Figure 4-5a**. The topography of many soft robots' actuators is periodic, making them compatible with MSN3D printing (**Figure 4-5b**). Our robot gripper modules are made up of three pneumatic actuators connected and pneumatically actuated through positive pressure. Upon applying pressure, the silicone walls of these actuators stretch, causing a vertical and lateral displacement of the stiff actuator body (**Figure 4-5 (b-e)**). Using a pattern consisting of overhanging walls and closed channels (**Figure 4-5e**), we simultaneously printed flexible (0.75 MPa; white) and stiff (2.4 MPa; blue) silicone inks simultaneously. After the soft actuator was cured at 120 °C for 6 hr, a thin film (~ 1 mm) from the UV curable silicone was coated using dip coating (*Appendix 2 Figure 8-4*). This is because the soft actuator before the dip-coating was only handled low pressure due to the low interface bonding between the printed layers. Thus, the dip-coating was performed, and the soft actuators could handle the pressure of about 100 kPa.

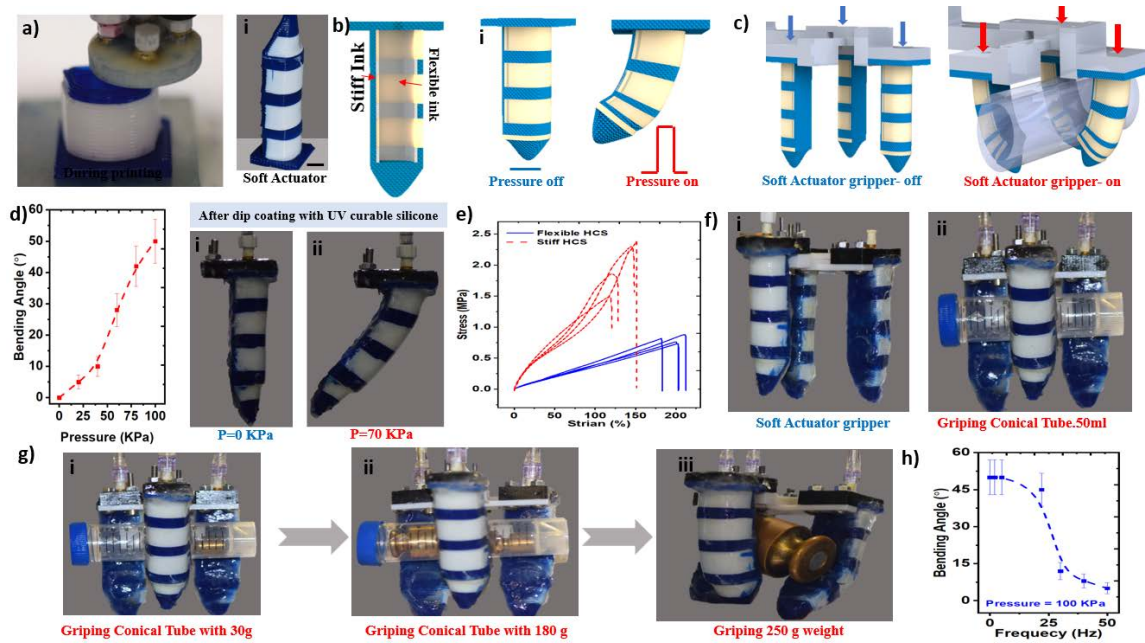


**Figure 4-5 MSN3D printing of soft-actuator gripper.** a) MSN3D printing of a soft actuator using two-material MSN3D printhead. Print time, 40 min, **i**- the printed actuator after curing, scale bar, 10 mm. b) Illustration of the design elements of the actuator, **i**- actuation pattern for the single actuator used to produce bending motion. c) Actuation pattern for three soft actuators network used to work like a gripper. d) Illustration of the bending angle of a single actuator as a function of input pressure. Front view of the soft actuator under, **i**- P=0 KPa, **ii**- P=70 KPa. e) Stress-strain curves from  $n = 4$  tensile tests for stiff heat-curable silicone “HSC” (2.4 MPa; red) and Flexible HSC (0.75 MPa; blue). f) Photographs of the soft gripper under two states, **i**- pressure off, **ii**- pressure on grasping and lifting test empty conical tube. g) The soft gripper was attached to the 3d printer frame for the grasping test. **i**- 30 g weight inside a conical tube, **ii**- 180 g weight inside a conical tube, **iii**- 250 g weight. h) Illustration of the bending angle of a single actuator as a function of actuation frequency at input pressure 100 KPa.

The actuators were pneumatically actuated by alternating internal pressure of these chambers to control the  $\Delta X$  displacement. We evaluated the fabricated actuator by testing it at different pressures and measuring the bending angle that would occur, as shown in **Figure 4-5d**. These soft actuators were able to handle pressure of about 100 kPa, which resulted in bending angles of up to  $50^\circ$  (**Figure 4-5d**). A gripper configuration (**Figure 4-5f**) consisting of three soft printed actuators was used to test how well they could grasp and lift five different bodies to evaluate our soft actuators' applicability. A variety of bodies with various weights and shapes were evaluated (**Figure 4-5(f-g)**). This soft actuator could

lift and grasp up to 250g, as indicated in **Figure 4-5g**. A second test was performed to assess the soft actuator with a different pneumatic cyclic frequency; the soft actuator response was the same at low frequencies lower than 4 Hz. However, the bending angles start to decrease at higher frequencies ( $> 4$  Hz) (**Figure 4-5h**).

## 4.5 Conclusion

We demonstrate a robust and tunable multimaterial printhead with ultrarapid switching capabilities for producing pixelated patterns from viscous and viscoelastic inks. By leveraging the pressure-driven flow behavior of various inks along with adjustable pressure, we can flawlessly switch between several viscous or viscoelastic materials for continuous printing of controllable segmented filaments. Rapid and reliable switching of viscous inks is difficult due to its rheology. Using computer simulations of fluid flow in the nozzle as well as its extrusion onto the printhead, we have mapped the instantaneous pressure generated at the junction between the ink inlets at various operating frequencies, extrusion speeds and inlet pressures. We find that providing an backpressure to ink reservoirs that are not active can neutralize the pressure gradient that causes ingress of one ink into the inlet channel of the other. Interestingly, we find that this backpressure needed is dependent on the frequency of switching, and therefore it has to be dynamically changed depending on the switching frequency associated with the pixelated printing. Once the conditions required for a particular combination of inks are determined, they can be easily incorporated into the software that can simultaneously control the G-code for movement of the nozzle and applied pressure on the ink reservoirs. We demonstrate the versatility of this method by printing pixelated 2D patterns with up to 4 inks and 3D patterns with 2 inks. Resolutions of 500  $\mu\text{m}$  were achieved. We also demonstrate the use of the same printhead

with viscoelastic inks and print soft robotic actuators that exploit the combination of hard and soft materials co-printed to perform pneumatically driven gripping functions. This work has demonstrated that a narrow range of conditions exist where fast and reliable switching of viscous inks are possible for accurate pixelated 3D extrusion printing. However, it also shows that the frequency of switching is a key determinant of the operating point, and fine and dynamic control of reservoir pressure both for the active ink as well as other inks is required. In the future, a sensory feedback-driven dynamic adjustment of the ink reservoir pressure based on the position of the interface in the respective inlet channels into the printhead can be integrated to obtain greater accuracy and reliability. Nevertheless, by providing a method for printing viscous inks, this approach expands the range of inks used for pixelated 3D printing and can significantly apply in silicone and epoxy multimaterial 3D printing with functional properties.

## **Acknowledgements**

We acknowledge the financial support of the Natural Sciences and Engineering Research Council of Canada. We also would like to thank Dr Michael Brook and Robert for their support with the UV curable ink formulation. PRS also thanks to the Canada Research Chair Program for support. We are very grateful for the gift of a photoinitiator from IGM Resins, Inc. We are very grateful for the academic licence of flow-3d software from flow science, Inc.

## **References**

- [1] C. Bader *et al.*, "Making data matter: Voxel printing for the digital fabrication of data across scales and domains," *Science advances*, vol. 4, no. 5, p. eaas8652, 2018.
- [2] M. Rafiee, R. D. Farahani, and D. Therriault, "Multi-Material 3D and 4D Printing: A Survey," *Advanced Science*, vol. 7, no. 12, p. 1902307, 2020.

- [3] J. R. Raney, B. G. Compton, J. Mueller, T. J. Ober, K. Shea, and J. A. Lewis, "Rotational 3D printing of damage-tolerant composites with programmable mechanics," *Proceedings of the National Academy of Sciences*, vol. 115, no. 6, pp. 1198-1203, 2018.
- [4] M. Wehner *et al.*, "An integrated design and fabrication strategy for entirely soft, autonomous robots," *Nature*, vol. 536, no. 7617, pp. 451-455, 2016.
- [5] A. D. Valentine *et al.*, "Hybrid 3D printing of soft electronics," *advanced Materials*, vol. 29, no. 40, p. 1703817, 2017.
- [6] R. Sochol *et al.*, "3D printed microfluidic circuitry via multijet-based additive manufacturing," *Lab on a Chip*, vol. 16, no. 4, pp. 668-678, 2016.
- [7] L. Leng, A. McAllister, B. Zhang, M. Radisic, and A. Günther, "Mosaic hydrogels: one-step formation of multiscale soft materials," *Advanced materials*, vol. 24, no. 27, pp. 3650-3658, 2012.
- [8] A. Hosny *et al.*, "From improved diagnostics to presurgical planning: high-resolution functionally graded multimaterial 3D printing of biomedical tomographic data sets," *3D Printing and Additive Manufacturing*, vol. 5, no. 2, pp. 103-113, 2018.
- [9] C. J. Hansen *et al.*, "Inkjet Printing: High-Throughput Printing via Microvascular Multinozzle Arrays (Adv. Mater. 1/2013)," *Advanced Materials*, vol. 25, no. 1, pp. 2-2, 2013.
- [10] X. Li, J. M. Zhang, X. Yi, Z. Huang, P. Lv, and H. Duan, "Multimaterial microfluidic 3D printing of textured composites with liquid inclusions," *Advanced Science*, vol. 6, no. 3, p. 1800730, 2019.
- [11] N. Bhattacharjee, C. Parra-Cabrera, Y. T. Kim, A. P. Kuo, and A. Folch, "Desktop-Stereolithography 3D-Printing of a Poly (dimethylsiloxane)-Based Material with Sylgard-184 Properties," *Advanced materials*, vol. 30, no. 22, p. 1800001, 2018.
- [12] L. Hao *et al.*, "Direct Ink Writing of Mineral Materials: A review," *International Journal of Precision Engineering and Manufacturing-Green Technology*, vol. 8, pp. 665-685, 2021.
- [13] N. W. S. Pinargote, A. Smirnov, N. Peretyagin, A. Seleznev, and P. Peretyagin, "Direct Ink writing technology (3D printing) of graphene-based ceramic nanocomposites: A review," *Nanomaterials*, vol. 10, no. 7, p. 1300, 2020.
- [14] Y. L. Yap, S. L. Sing, and W. Y. Yeong, "A review of 3D printing processes and materials for soft robotics," *Rapid Prototyping Journal*, 2020.
- [15] S. Zheng, M. Zlatin, P. R. Selvaganapathy, and M. A. Brook, "Multiple modulus silicone elastomers using 3D extrusion printing of low viscosity inks," *Additive Manufacturing*, vol. 24, pp. 86-92, 2018.
- [16] C. Xu, B. Quinn, L. L. Lebel, D. Therriault, and G. L'Espérance, "Multi-material direct ink writing (DIW) for complex 3D metallic structures with removable supports," *ACS applied materials & interfaces*, vol. 11, no. 8, pp. 8499-8506, 2019.
- [17] D. Han and H. Lee, "Recent advances in multi-material additive manufacturing: methods and applications," *Current Opinion in Chemical Engineering*, vol. 28, pp. 158-166, 2020.
- [18] I. Hassan and P. R. J. A. M. Selvaganapathy, "A Microfluidic Printhead with Integrated Hybrid Mixing by Sequential Injection for Multimaterial 3D Printing," p. 102559, 2021.
- [19] W. Liu *et al.*, "Rapid continuous multimaterial extrusion bioprinting," *Advanced materials*, vol. 29, no. 3, p. 1604630, 2017.
- [20] T. K. Merceron *et al.*, "A 3D bioprinted complex structure for engineering the muscle-tendon unit," *Biofabrication*, vol. 7, no. 3, p. 035003, 2015.
- [21] D. B. Kolesky, R. L. Truby, A. S. Gladman, T. A. Busbee, K. A. Homan, and J. A. Lewis, "3D bioprinting of vascularized, heterogeneous cell-laden tissue constructs," *Advanced materials*, vol. 26, no. 19, pp. 3124-3130, 2014.

- [22] C. J. Hansen *et al.*, "High-throughput printing via microvascular multinozzle arrays," *Advanced Materials*, vol. 25, no. 1, pp. 96-102, 2013.
- [23] J. O. Hardin, T. J. Ober, A. D. Valentine, and J. A. Lewis, "Microfluidic printheads for multimaterial 3D printing of viscoelastic inks," *Advanced materials*, vol. 27, no. 21, pp. 3279-3284, 2015.
- [24] M. A. Skylar-Scott, J. Mueller, C. W. Visser, and J. A. Lewis, "Voxelated soft matter via multimaterial multinozzle 3D printing," *Nature*, vol. 575, no. 7782, pp. 330-335, 2019.
- [25] Materials Guide, Address the most demanding prototyping and production applications with an advanced plastics materials portfolio, 333 Three D Systems Circle, Rock Hill, SC 29730: 3D Systems Corporation, 2021, p. 47. [Online]. Available.
- [26] R. Tanner and M. Keentok, "Shear fracture in cone-plate rheometry," *Journal of Rheology*, vol. 27, no. 1, pp. 47-57, 1983.
- [27] J. M. Krishnan, A. P. Deshpande, and P. S. Kumar, *Rheology of complex fluids*. Springer, 2010.
- [28] J. M. Ottino and S. Wiggins, "Introduction: mixing in microfluidics," ed: The Royal Society, 2004.
- [29] H. A. Stone, A. D. Stroock, and A. Ajdari, "Engineering flows in small devices: microfluidics toward a lab-on-a-chip," *Annu. Rev. Fluid Mech.*, vol. 36, pp. 381-411, 2004.
- [30] F. M. White and I. Corfield, *Viscous fluid flow*. McGraw-Hill New York, 2006.
- [31] T. Restivo, J. Rodrigues, F. Chouzal, and P. Menezes, "Online virtual system for straightness evaluation," in *2013 2nd Experiment@ International Conference (exp.at'13)*, 2013, pp. 192-193.

## **5 Chapter 5**

# **Contour tracing printheads for multimaterial printing over complex surfaces**

### **Complete Citation:**

I. Hassan and P. R. Selvaganapathy, " Contour tracing printheads for multimaterial printing over complex surfaces", under review in Additive Manufacturing, 2022.

### **Contribution:**

I. Hassan: Designed and performed all experiments, interpretation and analysis of data, wrote the manuscript draft.

P. R. Selvaganapathy: Supervised I. Hassan and provided guidance, revised and edited the manuscript.

## 5.1 Abstract

3D extrusion printing generally is performed on a planar surface with precise control over the distance between the print nozzle and the print bed to ensure continuous and accurate printing. Changes in gap spacing between the nozzle and the print head can result in breakup of the extruding print filament and loss of resolution or discontinuous line formation. One approach to resolving this issue can be to use a computer vision system that uses the tool path to determine the surface topography on the printbed and provides closed loop control to dynamically change the height of the print nozzle for effective printing. This method is expensive and computationally intense. Here, we provide a simpler and more effective alternative by using simple mechanical means to provide a dynamic self adjusting feedback that automatically maintains the nozzle substrate gap that results in effective 3D printing on a variety of surface topographies. Our multimaterial microfluidic printhead tracker (MM-PHT) uses roller bearings at the tip of the printhead to obtain mechanical feedback and a spring loaded printhead that dynamically adjusts the distance of separation of the nozzle from the printbed based on that feedback. This system does not require real-time computation and is simple, low cost and robust to implement on any 3D printer. We have optimized the design of the MM-PHT using modal and transient analysis and validated its performance experimentally by printing a variety of 2D patterns over complex surfaces like a human hand and dome like structures. 3D printing on complex surfaces can also be performed by initially printing using the MM-PHT and then using a stiffer printhead used in conventional extrusion printing. We also combine the tracker with a multimaterial printhead to demonstrate four color multimaterial printing over a Bézier surface and dome substrate. This simple and low-cost modification can extend the

application of extrusion printing directly onto surfaces of equipment and parts that are not always planar.

## 5.2 Introduction

Due to its origins in prototyping, 3D extrusion printing has mostly been performed on planar substrates or printbeds.[1, 2] In many instances the distance between the nozzle and the printbed is critical in maintaining an effective extrusion and deposition shape of the filament and the print resolution. More recent applications where 3D printing can be used such as the fabrication of next-generation wearable devices [3] including monitoring the body's health,[4, 5] or in industrial applications like integrating sensors on wind turbine blades [6] require direct deposition of the printed material on to surfaces that are anything but planar. [3, 7-11] Target substrates such as skin, organs, turbine blades and other wavy textured surfaces contain non planar surfaces that may be smoothly varying in 3D and may not conform to a defined geometrical shape or profile. Such a shape when used as a printbed of a conventional extrusion printer, results in dynamic variation in distance between the nozzle and printbed as the printhead moves over the surface resulting in discontinuous and intermittent deposition that makes extrusion printing unsuitable. One approach that has been taken is to visually acquire the nonplanar shape a priori and modify the toolpath contours to accommodate it while printing on a supporting bath.[12-14] This makes the operation more complex, and alignment of the start point is important. Another approach is to design the printed part from a stretchable material such as silicone and print it flat and then transfer it on to the non planar target substrate for a conformal contact.[15-19] Many devices have been fabricated using this approach to produce flexible, stretchable sensors,[20, 21] energy harvesting devices,[22, 23] and even wearable devices.[24-26]

Although it is widely used, the stretched fit on to the nonplanar surface introduces interfacial stresses that will delaminate the 3D printed feature over the long run.

Several techniques have been developed to accommodate additive 3D printing on nonplanar structures. One method was to use laser scanning to acquire the topography and use it to determine the tool path which has been implemented to print 3D conformal features on inflatable elastomeric substrates.[27] Alternatively, using Curved-Layer Manufacturing (CLM), additive parts can be created by following the local geometry rather than employing the traditional planar layer by layer stacking approach.[28-30] However, these approaches require significant pre-processing to acquire the topography of the non-planar surface to then create a specific tool path for the target nonplanar surfaces. Other recent methods have used vision based imaging for real time tracking of the print substrate and open-loop calibration processes to print nanoparticle inks or hydrogels.[3, 4] Nevertheless, they still require pre-mapping of the topography or a 3D vision system that is expensive and can be affected by lighting and other environmental conditions. An adaptive 3D printing system composed of a passive closed-loop feedback system would be ideal to dynamically accommodate local changes in topography in real time. Vision based systems require significant and computationally expensive post processing to provide real-time closed loop feedback and may not be ideal for these purposes.

Here, we have designed and implemented a multimaterial microfluidic printhead tracker (MM-PHT) that can track the changes in surface topography in real-time using a simple mechanical passive control mechanism to provide instantaneous closed loop feedback that can be used to move the printhead automatically to accommodate the changes in topography. This approach is low-cost, high bandwidth and scalable to accommodate a

variety of complex substrate topographies. In addition, due to its multimaterial capability it can print up to four different inks and effortlessly switching between them during printing. Most importantly, the MM-PHT device can be easily dismantled to maintain and clean and quickly reassembled. The design parameters of the tracker such as tip gap, coefficient of friction, tracker feed rate, inlet pressure, structure weight were investigated using a computational mechanical model and validated through experimental results. They show that the tracker geometry which uses one ball support was the most suitable. To demonstrate the scalability of this method, we printed various features such as a 2D mesh network, spiral path over different complex profiles, and a 3D structure over the dome surface. Also, we printed a 2D colored map of four different colors over complex substrates using UV curable silicone elastomer inks. By enabling real-time tracking, the printhead tracks different surface topologies, and this approach vastly expands the palette of features that can be embedded and printed over complex objects.

## 5.3 Materials and Methods

### 5.3.1 Materials

As described in **Table 3-1**, [31] UV curable Silicone inks with different recipes have been utilized. vinylsilicones: vinyl terminated polydimethylsiloxane, DMS-V31, and DMS-V35 with molecular weights of 3853, 21500, 42300  $\text{g}\cdot\text{mol}^{-1}$ , respectively and [13-17% (mercaptopropyl)methylsiloxane] – dimethylsiloxane copolymer (SMS-142) were bought from Gelest, Inc, US. Photoinitiator TPO-L 6 was gotten as a sample from IGM Resins, Inc. Red, blue, yellow, and green silicone dyes were purchased from Smooth-On. Moreover, the used UV curable inks have a rheological feature obtained using a rotational

rheometer. A Newtonian response was received for the V31 and V35 with a viscosity of 1.6 and 5 Pa.s.

### **5.3.2 Fabrication of Single Material Tracker**

The tracker devices were designed using CAD software (SolidWorks, Dassault Systèmes, Inc). The AutoCAD files were converted to STL (Stereolithography) files. The slider and slider support were 3D printed using a PLA filament in Prusa 3D printing at high-resolution settings. While, the ball socket was 3D printed using ProJet 2500 Plus 3D printer set to the XHD (Xtreme High Definition) printing configuration with high resolution, up to 1600 x 900 x 790 DPI. Following printing, we put the printed part in an oven at ~60 °C and kept it to ensure that the wax was melted. To clean the printed piece, we also immerse the part in a heated ultrasonic bath. After that, the printed parts were underwater in soap and sonicated water “DI water” for 10 min for eradicating any wax or oil residual from the parts. Then, we assembled the steel ball instead of the ball socket. Following, we interfered fit the socket with a steel needle (25 gauge), which attached at the end of the outlet. Then, the assemble tip tracker is integrated using a thread connection with an ink barrel mounted with the slider tracker. When we printed multimaterial structures, we used a predesign microfluidic printhead described in detail at the following reference.[32]

### **5.3.3 Numerical model Governing Equations**

In addition, a material model is a requirement for creating a numerical model. Thus, we used a linear elastic model for our design with two different materials. First is a structural steel material that was predefined in the Ansys Workbench library. The second material used in our model is a “thermoplastic” polyester called PLA material. Two types of elements were applied to create the discretized model. Tetrahedral elements with ten nodes

(Tet10) were used for most of the design parts. Hexahedron elements with 20 Nodes (Hex20) were utilized to meshing the tracking mechanism's sliding walls to provide excellent accuracy when required. After carrying out a mesh independence study, an automatic grid generation is used for the mechanical tracking model, consisting of 87919 nodes and 43891 elements.

### ***Modal Analysis***

Under the assumptions of an undamped scheme, the equation of motion can be presented in matrix form as follows:[33]

$$[M]\ddot{u} + [K](u) = [0] \quad (1)$$

Note that [K], the structure stiffness matrix. For a linear system, free vibrations will be a harmonic form: [33]

$$\{u\} = \{\phi\}_i \cos \omega_i t \quad (2)$$

where:  $\{\phi\}_i$  = eigenvector representing the mode shape of the  $i^{\text{th}}$  natural frequency

$\omega_i$   $i^{\text{th}}$  natural circular frequency (radians per unit time)

t = time

Thus, equation (1) becomes: [33]

$$(-\omega_i^2 [M] + [K])\{\phi\}_i = \{0\} \quad (3)$$

This equality is satisfied if either  $\{\phi\}_i = \{0\}$

or if the determinant of  $([K] - \omega^2[M])$  is zero. The first option is the trivial one and, therefore, is not of interest. Thus, the second one gives the solution: [33]

$$|[K] - \omega^2[M]| = 0 \quad (4)$$

This is an eigenvalue problem that may be solved for up to  $n$  values of  $\omega^2$  and  $n$  eigenvectors  $\{\phi\}_i$  which satisfies equation (4), where  $n$  is the number of DOFs. Rather than outputting the natural circular frequencies  $\omega$ , the natural frequencies ( $f$ ) are output; where:

[33]

$$f_i = \frac{\omega_i}{2\pi} \quad (5)$$

where:

$f_i$   $i^{\text{th}}$  natural frequency (cycles per unit time)

### ***Transient Analysis***

For the Mechanical tracking application module, ANSYS Mechanical APDL solver was utilized to conduct a transient structural analysis (also known as a time history analysis). It can also be used to mathematically calculate the time-varying displacements, stresses, and forces in a structure when subjected to transient loads. The transient analysis solution method used depends on the DOFs involved. If the analysis contains both first and second-order DOFs (e.g., structural and magnetic), each DOF is solved using the appropriate method. Following performing an independent mesh test, an automatic mesh option was used, consisting of 16675 nodes and 5051 elements. For matrix coupling between first and second-order effects, a combined procedure is used. The transient dynamic equilibrium equation of interest is as follows for a linear structure:[33]

$$[M]\{\ddot{u}\} + [C]\{\dot{u}\} + [K]\{u\} = \{F^a\} \quad (6)$$

where:

$[M]$  = structural mass matrix

$[C]$  = structural damping matrix

$[K]$ = structural stiffness matrix

$\{\ddot{u}\}$ = nodal acceleration vector

$\{\dot{u}\}$ = nodal velocity vector

$\{u\}$  =nodal displacement vector

$\{F^a\}$ = applied load vector

The Newmark method is used for implicit transient analyses and is described below. The Newmark method uses finite-difference expansions in the time interval  $\Delta t$ , in which it is assumed that: [33]

$$\begin{aligned} \{\dot{u}_{n+1}\} &= \{\dot{u}_n\} + [(1 - \delta)\{\ddot{u}_n\} + \delta\{\ddot{u}_{n+1}\}]\Delta t \\ \{u_{n+1}\} &= \{u_n\} + \{\dot{u}_n\} \Delta t + \left[\left(\frac{1}{2} - \alpha\right)\{\ddot{u}_n\} + \alpha\{\ddot{u}_{n+1}\}\right] \Delta t^2 \end{aligned} \quad (7)$$

Where: [33]

$$\begin{aligned} \alpha, \delta &= \text{Newmark integration parameters} \\ \Delta t &= t_{n+1} - t_n \\ \{u_n\} &= \text{nodal displacement vector at time } t_n \\ \{\dot{u}_n\} &= \text{nodal velocity vector at time } t_n \\ \{\ddot{u}_n\} &= \text{nodal acceleration vector at time } t_n \\ \{u_{n+1}\} &= \text{nodal displacement vector at time } t_{n+1} \\ \{\dot{u}_{n+1}\} &= \text{nodal velocity vector at time } t_{n+1} \\ \{\ddot{u}_{n+1}\} &= \text{nodal acceleration vector at time } t_{n+1} \end{aligned}$$

Since the primary aim is the computation of displacements  $\{u_{n+1}\}$ , the governing equation is evaluated at time  $t_{n+1}$  as [33]

$$[M]\{\ddot{u}_{n+1}\} + [C]\{\dot{u}_{n+1}\} + [K]\{u_{n+1}\} = \{F^a\} \quad (8)$$

## 5.4 Results and Discussion

### 5.4.1 Printer Design

A customized 3D printer system with z-axis feedback control, as shown in **Figure 5-1**, was designed to dispense and print soft inks like silicone-based materials (*Appendix I Table 3-1, see the experimental section for more details*) over complex surfaces. A conventional direct writing extrusion system includes a reservoir (usually in the form of a syringe containing ink), a nozzle having a defined circular cross-section, and a print substrate, where the ink is deposited and cured upon. In addition, the system contains a computer controller that synchronizes the extrusion and deposition of inks from the print nozzle with its motion on the print bed. A fiber bundle positioned opposite to the nozzle output exposes the extruded ink filament to UV illumination. Since the inks used are rapid cure, the UV light beam was directed just below the tip of the nozzle, in order to prevent polymerization at the tip that can initiate clogging. A z-axis feedback was included in order to provide real-time measure of the print substrate topography immediately in front of the tool path and to accommodate the non-planar geometry of the print substrate. This feature can be achieved in two ways - passive control and active control. Unlike other approaches where an active, vision-based, computationally expensive real time feed back is used, we have introduced a passive, simple, robust mechanical feedback system that is capable of achieving the same functionality but in a more elegant manner. Inspired by a ballpoint pen that exploits a small steel rotating ball to move and dispense ink as we write, we have designed a tracker mechanism that allows smooth motion of the printhead over nonplanar surfaces and combined it with a spring-loaded tracker that can follow the z-axis changes in

the underlying topography and move the printhead accordingly to conform to the underlying surface for effective extrusion printing (**Figure 5-1a**).

Specifically, we use a spring-loaded rolling ball head to mechanically contact the print substrate for tracing the topography and providing instantaneous feedback (see **Figure 5-1a**). The rolling ball head significantly reduces the frictional resistance to the movement of the printhead and also is gentle enough to not damage the previously printed layers. The passive control system consists of a spring-loaded sliding system that tracks the changes of the surface's height by making the printhead slide up and down. The actual printhead tracker is presented with an printed spiral over a dome like structure in **Figure 5-1a-i**. The weight of this mechanism was sufficient to maintain contact between the ball and the nonplanar print surface thereby tracking the z-axis location of the print substrate in real-time and adjusting the position of the nozzle accordingly. The steel ball was located between the nozzle tip and the surface by a socket that can hold roller balls and also provides a fixed standoff distance (**Figure 5-1a-ii**). The socket is designed similar to a ball point pen so that the ball is held but can roll in two directions freely. This allows unconstrained but conformal motion of the printhead on the non-planar topography of the print substrate. The rigidity and compliance of the mechanical passive control system along with the required contact force should be optimized to obtain the best print characteristics. Contact force and printing speed in the mechanical tracking system significantly influence the printed filament height and width. We considered three different designs that included 1-3 ball sockets (**Figure 5-1b**) to adjust rigidity and compliance of the tracker mechanism. We performed a finite element analysis using modal analysis (**Figure 5-2a-2b**) and

transient structural analysis (**Figure 5-2c-2d**) to optimize these parameters and arrive at the right configuration for the tracker mechanism.

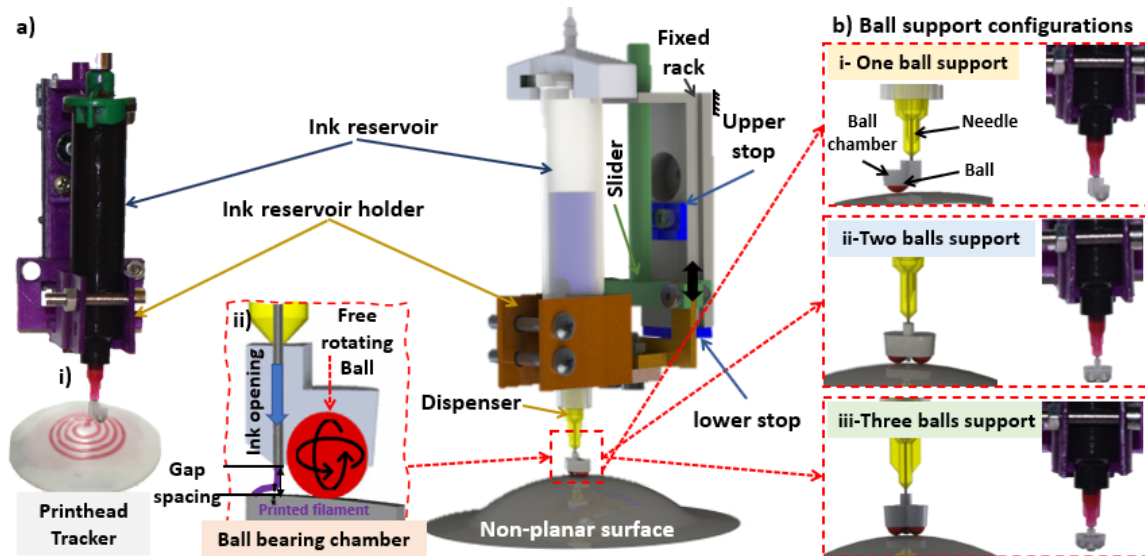


**Figure 5-1** Direct ink writing 3d printing platform with a passive mechanical system tracker. **a)** A schematic diagram of the customized printhead attached to the ink barrel connected to pressure regulators. **i)** On the left is the actual mechanical model for tracking z motion. **ii)** The internal structure of the ball bearing chamber showing the free rotating ball and ink opening. **b)** At the contact between the needle and the complex surface, different ball support configurations have been used to allow smooth movement, **i)** one ball support configuration, **ii)** two balls support configuration, and **iii)** three balls support configuration.

## 5.4.2 FEA Modeling

### 5.4.2.1 Mode-Frequency Analysis (Modal Analysis Modeling)

The mechanical tracking system has been modeled using a nonlinear finite element analysis, which commonly used for evaluating mechanical systems.[34-36] In the design of an assembly for dynamic loading circumstances, natural frequencies and mode shapes play a vital part. The vibration characteristics of a structure or mechanism module can be measured by modal analysis (natural frequencies and mode shapes). First, we used a modal analysis model using ANSYS workbench to determine the natural frequencies and the corresponding mode shapes to show how far our design is from resonance (*see Methods section*). A 3D model of the mechanical tracking system was created as shown in **Figure**

**5-2a**, and finite solid elements were used to discretize the 3D model resonance (*see Methods section*). To decrease the simulation time, the intricate design features in the tracker design that do not influence the modal analysis, such as grooves, were not included. The boundary conditions have been defined as shown in **Figure 5-2a**. For instance, a fixed support constraint was applied for the fixed rack, while frictional contact was used to define the contact between the slider and fixed rack. Based on the estimated coefficient of friction used during the experimental work, the coefficient of friction was set to be 0.2 in the model. Similarly, the contact between the ball bearing and the nonplanar substrate was defined as frictional contact with coefficient of friction of 0.2. The ball bearing was allowed to rotate inside the bearing socket with only a frictional contact with the bearing socket. Other contacts were set to be bonded connection to stimulate the rigid body behaviour. Most importantly, the contact stiffness of the ball was allowed vary between 0.01 and 0.1 as shown in the literature.[37] Using the predefined modal analysis module in Ansys workbench, the first three natural frequencies along with the mode shapes were obtained as shown in **Figure 5-2b**.

Interestingly, the contact stiffness has only a small effect on the natural frequencies and mode shapes, when we tested different values ranging from 0.01 to 0.1. At contact stiffness of 0.01, the calculated first three natural frequencies were 94.095 Hz, 106.33 Hz, and 193.06 Hz. Then, the contact stiffness of 0.1 was used, the first three natural frequencies were 95.67 Hz, 107.064 Hz, and 194.65 Hz. It can be seen that the difference was only around 0.8% in the natural frequencies. Therefore, the contact stiffness of 0.01 was used with the rest of the simulations as the convergence of the solution was faster. The maximum operating frequency used during the experimental work was around 20 Hz, while

the first natural frequency was at 94 Hz. Therefore, the energy is not coupled into the tracker mechanism that may result in unintended displacement of the nozzle's actual location from its intended location. The modal analysis results also indicated that the tracker mechanism is robust, and the tracker design rigidity will not be influenced by the printhead movement. Next, transient structural analysis of the various configurations was used to optimize the process parameters such as the feed rate, friction, and needle length.

#### ***5.4.2.2 Transient Structural Analysis***

Transient analysis was used to determine the dynamic response for time-dependent loading of the printhead during the printing process. We use a nonlinear FEA model for this purpose and reduce in mechanical complexity to include only the ball, ball socket, needle, and nonplanar substrate, as shown in **Figure 5-2c**. The remaining parts were replaced with a defined load on the top of the needle. The FEA model was established using the Transient Structure module in ANSYS Workbench 2020 R1 using the large deflection option. A one-step simulation was developed to simulate the tracker motion onto a dome surface. In the one-step simulation (**Figure 5-2c**), fixed support was used for the substrate. A force on the printhead was applied in lieu of the system weight, also referred to as the load, on the top of the needle. Displacement boundary condition was applied to the ball, ball socket, and needle in the x-direction. In addition, two joints connections were defined. The first joint connection was for the substrate as a fixed to ground joint. The second joint connection was defined for the steel balls as a planar joint with respect to the ground. The specified model was used to determine the impact of the operating parameters and different configurations on the deflection of the print nozzle, which has considerable influence on the printing pattern accuracy. The tracker feedrate, contact friction between the ball and

the nonplanar substrate as well as the weight of the printhead and the length of the nozzle are all operating parameters that can affect the performance of the printing. Finally the configuration of the tracker in terms of the number of contact points it has on the substrate is also important for its stability. Therefore, various configuration including one, two and three ball support configurations were analyzed as the tracker moves over a dome like substrate (**Figure 5-2d**).

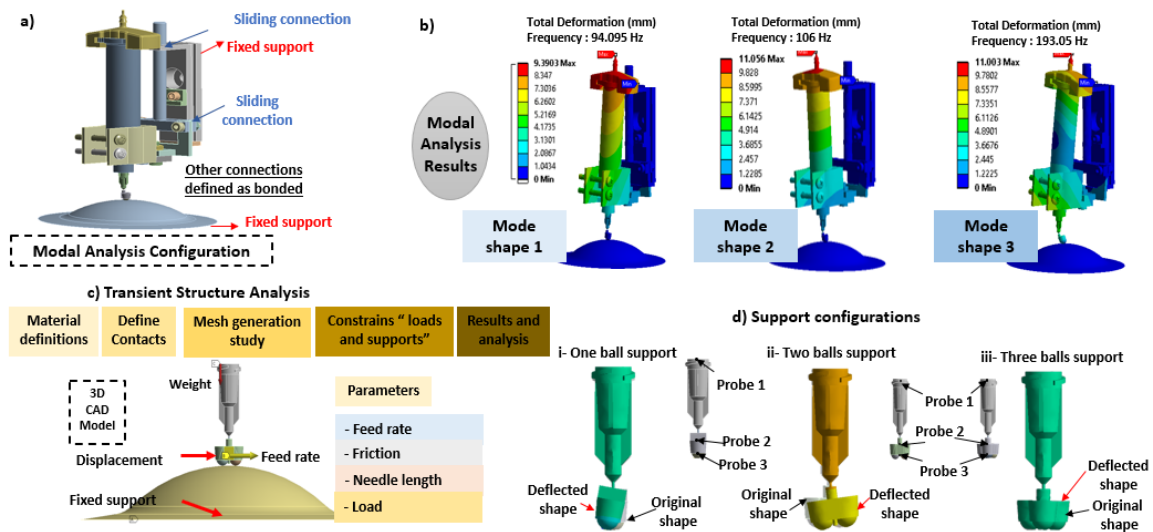


**Figure 5-2** Finite element analysis for investigating the operating frequencies and optimizing the process parameters. **a)** Modal analysis FEA with showing the used boundary conditions and constraints. **b)** The first three mode shapes show each mode's natural frequencies while the maximum working frequency will not exceed 20 Hz. **c)** Transient structure analysis FEA model, showing the simplified model used in the transient analysis and boundary conditions, on the right are the parameters investigated using the transient model. **d)** The support configurations showing the studied probes in each configuration; **i)** one ball support, **ii)** two balls support, and **iii)** three balls support.

### 5.4.3 Optimization of tracker design using FEA

The design of the tracking printhead was analysed using FEA in order to minimize the deflection of the tip of the printhead as it contacts the substrate due to movement of the printer. To validate the model, the deflection of the tracker obtained from the simulation were compared with those observed in experiments. In the simulation, the tracker was made to move over the curved surface as shown in **Figure 5-3**. The feed rate was set as 2 mm/s

while other parameters were set as follows: coefficient of friction of 0.2, needle length of 0 mm, load of 2 N, and the one ball support configuration were used. As shown in **Figure 5-3a**, the deflection of the tracker increased as soon as it began to move over the substrate and reached a maximum after which it decreased. The maximum deviation between the experimental and simulation results was around 40  $\mu\text{m}$  occurred at 0.2 sec and 4 mm displacement from the starting point. This is due to transition from static to dynamic friction when the motion is initiated, as surfaces in contact can have different coefficients of friction based on their relative velocity.[38] The experimental and simulation results followed the same trend as shown in **Figure 5-3a**. Yet, there is a small difference between the experimental and simulation results. This can be attributed to the difference between the friction co-efficient assumed in the simulation vs. the real friction co-efficient experienced by the tip. Nevertheless, due to similarity in the trend the transient model can be used for the optimization process. The deflection and stresses were obtained numerically at various timepoints to understand and optimize the tracker performance. Since the tracker system is mechanical, multiple parameters such as the needle length, feed rate, coefficient of friction, structure weight, and ball support configurations were modified to determine the set of parameters that will produce optimal performance of the tracker.

The first parameter examined was the needle length, with other parameters set to feed rate of 8 mm/s, coefficient of friction of 0.2, structure load of 10 N, and a one ball support configuration (*Appendix 3 Figure 9-1a*). The deflection of the tracker was obtained when it had two different needle lengths (0 and 4 mm) that span the range of length that are feasible and is shown in **Figure 5-3b**. The initial deflection is large due to static friction (till point 1). As the static friction is over come the frictional force reduces and the

deflection also slowly reduces as also seen in both the initial simulation and experimental results in Figure 3a. The deflection reverses (point 2) when the path of the printhead reverses. The deflection is more pronounced as the length of the needle is increased as was expected. Longer the needle tip, higher the stresses (*Appendix 3 Figure 9-1b*) that it encounters on contact and friction at the surface and hence greater the deflection.

We also investigated the effect of tracker feed rate on its deflection. Various speeds (1-8 mm/s) were chosen based on the typical printing speeds in a conventional extrusion printing. Other parameters were set as follows: coefficient of friction of 0.2, structure load of 10 N, needle length of 4 mm, and a two ball support configuration. Similar trend in deflection was observed like the one in **Figure 5-3b**, owing to the back-and-forth path over the curved substrate. However, the characteristic features in the trend were different due to the use of the two-ball support. When two ball support is used the contact made with the substrate during its back-and-forth motion on a curved substrate is more complicated. Contact is made with both the balls at the top of the curved substrate after with one of the balls lose contact which is reflected in the deflection achieved. At faster feed rate, the static friction is overcome quicker and the tracker is released. The simulation results, as shown in **Figure 5-3c** and *Appendix 3 Figure 9-1c-i*, indicated that the printing speed has a negligible effect on the tracker deflection especially at lower friction. The two-ball configuration seems to have a lower deflection as compared with the equivalent one ball tracker. At higher friction coefficient however, there is some effect of the feed rate as shown in the simulation when the higher friction rate (0.5) was used (*Appendix 3 Figure 9-1c-ii*). Here the lower feed rate corresponds to lower deflection.

A critical parameter that can be controlled to achieve lower deflection is the coefficient of friction. The coefficient of friction represents the degree of contact and interaction between the surfaces and represents the effect of the normal force in resisting tangential motion. Various friction coefficients (0- 0.4) were used with a feed rate of 1 mm/s, a load of 10 N, a needle length of 4 mm, and two balls support configuration. The characteristics of the deflection and its relationship with the motion of the tracker over the substrate was similar as previous simulations. However, the coefficient of friction had a significant effect on the deflection with higher deflections obtained at higher coefficient of friction values. These results show that designing the tracker with low coefficient of friction between the balls and the surface is effective in minimizing deflection of the tip during printing (**Figure 5-3d** and *Appendix 3 Figure 9-1d*).

Another critical parameter is the structure weight, which significantly affects the tracker performance. We conducted the transient simulation at different loads ranging from 2-10 N (identified as typical loading for multiple ink reservoirs), using a feed rate of 8 mm/s, coefficient of friction of 0.2, needle length gap of 4 mm, and two balls support configuration. The deflection of the tracker was larger when the weight was higher as shown in **Figure 5-3e** and *Appendix 3 Figure 9-1e*. The effect of the weight on deflection can be considered in two ways. The first is that it increases the resistance to motion through friction which then results in more extreme deflections. The other is the inertial effect that it has especially during the changes in direction of the print head. Combined, higher weight leads to greater deflection of the tracker and has to be minimized as much as possible. Higher loads change the characteristic profile of the deflection due to the greater effect of static friction during the initial starting phase.

Finally, we compared three proposed ball support configurations, by conducting a transient simulation for each configuration under the following conditions: feed rate of 8 mm/s, a load of 10 N, coefficient of friction of 0.2, and needle length of 4 mm. Having more than one ball for contact can provide greater stability and more balanced bending moments to the tracker which can facilitate smaller deflections. It can be seen from the results (**Figure 5-3f** and *Appendix 3 Figure 9-1f*) that the one ball configuration had the highest deflection while the two and three ball configurations had progressively lower deflections.

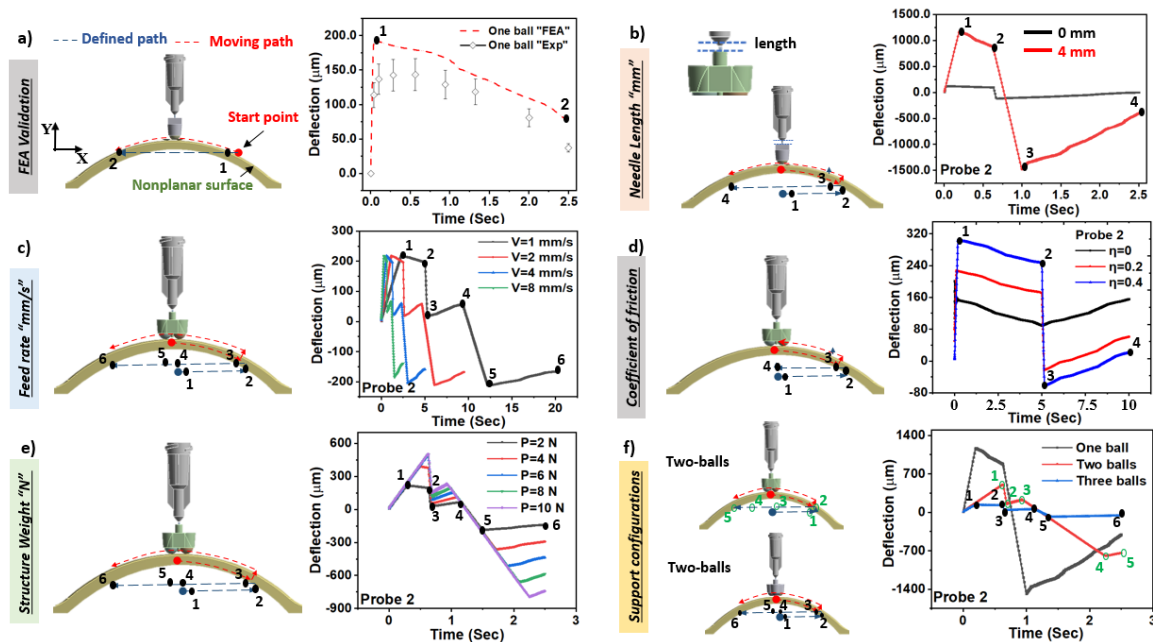


**Figure 5-3** FEA results **a)** FEA validation by conducting a Comparison between FEA deflection and experiment results using on ball confirmation, on the left the moving bath used in the FEA and experimental. Then, we tested different parameters, illustrated the moving path on the left, and investigated the process parameters to get minimum deflection. **b)** needle length using one ball configuration with two different values at feed rate eight mm/s, coefficient of friction of 0.2, a load of 10 N. **c)** The effect of feed rate on the structure deflection, while using a coefficient of friction of 0.5, a load of 10 N and needle length of 4 mm. **d)** The effect of friction between ball and substrate on the model deflection, while using feed rate of 1 mm/s, a load of 10 N and needle length of 4 mm. **e)** The effect of the structure weight on the model deflection, while using feed rate of 8 mm/s, coefficient of friction of 0.2 and needle length of 4 mm. **f)** Comparing between the three-ball support configurations on the model deflection, while using feed rate of 8 mm/s, a load of 10 N, coefficient of friction of 0.2 and needle length of 4 mm.

The one ball configuration has an off centric location and is prone to introduce greater bending moment as the point of contact with the substrate is not align with the central axis of the needle. However, the two and three ball configurations have this alignment, and this results in smaller deflections. Nevertheless, the one ball configuration has the advantage that the same ball will be in contact with the substrate all the time which is not the case with the two ball and three ball configurations especially on nonplanar topography. Therefore, experiments on a variety of nonplanar geometries are needed to determine the most robust configuration of the tracker.

#### **5.4.4 Printing on Wavy Surface**

The ability of the passive tracker mechanism to dynamically change the z-axis position and deposit the ink to create a wide variety of complex patterns over non planar topography with topographical modulation in one dimension was demonstrated with UV curable silicone inks.[31] For that, we choose a non planar topography with a sinusoidal profile as a well defined geometry where the parameter such as amplitude and wavelength can be precisely changed to study the impact of printing and tracker parameter on complex surfaces. Although, the one ball support configuration has the lowest stability in the simulation study, it was also included here as the behaviour in this surface profile may be different. The V31H silicone UV curable ink (composition in **Table S1**) was mixed with red color dye and deposited in a back-and-forth line pattern with a 5 mm pitch between the lines to cover the target region. The back-and-forth pattern was printed using the one, two, and three three-ball support configurations along two orientations: longitudinal (**Figure 5-4**) and transverse (*Appendix 3 Figure 9-2*). The back-and-forth pattern was printed over a region of (8 x 6 cm). The printing of this pattern over different wavy surfaces, and the

final printed feature is shown in **Figure 5-4** and *Appendix 3 Figure 9-2*. The printing time (4 min) over the wavy surface was identical to that of printing over a planar surface of equivalent dimension indicating no extra time for feedback and adjustment of the printhead to the underlying topography. Printing was performed over various topographies with relative wavelengths between 2-18 and relative heights between 1-3 and the printed patterns were scored as feasible and not feasible based on the congruence of the printed pattern to the design. The relative wavelength and height are non-dimensional quantities in which the sinusoidal profile wavelength and height are determined corresponding to the ball diameter, respectively. The printing was deemed successful and feasible if the printed pattern was clear and followed the desired pattern without any discontinuity. Otherwise, the printing failed and was deemed not feasible. A feasibility map for each configuration is shown in **Figure 5-4a** and *Appendix 3 Figure 9-2a* where the red color indicates printing is feasible) while the blue color indicates that the printing was not feasible. **Figure 5-4(b-e)** and *Appendix 3 Figure 9-2(b-e)* illustrate the actual printed pattern for printing along longitudinal and transverse orientations respectively. During these experiments, we set the pneumatic pressure to be 6 bar, the tracker speed set to be 2 mm/s, the substrate roughness was around 10  $\mu\text{m}$ , and the structure's weight was around 2 N. The feasibility map presented in **Figure 5-4a** for the longitudinal orientation show that the printable range is considerably smaller for the three-ball configuration as compared with the one and two ball configurations on this one-dimensional nonplanar surface. For instance, a wavy surface with relative wavelength of 8, and relative height of 2 is printable using one ball support and two balls support, but it is not printable using three ball configurations. The one ball configuration has a slightly wider range of applicability as compared with the two balls.

As an example, the surface at relative wavelength of 6, and relative height of 3 is only printable using one ball support. In addition, **Figure 5-4d(i-iii)** show that when printing the back and forth pattern over a wavy surface with wave length of 6 and relative height of 2.5, the one ball configuration produces the best replication of the design while the pattern is not completely printed with two ball can cannot be printed at all by the three ball configuration. These results indicate that the single ball support due to its minimal contact area with the substrate is able to accommodate the rapid changes in topography while the two and the three ball supports that have a wider width are less flexible. In the case of transverse orientation of the pattern over this surface, the changes in topography have even more significant effect and the one ball configuration is better able to accommodate it as compared with the two and three ball configurations. Based on these results, one can conclude that the one ball support is better able to accommodate a complex topography such as the wavy surface despite the fact that its deflection is higher. A configuration where the load on the tracker is just sufficient to retain contact and a one ball configuration would be most suitable for printing on such surfaces.

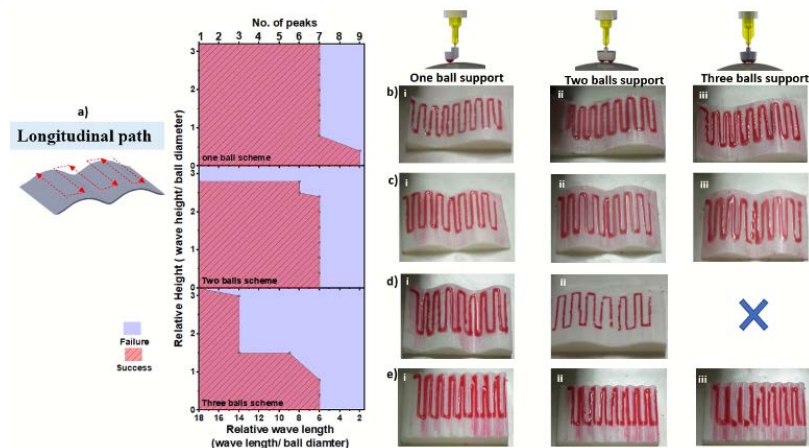


**Figure 5-4** Printing feasibility study of each configuration with complex wavy surface. **a)** Feasibility contours by varying the wavy relative height and wavelength using longitudinal path pattern. The actual printed patterns with different wavy textures are on the right using the three ball support configurations: **b)** one peak wavy surface, **c)** two peaks wavy surface, **d)** three peaks wavy surface, and **e)** multiple peaks wavy texture. All scale bars are 10 mm.

#### 5.4.5 Printing on Dome Surface

We then used the configurations with different number of balls supports to print on topographies that are nonplanar in two dimensions such as the dome. (**Figure 5-5a**). The designs were deconstructed into tool paths that ensured that the tracker does not cross over already printed lines. Specifically, a mesh pattern was printed over a circular region of 7 cm. The printing of this mesh pattern over different dome heights with the final printed feature is shown in **Figure 5-5a**. Compared to printing over a planar surface for the same circular area, the printing time was the same and it was only 2 minutes for each mesh pattern for various dome surface heights. While performing these mesh printing, we set the extrusion pressure to be 6 bar, the tracker speed to be 3 mm/s, and the structure's weight was around 2 N. The printing quality as shown in **Figure 5-5a**, is better using the one ball support, while it was progressively worse with the three-ball support configuration, for both dome heights (6 and 15 mm). These results also show that the most feasible configuration was the one ball support configuration as the tracker contact area is minimal and it does not interfere with the printing pattern (**Figure 5-5a-i**). As for the three-ball configuration, the tracker contact area was more extensive, and one of the balls rolls over prior printed features before it is completely cured which affects the pattern integrity and resolution (**Figure 5-5a-iii**). Although, some of it can be avoided by allowing greater time for cure, it will extend the print time. Therefore, the one ball configuration was considered as the most suitable tip configuration for the tracker.

Next, to investigate the printed line thickness we can obtain, we printed a back-and-forth toolpath with a 5 mm pitch over a Bézier surface using the one ball configuration using V31H ink. Bézier surfaces are a combination of mathematical splines that are

defined by a group of predefined points, and the interpolated surface does not go through the central control points. Therefore, Bézier surface is considered as a nonplanar surface with continuous variation in curvature over two dimensions unlike a dome. First, we performed different printing patterns at various extrusion pressures ranging from 1-6 bar, with a tracker speed of 2 mm/s and the structure's weight was around 2 N. After that, we measured the line thickness obtained from those printed patterns. The results illustrated in **Figure 5-5b** indicate that the higher the extrusion pressure resulted in thicker lines. At a 6 bar pressure, the line thickness of the pattern after complete curing was around 2 mm (**Figure 5-5b-i**). The minimum line thickness we obtained was around 0.8 mm at extrusion pressure around one bar; however, the generated path was not continuous, and the line was not complete (**Figure 5-5b-ii**). The minimum line thickness we obtained with completely printed design was around 1.2 mm. It should be noted that the line width is a function of not only printing process and the extrusion pressure but also on the nozzle diameter, viscosity of the ink, its spreading properties on the print bed and then rate of curing. All of these can be modified to achieve a higher resolution of printing. We then printed a 2d spiral path over a dome surface using the one ball configuration as a demonstration of a possible application of this printhead in print antenna like features on curved surfaces using an extrusion pressure of 6 bar, the tracker speed set to be 3 mm/s, and the structure's weight was around 2 N. The printing of this 2d spiral pattern over the dome **Figure 5-5c**, which took only 2 min and was comparable to the duration it would have taken for printing on planar surfaces. This demonstration shows the ability of the printhead tracker to print over a nonplanar topography varied in two dimensions with smoothly tracking circular pattern without affecting the printed trace due the tracker motion.

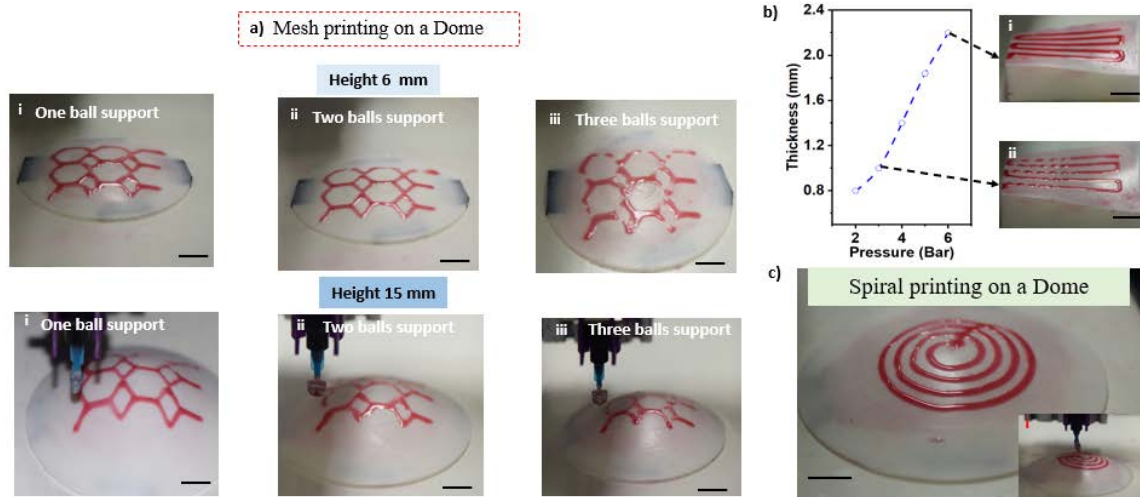


**Figure 5-5** a) Printing feasibility over dome surface by creating interfered structure like mesh pattern using the three-ball support configurations two different dome heights. b) Investigating the printed line thickness range with different inlet air pressure. We got a minimum thickness of 0.8 mm; however, the bath was not continuous. c) Spiral pattern printing over a doom planer using one ball configuration. All scale bars are 10 mm.

#### 5.4.6 Printing 2D and 3D patterns over complex surfaces

To show the potential capability of the proposed mechanical tracker, we printed 2D and 3D objects over different complex substrates. As a first demonstration, we printed a 2D mesh network of 36 cells using the one ball configuration doped with red V31H ink (**Figure 5-6a**). A toolpath for a 2D mesh network was created for continuous extrusion with overlapping lines, while the tracker was used to mechanically make contact with the Bézier surface topography at all times. This demonstration was performed under the following printing conditions: extrusion pressure of 6 bar, tracker feed rate of 2 mm/s, and structure weight around 3 N. The total printing time was around 4 min, the same time to print the same features in a planar surface. **Figure 5-6a-i** shows the final printing over the Bézier surface alongside the tracker tip. **Figure 5-6a** demonstrates the ability to print over complex surface like Bézier planar with 2D intercrossed pattern like mesh, unlike the demonstration in **Figure 5-6b** which illustrate only printing continuous pattern without the

need to pass over or cross other printed lines. The inset in **Figure 5-6a-ii** shows the printed structure that was then removed from the substrate demonstrating that the topographic profile of the substrate is retained in the printed pattern and that the print was cohesive and maintained its integrity upon removal from the base. Each mesh cell was printed over a region of (1 x 1 cm). The obtained printing resolution on nonplanar Bézier surface was slightly larger than the printing resolution over planar surface using same printing conditions. For example, the smallest printed line width in mesh network in **Figure 5-6a** was around 1.98 mm in some regions with higher slope, while it was around 1.73 mm on a planar or near planar surfaces. The printing resolution can be enhanced by using a more viscous ink or faster curing conditions. To illustrate, the mesh network was also printed using the V35H ink which was more viscous, and a print line width of 1.88 mm was obtained. Next, we printed the same mesh network over an inclined surface that had different curvatures (slopes) along it ranging from  $4^{\circ}$ - $55^{\circ}$  with an average sloped angle of  $29^{\circ}$  as shown in **Figure 5-6b**. This experiment was done to the range of slopes that would allow printing and the line widths obtained in them. The parameters of the printing were the same as before. It can be seen from **Figure 5-6b** that the printing was successful except at the region where the slope was very sharp ( $55^{\circ}$ ). In some regions with higher slopes ( $35^{\circ}$ - $55^{\circ}$ ) in **Figure 5-6b**, the minimum line width obtained was around 2 mm, but it was around 1.76 mm on a region with lower slopes (up to  $30^{\circ}$ ). In addition, we printed different patterns over complex surfaces with the same set of parameters, and the final patterns can be seen in *Appendix 3* **Figure 9-3**. We printed a wavy mesh network over an inclined surface (*Appendix 3* **Figure 9-3a**), with a region of (0.5 x 0.5 cm) for each mesh cell. A zig-zag pattern was printed over a dome surface with a 4 mm gap between each line, as

shown in *Appendix 3 Figure 9-3b*. A wavy zig-zag pattern was printed over an inclined surface with an 8 mm gap between lines (*Appendix 3 Figure 9-3c*). These experiments were done to show the ability to print different patterns with varying gaps. It can be noticed that the printing was successful except for the zig-zag mesh pattern in *Appendix 3 Figure 9-3a*, where the printed pattern was not clear, and some lines had interfered with others.

We also used the mechanical tracker to print on soft nonplanar objects such as a person's hand. In this experiment, shown in **Figure 5-6c**, a 2D spiral pattern was used to print over a gloved hand using the V31H ink and print parameters similar to those used in the previous experiments. The printing process needed only 2 min for printing. Interestingly, the spiral path printed over solid complex structure like dome in **Figure 5-5c**, has better resolution than the one printed over the freeform surface like human hand. The resolution of the spiral over solid surface was around 1.83 mm, while the one over the soft human hand was around 1.9 mm. The fidelity of the pattern was also much less over the hand as compared with the hard surface. This may be due to the compliant nature of the hand that upon contact with the mechanical tracker is capable of displacement. The anisotropic nature of compliance of the hand also leads to loss of fidelity of the printed pattern. Nevertheless, this demonstration suggests that the PHT provides a simple modification to existing extrusion printers to print on both hard as well as soft non-planar surfaces. Further control over the process can be provided by integrating a sensor that measures the compliance of the underlying substrate and adjusts the applied force accordingly to maintain fidelity of the patterns printed.

Although the PHT demonstrates capabilities for 2D patterning on non-planar surfaces, extending it to 3D printing will require additional modifications. We recognized

that the tracker was needed only in the initial phase of printing of a 3D structure till the nonplanar topography and its feature dimensions are at the scale of the structures printed. Larger structures can be printed by using the PHT at the initial phase to print conformally to the substrate and extend the features to a height that is larger than the topographical features present. After this stage conventional extrusion printing approach can be used by making the compliant mechanism in the print head rigid. To demonstrate this approach we printed a 3D box with walls that were taller than the underlying topographical variations of a dome (**Figure 5-6d(i-v)**). The first stage of printing was performed using the PHT and V35H ink doped with red color to produce a flexible walled box structure over a 3x3 cm area on top of a dome (**Figure 5-6d (i-ii)**). The print parameters used were an extrusion pressure of 6 bar, feed rate of 3 mm/s, and a structured weight of 2 N. We found that the height of the structure built did not increase linearly as expected but instead plateaued over 30 layers. This may be due to the small pressure exerted on the printed wall by the movement of the tracker ball over it. More interestingly, due to that the top surface of the printed wall became progressively planar over the same 30 layers. The wall printed over the 30 layers was ~ 1 cm in height and had a thickness of ~ 3 mm. The relation between the print thickness and the printed layers is shown in **Figure 5-6d-v**. In this printing a three ball configuration was used to maintain the contact of the PHT to the evolving printed wall at all times. Next, we followed that with conventional extrusion printing where the print nozzle was rigid and moved higher each layer (**Figure 5-6d(iii-iv)**). We used the same pattern but used V35H doped with yellow color to distinguish between the two steps of the print. Since the top surface of the printed was planar, the conventional printing did not have any issues and 14 layers of printing produced a higher aspect ratio structure which was ~ 3

cm in height. The change in height to the printed layers is shown in **Figure 5-6d-v**, which shows the linearity of the subsequent conventional extrusion print on the previous PHT print. These results show the surprising consequence of using the mechanical tracker was planarization of the top printed surface which can then be used to further extend the printing into 3D using conventional extrusion printing with a rigid printhead. Using this method, a variety of tall and high aspect ratio structures can be printed on nonplanar surfaces.

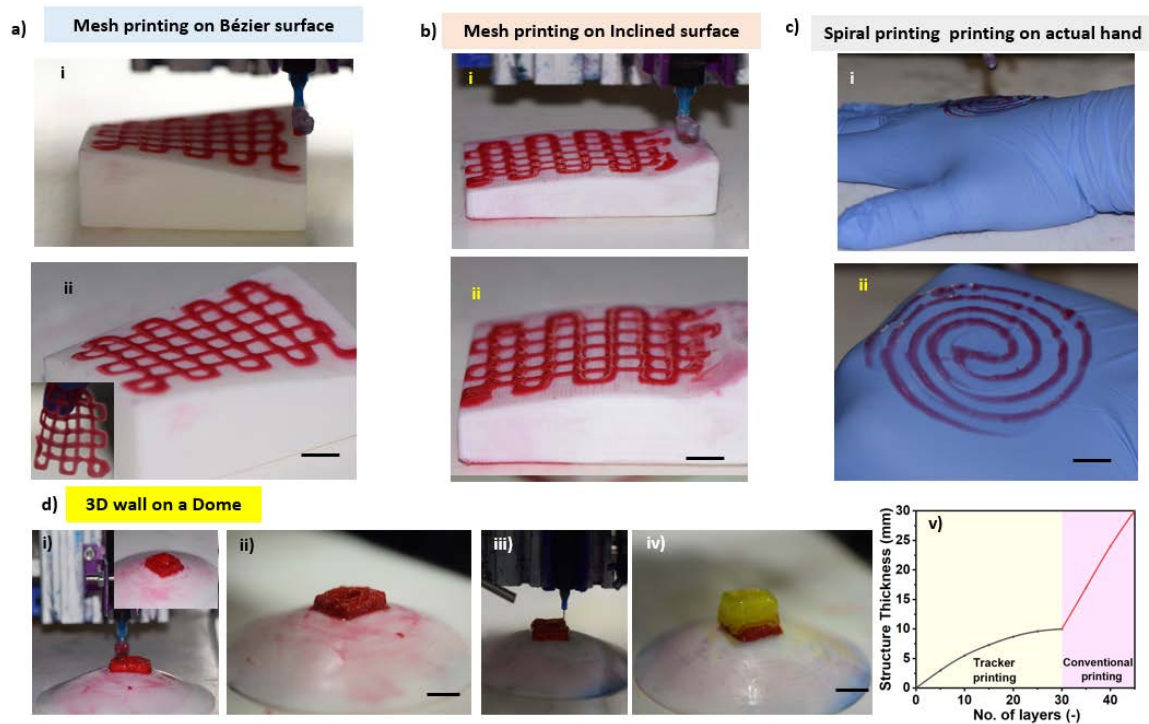


**Figure 5-6** a) Mesh printing over a Bézier surface using the one ball configuration, with mesh element size 5mm\*5mm. b) Mesh printing over an inclined surface using the one ball configuration, with mesh element size 5mm\*5mm. c) Spiral pattern printing over an actual hand planer using one ball configuration, with a pitch of 4 mm. d) 3D Wall printing over dome surface using a hybrid system in two steps, i, ii) printing low aspect ratio over a nonplanar surface using the three-ball support configuration, then iii, iv) print higher aspect ration structure "yellow color" using conventional extrusion printing. All scale bars are 10 mm v) The print thickness as different number of layers are printed using the tracker first, then continue with a conventional extrusion printing.

#### 5.4.7 Multimaterial Printing 2D pattern over complex surfaces

So far the MM-PHT was capable of printing single inks. However, many of the intended applications will require printing multiple inks in close alignment with each other to create

functional devices. We used the multimaterial microfluidic printhead [39] that was previously developed with the mechanical tracker to form the multimaterial printhead tracker ``MM-PHT`` that is capable of printing at least four different inks. The challenges in including multimaterial printing capability with the tracking are the design complexity associated with the incorporation of different materials and the MM-PHT weight which can lead to have more jerky movement and can affect the print resolution. Briefly, the MM-PHT consisted on a 3D printed structure with multiple inlet channels that converge onto a central chamber which is then attached to a nozzle [39]. Each of the inlet channels are connected to their respective ink reservoirs and can be actuated pneumatically independent of each other. The mechanical tracker (one ball support) was attached to the tip of this multimaterial printhead to form the MM-PHT. The final realised prototype is shown in **Figure 5-7ai**. Four ink barrels were then loaded on to the print head as shown in **Figure 5-7a-ii**. The loading of the ink barrels resulted in a substantial increase of weight of the printhead from  $\sim 2\text{N}$  for single ink to  $\sim 8\text{N}$  for four inks. This increase in weight is likely to have an effect on the deflection of the nozzle as the tracker contacts the substrate as well as introduce intermittent stiction during operation. 2D patterns of spirals and four squares with different colored UV curable silicone inks (V35H) were printed on a variety of soft and hard non-planar surfaces to determine the influence of the added weight as well as the switching of inks at the printhead on the print resolution and accuracy (**Figure 5-7**).

First, we printed a 2D spiral pattern over a freeform surface like an actual hand using V35H with three different colors (red, green, and yellow) (**Figure 5-7b**). The extrusion pressure was 6 bar, and the feed rate was 2 mm/s. The printing duration was only 2 min, and the time was identical to printing the same pattern using a single color without

switching. However, due to the large contact load in this case, the printed line width was around 2.5 mm as compared with a line width of 1.75 mm when single material printing is performed with a lighter printhead. Furthermore, the added weight also had a significant effect on the fidelity of the print as compared to the design due to the soft and compliant nature of the substrate. However, clear interfaces between the two-colored inks were obtained indicating that the switching performance of the MM-PHT was not affected. For example, the desired length of the yellow line was 12.5 cm, but the length of the printed yellow was 13 cm.

Next, we printed a 2D color map that consisted of 4 colors using the MM-PHT over a dome surface (**Figure 5-7c**). The inks were composed of UV curable silicone material “V35H” doped with different colors (cyan, yellow, magenta, and green). A toolpath was determined to cover the 2D map zone for continuous extrusion, with defining the switching points at the beginning of each zone. Each color region was printed over an area of (4 x 4 cm). The switching time between the ink formulations within the microfluidic printhead was around 4 s, which is correlated to the priming volume of the printhead junction of 15  $\mu\text{l}$  (**Figure 5-7c-ii**). The process took only 8 min to print one layer for each color region, which was similar to the time need to print with a single ink. The same patten was printed on top of a dome substrate which has 2D constant curvature and a Bézier surface which has a 2D variable curvature (**Figure 5-7d**). The thickness of the printed layer presented in **Figure 5-7(c-d)** and *Appendix 3 Figure 9-4* was around 2.1 mm, which was smaller than single material printing by ~ 30%. This can be attributed to the larger weight of the MM-PHT printhead that lead to the flattening of the printed line. We also compared the capabilities of our tracking method with more expensive and complicated feedback or

multimaterial printing methods that have been used in the literature (see *Appendix 3 Table 9-1*). None of the tracking methods published in the literature have demonstrated multimaterial capability while ours does. All of the other systems use active feedback that is expensive to implement and may not function effectively under different lighting conditions. Ours is a passive and instantaneous feedback system that is robust and will operate under all environmental conditions. Most of the other tracking systems work with thermoplastic or nanomaterials (in the case of aerosol jet printing) and none have demonstrated silicone printing, which due to its lower viscosity leads to a higher line width (feature size) for our printing. Implementing this passive feedback approach to thermoplastic printing or using smaller nozzle, higher viscosity or faster curing silicone materials can lead to achieving the same high resolution of the other methods. As our method is simple, robust, low-cost and does not require significant modification to the print hardware, it can be integrated into any extrusion printing setup and facilitate printing on a wide range of non-planar surfaces.

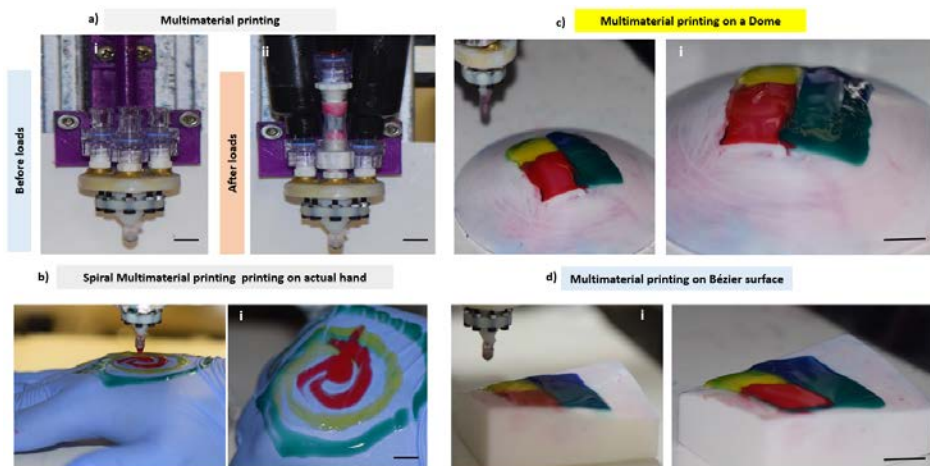


**Figure 5-7** Multimaterial printing over complex surfaces. **a)** Multimaterial passive control mechanical system for printing over nonplanar surfaces by integrating microfluidics printhead with the tracking mechanism, the actual figure on the left before loading the inks, and the right one after loading four barrels inks. **b)** Printing a multimaterial spiral pattern over an actual hand planer using one ball configuration with three different inks. Printing four colors regions over complex surfaces using one ball configuration; **c)** dome surface, and **d)** Bézier surface. All scale bars are 10 mm

## 5.5 Conclusion

To conclude, we have designed and implemented a passive mechanical tracking system integrated with multimaterial microfluidic printhead for achieving fast switching with the ability to print on to complex surfaces smoothly. The unique printhead mechanical tracking system combines pulsatile injection of different inks and a simple mechanism for tracking z-axis motion. Simulations of the tracker motion provided a feasible understanding of the process parameter's influence over the system deflection to obtain high printing performance and optimize the tracker design. The simulations were compared with experimental results for validation using UV curable inks. Various configurations of the ball point contact were tested, and the single ball contact was found to be versatile and robust as compared with the two and three ball contact for 2D printing. The three-ball contact was better for extending it into 3D printing. Various surfaces including a dome shape and Bézier surface were used to demonstrate the robustness of the method. Several features including a spiral, color boxes and a 2D box with walls were printed. The limitations of this printing method are that the contact made by the ball onto the substrate can flatten partially crosslinked material from the previous layer. This can lead to flattening in the printed layer thickness during 3D printing. To overcome that, the initial print was conducted using the mechanical feedback tracker to achieve conformal contact and build up a base layer whose top was planarized by the tracker contact. Subsequently, conventional extrusion printing with a stiff printhead was used to extend the height of the printed structure. This combination provided a hybrid way to print 3D structures using this approach.

In the future, the performance of the MM-PHT design can be enhanced by incorporating lighter microfluidic printhead based on structural and fluid mechanics

analysis to ensure an improved in the printing resolution. The range of materials printed can be expanded by using this tracker on thermoplastic extrusion printers as well on aerosol and spray coating printheads. The size of the ball contact can be optimized to ensure that large and small topographical features can be accommodated with ease. To summarize, the adaptable and straightforward printhead tracker established here is of broad application to 3D print objects that can be utilized for flexible electronics and even skin engineering applications.

## Acknowledgements

We acknowledge the financial support of the Natural Sciences and Engineering Research Council of Canada. PRS also thanks to the Canada Research Chair Program and Distinguished Engineering Professor award for support. We are very grateful for the gift of a photoinitiator from IGM Resins, Inc.

## References

- [1] T. D. Ngo, A. Kashani, G. Imbalzano, K. T. Nguyen, and D. Hui, "Additive manufacturing (3D printing): A review of materials, methods, applications and challenges," *Composites Part B: Engineering*, vol. 143, pp. 172-196, 2018.
- [2] J. Beaman, D. L. Bourell, C. Seepersad, and D. Kovar, "Additive manufacturing review: Early past to current practice," *Journal of Manufacturing Science Engineering*, vol. 142, no. 11, p. 110812, 2020.
- [3] R. A. Johnson, J. J. O'Neill, R. L. Dockter, and T. M. Kowalewski, "Toward Inkjet Additive Manufacturing Directly Onto Human Anatomy," in *Frontiers in Biomedical Devices*, 2017, vol. 40672, p. V001T11A016: American Society of Mechanical Engineers.
- [4] N. Matsuhsa *et al.*, "Printable elastic conductors with a high conductivity for electronic textile applications," *Nature communications*, vol. 6, no. 1, pp. 1-11, 2015.
- [5] H. Kai *et al.*, "Accelerated wound healing on skin by electrical stimulation with a bioelectric plaster," *Advanced healthcare materials*, vol. 6, no. 22, p. 1700465, 2017.
- [6] E. Madi, K. Pope, W. Huang, and T. Iqbal, "A review of integrating ice detection and mitigation for wind turbine blades," *Renewable and Sustainable Energy Reviews*, vol. 103, pp. 269-281, 2019.
- [7] W. Gao *et al.*, "Fully integrated wearable sensor arrays for multiplexed in situ perspiration analysis," *Nature communications*, vol. 529, no. 7587, pp. 509-514, 2016.
- [8] J. Kim *et al.*, "Miniaturized battery-free wireless systems for wearable pulse oximetry," *Advanced functional materials*, vol. 27, no. 1, p. 1604373, 2017.

- [9] H. Teymourian, F. Tehrani, K. Mahato, and J. Wang, "Lab under the Skin: Microneedle Based Wearable Devices," *Advanced Healthcare Materials*, p. 2002255, 2021.
- [10] J. Wei *et al.*, "Bioinspired 3D printable, self-healable, and stretchable hydrogels with multiple conductivities for skin-like wearable strain sensors," *ACS Applied Materials Interfaces*, vol. 13, no. 2, pp. 2952-2960, 2021.
- [11] A. Boem and G. M. Troiano, "Non-Rigid HCI: A review of deformable interfaces and input," in *Proceedings of the 2019 on Designing Interactive Systems Conference*, 2019, pp. 885-906.
- [12] C. Rodriguez-Padilla, E. Cuan-Urquizo, A. Roman-Flores, J. L. Gordillo, and C. Vázquez-Hurtado, "Algorithm for the Conformal 3D Printing on Non-Planar Tessellated Surfaces: Applicability in Patterns and Lattices," *Applied Sciences*, vol. 11, no. 16, p. 7509, 2021.
- [13] A. V. Shembekar, Y. J. Yoon, A. Kanyuck, and S. K. Gupta, "Trajectory planning for conformal 3d printing using non-planar layers," in *International Design Engineering Technical Conferences and Computers and Information in Engineering Conference*, 2018, vol. 51722, p. V01AT02A026: American Society of Mechanical Engineers.
- [14] A. M. Cendrero, G. M. Fortunato, J. M. Munoz-Guijosa, C. De Maria, and A. Díaz Lantada, "Benefits of Non-Planar Printing Strategies Towards Eco-Efficient 3D Printing," *Sustainability*, vol. 13, no. 4, p. 1599, 2021.
- [15] W. S. Tan, M. A. B. Juhari, Q. Shi, S. Chen, D. Campolo, and J. Song, "Development of a new additive manufacturing platform for direct freeform 3D printing of intrinsically curved flexible membranes," *Additive Manufacturing*, vol. 36, p. 101563, 2020.
- [16] Y. Bao, Y. Liu, Y. Kuang, D. Fang, and T. Li, "3D-printed highly deformable electrodes for flexible lithium ion batteries," *Energy Storage Materials*, vol. 33, pp. 55-61, 2020.
- [17] H. Yang, W. R. Leow, and X. Chen, "3D printing of flexible electronic devices," *Small methods*, vol. 2, no. 1, p. 1700259, 2018.
- [18] T. Umedachi, V. Vikas, and B. Trimmer, "Softworms: the design and control of non-pneumatic, 3D-printed, deformable robots," *Bioinspiration biomimetics*, vol. 11, no. 2, p. 025001, 2016.
- [19] C.-L. Tai *et al.*, "Ultrastable, Deformable, and Stretchable Luminescent Organic–Inorganic Perovskite Nanocrystal–Polymer Composites for 3D Printing and White Light-Emitting Diodes," *ACS applied materials interfaces*, vol. 11, no. 33, pp. 30176-30184, 2019.
- [20] H. Yang, W. R. Leow, and X. Chen, "3D printing of flexible electronic devices," *Small methods*, vol. 2, no. 1, p. 1700259, 2018.
- [21] S. Z. Guo, K. Qiu, F. Meng, S. H. Park, and M. C. McAlpine, "3D printed stretchable tactile sensors," *Advanced Materials*, vol. 29, no. 27, p. 1701218, 2017.
- [22] Y. Tong, Z. Feng, J. Kim, J. L. Robertson, X. Jia, and B. N. Johnson, "3D printed stretchable triboelectric nanogenerator fibers and devices," *Nano Energy*, vol. 75, p. 104973, 2020.
- [23] Y. Tong, Z. Feng, J. Kim, J. L. Robertson, X. Jia, and B. N. Johnson, "3D printed stretchable triboelectric nanogenerator fibers and devices," *Nano Energy*, vol. 75, p. 104973, 2020.
- [24] I. S. Yoon *et al.*, "3D Printing of Self-Wiring Conductive Ink with High Stretchability and Stackability for Customized Wearable Devices," *Advanced Materials Technologies*, vol. 4, no. 9, p. 1900363, 2019.
- [25] A. Kalkal *et al.*, "Recent advances in 3D printing technologies for wearable (bio) sensors," *Additive Manufacturing*, p. 102088, 2021.
- [26] Y. Zhang *et al.*, "Recent progress of direct ink writing of electronic components for advanced wearable devices," *ACS Applied Electronic Materials*, vol. 1, no. 9, pp. 1718-1734, 2019.

- [27] F. B. Coulter, B. S. Coulter, E. Papastavrou, and A. J. Ianakiev, "Production techniques for 3D printed inflatable elastomer structures: part II—four-axis direct ink writing on irregular double-curved and inflatable surfaces," *3D Printing Additive Manufacturing*, vol. 5, no. 1, pp. 17-28, 2018.
- [28] J. C. McCaw and E. J. Cuan-Urquizo, "Curved-layered additive manufacturing of non-planar, parametric lattice structures," *Materials Design*, vol. 160, pp. 949-963, 2018.
- [29] T. Llewellyn-Jones, R. Allen, and R. J. Trask, "Curved layer fused filament fabrication using automated toolpath generation," *3D printing Additive Manufacturing*, vol. 3, no. 4, pp. 236-243, 2016.
- [30] G. Zhao, G. Ma, J. Feng, and W. Xiao, "Nonplanar slicing and path generation methods for robotic additive manufacturing," *International Journal of Advanced Manufacturing Technology*, vol. 96, 2018.
- [31] S. Zheng, M. Zlatin, P. R. Selvaganapathy, and M. A. Brook, "Multiple modulus silicone elastomers using 3D extrusion printing of low viscosity inks," *Additive Manufacturing*, vol. 24, pp. 86-92, 2018.
- [32] I. Hassan and P. R. Selvaganapathy, "Microfluidic Printheads with Integrated Hybrid Mixing by Sequential Injection for Multimaterial 3D Printing " *Additive Manufacturing*, Submitted 2021.
- [33] P. J. C. Kohnke, PA, USA: ANSYS Inc, "ANSYS mechanical APDL theory reference," 2013.
- [34] P. Kagan, A. Fischer, and P. Z. Bar-Yoseph, "Mechanically based models: Adaptive refinement for B-spline finite element," *International Journal for Numerical Methods in Engineering*, vol. 57, no. 8, pp. 1145-1175, 2003.
- [35] W.-S. Hwang and H. C. J. Park, "Finite element modeling of piezoelectric sensors and actuators," *AIAA journal*, vol. 31, no. 5, pp. 930-937, 1993.
- [36] S. Narayanan and V. J. Balamurugan, "Finite element modelling of piezolaminated smart structures for active vibration control with distributed sensors and actuators," *Journal of sound vibration*, vol. 262, no. 3, pp. 529-562, 2003.
- [37] S. Pandit and V. Kamble, "Finite Element analysis for stress analysis and Non-linear contact analysis of Multi range load cell in ANSYS software," *Int. Res. J. Eng. Technol.*, vol. 5, no. 6, pp. 283-287, 2018.
- [38] D. Ansys, "ANSYS mechanical APDL contact technology guide," *Notes*, vol. 3304, pp. 724-746, 2015.
- [39] I. Hassan and P. R. Selvaganapathy, "A microfluidic printhead with integrated hybrid mixing by sequential injection for multimaterial 3D printing," *Additive Manufacturing*, vol. 50, p. 102559, 2022/02/01/ 2022.

## **6 Chapter 6**

### **Conclusion and future work**

#### **6.1 Conclusion**

This thesis presents the development of new deposition-controlled printheads using microfluidic designs for 3D printing multifunctional devices. One of the highly desirable multimaterial additive manufacturing approaches is the extrusion-based multimaterial printing technique due to its compatibility with different ink-based materials. The extrusion-based multimaterial printing approach offers inexpensive, rapid, and scalable fabrication of multifunctional devices that can be integrated into practical applications. One of the main challenges of extrusion-based multimaterial printing previously was the inability to achieve rapid switching while using viscous inks. Another challenge was the ability to mix inks during extrusion printing at low Reynolds numbers regime. The coordination of mixing, deposition, and stage motion by individual printheads is exceptionally challenging when complex architectures with different compositions are required. Extrusion 3D printing method also poses problems associated with direct multimaterial printing on complex surfaces. Printheads with self controllable feedback are still required to enable rapid fabrication on nonuniform surfaces with AM using extrusion. This thesis tackled these challenges and developed innovative solutions to extend the 3D

printing DIW approach in the multimaterial fabrication field for creating multifunctional appliances.

In order to demonstrate an application of a previously developed silicone 3D printing method, a snow-based triboelectric nanogenerator (SNTENG) was developed. Using the developed system, a multilayer device was fabricated. The device consisted of multiple layers; the top and bottom layers were fabricated using silicone-based inks, while the middle layer was built using PEDOT: PSS ink as an electrode. The proposed SNTENG can be used as a self-powered arctic multifunctional weather station to measure snowfall rate, snow depth, wind direction, and speed in snowy/icy environments. Furthermore, the designed SNTENG can be used as a wearable power source and biomechanical sensor to detect human body motions in a snowy environment, useful in snow-related sports. Although the fabrication method used here was one of the early demonstrations of silicone 3D printing, it had the following limitations. This 3D printing method had no mixing capability during the 3D printing. In addition, it had a large dead volume which resulted in a substantially longer switching time than desired. Furthermore, it was not possible to print over complex topography that was not planar. All of these are issues with many of the other 3D printing techniques in the literature as well.

In order to address these challenges, a new type of extrusion printhead was developed in this thesis with an integrated mixer that combines pulsatile pneumatic injection with chaotic advection to achieve fast and reliable mixing. This printhead can combine several base inks into many combinations depending on the pulse parameters applied pneumatically. For the first time, four inks were used to create nine different ink combinations in real-time to print multi compositional materials with a high degree of

accuracy. The print head was able to switch its compositions in under less than 4 sec making it the fastest such mixing printhead reported. A 3D Rubix cube was demonstrated with very sharp and clear interfaces between the cubes of different colors made by mixing base colors in real-time. This approach that has been demonstrated with four inks is also scalable to more inks. The control of the duty cycle of the pneumatic signal and their sequencing between the different ink reservoirs were investigated to produce scalably a variety of ink (material) combinations. The flexibility of this methodology is of broad applicability to produce multi-functional materials with gradient properties that can be useful in soft robotics, flexible electronics, and other emerging applications. Although a proper mixing at low Reynolds number flow was achieved, some applications require a higher switching rate. For that reason, we had to sacrifice the mixing features to decrease the intersection junction dead volume and reach a high switching speed, which will allow fabricating multimaterial structures in a 3D pixelated manner.

In order to address the high switching rates challenge with viscous inks to create pixelated structures, an innovative type of extrusion system was established. The developed system had the capability to switch rapidly between several base inks “including both viscous and viscoelastic materials” into a multitude of combinations depending on the pulse parameters applied pneumatically. The key parameters for eliminating the backflow during the switching high viscous inks are the backpressure at the opposed junctions coupled with the switching frequency. For tackling this problem, a numerical solution was demonstrated for mapping the pressure distribution and ink concentration inside the printhead at different switching rates, applied pressures, and extrusion feed rates. The numerical solution outcomes were indicated, such that to successfully deliver the inks

without backflow, the pressure gradient at the non-active channels has to be neutralized. Additionally, the backpressure was found to be greatly influenced by the switching rates, which indicates that the required backpressure changed with the operating switching frequencies correlated to the needed pixelated printing. After the operating conditions were optimized for the required pixelated application, the determined inlet pressure and feed rates entered to the G-code file. For the first time, four viscous inks were used to create voxelated structures without any backflow. The printhead was able to switch its compositions in flawlessly speed up to 50 Hz with a resolution up to 500  $\mu\text{m}$ . A demonstration of printing a 2D and 3D architecture “soft gripper” with very sharp and clear interfaces between the segments of different colors made was performed. This approach that has been demonstrated with four inks is scalable to more inks. The versatility of this approach is of broad applicability to produce multi-functional materials with complex structures that can be useful in soft robotics, flexible electronics, and other emerging applications.

In order to address the challenge associated with printing on nonplanar surfaces, an innovative type of extrusion system that can track nonplanar topography profiles and print multimaterial structures was developed. The challenge is maintaining the gap between the printhead and the targeted nonplanar surface as the topography underneath the printhead changes. The developed printhead tracker maintained the gap between the printhead and the nonplanar surface using self-adapting mechanical feedback. The developed approach used simple mechanical elements like roller bearings for allowing smooth tracking and spring-loaded structure for retaining the contact between the printhead ball bearings and nonplanar surfaces. By fabricating the tracker with a particular distance between the nozzle

tip and the ball bearings, the gap spacing was defined. In comparison with other approaches, the developed system is simple, elegant and appropriate for many 3D printer platforms. In addition, modal and transient numerical simulations were established to evaluate the tracker mechanical design and eventually optimize the tracker design. Next, demonstrations of printing 2D architectures were performed over different nonplanar surfaces such as human hand, inclined surface, and dome surface. Interestingly, a 3D structure can be printed using the developed tracker followed by conventional extrusion printhead for achieving high aspect ratio structures over nonplanar surfaces. More importantly, multimaterial printing were performed over a Bézier surface and dome substrate with very sharp interface between colored segments, by combining the tracker with the mixer printhead used in chapter 3. This technique enables the printhead to track topologies in real-time, allowing a broader range of features to be embedded and printed over complex objects.

The work presented in this thesis has solved some of the key challenges in enabling multimaterial fabrication of various patterns and structures on a variety of surface topographies. The developed fabrication approaches can be adapted to print multi-inks patterns with proper mixing, high switching rate up to 50 Hz, and deposition over freeform surfaces. This has broad applications in device fabrication for applications, including sensors, functional devices, and soft robotics.

## **6.2 Recommendations for future work**

The developed 3D printing approaches using integrating microfluidic printheads have great potential as unconventional multimaterial fabrication methods. However, these techniques can further be investigated for implementing them for more complex and beneficial

multifunction devices. In the following section, recommendations and directions for further investigation to improve outcomes are presented.

(i) DIW system for regulating the pressure flow during deposition: In Chapter 4, both simulation and experimental results revealed that the frequency and pressure values are crucial in determining the correct switching sequence. Experimental results with the current system also indicate that achieving the desired proper pattern without controlling the pressure value during printing may lead to have wrong switching point. The current setup could be improved by using pressure regulators that can be controlled. Further development for the current system is recommended by integrating the pressure value inside the toolpath G-code using controllable pressure system for adapting the ink reservoir pressure. Such development requires modifying the base python code of the controller system to add the pressure value. The pressure value can be defined as a new printing function that can be altered using the G-code. In addition, the integrated pressure function should reflect the effect of the switching frequency and fluid viscosity. The proposed modifications can have a significant impact on enhancing the switching accuracy. It can also allow creating of complex pixelated structures using viscous and viscoelastic inks, which can be employed in applications like bioprinting organs-like structures.

(ii) DIW system for reaching high resolution: In order to achieve voxel printing in a nanoscale with high-resolution printing-based extrusion DIW. A high electric field can be integrated with the current DIW system to tackle the current system's limitations, including the pressure flow and nozzle gauge. The process employed a high electric field called electrohydrodynamic (EHD) printing, which efficiently overcomes the limitation in resolution arising from the nozzle size. The process relies on some crucial parameters,

including material factors and setup parameters. All these parameters should be investigated to get their effect on printing resolution and jet stability. One recommended improvement is combining EHD operation with the current system (the one used in this thesis) to switch printing between large patterns (millimeter scale) and high-resolution patterns (nanometers scale features). Further, a nanofluidic printhead can be designed to allow multimaterial printing with high switching and mixing capabilities. Such development will require an advanced fabrication technique followed by an excessive study for controlling the fluids at nanometer scale. The proposed improvement is intended to be used for fabricating multifunctional devices for bioengineering and biotechnology applications.

(iii) Printhead design modifications: One avenue to solve the backflow issue regardless of which inks we need to use (viscous or viscoelastic inks) is to introduce a check valve inside the printhead. The nearer the check valve to the intersection point, the better switching performance without backflow issue. During the course of investigations for this thesis, a check valve was integrated inside the printhead to prevent back-flows. The printhead comprises three major elements: an inlets chamber, a switching chamber, and an elastic membrane that functions as a check valve. However, the developed printhead with the check valve still has the backflow issue which could not be eliminated. The reason was that the check valve location was far from the interaction, and the membrane used was very flexible. Thus, the membrane could be deflected, and inks from the pressurized channel will push ink into the static channel, and the switching sequence will be distributed. One potential modification is fabricating the check valve inside the printhead using one-step fabrication and locating the check valve at the intersection point. It should be noted that

the manufacturing process of such design is very challenging due to the check valve assembly at the intersection area. Another avenue might be to design the check valve as an insertable “cartridge” style. This could occur by designing a sub-assembly that gets inserted and glued into the main housing. Moreover, to help enhancing lubricity and diminishing surface friction inside the printhead channels, a modification to the printhead surface can be introduced to make it hydrophilic using a hydrophilic coating. Using the current improvement, regardless of the ink properties, the printhead design will no longer impose cyclicity constraints while enhancing feature resolution. With such modification, a 3D multimaterial voxelated matter can be created on-demand with exceptional accomplishment for viscous and viscoelastic inks.

## **7 Appendix 1**

### **Supplementary Information for Chapter 3**

**A Microfluidic Printhead with Integrated Hybrid Mixing by Sequential Injection for Multimaterial 3D Printing**

## 7.1 Flowrate measurements

Flowrate experiments were investigated with a simple setup. A multiple inlets printhead were connected to the 10 ml syringe barrel by its Luer lock connection and commercial check valve with a steel needle at the output nozzle. To determine the purge duration, we collected and weighed the amount of ink flowing through the nozzle (length of  $13.2 \pm 0.1 \text{ mm}$ ) to discover the flow rate under different pressures (10 to 90 Psi). A value of  $0.96 \text{ g/ml}$  was used as the density of the ink (V31). A standard graduated cylinder (whose weight was measured before) was used to collect the ink flow over a specified volume. At which point the pressure was removed, then the dish was then weighted with standard lab scales (resolution of  $0.01 \text{ g}$ ), and the results logged. The flowrate vs. pressure relation for these needles and inks is presented in supplementary **Figure 7-1a**. The V31 ink behaves like a Newtonian fluid under the operating conditions, as can be seen from their near-linear trends. The Reynolds number range is  $0.003$  to  $0.02$ , which indicates low Reynolds number regime where the inertial forces play no role in the flow dynamics, as shown in supplementary **Figure 7-1b**. Viscous and capillary forces are more dominant as evidenced by the accumulation of the material extruded from the nozzle up its outer side to form a bulb of ink at the tip of the needle. Moreover, supplementary **Figure 7-1c** shows that the entrance length was ranging from  $0.05$  to  $0.35 \mu\text{m}$ , which indicates that the flow is fully developed, and no turbulence or secondary flow exists.

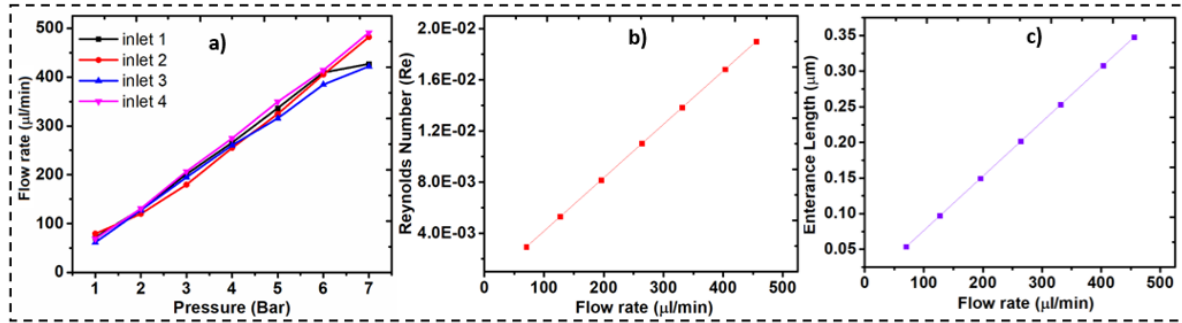


**Figure 7-1** a) Flowrate as a function of Pressure by varying it from 1 to 7 bar. b, c) Reynolds number and entrance length as a function of flow rate from 50 to 500  $\mu\text{l}/\text{min}$ .

The flow rate of the ink, the height of the nozzle tip from the substrate surface ( $Z$  offset), and the feed-rate of the printhead were the parameters that were varied in order to characterize the printing process. In this experiment, seven  $Z_{offset}$  based on the effective  $Z$  beginning with  $Z_{eff}$  and ending with  $4 \cdot Z_{eff}$  and six feed rates (250, 500, 750, 1000, 1500, 2000) [mm/min] were tested by printing a serpentine pattern of 20 mm length as shown in **Figure 7-2h**. These patterns were repeated seven times for each combination of conditions. The ink was printed onto a PVC substrate. The printing regions under different circumstances that result in a continuous or periodic deposition for a flowrate of  $70 \mu\text{L}/\text{min}$ – $455 \mu\text{L}/\text{min}$  are shown in **Figure 7-2(a-g)**. It can be seen that cyclic deposition occurs above a specific ratio of  $Z$  offset to feed-rate, as the  $Z$  offset is increased periodic situation occurs at higher feed rates. While at high feed rates, another deposition approach has been shown. The sloped deposition is continuous; however, the line is not perfectly straight, which indicates the ability of printing from a higher distance. This result is related to the elasticity behavior of the V31 ink, which keeps the deposited filament robust and able to be printed from a higher range. Even it can be used for printing on complex surfaces without the need for feedback control.

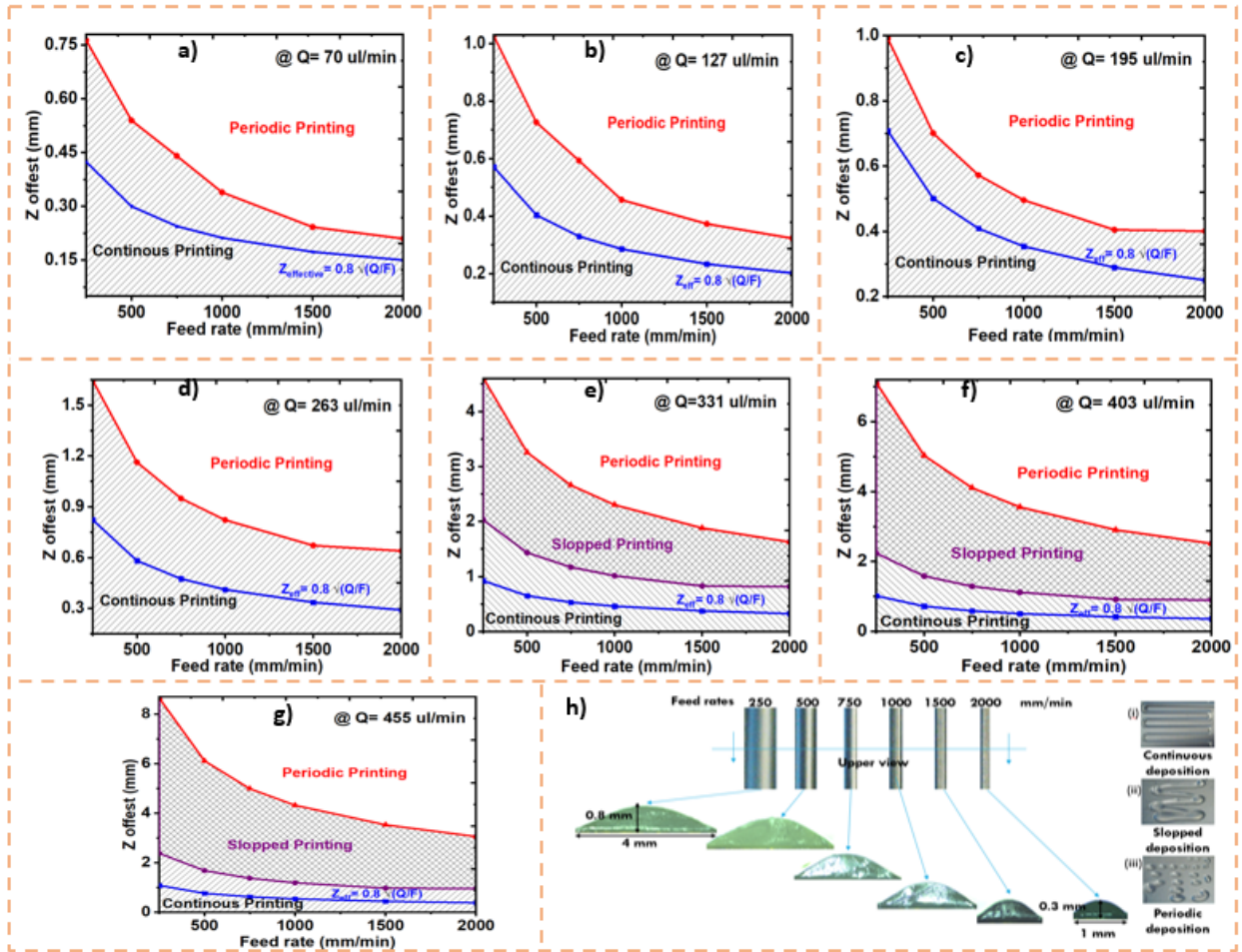


**Figure 7-2** Shows the periodic and continuous deposition regions for the a)  $Q=70\mu\text{L}/\text{min}$ , b)  $Q=127\mu\text{L}/\text{min}$ , c)  $Q=195\mu\text{L}/\text{min}$ , d)  $Q=263\mu\text{L}/\text{min}$ , e)  $Q=331\mu\text{L}/\text{min}$ , f)  $Q=403\mu\text{L}/\text{min}$ , g)  $Q=455\mu\text{L}/\text{min}$  condition. h) The resulting traces under four lights with 4 cm distance between the light and needle tip at an intensity of 20% - at 7 bar, with (i-iii) real example of three printing deposition continuous, slopped, and periodic.

A study of the cross-sectional shape of the printed trace was performed to determine the effect of various print parameters on the final trace shape. To ensure the continuity of the deposited trace, a design criterion of  $Z_{offset}=0.80\sqrt{QF}$  was used. In this experiment, a PVC transparent sheet was cut into rectangles of roughly 80mmx80mm to serve as a substrate, using the printer, a raster code was used to print two sets of traces of the V31H ink with varying feed rates on top of the PVC substrate. In contrast, the flow rate (and the pressure used to generate it) was held constant. A light guide was fixed at 4 cm, and a UV light

power of 30% was used. Various feed rates between 250 - 2000 mm/min and pressure setting between 30-90 psi was characterized. Also, traces were characterized when the deposited traces was exposed with 4 lights and 2 lights configuration (**Figure 7-3(n,k)**). Each trace section was imaged and analyzed with ImageJ software. From the cross-sectional image, various parameters, such as the trace width, height, and area for each trace cross-section, can be extracted. The trends in the trace height (**Figure 7-3a**) and the width (**Figure 7-3b**) as the feed rate was changed are displayed in **Figure 7-3**. It shows that the height of the trace and its width reduces as the feed rate is increased. Besides, we can notice that as pressure increased, the width and the height of the trace also increase. However, **Figure 7-3(a-f)** categorize light configurations, and the amount of illumination that is received by the material deposited, a bimodal distribution of the width, and the height can be observed. The significant difference between the two directions illustrates that the short timeframe (sub-second) following deposition is critical as it has a powerful effect on the resulting trace shape. This result can be seen by comparing the absolute width (**Figure 7-3a**) and heights (**Figure 7-3d**) for the same conditions but different illumination. The bimodal distribution is better illustrated when the aspect ratio (height/width) of the trace is plotted against the feed rate, as shown in **Figure 7-3(c,f)**. It was clear that the maximum aspect ratio is better in the case of 4 lights, as shown in **Figure 7-3q**.

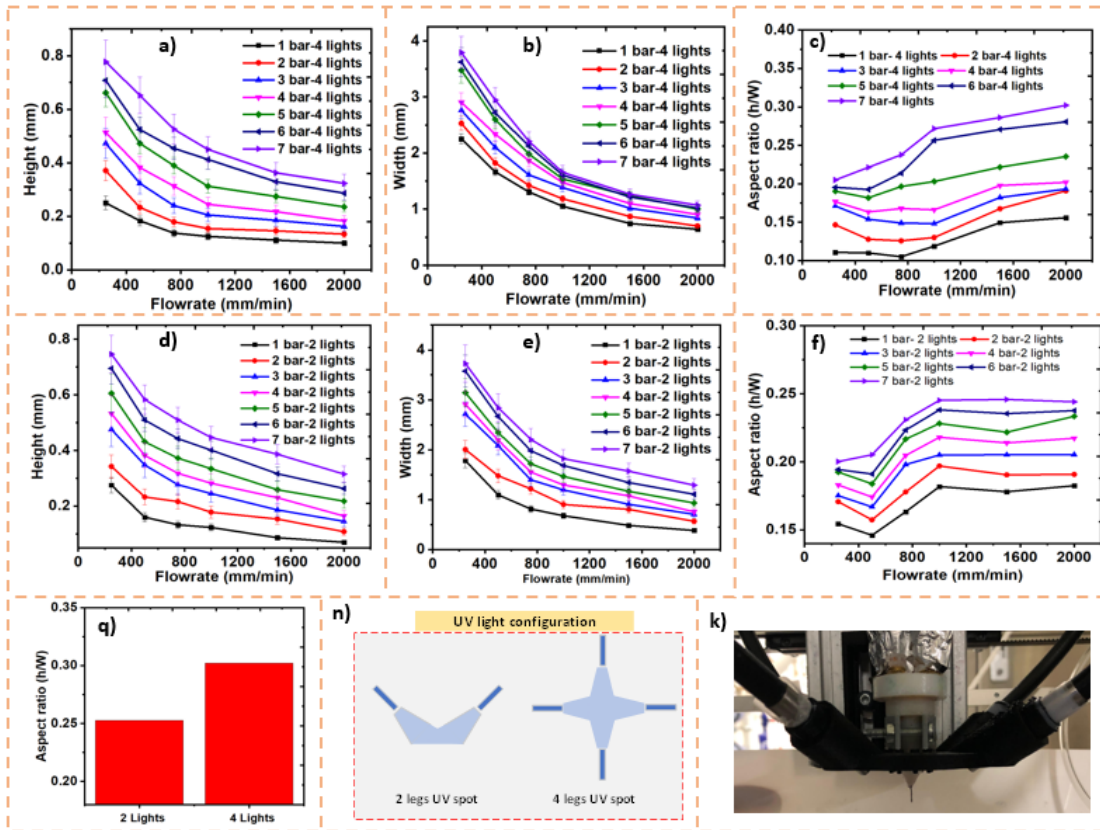


**Figure 7-3** Trace height, trace width, and aspect ratio as functions of pressure at (a-c) 4 lights configuration. (d-f) 2 lights configuration. (g) comparison between maximum aspect ratio between different settings. (h) Schematic and real photo of the 4-light setup.

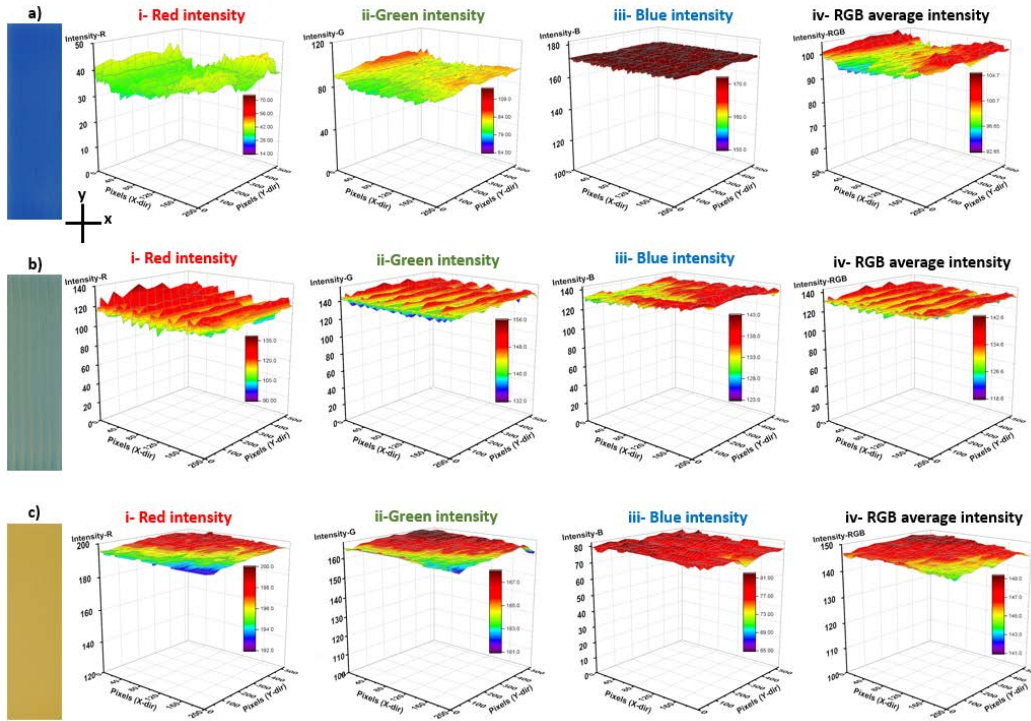


**Figure 7-4** RGB analysis for quantifying the printed object homogeneity, for three different regions a) blue zone, b) green zone, and c) yellow zone. For each zone i- R, ii-G, iii-B, and iv- average RGB intensities were presented.

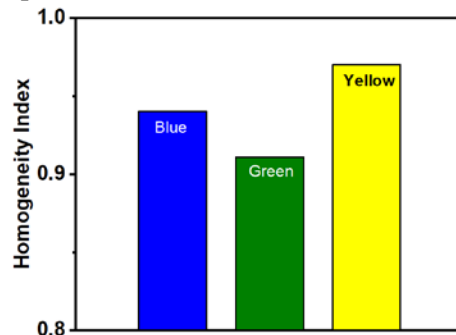


**Figure 7-5** Homogeneity index measurements for three different printed zones.

**Table 7-1.** Comparison between the published mixing systems with the current work.

Author	Materials	No. of inks	Mixing Technique	Mixing performance	Applications	Ref.
Ober .et. al	Lubricant gel, Pluronic F127, SE 1700	Two	Impeller-based active mixer	Residence time 30 sec	Mixing yield stress fluids	[1]
Bakarich, et. al	urethane UV-curable adhesive	Two	Static chaotic mixer	-----	Tough hydrogel composites	[2]
Lan, et. al	Photoresistive resin	Two	Impeller-based active mixer	12 sec with low viscous 10 cps	Multifunctional heterogeneously objects	[3]
Golobic, et. al	Al and CuO inks	Two	Impeller-based active mixer	Residence time 7.16 sec	Reactive thermite system	[4]

Ortega, et. al	Three siloxane elastomer	Two	Impeller-based active mixer	Response time 5.352 sec	Thermally engineered, flexible, mechanical pad	[5]
Kokkinis, et. al	Polyurethane acrylate (PUA) oligomers	4 inks - separate nozzles	Static mixing using two magnetic	15 sec to orient at least half particles	Complex heterogeneous composite	[6]
Deuser, et.al	Filament-based thermoplastic 8400 flexible rubber,	3 inks	Static mixer, with nozzle heater, FFF	----	Monolithic and functionally graded parts	[7]
Ren, et. al	Photosensitive resin, Fumed silica particles	3 inks	Impeller-based active mixer	----	Polyurethane (PU) objects	[8]
Current work.	UV curable silicones	Up to 4 inks	Hybird mixing	Response time less than 4 sec	2D colored gradient map, and 3D Rubix cube	--

## References

- [1] T. J. Ober, D. Foresti, and J. A. Lewis, "Active mixing of complex fluids at the microscale," *Proceedings of the National Academy of Sciences*, vol. 112, no. 40, pp. 12293-12298, 2015.
- [2] S. E. Bakarich, R. Gorkin III, R. Gately, S. Naficy, M. in het Panhuis, and G. M. Spinks, "3D printing of tough hydrogel composites with spatially varying materials properties," *Additive Manufacturing*, vol. 14, pp. 24-30, 2017.
- [3] H. Lan, "Active mixing nozzle for multi-material and multi-scale 3d printing," in *International Manufacturing Science and Engineering Conference, 2017*, vol. 50732, p. V002T01A024: American Society of Mechanical Engineers.
- [4] A. M. Golobic *et al.*, "Active Mixing of Reactive Materials for 3D Printing," *Advanced Engineering Materials*, vol. 21, no. 8, p. 1900147, 2019.
- [5] J. M. Ortega *et al.*, "Active Mixing of Disparate Inks for Multimaterial 3D Printing," *Advanced Materials Technologies*, vol. 4, no. 7, p. 1800717, 2019.
- [6] D. Kokkinis, M. Schaffner, and A. R. Studart, "Multimaterial magnetically assisted 3D printing of composite materials," *Nature Communications*, vol. 6, no. 1, p. 8643, 2015/10/23 2015.
- [7] B. K. Deuser, L. Tang, R. G. Landers, M. C. Leu, and G. E. Hilmas, "Hybrid Extrusion Force-Velocity Control Using Freeze-Form Extrusion Fabrication for Functionally Graded Material Parts," *Journal of Manufacturing Science and Engineering*, vol. 135, no. 4, 2013.
- [8] L. Ren *et al.*, "3D printing of materials with spatially non-linearly varying properties," *Materials & Design*, vol. 156, pp. 470-479, 2018/10/15/ 2018.

## **8 Appendix 2**

### **Supplementary Information for Chapter 4**

#### **Microfluidic Printheads for Highly Switchable Multimaterial 3D Printing of Soft Materials**

**Table 8-1** UV curable silicone inks formulations used in this work given in weight percentage

Inks	Vinyl Terminated PDMS	SMS-142	SMS-022	Photoinitiator TPO-L	Silicone pigment	AEROSIL -150 "Silica"
	MW "g/mol" (wt %)	MW "g/mol" (wt%)	MW "g/mol" (wt%)	wt (%)	wt%	wt%
V31H	21500 (90)	578 (7)	--	1	2	--
V35H	42300 (93)	578 (4)	--	1	2	--
V35H stiff	42300 (93)	578 (2.4)	578 (1.6)	1	2	(3) 1.3
V35H flex	42300 (93)	578 (4)	578 (4)	1	2	(3) 1.3

a: Stoichiometry (vinyl/SMS-142) = 1:1.4 TPO-L 10 mol% (164 mg)

b: UV radiation supply: Black-Ray B-100SP, 365nm UV, 1.27 W/cm<sup>2</sup>.

**Table 8-2** Heat curable silicone inks formulations used in this work given in weight percentage.

Inks	Base (wt %)	Catalyst (wt %)	Pigment (wt %)	Sylgard 527 part A (wt %)	Sylgard 527 part B (wt %)
Stiff SE 1700	89	9	2	-	-
Flexible SE 1700	80	3	2	7.5	7.5

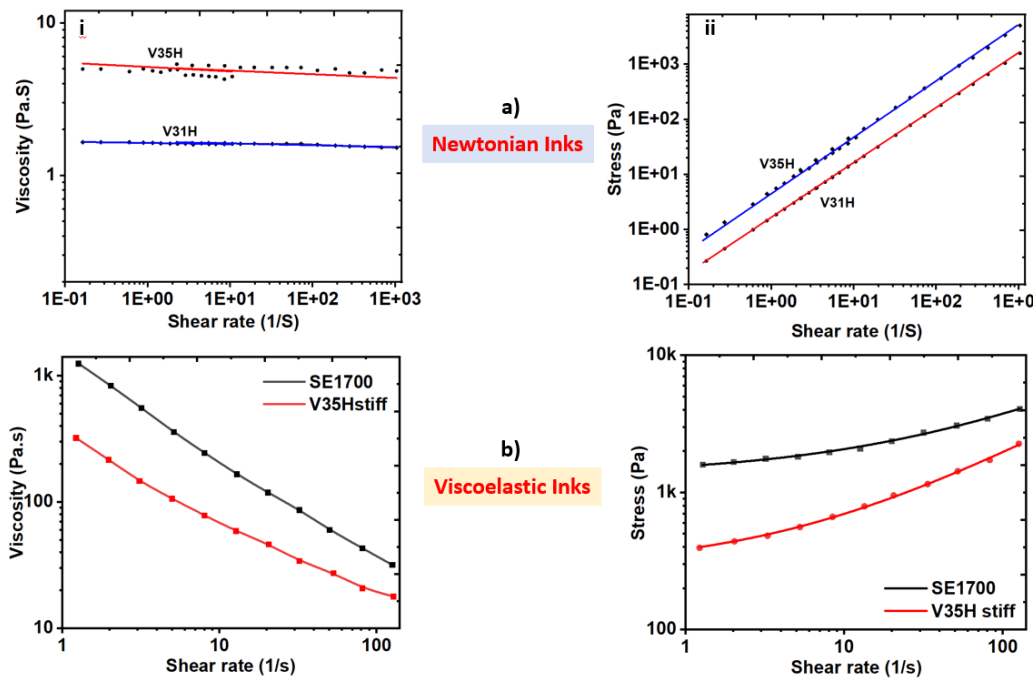


**Figure 8-1** Rheological properties of different silicone inks. Log-log plots of the apparent viscosity (i) and the shear stress (ii) as a function of shear rate for UV curable silicone elastomer inks (a-Newtonian inks, b- Viscoelastic inks), fitted by the Herschel–Bulkley model.

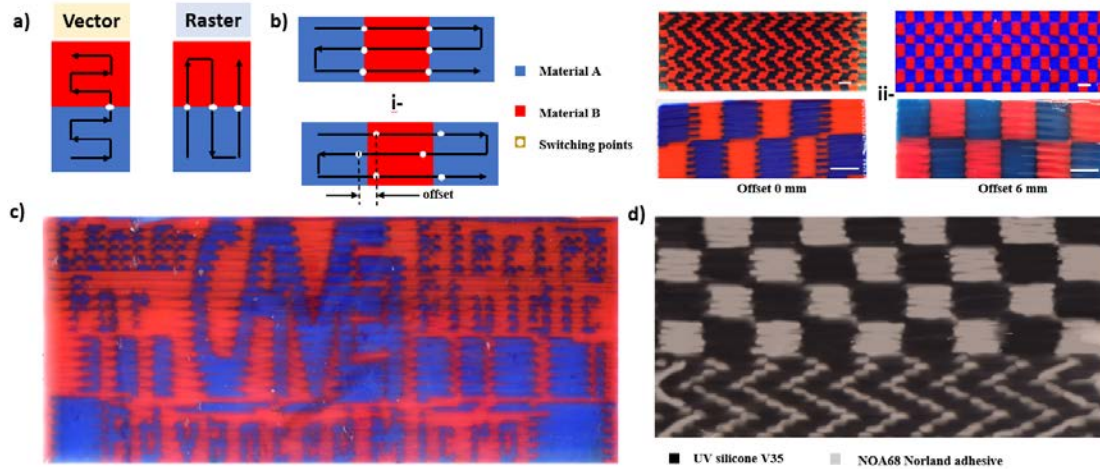


**Figure 8-2a)** Material transitions schemes for the raster and vector scan methods of printing. b) Offset length and print-path design. i- Due to the finite output of the channel,  $L_o$ , and inductance in the system, a delay occurs when switching between materials. This delay can be corrected by introducing an offset length and during parallel printing of horizontal lines in silicones (red, and blue). ii- Offset corrected printing of resolution grids using silicone viscous inks, showing gradually smaller features. Scale bars: bottom, 8 mm; top, 4 mm. c) Printing a CAMEF logo word (V35H black, V35H white) for without using offset, which created a distorted pattern. d) Segmental pattern using MSN3D printhead with two different inks, UV curable silicone V35; black, UV curable adhesive NOA68, white.

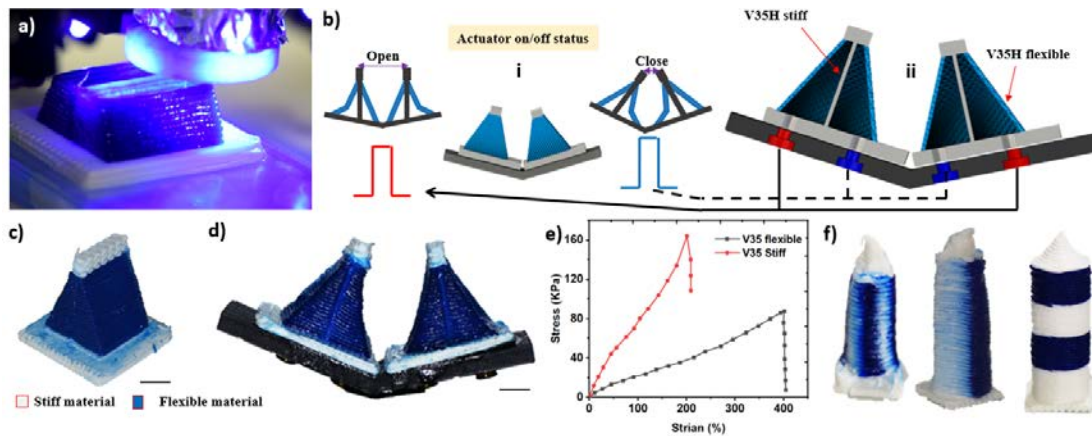


**Figure 8-3** MSN3D printing of soft-robotic actuator. a) MM3D printing of a soft robotic MSN3D printhead under UV curing. b) Illustration of the design elements of the two chambers actuator. i- schematics of the two states on/off actuator corresponding to the step pulse. ii- Cad model of the actuator. c, d) Photographs of the printed actuator and the assembled actuators. e) Stress–strain curves from tensile tests for V35H stiff (0.6 MPa) and V35H flexible (0.8 MPa) silicones. f) Printed 3d patterns like finger with two materials with different periodical arrangements.

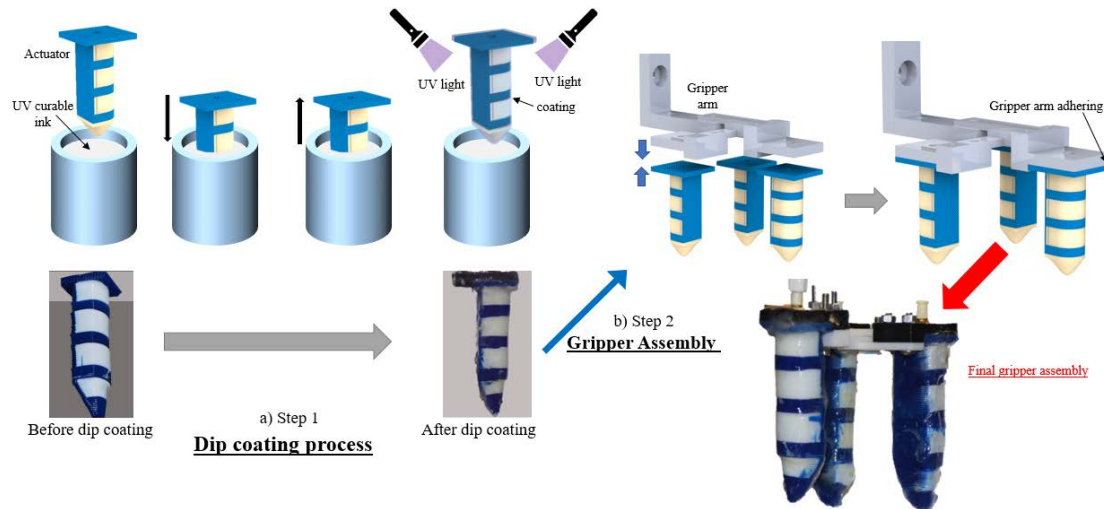


**Figure 8-4**Assembling steps used to create a soft-gripper. a) Dip coating process using UV curable silicone, to create thin film covering the printed soft actuator (around 1 mm). b) Assembling operation with the gripper arm, which made from PLA using conventional 3d printer. The arm was attached to the soft actuator using super glue and left for 24 hrs for curing.

In general, the current DIW printing relies on inks of specific rheology to compromise with printing process, levying limitations on the selection of the printable materials. The viscosity range utilized in our printhead ranges from  $10^{-1}$  to  $10^3$  Pa·s, based on the designed printhead channels and the printing process conditions constrains in our pneumatic system.

## **9 Appendix 3**

### **Supplementary Information for Chapter 5**

**Contour tracing printheads for multimaterial printing over complex surfaces**

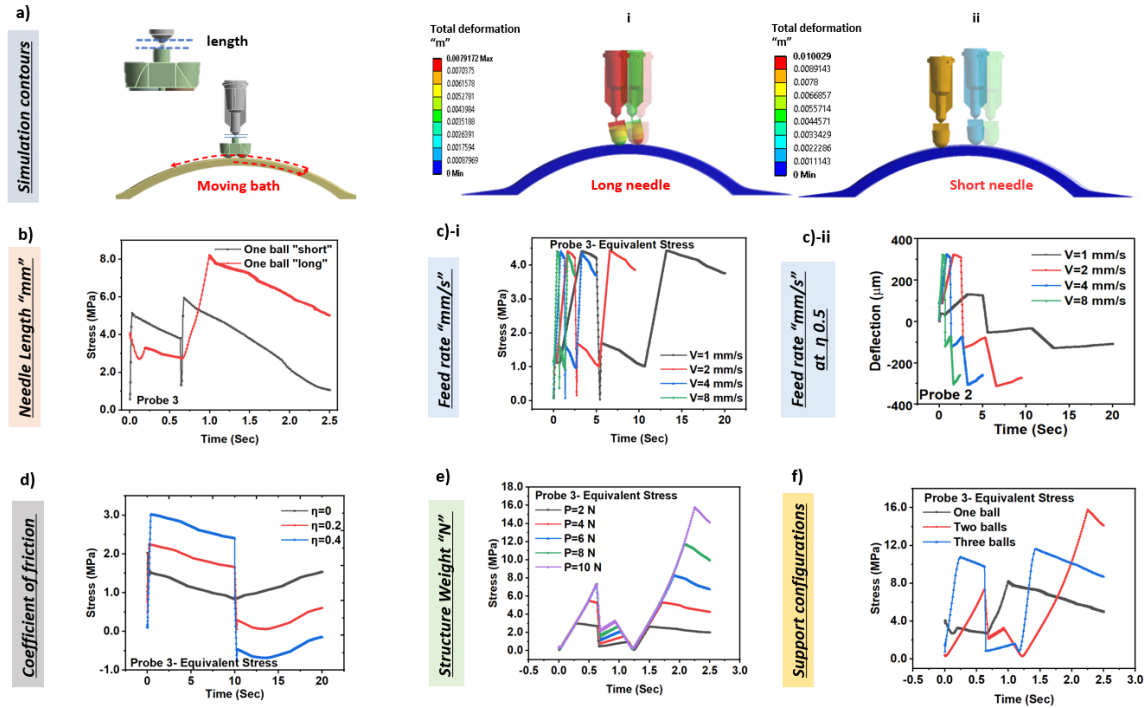


**Figure 9-1 FEA results a)** Deformation contours in case of one ball configuration with different needle length showing the deflection with different positions. Then, we tested different parameters investigated the process parameters to get the effect on the generate stress; **b)** needle length using one ball configuration with two different values at feed rate 8 mm/s, coefficient of friction of 0.2, load of 10 N. **c) i-** The effect of the structure weight on the model equivalent stress, while using feed rate of 8 mm/s, coefficient of friction of 0.2 and needle length of 4 mm. **ii-** The effect of feed rate on the structure deflection, while using a coefficient of friction of 0.5, a load of 10 N and needle length of 4 mm. **d)** The effect of feed rate on the structure equivalent stress, while using coefficient of friction of 0.5, load of 10 N and needle length of 4 mm. **e)** The effect of friction between ball and substrate on the model equivalent stress, while using feed rate of 1 mm/s, load of 10 N and needle length of 4 mm. **f)** Comparing between the three ball support configurations with the model equivalent stress, while using feed rate of 8 mm/s, load of 10 N, coefficient of friction of 0.2 and needle length of 4 mm.

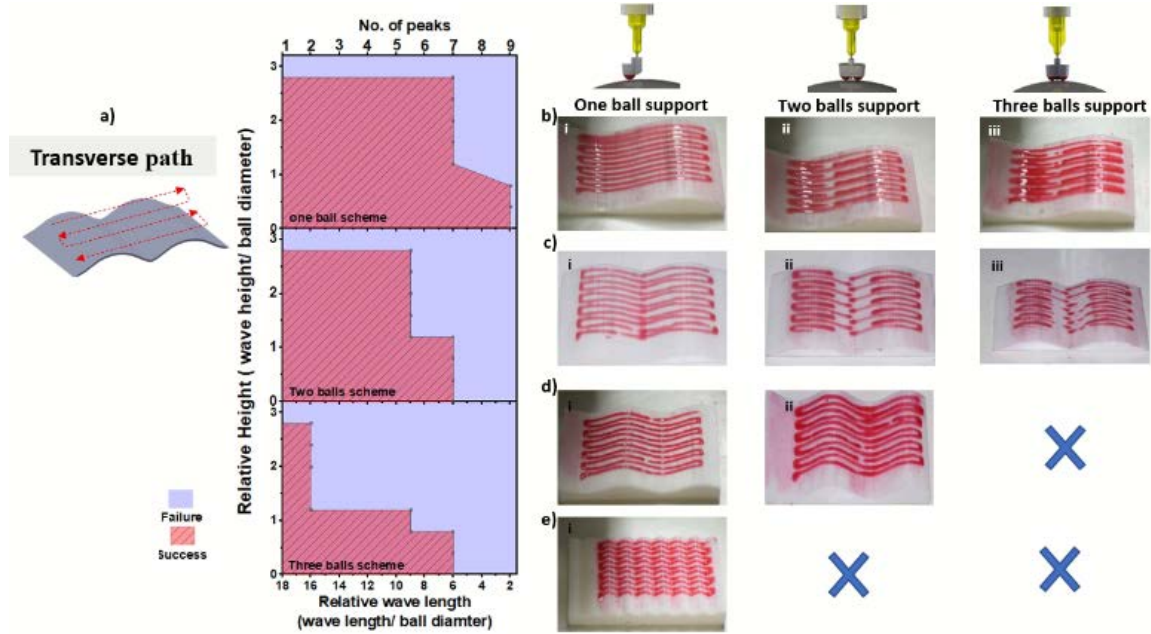


**Figure 9-2** Printing feasibility study of each configuration with complex wavy surface. **a)** Feasibility contours by varying the wavy relative height and wavelength using transverse path pattern. On the right is the actual printed patterns with different wavy surfaces using the three ball support configurations, **b)** one peak wavy surface, **c)** two peaks wavy surface, **d)** three peaks wavy surface, and **e)** multiple peaks wavy surface.

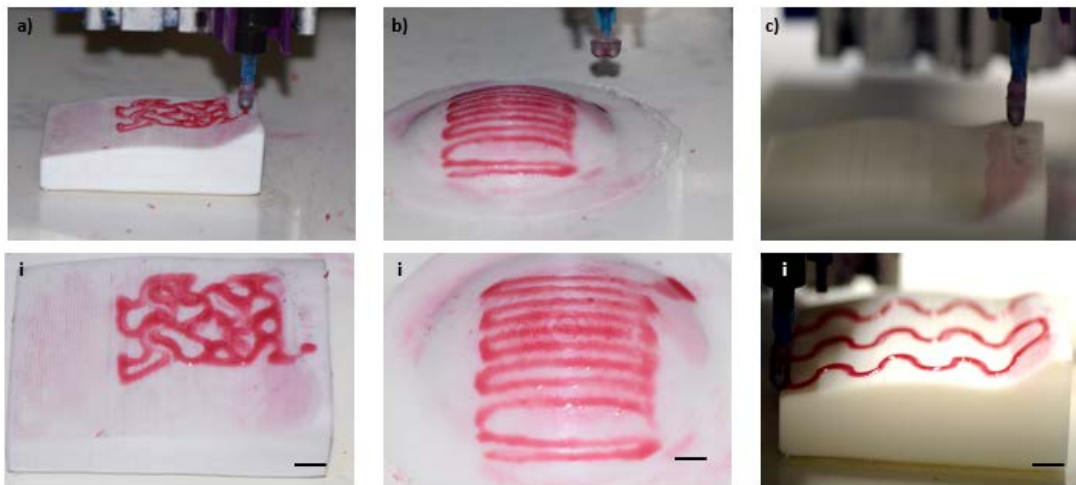


**Figure 9-3** **a)** Mesh wavy interfered pattern printing over an inclined surface using the one ball configuration, with mesh element size 2mm\*2mm. **b)** Zig-zag pattern printing over a dome surface using the one ball configuration, with pitch size of 4 mm. **c)** Wavy zig-zag pattern printing over an inclined surface using one ball configuration, with pitch of 7 mm. All scale bars are 10 mm.

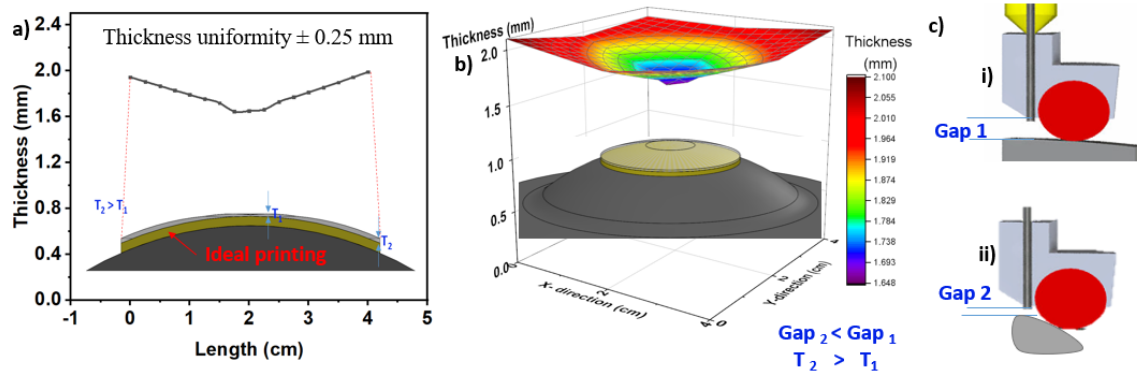


**Figure 9-4** a) 2D plot for thickness uniformity for the printed color maps over the dome surface. b) 3D surface contour for the printed color maps over the dome surface. c) the gap scheme in case of i) the top of the dome surface and ii) at the near bottom level, showing how the gap is decreased in which affects the printed thickness.

**Table 9-1.** Comparison between the published tracking printing systems with the current work.

Author	3D printing method	Tracking Technique	Printing Resolution	Target Topography	System Complexity	Ref.
N. Bausch et.al.	FDM – Single material.	Multiple axis M/C. with 3D scanning	Nozzle Gap 0.2±0.04 mm	Priori unknown uneven objects	High	[1]
Shembekar et.al.	FDM– Single material.	6 DOF robot arm with free trajectory planning	0.5 mm	Nonplanar surfaces with minimum roughness of 1.088	High	[2]
Huang et.al.	Inkjet- EHD printing. single material.	Machine vision programmable robotization techniques	100 nm	3D curved electronics	Too High	[3]
Adams et.al.	DIW – Single material.	Modified G-code based on standard surface with substrate alignment	100 µm	Printing on curvilinear surfaces	Moderate-but limited to one shape	[4]
Padilla et.al.	FDM – Single material.	Mathematical algorithm to project a printing trajectory	0.5 mm	Hilbert curve and lattices printed on curved surfaces	High complex mathematical algorithm	[5]
McCaw et.al.	FDM – Single material.	Curved-Layer Manufacturing	0.15 mm	Bézier surfaces	High complex mathematical algorithm	[6]
Zhu et. al.	DIW – Single material.	Integrated robotic system aided by computer vision	--	Cell-laden hydrogels onto of live mice and human hand.	High	[7]
Coulter et. al.	DIW – Single material.	Four-axis 3D printer with triangulation laser measurement device	0.5 mm	Inflated balloon substrate mounted on fourth axis.	High	[8]
Yu et.al.	Aerosol printing– Single material.	Aerosol printing	300 µm	Multiscale surface topologies	High	[9]
Current work	DIW- Multimaterial (up to 4 inks)	Passive spring-loaded mechanical system	0.8 mm	Human hand, dome, uneven inclined, Bézier surfaces	Low	-

## References

- [1] N. Bausch, D. P. Dawkins, R. Frei, and S. Klein, "3D printing onto unknown uneven surfaces," *IFAC-PapersOnLine*, vol. 49, no. 21, pp. 583-590, 2016.
- [2] A. V. Shembekar, Y. J. Yoon, A. Kanyuck, and S. K. Gupta, "Trajectory planning for conformal 3d printing using non-planar layers," in *International Design Engineering Technical Conferences and Computers and Information in Engineering Conference*, 2018, vol. 51722, p. V01AT02A026: American Society of Mechanical Engineers.
- [3] Y. Huang *et al.*, "Programmable robotized 'transfer-and-jet' printing for large, 3D curved electronics on complex surfaces," *International Journal of Extreme Manufacturing*, vol. 3, no. 4, p. 045101, 2021.
- [4] J. J. Adams *et al.*, "Conformal printing of electrically small antennas on three-dimensional surfaces," *Advanced Materials*, vol. 23, no. 11, pp. 1335-1340, 2011.
- [5] C. Rodriguez-Padilla, E. Cuan-Urquizo, A. Roman-Flores, J. L. Gordillo, and C. Vázquez-Hurtado, "Algorithm for the Conformal 3D Printing on Non-Planar Tessellated Surfaces: Applicability in Patterns and Lattices," *Applied Sciences*, vol. 11, no. 16, p. 7509, 2021.
- [6] J. C. McCaw and E. Cuan-Urquizo, "Curved-layered additive manufacturing of non-planar, parametric lattice structures," *Materials & Design*, vol. 160, pp. 949-963, 2018.
- [7] Z. Zhu *et al.*, "3D printed functional and biological materials on moving freeform surfaces," *Advanced Materials*, vol. 30, no. 23, p. 1707495, 2018.
- [8] F. B. Coulter, B. S. Coulter, E. Papastavrou, and A. J. Ianakiev, "Production techniques for 3D printed inflatable elastomer structures: part II—four-axis direct ink writing on irregular double-curved and inflatable surfaces," *3D Printing Additive Manufacturing*, vol. 5, no. 1, pp. 17-28, 2018.
- [9] X. Yu *et al.*, "Customizable Nonplanar Printing of Lithium-Ion Batteries," *Advanced Materials Technologies*, vol. 4, no. 11, p. 1900645, 2019.